

**UCLA**

**UCLA Electronic Theses and Dissertations**

**Title**

Strain-mediated Multiferroics Heterostructures for Life Science Applications

**Permalink**

<https://escholarship.org/uc/item/59h9n01w>

**Author**

Xiao, Zhuyun

**Publication Date**

2021

Peer reviewed|Thesis/dissertation

UNIVERSITY OF CALIFORNIA

Los Angeles

Strain-mediated Multiferroics Heterostructures

for Life Science Applications

A dissertation submitted in partial satisfaction  
of the requirements for the degree Doctor of Philosophy  
in Electrical and Computer Engineering

by

Zhuyun Xiao

2021

© Copyright by

Zhuyun Xiao

2021

# ABSTRACT OF THE DISSERTATION

Strain-mediated Multiferroics Heterostructures

for Life Science Applications

by

Zhuyun Xiao

Doctor of Philosophy in Electrical Engineering

University of California, Los Angeles, 2021

Professor Robert N. Candler, Chair

Magnetism is a workhouse for electric power generation at the macroscale, responsible for a large fraction of the electricity generation today. However, conventional approaches to energy conversion using magnets fail at a small scale due to Joule heating from electric currents. Recently, a method has emerged – room-temperature composite multiferroics coupling electrics and magnetics - that allows for control of magnetism via voltage as opposed to current. With this newfound capability, industrial & commercial application spaces are rapidly opening up for domains, including ultra-low-power spintronics devices, microwave devices, and even magnetic particle and cell sorting platforms.

Meanwhile, personalized medical therapies hold the potential of new forms of highly effective therapies. One example of personalized medicine is CAR T-cell therapy, which uses patients' cells for cancer treatments. However, such an approach requires technology that can analyze and sort these cells in high quantity, selecting only the cells that will be the most effective cancer fighters. Magnetic cell sorting is a popular approach for high throughput cell

sorting. Still, there is no current method capable of capturing and culturing arrays of cells and then selectively releasing the desired ones.

Recent advances in room-temperature multiferroic devices, such as devices where magnetism is controlled by electric fields, provide a path for capture, culture, and selective release of cells. However, work remains to understand how to manipulate the magnetic structures that capture these cells.

This work aims to develop a multiferroics-based cell manipulation platform with high scalability and can achieve cell control locally. This work first conducts an in-depth study of the magnetization and multiferroic properties of various magnetostrictive layers, including Ni, FeGa, Ni/CoFeB, and Terfenol-D micromagnets on  $\text{Pb}(\text{Mg}_{1/3}\text{Nb}_{2/3})\text{O}_3]_{0.69}[\text{PbTiO}_3]_{0.31}$  (PMN-PT) piezoelectric substrates. It then selects the highly magnetostrictive Terfenol-D micromagnets in the same size scale as human cells as the candidate for life science applications. It also investigates the interaction between these micromagnets and cells before and after a voltage is applied across the PMN-PT substrate. The key questions addressed include how to create structures from a magnetoelastic material that are in the same size scale as human cells ( $20 \mu\text{m}$ ) and control the magnetization of these structures to release cells on-demand via electric fields. Furthermore, this work demonstrates the potential of using patterned surface electrodes to generate localized strain in order to control the behavior of the micromagnets both locally and selectively.

The dissertation of Zhuyun Xiao is approved.

Gregory P. Carman

Sam Emaminejad

Benjamin S. Williams

Robert N. Candler, Committee Chair

University of California, Los Angeles

2021

# Table of Contents

List of Figures .....	ix
List of Tables.....	xxv
<b>Chapter 1 Introduction.....</b>	<b>1</b>
<b>1.1 Multiferroics and Magnetoelectric Materials .....</b>	<b>1</b>
<b>1.2 Composite Multiferroics Heterostructures and Electric-field control of Magnetization .....</b>	<b>3</b>
<b>1.3 Application of Multiferroics .....</b>	<b>5</b>
<b>1.4 Cell sorting state-of-the-art .....</b>	<b>7</b>
1.4.1 Isolated functional cells and Immunotherapy .....	9
1.4.2 Magnetic-based magnetic particle control.....	9
1.4.3 Microchannels for bead-based cell manipulation .....	10
<b>1.5 Ferromagnetic domains .....</b>	<b>10</b>
<b>1.6 Magnetization Energy.....</b>	<b>11</b>
1.6.1 Micromagnetics and Magnetic Energy .....	11
1.6.1.1 Magnetostatic energy .....	12
1.6.1.2 Exchange energy .....	13
1.6.1.3 Magnetocrystalline energy .....	14
1.6.1.4 Magnetoelastic /Magnetostrictive energy.....	14
<b>1.7 Simulation of strain-mediated magnetic domain reorientation in magnetostrictive microstructures .....</b>	<b>15</b>
<b>1.8 Common Piezoelectric Constituent in multiferroic heterostructures .....</b>	<b>19</b>
<b>Chapter 2 Characterization of Magnetoelectric Multiferroic Devices .....</b>	<b>21</b>

<b>2.1</b>	<b>Magnetic characterization .....</b>	<b>21</b>
2.1.1	SQUID Magnetometer .....	21
2.1.2	Magneto-Optical Effect and Magneto-optic Kerr Effect (MOKE).....	22
2.1.3	Magnetic Force Microscopy .....	25
2.1.4	From X-ray Circular Dichroism to X-ray Photoemission Electron Microscopy (XMCD-PEEM) .....	28
<b>2.2</b>	<b>Piezoelectric characterization – Strain .....</b>	<b>30</b>
2.2.1	Metal Foil Strain Gauge .....	30
2.2.2	Laue X-ray Microdiffraction for probing strain at micron-scale .....	32
<b>Chapter 3</b>	<b>Tunable magnetoelastic effect in voltage-controlled exchange-coupled composite multiferroic microstructures .....</b>	<b>38</b>
<b>3.1</b>	<b>Multiferroics systems with composite magnetic layer.....</b>	<b>38</b>
<b>3.2</b>	<b>Experimental setup and magnetic characterization.....</b>	<b>39</b>
3.2.1	Sample Preparation .....	42
3.2.2	X-ray diffraction measurements of four thin film samples with varied thickness combinations .	43
3.2.3	Magnetic characterization of the exchange-coupled multiferroic heterostructures .....	43
3.2.4	Magnetic contrast study by XMCD-PEEM.....	45
<b>3.3</b>	<b>In-operando magnetic imaging &amp; Simulation .....</b>	<b>46</b>
3.3.1	Magnetic moment reorientation as a function of field in microstructures of different lateral dimensions.....	52
3.3.2	Quantitative analysis of the magnetic moment direction from PEEM images.....	58
3.3.3	Micromagnetic simulations of magnetic energy variation in single layer and bilayer systems....	67
<b>3.4</b>	<b>Concluding Remarks .....</b>	<b>69</b>
<b>Chapter 4</b>	<b>Magnetic particle control via cytocompatible magnetostrictive microstructures .....</b>	<b>71</b>
<b>4.1</b>	<b>Magnetic particle control with magnetic stray field .....</b>	<b>71</b>



<b>4.2</b>	<b>Experimental methods.....</b>	<b>74</b>
4.2.1	Fabrication of microstructures on piezoelectric substrate and magnetization state initialization 74	
4.2.2	XMCD-PEEM for magnetic domain imaging .....	75
4.2.3	Nano-magnetic particle preparation .....	76
4.2.4	Trapping of superparamagnetic beads by stray field from Ni and FeGa microstructures.....	77
4.2.5	Electric field-driven particle motion .....	78
4.2.6	Optical microscope and Fluorescent microscope imaging and data analysis.....	78
4.2.7	Microfluidics Integration .....	79
4.2.8	Cell viability test.....	79
<b>4.3</b>	<b>Results and Discussion.....</b>	<b>80</b>
4.3.1	XMCD-PEEM imaging of the microstructure arrays and localized fluorescent bead trapping .....	80
4.3.2	Strain profile characterization .....	85
4.3.3	Electric-field driven particle displacement .....	86
4.3.4	Cell viability on magnetoelectric devices.....	88
<b>4.4</b>	<b>Concluding Remarks .....</b>	<b>89</b>
<b>Chapter 5</b>	<b>Single-domain Multiferroic Array-addressable Terfenol-D (SMArT)</b>	
	<b>Micromagnets for Cell Capture and Release.....</b>	<b>91</b>
<b>5.1</b>	<b>Overview of Terfenol-D based single-cell control .....</b>	<b>91</b>
<b>5.2</b>	<b>Magnetic cell separation: bulk and single-cell .....</b>	<b>92</b>
5.2.1	Domain structures in Magnetoelastic materials -- State of the Art.....	94
<b>5.3</b>	<b>Fabrication of Terfenol-D thin film and microdisks.....</b>	<b>95</b>
<b>5.4</b>	<b>Magnetic Property Characterization .....</b>	<b>98</b>
5.4.1	X-ray Absorption Spectra & X-ray Magnetic Circular Dichroism for Terfenol-D .....	99
5.4.2	SQUID & MFM for magnetic microdisk property characterization.....	104

5.4.3	XMCD-PEEM imaging of single-domain and multi-domain magnetoelastic microstructures ....	109
5.4.4	In-situ mapping of the magnetic domain capture regions via fluorescently-labeled magnetic beads (FMBs) .....	114
<b>5.5</b>	<b>Magnetic force landscape .....</b>	<b>119</b>
5.5.1	In-situ high-throughput measurement of the magnetoelastic stray field (H <sub>s</sub> ) magnetic binding force in a viscous medium .....	121
<b>5.6</b>	<b>Electric-field-driven single cell release from Terfenol-D microdisk .....</b>	<b>126</b>
5.6.1	Effect of strain on Terfenol-D microstructures and cells .....	131
<b>5.7</b>	<b>Time-dependent measurement of single-cell secretion .....</b>	<b>134</b>
<b>5.8</b>	<b>Concluding Remarks .....</b>	<b>136</b>
<b>Chapter 6</b>	<b>Localized Strain Profile in Surface Electrode Array .....</b>	<b>138</b>
<b>6.1</b>	<b>Patterned Surface Electrodes and Induced-Strain .....</b>	<b>138</b>
<b>6.2</b>	<b>Single crystal PMN-PT substrates with different electrode configurations.....</b>	<b>140</b>
6.2.1	Deviatoric strain tensor .....	142
<b>6.3</b>	<b>Experimental details for electrically-induced deviatoric strain calculation .....</b>	<b>143</b>
6.3.1	Effect of poling to the local deviatoric strain distribution .....	145
6.3.2	Experiment vs Simulation results .....	149
6.3.3	Outlier removal for strain mapping .....	152
6.3.4	Voltage-induced axial deviatoric strain ratio $\epsilon_{yy}'/\epsilon_{xx}'$ .....	156
<b>6.4</b>	<b>Concluding Remarks .....</b>	<b>160</b>
<b>Chapter 7</b>	<b>Conclusions .....</b>	<b>161</b>
<b>References.....</b>		<b>172</b>

## List of Figures

<b>Figure 1.1.</b> Number of publications on multiferroics in the past two decades. ....	1
<b>Figure 1.2.</b> Venn diagram illustrating the relationship between multiferroic and magnetoelectric materials, adapted from [1]. ....	2
<b>Figure 1.3.</b> Schematics of coupling in multiferroic and magnetoelectric materials. The phase control diagram in the center has been adapted from [14].....	5
<b>Figure 1.4.</b> Timeline of the recent strain-mediated multiferroic platforms developed at TANMS (Translational Applications of Nanoscale Multiferroic Systems) research center. Figures from [17], [19]–[24]......	6
<b>Figure 1.5.</b> A white space chart for cell sorting state of the art. DEP: Dielectrophoretic sorting. MACs: Magnetic-assisted cell sorting. FACs: Fluorescence-assisted cell sorting. OEW: Optoelectronic tweezers.....	8
<b>Figure 1.6.</b> (a)-(b) Conventional methods for controlling micromagnets at sub-micron-meter scale involve remote/bulky external magnets to generate a magnetic field. (a) Rotating magnetic field $H$ from an external magnetic source displaces domain walls in a circular Py ring [31]. (b) A rotating magnetic wheel magnetizes micropillars to manipulate the magnetic potential energy landscape to move particles. ....	9
<b>Figure 1.7.</b> Domain formation in a ferromagnet with reduced magnetoelastic energy from left to right. Figure from [36]......	13
<b>Figure 1.8.</b> Description of the two simulation approaches: the unidirectional model only tracks inverse magnetostrictive effect, while the bidirectional model considers both the magnetostrictive and inverse magnetostrictive effects. ....	16
<b>Figure 1.9.</b> Generates in-plane anisotropic strain with parallel-plate electrodes on (011)-cut PMN-PT.....	19
<b>Figure 2.1.</b> Schematics of a SQUID flux sensor. Figure from [54]......	21

**Figure 2.2.** The polarized light angle rotates by  $\theta$  after reflection. The ellipticity of the reflected polarized light also changes with respect to magnetization  $M$ . Figure adapted from [56]......23

**Figure 2.3.** Example hysteresis loops of Ni thin film on PMN-PT [58]. Normalized magnetic Kerr rotation  $M$ - $H$  curves measured at different electric fields with magnetic field parallel to  $\theta = 0^\circ$ ,  $\theta = 45^\circ$  and  $\theta = 90^\circ$  directions, where  $\theta$  is the angle between in-plane magnetic field  $H$  and  $[100]$  direction of PMN-PT. (a)(c)(e) Without polymer. (b)(d)(f) With polymer.....24

**Figure 2.4.** A large coercivity change can be seen from the Kerr rotation vs Magnetic Field hysteresis loop of Terfenol-D thin film on PMN-PT after being poled at 0.6 MV/m. Figure adapted from [59]. Copyright © 2015 AIP Advances. ....25

**Figure 2.5.** Working principle of Magnetic Force Microscopy (MFM). Figure from [61]. ...26

**Figure 2.6.** Magnetic Force Microscope is a helpful tool to characterize domain walls and stray-field in micro- and nanoscale magnetic structures. (a) Ni nanoscale disks on PZT substrate with a rotatable single domain. Figure adapted from [20]. (b) Single domain in Terfenol-D disk on Si wafer. Figure from [65]–[67]......28

**Figure 2.7.** Element-specific X-ray magnetic circular dichroism obtained at the absorption edge of the element of interest (e.g., for the L-edge absorption in Fe) provides magnetic information. (a) An example of X-ray absorption spectra taken with opposite circular polarizations for Fe. (b) XMCD is the difference between the LCP and RCP spectra. (c) Origin of XMCD, adapted from [60]. ....29

**Figure 2.8.** Schematic of a PEEM microscope and image formation at CCD, based on PEEM-3 microscope at the Advanced Light Source, Berkeley National Lab. ....30

**Figure 2.9.** (a) Schematic of a resistive strain gauge. (b) An example biaxial rosette with two strain gauges mounted perpendicular to each other. Figure from [71], annotated. (c) Schematic

of strain gauge glued to the top electrode on a bulk piezoelectric material PMN-PT to measure principal strains in both x and y directions. Figure from [11]. .....32

**Figure 2.10.** (a) Setup of the experimental area of the X-ray Microdiffraction beamline. A MAR 133 x-ray CCD camera placed in the 45 degree reflective geometry collects the diffracted x-ray from the sample. (Beamline 12.3.2, Advanced Light Source of Lawrence Berkeley National Laboratory) (b) A Laue pattern with the most intense reflections indexed with *hkl* Miller indices. It can be used to obtain the deviatoric strain tensor. Figure from [72]......32

**Figure 2.11.** Schematics of Bragg’s law and difference between the two types of basic x-ray diffraction experiment: monochromatic method (top right) and Laue method (bottom right). .....34

**Figure 3.1 .** (a) Sample schematic and crystallographic orientation of the PMN-PT crystal, with the surface normal along the [011] direction. After patterning, the magnetic microstructures were initialized by an external magnetic field,  $\mu_0 H_{init} = 300$  mT, applied as in the schematic. (b) SQUID magnetometry hysteresis loops for the different magnetic thin-films, before patterning, on PMN-PT investigated in this study (layers thickness in nm). The magnetic field was applied in-plane along the [01-1] direction. ....40

**Figure 3.2.** X-ray diffraction (XRD) measurements of four thin film samples on PMN-PT and a reference PMN-PT sample. The result shows no diffraction peak from the magnetic layer. ....43

**Figure 3.3.** (a) Zoomed-in SQUID magnetic hysteresis loops (from Fig. 1(b) from main text) of the corresponding magnetic thin films on PMN-PT investigated in the study. (b) Normalized x-ray magnetic circular dichroism hysteresis loops for Fe and Ni taken at room temperature in Ni (2 nm)/CoFeB (2 nm)/PMN-PT and CoFeB (2 nm)/Ni (2 nm)/PMN-PT (the element used for the measurement is underlined and indicated in bold). The magnetic field was applied at a grazing incidence of  $20^\circ$  with respect to the surface of the sample, with its in-plane component

along the [01-1] direction. (c) Same as in (b), with magnetic field axis corrected by multiplying  $\cos(20^\circ)$  to reflect the amplitude of in-plane component of the applied magnetic field.....44

**Figure 3.4.** (a) Schematic of the XMCD-PEEM imaging setup. The orientation of the device with respect to the incident x-ray beam is illustrated. Prior to imaging, an initialization magnetic field ( $H_{init}$ ) was applied. The crystallographic orientations of the [011]-cut PMN-PT are highlighted, with [100] being the compressive strain axis, and [01-1] being the tensile strain axis. (b) A completed device on an LCC with crystallographic directions of [011] cut PMN-PT and the orientation of the magnetic field for magnetization state initialization ( $H_{init}$ ) marked. The substrate is mounted on a piece of Si wafer of 0.3 mm thick so that the sample surface is at the proper height (0.8 mm from the LCC surface) for XMCD-PEEM imaging. The top surface of the multiferroic heterostructure is grounded (as indicated by “GND”, and the bottom is connected to a hot wire (as indicated by “+V”). (c) A device is mounted onto a PEEM-3 sample holder at beamline 11.0.1.1 of ALS, LBNL. Figure from [91] .....46

**Figure 3.5.** (a) XMCD-PEEM images at Fe and Ni  $L_3$  edges showing the initial magnetic state in bilayer microsquares. Note the similarity in magnetic state for each device in both the Fe  $L_3$ -edge and Ni  $L_3$ -edge, evidence of exchange coupling in this system. The purple and turquoise frames indicate where a Landau magnetic flux closure state is initially observed. The green arrows indicate the initializing magnetic field,  $\mu_0 H_{init} = 300$  mT. The grey scale bar with the arrows describes the contrast levels of magnetic orientation in the PEEM images. (b) Ni- $L_3$  edge XMCD-PEEM of Ni (2 nm) microsquares shows no magnetic contrast, as expected for a paramagnetic state. (c) Description of the two types of magnetic vortex states observed in the investigated samples. The schematics of squares in grey-scale describe the magnetic configurations in the PEEM images. ....49

**Figure 3.6.** Electric field-controlled magnetic reorientation in 2- $\mu\text{m}$  microsquares from four different Ni-CoFeB bilayer systems. The ratio between the Ni and CoFeB magnetic volumes controls the magnetoelectric effect in these multiferroic systems. ....51

**Figure 3.7.** XMCD-PEEM images of the microsquare arrays with different lateral dimensions, acquired at Fe- and Ni-  $L_3$  edges as a function of applied electric field ranging from 0 to 0.8 MV/m. (Left) CoFeB (2 nm)/ Ni (2 nm)/ PMN-PT microsquares with side length ranging from 1 to 4  $\mu\text{m}$ . CoFeB contributes more strongly to the observed magnetic domain reorientation. (Right) CoFeB (2 nm)/ Ni (15 nm)/ PMN-PT microsquares with side length ranging from 1 to 4  $\mu\text{m}$ . In both samples, the magnetic moments are exchange coupled in microsquares of all dimensions, at all electric fields.....53

**Figure 3.8. (a)** Simulated bilayer micromagnetic system started from a vortex state 0 MV/m (top row), and 0.8 MV/m (bottom row). In the bottom row, the micromagnetic results of single layer Ni and CoFeB are included on both ends of the spectrum, where the magnetostrictive coefficient of CoFeB is tuned in the range of interest between 50 and 90 ppm. **(b)** Comparison between micromagnetic outcomes and experimental findings for the CoFeB (2 nm)/ Ni (2 nm) system indicate the suitable  $\lambda S$  value of CoFeB to be 85 ppm. **(c)** Electric-field induced magnetic moment reorientation angles in CoFeB (2 nm)/ PMN-PT and CoFeB (2 nm)/ Ni (2 nm)/ PMN-PT samples, calculated from both experiment and simulation results. ....57

**Figure 3.9.** Quantitative analysis of the magnetic contrast and magnetic moment direction variation in (a) CoFeB (2 nm)/ PMN-PT and (b) CoFeB (2 nm)/ Ni (2 nm)/ PMN-PT. The mean and standard deviations of the color contrasts from four triangular domains before and after the electric field is applied (i.e., at both 0 MV/m and 0.8 MV/m) are used to calculate the extent of magnetic moment reorientation. The first row (in a blue box) in each table shows the analysis of the XMCD-PEEM experiment data, denoted by “(Exp.)” in the legends of the plots.

The second row (in a red box) in each table presents the analysis of the micromagnetic simulation data, denoted by “(Sim.)” in the legends of the plots. ....61

**Figure 3.10.** Comparison of energy variations in different 2- $\mu\text{m}$  microsquare systems using micromagnetic simulations, starting from vortex state until reaching an equilibrium state once the equivalent uniaxial anisotropy is applied. We report the variation of exchange energy, demagnetization energy, anisotropy energy and total energy in: **(a)** single 2 nm-thick Ni layer; **(b)** single 2 nm-thick CoFeB layer; **(c)** system whose energies are the sum of individual energy terms from (a) and (b); **(d)** 2 nm-thick Ni layer from the CoFeB/Ni bilayer system; **(e)** 2 nm-thick CoFeB layer from the CoFeB/Ni bilayer system; **(f)** Ni(2 nm)\CoFeB(2 nm) bilayer system; **(g)** a 4 nm thick single layer that takes the averages of the magnetic properties of the CoFeB and Ni ( $M_s = 7.4 \times 10^5 \text{ A/m}$ ,  $\lambda_s = 26 \text{ ppm}$ ); and **(h)** a 4 nm thick single layer similar to that of (g), but with a  $\lambda_s$  of 52 ppm as the sum of  $\lambda_s$  from CoFeB and Ni. **(i)** The total energy variation in the eight aforementioned layers and systems. The micromagnetics parameters used for the simulation are reported in Section 3.3.3 -Table 3.3. At the top of each graph, the saturation magnetostriction coefficients (in ppm) used to model the layers are and the layer thicknesses are listed in the parentheses. Inset images are the magnetic configurations ( $m_x$ ) at the final equilibrium states.....66

**Figure 3.11.** Oscillation of the energy vs. time profile in the simulation of bilayer system. The plot here shows the energy variation of a bilayer system that takes the average of Ni and CoFeB material parameters for individual layers, and with a saturation magnetostriction of 26 ppm. ....68

**Figure 3.12.** Final magnetic states of the bilayer stack for the “Uniform and Average” case from (a) when treated the bilayer as a single film stack and (b) when treated as a bilayer system are identical.....69



**Figure 4.1.** Schematic of the sample and the relative orientations between the initial field direction and the PMN-PT principal strain axes. After the initialization field,  $H_{init}$ , is removed, an electric field is applied through the thickness of the ferroelectric PMN-PT via the top and bottom electrodes made of Pt thin films, inducing a differential in-plane strain.....75

**Figure 4.2.** The magnetization hysteresis loop measured by SQUID magnetometry for a suspension of the superparamagnetic nanobeads (~600 nm in diameter) used for the fluorescent imaging. ....76

**Figure 4.3.** Microfluidic chip integrated on the top surface of the magnetoelectric device. Arrays of magnetostrictive micropatterns are located at the center of the device, viewed by optical microscopy. ....79

**Figure 4.4.** Fluorescent beads of 0.6  $\mu\text{m}$  (green) trapped and localized on the magnetic domain walls of the Ni microstructures. (a) XMCD-PEEM images of Ni rings. (b) Overlay of bright field and fluorescent microscope images of fluorescent beads coupled to rings of 6  $\mu\text{m}$ , 4  $\mu\text{m}$ , and 2  $\mu\text{m}$  in diameter. (c) Time lapse images of 4  $\mu\text{m}$  Ni rings capturing fluorescent bead (0.6  $\mu\text{m}$  in diameter) in the microfluidic channel, corresponding to the location of the DWs of Ni rings, as shown in the PEEM images. (d) XMCD-PEEM images of Ni squares with 2  $\mu\text{m}$  in length. (e) Overlay of bright field and fluorescent microscope images of fluorescent beads captures at the corners of 2  $\mu\text{m}$  squares. (f) Time lapse images of FeGa squares of 2  $\mu\text{m}$  in length capturing fluorescent bead at the corner. Dashed circle highlighted the position of the fluorescent bead. ....82

**Figure 4.5.** (a) Representative particle trapping event in the absence of flow (1  $\mu\text{m}$  particle, 4  $\mu\text{m}$  diameter ring. Left: Particle path overlaid on image of 4  $\mu\text{m}$  Ni ring. (b) Particle displacement relative to position at time 0 (Euclidean distance) vs time over the course of the trapping event. Trapping occurs around 1.5 seconds and most random motion ceases. ....83

**Figure 4.6.** (a) Initialized onion states in polycrystalline FeGa rings of varied width and diameter, with a thickness of 20 nm, observed by XMCD-PEEM. (b) Rings of various sizes in (a) trapping fluorescent nanoparticles via the magnetic stray field emanating from the onion state domain. (c) Squares of 2  $\mu\text{m}$  in length trapping fluorescent particles on the corners. ....84

**Figure 4.7.** Time lapse images of 2  $\mu\text{m}$  ring (No.3) capturing a fluorescent bead in the microfluidic channel, corresponding to the location of the DWs of FeGa rings, as shown in the PEEM images. Ring No. 1 and No. 2 have captured beads prior to No. 3. All the three rings trapped beads locally along the x direction, in which  $H_{\text{init}}$  was applied. ....85

**Figure 4.8.** (a) Magnetolectric device is mounted on a leadless chip carrier (LCC), and a biaxial strain gauge is mounted on the surface of the device for strain profile characterization. (b) Linear strain response along the [01-1] and [100] directions of the PMN-PT substrate to the applied electric-field is measured using the strain gauge. Figure from [58]. ....86

**Figure 4.9.** Continuous magnetic bead movement, driven by applied electric field to the PMN-PT with linear strain response, along the perimeter of the Ni ring, 4  $\mu\text{m}$  in diameter and 600 nm in width, captured by optical microscope. The diameter of the bead is 1  $\mu\text{m}$ . ....86

**Figure 4.10.** (a) XMCD-PEEM images of a Ni square with a magnetic vortex state at zero electric field, and evolves into a two-domain state at 0.36 MV/m, (b) a Ni square of 2  $\mu\text{m}$  in length trapping fluorescent beads on the corners before and after applying voltage. (c) Sample orientation with respect to the initialization magnetic field direction. ....88

**Figure 4.11** - Viability test on multiferroic heterostructure platform using Calcein AM stain (a) stained viable cells (b) stain leakage of damaged cells. (c) before applying voltage (d) after ramping up the voltage to 400 V applied to the top and bottom electrodes, with corresponding electric field up to 0.8 MV/m, the cells are viable for downstream bio-applications.....89

**Figure 5.1.** An abbreviated view of technological development of magnetic cell separation. Three decades ago, permanent magnets were introduced to control cell on the bulk level. Since

then, magnetic-based cell sorting has been among the popular commercialized cell sorting mechanisms. This work aims for single cell manipulation by combining a multiferroics platform with microfluidics channels. ....93

**Figure 5.2.** Cross-sectional schematic of SMArT micromagnet for single-cell separation via strain-mediated multiferroics to turn on and off the capture and release of cells via voltage application to the device. ....94

**Figure 5.3.** Fabrication process and characterization of Terfenol-D microstructures. (a) Fabrication process. (b) Scanning electron microscope (SEM) micrograph of (b) 3  $\mu\text{m}$  diameter and (c) 20  $\mu\text{m}$  diameter microdisks. Figure from [65]. ....98

**Figure 5.4.** X-ray magnetic circular dichroism of Terfenol-D thin film and microdisks confirm the overall good magnetic quality of the film and etched microdisks. For the disks, a few nm of oxidation of Fe also occurs at surface below the 4 nm thick Ta capping..... 100

**Figure 5.5.** XAS and XMCD spectra of Terfenol-D continuous film and micropatterned film (a) electron yield measured with Fe  $L_{3,2}$  edge for the continuous film (b) electron yield measured with Dy  $M_{5,4}$  edge for the continuous film (c) fluorescence yield measured with Fe  $L_{3,2}$  edge for continuous film (d) fluorescence yield measured with Dy  $M_{5,4}$  edge for continuous film (e) electron yield measured with Fe  $L_{3,2}$  edge for the micropatterned film (f) electron yield measured with Dy  $M_{5,4}$  edge for the micropatterned film (g) luminescence yield measured with Fe  $L_{3,2}$  edge for micropatterned film (h) luminescence yield measured with Dy  $M_{5,4}$  edge for micropatterned film..... 102

**Figure 5.6.** M vs H plots of patterned Terfenol-D microdisks measured over the course of 100 days. .... 105

**Figure 5.7.** Fabrication and characterization of single-domain Terfenol-D microstructures. (a) Schematic of the SMArT device and microscope image showing magnetic bead capture (green) on Terfenol-D single-domain micropatterns on a PMN-PT substrate without the use of an

external magnet. (b) Scanning electron microscope (SEM) image of a 3  $\mu\text{m}$  Terfenol-D disk and (c) cross sectional cut by focused ion beam (FIB) showing (d) Terfenol-D microstructure on PMN-PT. (e) Magnetic force microscopy image of the 3  $\mu\text{m}$  disk reveals a single domain configuration (f) that enables strong and precise magnetic trapping of magnetic beads on the magnetized poles (scale bar, 1  $\mu\text{m}$ ). (g) Magnetic hysteresis loop of the Terfenol-D disks shows a large saturation magnetization of 780 kA m<sup>-1</sup> and a coercivity of 0.3 T, as measured by SQUID. A large fraction of the magnetization is retained upon the removal of the saturation magnetic field..... 109

**Figure 5.8.** XMCD-PEEM imaging is used to image the magnetic domain state of Terfenol-D micromagnets of 20  $\mu\text{m}$  in diameter. Magnetic contrast in a 20  $\mu\text{m}$  disk at the elemental absorption edges of Fe, where white contrast indicates the magnetization is pointing in the -x direction and the black contrast indicates the magnetization is pointing in the +x direction. The opposite contrast of XMCD-PEEM images taken at two absorption edges of Fe confirms the effective single-domain magnetic configuration without an external magnetic field..... 110

**Figure 5.9. XMCD-PEEM imaging of single domain and multi-domain magnetoelastic microstructures.** (a) An example of single domain and multi-domain states in disks at relaxation, simulated by mumax3 micromagnetics modeling, a 2D plane on the surface of microstructure [102]. (b) X-ray absorption spectrum (XAS) image of the magnetic domain at Fe absorption edges. The X-ray energies were then tuned to the energies of Fe L<sub>3</sub> (706.9 eV) and L<sub>2</sub> (719.9 eV) absorption edges, respectively to excite the electron 2p→3d transition with circularly polarized x-ray demonstrated in the (c) XMCD-PEEM images of the magnetic contrast at the elemental absorption edges of all three elements (Tb, Dy, Fe) in the Terfenol-D confirm the single domain configuration in the 20  $\mu\text{m}$  Terfenol-D microstructures. The black contrast indicates the magnetization is pointing along the +x direction; the white indicates the magnetization is pointing in the -x direction. The entire disk functions nearly as a magnet with

a single domain. (d) XMCD-PEEM images of Ni, FeGa, and CoFeB disks with 2  $\mu\text{m}$  in diameter grown on PMN-PT reveal multi-domain configurations at remanence..... 113

**Figure 5.10.** Comparison of length scales for single-domain states in different materials. Single-domain states in magnetoelastic Terfenol-D at remanence are observed for order of magnitude higher length scales (20  $\mu\text{m}$ ), while other magnetoelastic micromagnets (CoFeB, Ni, FeGa) switch to a multi-domain state around 1-2  $\mu\text{m}$  in diameter as observed in XMCD-PEEM after magnetic-field removal (**Figure 5.9**). ..... 113

**Figure 5.11.** Magnetic capture performance of single-domain Terfenol-D microstructure arrays. (a) Optical photograph of the microfluidic/multiferroic device (scale bar, 5 mm). (b) Mapping the magnetic capture distribution of fluorescently labeled magnetic beads on single-domain Terfenol-D microstructures. (c) FeGa structures of the same size transition into a multi-domain state, while Terfenol-D structures of less than 40  $\mu\text{m}$  in diameter remain single-domain. .... 117

**Figure 5.12.** High-throughput imaging of magnetic bead capture regions on magnetoelastic microstructures in a large array. (a) Microfluidic device integration on top of Terfenol-D micropatterns fabricated on sapphire (top) and silicon (bottom). Fluorescence microscopy images of the large array were acquired after introducing fluorescently labeled magnetic beads (FMB) to a number of n magnetoelastic microstructures. Uniform magnetic bead capture were observed across a massive array of magnetically initialized Terfenol-D single-domain microstructures. (b) Image analysis software was used to quantify measurements and generate heatmaps of the magnetic bead capturing regions, where pixels with higher intensity correspond to the magnetic bead locations. Single-domain Terfenol-D microstructures demonstrated uniform magnetic bead capture locations on the magnetized poles. (c) Heat maps of multi-domain microstructures 250  $\mu\text{m}$  and 500  $\mu\text{m}$  in diameter demonstrated scattered bead capture locations between the magnetized dipoles. .... 118

**Figure 5.13.** (a) Optimized magnetic capture ( $F_m > F_d$ ) and release ( $F_m < F_d$ ) flow conditions to map the magnetic capture behavior of Terfenol-D micromagnets in-situ with different magnetic beads sizes (2.8-9.1  $\mu\text{m}$ ) illustrated in bright field images in (b) with the governing forces: magnetic binding force  $F_m$  and hydrodynamic drag  $F_d$ . The solid lines are the theoretical Faxén drag correction force given by Eq (1). (c) The magnetic binding force ( $F_m$ ) is measured as a function of magnetization angle ( $\theta$ ) on single-domain Terfenol-D 20  $\mu\text{m}$  microdisks via a range of flow velocities to increase the spatial resolution of the 2D magnetic force map illustrated in (d)..... 120

**Figure 5.14.** High-throughput in-situ measurement of the magnetic binding force for Terfenol-D microstructures in a large array. (a) Hydrodynamic drag force for different bead diameters were computed numerically using experimental flow rates, microfluidic channel dimensions and the Terfenol-D microstructure geometry. (b) The fraction of magnetic beads released increases at higher flow rates. (c) Under the same flow rates, 2.8, 4.3, 7.3 and 9.1  $\mu\text{m}$  beads experience different hydrodynamic drag forces. At the magnetic bead release flow condition, the hydrodynamic drag force measurement is estimated to equal the magnetic binding force  $\sim 36$  pN for different bead diameters. .... 125

**Figure 5.15.** (a)-(b) Surface distribution of magnetic field norm of both 2.8  $\mu\text{m}$  and 9.1  $\mu\text{m}$  beads with a magnetic shell thickness of 60 nm. The magnetic field norm decays toward zero a few  $\mu\text{m}$  away from the beads. (c) Angle dependence of magnetic force components on the 2.8  $\mu\text{m}$  bead with shell thickness of 60 nm. The magnitude of total magnetic force reaches the highest when the bead is located along the magnetization  $y$ -axis ( $\theta = 0^\circ$ ). Here  $F_y$  and  $F_z$  are pointing in the  $-y$  and  $-z$  directions. (c) Finite Element simulation result of magnetic force  $F_y$  on the magnetically coated beads with different combinations of bead diameter and magnetic coat thickness. The beads are located at the magnetization axis, as shown in the schematics, corresponding to the experimental observation. .... 126

**Figure 5.16.** Microfluidic/Multiferroic SMArT device set up. The blue arrow indicates the flow direction of the microfluid in the channel. ....127

**Figure 5.17.** Strain response of the PMN-PT substrate along [100] and [01-1] crystallographic directions with respect to the out-of-plane electric field, measured by a biaxial strain gauge. Applying a 0.8 MV/m electric field induces compressive strain of 1300 ppm along the [100] direction and tensile strain of 850 ppm along [011], illustrated in the PMN-PT crystal structure in **Figure 1.9**. ....128

**Figure 5.18.** A total strain of 2150 ppm induced by an electric field of 0.8 MV/m perturbs the single domain state due to magnetoelastic coupling, reorients the magnetic domain  $\sim 40$  degrees to the electrically-induced easy axis (along [01-1] direction). In contrast, multi-domains rearrange in a manner that has little impact on the net direction of magnetization. 129

**Figure 5.19.** (a) Real-time tracking of the displacement on the surface due to strain in the PMN-PT substrate (reference location labeled with \*). (b) Bight field and fluorescent images of a magnetically labeled and fluorescently labeled single cell. (c) When subjected to electrically-induced strain, individual magnetically labeled single cells were released from the Terfenol-D micromagnets to the outlet of the microchannel..... 130

**Figure 5.20.** Experimental procedure for tracking the change in magnetization pole reorientation of Terfenol-D microstructures after applying strain on PMN-PT substrate (yellow). (a) First, we image the Terfenol-D microstructures before introducing beads or applying beads or strain. Second, we flow beads in a microfluidic channel on the PMN-PT substrate and image the Terfenol-D microstructures. Third, we wash away the beads then apply voltage-induced strain on the PMN-PT substrate. Fourth, we flow new magnetic beads and image their locations after strain. We noticed the beads settle on a newly induced magnetic easy axis in the Terfenol-D microstructure. (b) We repeat the same procedure but without the washing step (3) on larger microstructures that capture more than one bead on their magnetized

pole. We noticed beads that are not directly attached to the magnetized pole dislocate to the new magnetization angle after applying strain. Scale bar, 5  $\mu\text{m}$ . ..... 132

**Figure 5.21.** Magnetically labeled cell preparation for capture and release via voltage induced strain. (a) Fluorescently stained cells coated with magnetic beads are imaged with bright field and fluorescence microscopy. (b) Microchannel flow conditions were optimized for cell capture at a flow velocity  $U_{(F_m > F_d)}$  and release at  $U_{(F_m < F_d)}$  on Terfenol-D microstructures. (c) Terfenol-D microstructures were cytocompatible for cell growth and expansion for downstream applications. Scale bar, 20  $\mu\text{m}$ . ..... 133

**Figure 5.22. Time-dependent secretion measurement of magnetically captured single cells.**

(a) Schematics of the adapted immunoaffinity assay to measure IL-2 secretion from single human primary T cells. (b) Fluorescent images of IL-2 secretion signals (TRITC) from human primary T cells (DAPI) at the end of a 2-hour incubation (scale bar, 50  $\mu\text{m}$ ). One representative low-secreting cell (cell ①) and one high-secreting cell (cell ②) are identified, and their secretion signals at 0, 1 and 2 hours are magnified in (c) (scale bar, 20  $\mu\text{m}$ ). (d) Single-cell IL-2 secretion signals tracked every 10 minutes for 2 hours. Sub-populations of high-secreting cells ( $n_1 = 4$ ) are characterized from low-secreting cells ( $n_2 = 17$ ) by a threshold of normalized fluorescence  $> 1.20$  at the end of 2 hours. The highlighted lines ① and ② signify the time-dependent IL-2 secretion signals from the two identified cells in (b) and (c). \*\*\* $P < 0.001$  using two-tailed Student's t-test. .... 136

**Figure 6.1.** (a) Schematics of PMN-PT with parallel-plate electrodes. (i) (top) (011)-cut exhibits a strong in-plane anisotropic strain; (bottom) X-ray microdiffraction results confirm the presence of a negative compressive deviatoric strain along [100] and a positive tensile deviatoric strain along [01-1] when voltage is applied. (ii) (top) (001)-cut with in-plane compressive strains when voltage is applied; (bottom) X-ray microdiffraction results show compressive deviatoric strain along both [100] and [010] directions. (b) Total in-plane strain



(difference between deviatoric strains in the directions highlighted in (a)) vs electric field. Error bars represent the standard deviation of the pixel-wise micron-scale strain. (c) (Left) Schematics of X-ray microdiffraction with *in situ* voltage applied. Surface electrode arrays on (001)-cut PMN-PT. (Middle) Samples B and C have varied electrode pair distances, spacing and angle arrangements. In each region, four dot squares serve as location reference points. (Right) A demonstration of the reconstructed regional strain maps ( $\epsilon_{xx'}$ ) of the 12 dotted regions from Sample C. .... 141

**Figure 6.2.** Strain maps showing different deviatoric strain components in Region 12, Sample B. The strain values reflect the difference between deviatoric strains taken at 400 V and 0 V. (a) Normal components of deviatoric strain tensor:  $\epsilon_{xx'}$ ,  $\epsilon_{yy'}$ ,  $\epsilon_{zz'}$ ; (b) Shear components of deviatoric strain tensor:  $\epsilon_{xy'}$ ,  $\epsilon_{yz'}$ ,  $\epsilon_{xz'}$  ..... 142

Figure 6.3. Plots of average regional axial deviatoric strain vs voltage in the unpoled Sample B differ largely from these in the prepoled Sample B. .... 146

**Figure 6.4.** (a) A 3D zoomed-in view of an electrode pair on PMN-PT with an applied voltage, with axial strains illustrated by arrows. (b) From simulation, strain distribution in between electrode pairs and outside of electrode pairs. Each highlighted box has a size of  $250 \times 250 \mu\text{m}^2$ . .... 149

**Figure 6.5.** (a) X-ray microdiffraction scans are conducted locally with an area of  $250 \times 250 \mu\text{m}^2$  in 7 regions on Sample B. The electrode gap distance decreases from 600 to 400  $\mu\text{m}$  in 100  $\mu\text{m}$  decrements for regions 1-3, and 10-12. Reference region 5 is outside of the individual electrode pairs. (Top) 2D strain map for region 12, in both  $x$ - and  $y$ - directions. Each pixel has a size of  $10 \times 10 \mu\text{m}^2$ . (Bottom) Simulation results. (b) Violin plot with the distribution of (Left) the induced strains along  $x$ - and  $y$ - directions ( $\epsilon_{xx'}$  and  $\epsilon_{yy'}$ , respectively) and (Right) the in-plane biaxial strain difference. (c) Average axial strain vs. voltage for all regions in Sample B (Left) from experiment and (Right) simulation. .... 152

**Figure 6.6.** (a) Remove outliers by comparing the strain value of each pixel to its k-nearest neighbors ( $k = 8$ ). (b) Example of outlier removal for Region 11 in Sample B. Data collected when the applied voltage is 200V.....153

**Figure 6.7.** A parametric sweep study using finite element simulation shows the effect on the induced deviatoric strain from electrode gap distance and angle. Corresponding average strain values obtained experimentally from regions 1-3 (labeled R1-R3, respectively) in Sample B are highlighted in circles with error bars representing 95% confidence intervals. **(a)** Gap distance between the electrode pairs affects the axial strain magnitudes. For the range explored experimentally, an increase in gap distance leads to a decrease in strain (highlighted by a dotted circle). **(b)** Role of electrode angle (with respect to the [010] crystallographic direction). In Sample B, as the angle increases from  $0^\circ$  to  $11.25^\circ$ , the deviatoric strains decrease slightly. ....155

**Figure 6.8.** Average regional induced deviatoric strain vs applied voltage in Sample C. (a) Tensile strain along the  $x$ -direction. (b) Compressive strain along the  $y$ -direction. ....158

**Figure 6.9.** Comparison of axial deviatoric strain ratios  $\epsilon_{yy}' / \epsilon_{xx}'$  in regions 3 and 12 at 200 V and 400 V. From both (a) experiment and (b) simulation results, the ratios are higher in both regions from Sample C than those from Sample B, implying the additional electrodes in sample C couple with their neighbors and lead to increased anisotropic strain.....159

## List of Tables

<b>Table 3.1.</b> Magnetic easy axis reorientation direction upon applying electric field up to 0.8 MV/m. Table from [92]. .....	52
<b>Table 3.2.</b> Calculation of reorientation angle ( $\Delta\theta_{rot}$ ) of both experiment and simulation results for (a) CoFeB (2 nm) and (b) CoFeB (2 nm)/ Ni (2 nm) reported in the main text. Here $\theta_B$ , $\theta_W$ , $\theta_{G1}$ and $\theta_{G2}$ denote the average angle of the magnetic moment in the ROI marked by black, white, grey 1 and grey 2, respectively. $\theta$ is the average of the reorientation angle at 0.8 MV/m when compared to at 0 MV/m. Similarly, $\sigma_B$ , $\sigma_W$ , $\sigma_{G1}$ and $\sigma_{G2}$ are standard deviation of the angles for each ROIs, and $\sigma$ is the average standard deviation. ....	60
<b>Table 3.3.</b> Intrinsic material dependent constants used for the micromagnetics simulation, where $\lambda_s$ is the saturation magnetostriction coefficient, $\alpha$ is the damping constant, $A_{ex}$ is the exchange stiffness constant, and $Y$ is the Young's modulus [107]. ....	67
<b>Table 6.1.</b> Regional deviatoric strain components in Sample B, Region 12.....	143
<b>Table 6.2.</b> Regional $\varepsilon_{yy}' / \varepsilon_{xx}'$ in Sample B .....	157

## ACKNOWLEDGEMENTS

First and foremost, I would like to express my sincere gratitude to my advisor Prof. Rob N. Candler, for the continuous support during my graduate study. His guidance and vision have been instrumental to my Ph.D. journey. I am very grateful to Prof. Candler for providing me with helpful advice on research directions, giving me the freedom to explore and delve deeper into various research areas, and guiding me to grow in research and life. His kindness, patience, support, and trust have constantly motivated me to pursue my goals.

I am deeply grateful to my outstanding colleagues and collaborators for their indispensable support and contribution to my research work. I would like to thank my labmates in the Sensors and Technology Lab (Dr. Jere Harrison, Dr. Hyunmin Sohn, Dr. Srikanth Iyer, Dr. Yuan Dai, Dr. Max Ho, Dr. Sidhant Tiwari, Dr. Jimmy Wu, Dr. Ling Li, Siyuan Liu, Ben Pound) for all the great times spent together, my TANMS 3D thrust collaborators (Dr. Maite Goirienea, Dr. K.P. Mohanchandra, Dr. Roberto Lo Conte, Ruoda Zheng, Dr. Hanuman Singh, Dr. Marc Chooljian, Dr. Rachel Steinhardt, Dr. Jizhai Cui, Dr. Cheng-Yen Liang, Dr. Cai Chen, Dr. Hyunmin Sohn, Michael Guevara De Jesus, Dr. Elaine Wang, Dr. Reem Khojah, and other TANMS collaborators (Dr. Kevin Fitzell, C. Ty Karaba) for collaborating on multiple projects, and the undergraduate students I have worked with (Chelsea Lai, Cornelio Torres Juarez, Colin Perry, Rosie Zhu, Brendan Li, Ryan Doan, Bryant Espino, Edwin Jimenez, Isley Alvarado, Zachariah Mustafa).

My sincere thanks also go to the Magnetic Dichroism Group at Advanced Light Source, Lawrence Berkeley National Laboratory. I was a member from 2018-2019 as a doctoral fellow in residence. I would like to thank my supervisors Dr. Elke Arenholz and Dr. Alpha N'Diaye, group members Dr. Rajesh Chopdekar, Dr. Padraic Shafer, Dr. Christoph Klewe, and Dr. Ingrid

Hallsteinsen for their guidance and support. I would like to thank Dr. Rajesh Chopdekar and Dr. Nobumichi Tamura at Advanced Light Source, Lawrence Berkeley National Laboratory, for their instructive technical advice and help on beamline experiments and publications. Special thanks to Dr. Maite Goiriena and Dr. Hanuman Singh for working together on many memorable overnight beamline experiments in the past years.

I would also like to extend my sincere thanks to my committee members, Prof. Gregory P. Carman, Prof. Sam Emaminejad, and Prof. Benjamin Williams, for taking the time and effort to guide my dissertation writing and providing insightful comments and advice.

This work would not have been possible without the help of staff members and facilities, including the Nanoelectronics Research Facility (NRF), the Center for High-Frequency Electronics (CHFE), the Integrated Systems Nanofabrication Cleanroom (ISNC) in the California NanoSystems Institute (CNSI) at UCLA, and Advanced Light Source, Lawrence Berkeley National Laboratory. In addition, I would like to thank the Center for Translational Applications of Nanoscale Multiferroic Systems (TANMS) at UCLA, funded by National Science Foundation, for the financial and knowledge support. I would also like to thank the additional financial support for this work, including the UCLA EE Departmental Fellowship, ALS Doctoral Fellowship in Residence, and UCLA Dissertation Year Fellowship.

Finally, the emotional and financial support from my family and friends is indispensable for my graduate career. Special thanks to my parents Xiaomei and Yun, my grandma Yuli, aunt Amber and uncle Nick, aunt Nancy and Professor Tai for their unconditional support.

## VITA

### Education

---

- 2015-2017 M.S. in Electrical Engineering  
University of California, Los Angeles, California, United States
- 2011-2015 B.A. (Hons.) in Physics  
Minor in French, Computer Science, *Magna Cum Laude*  
Bryn Mawr College & Haverford College, Pennsylvania, United States

### Employment

---

- 2015-2021 Graduate Student Researcher  
Department of Electrical and Computer Engineering, UCLA
- 2018-2019 Doctoral Fellow in Residence  
Advanced Light Source, Lawrence Berkeley National Laboratory

### Honors and Awards

---

- 2020-2021 UCLA Dissertation Year Fellowship
- 2020 TANMS CLIMB Award
- 2019 CESASC Scholarship – Anna and John Sie Foundation Scholarship
- 2019 Best Student Presentation Award Winner (Sponsor: IEEE Magnetics Society)  
*14<sup>th</sup> Joint MMM-Intermag Conference, Washington, DC*
- Best Paper Award Finalist  
*PowerMEMS 2018 (The 18th International Conference on Micro and Nanotechnology for Power Generation and Energy Conversion Applications) Daytona, Florida*
- 2018-2019 ALS Doctoral Fellowship in Residence  
*Advanced Light Source, Lawrence Berkeley National Laboratory*
- 2017-2018 The Edward K. Rice Outstanding Masters Student Award  
*UCLA Henry Samueli School of Engineering*
- 2017-2018 UCLA ECE Outstanding Student Award, Distinguished Master's Thesis
- 2015-2016 UCLA EE Department Fellowship
- 2013 Science Horizon Fellowship, HHMI

### Journal Publications (\*: co-first author)

---

1. R. Khojah\*, **Z. Xiao\***, K. P. Mohanchandra\*, M. Goirienna, R. Chopdekar, G. P. Carman, J. Bokor, R. N. Candler, D. Di Carlo, "Programmable Single Domain Magnetoelastic Terfenol-D Micromagnets For Single-cell Manipulation", *Advanced Materials* (2021)
2. **Z. Xiao\***, C. Lai\*, R. Zheng, M. Goirienna, N. Tamura, C. T. Juarez, C. Perry, H. Singh, J. Bokor, G. P. Carman, R. N. Candler, "Localized Strain Profile in Surface Electrode Array for Programmable Composite Multiferroic Devices", *Applied Physics Letters* (2021)
3. M. Guevara De Jesus, **Z. Xiao**, M. Goirienna-Goikoetxea, R. V. Chopdekar, M. K. Panduranga, P. Shirazi, A. Acosta, J. P. Chang, J. Bokor, G. P. Carman, R. N. Candler, C. Lynch "Magnetic State Switching in FeGa Microstructures", *Smart Materials and Structures* (2021)
4. M. K. Panduranga, **Z. Xiao**, J. D. Schneider, T. Lee, C. Klewe, R. Chopdekar, P. Shafer, A. T. N'Diaye, E. Arenholz, R. N. Candler, G. P. Carman, "Single Magnetic Domain

- Terfenol-D Microstructures with Passivating Oxide Layer”, *Journal of Magnetism and Magnetic Materials* (2021)
5. M. Goiriena, **Z. Xiao**, A. El-Ghazaly, C. V. Stan, J. Chatterjee, A. Ceballos, A. Pattabi, N. Tamura, R. Lo Conte, F. Hellman, R. Candler, J. Bokor, “Influence of dislocations and twin walls in BaTiO<sub>3</sub> on the voltage-controlled switching of perpendicular magnetization”, *Physics Review Materials* (2021)
  6. **Z. Xiao\***, R. Lo Conte\*, M. Goiriena, R. Chopdekar, C-H. Lambert, X. Li, S. Tiwari, A. Chavez, A. Barra, A. Scholl, K. Wang, S. Salahuddin, E. Arenholz, G. P. Carman, J. Bokor, R. N. Candler, “Tunable magneto-elastic effect in voltage-controlled exchange-coupled composite multiferroic microstructures”, *ACS Appl. Mater. Interfaces* (2020)
  7. Y-C. Hsiao, R. Khojah, X. Li, A. Kundu, C. Chen, D. B. Gopman, A.C. Chavez, T. Lee, **Z. Xiao**, A. E. Sepulveda, R. N. Candler, G. P. Carman, D. Di Carlo, C. S. Lynch, “Capturing Magnetic Bead-based Arrays Using Perpendicular Magnetic Anisotropy”, *Applied Physics Letters* 115 (8), 082402 (2019)
  8. C. Chen, J. Sablik, J. Domann, R. Dyro, J. Hu, S. Mehta, **Z. Xiao**, R. N. Candler, G. P. Carman, A. Sepulveda, “Voltage Manipulation of Magnetic Particle using Multiferroics”, *Journal of Physics D: Applied Physics* (2019)
  9. **Z. Xiao\***, R. Khojah\*, M. Chooljian, R. Lo Conte, J. D. Schneider, K. Fitzell, Y. Wang, R. Chopdekar, A. Scholl, J. Chang, G. P. Carman, J. Bokor, D. Di Carlo, and R. N. Candler, “Cytocompatible magnetostrictive microstructures for nano- and microparticle manipulation on linear strain response piezoelectrics”, *IOP Multifunctional Materials* 1, 014004 (2018)
  10. **Z. Xiao**, R. Lo Conte, C. Chen, C-Y. Liang, A. Sepulveda, J. Bokor, G. P. Carman, R. N. Candler, “Bi-directional coupling in strain-mediated multiferroic heterostructures with magnetic domains and domain wall motion”, *Scientific Reports*, 8, 5270 (2018)
  11. R. Lo Conte, **Z. Xiao**, C. Chen, C. V. Stan, J. Gorchon, A. El-Ghazaly, M. E Nowakowski, H. Sohn, A. Pattabi, A. Scholl, N. Tamura, A. Sepulveda, G. P. Carman, R. N. Candler, J. Bokor, “Influence of Nonuniform Micron-Scale Strain Distributions on the Electrical Reorientation of Magnetic Microstructures in a Composite Multiferroic Heterostructure”, *Nano Lett.*, 18 (3), pp 1952–1961 (2018)
  12. **Z. Xiao**, K. P. Mohanchandra, R. Lo Conte, T. Karaba, J. D. Schneider, A. Chavez, S. Tiwari, H. Sohn, M. E Nowakowski, A. Scholl, S. H. Tolbert, J. Bokor, G. P. Carman, R. N. Candler, “Enhanced magnetoelectric coupling in a composite multiferroic system via interposing a thin film polymer”, *AIP Advances* 8 (5), 055907 (2018)

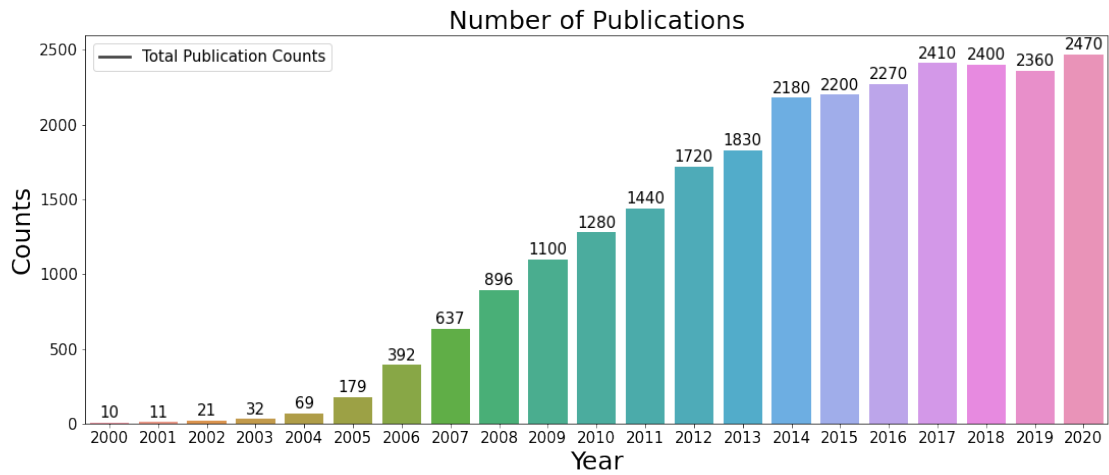
### Conference Publications

1. **Z. Xiao**, R. Lo Conte, M. Goiriena, R. V. Chopdekar, X. Li, S. Tiwari, C-H. Lambert, S. Salahuddin, G. P. Carman, K. Wang, J. Bokor, R. N. Candler, “Electric-field controlled magnetic reorientation in exchange coupled CoFeB/Ni bilayer microstructures”, *Journal of Physics: Conference Series*, IOP Publishing. PowerMEMS, 2018
2. A. Abiri, X. Guan, Y. Dai, A. Tao, **Z. Xiao**, E. P. Dutson, R. N. Candler, W. S. Grundfest, “Depressed-Membrane Pneumatic Actuators for Robotic Surgery”. 38th Annual International Conference of the IEEE Engineering in Medicine and Biology Society, 2016
3. Y. Dai, O. Paydar, A. Abiri, **Z. Xiao**, X. Guan, S. Liu, A. Tao, E. P. Dutson, W. S. Grundfest, R. Candler, “Miniature Multi-Axis Force Sensor for Haptic Feedback System in Robotic Surgery”. 38th Annual International Conference of the IEEE Engineering in Medicine and Biology Society, 2016

# Chapter 1 Introduction

## 1.1 Multiferroics and Magnetoelectric Materials

The term “multiferroics” refers to materials that possess two or more primary ferroic (i.e., has hysteresis) properties in the same phase: including ferroelectricity, ferromagnetism, ferroelasticity, and ferrotoroidicity [1]. Pioneering work in multiferroics can be dated to the 1950s [2], but it was not until 1994 that Schmid coined the term [1]. The concept has attracted substantial interest because of the unique physical properties arising from the coupling behavior between ferroelectric and magnetic orders. New developments in theory, improvements in synthesis, fabrication, and characterization methods have drawn a recent surge of interest in multiferroics and are leading to various potential technological applications.



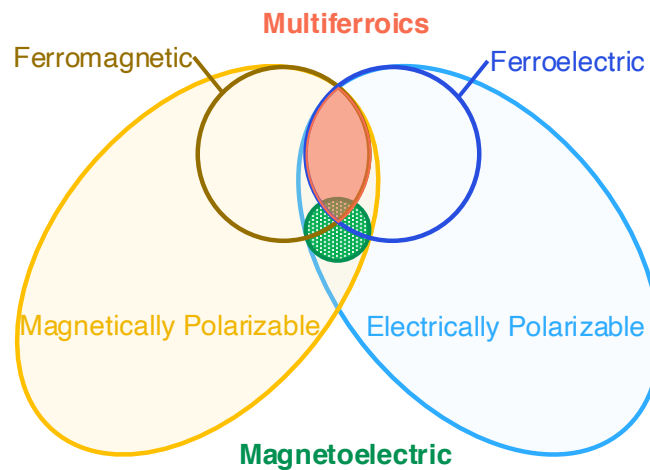
**Figure 1.1.** Number of publications on multiferroics in the past two decades.

For example, multifunctional multiferroic materials as a single device component have been experimentally prototyped in miniaturizing devices for various applications, such as information storage, including memory [5], logic devices [6, 7], and microscale sensors



[8]/actuators [9]. **Figure 1.1** shows the increasing interest in multiferroics research, with most of the work focusing on multiferroic magnetoelectric (ME) composite systems.

**Figure 1.2** shows the relations between different types of magnetic, electric, and magnetoelectric materials. For example, ferromagnetic materials exhibit spontaneous magnetization, switchable by an applied magnetic field. Ferroelectric materials have spontaneous polarization, convertible by an applied electric field. In multiferroic materials, the coexistence of multiple ferroic orders leads to cross-coupling, either direct or indirect, as illustrated in **Figure 1.3**. In magnetoelectric multiferroics, a magnetic field  $\mathbf{H}$  can control the electric polarization  $\mathbf{P}$ . An electric field  $\mathbf{E}$  can control the magnetization  $\mathbf{M}$ . Such coupling between ferromagnetic and ferroelectric order is capable of producing magnetoelectric effect as well as converse magnetoelectric effect (**Figure 1.3**), which is at the basis of energy-efficient non-volatile memory and scalable multiferroics-based microfluidic devices.



**Figure 1.2.** Venn diagram illustrating the relationship between multiferroic and magnetoelectric materials, adapted from [1].

Magnetoelectric coupling can either happen directly between magnetic and electric order parameters or be mediated indirectly by strain. Note that not all materials exhibiting

magnetoelectric effect are multiferroic, e.g.,  $\text{Cr}_2\text{O}_3$ , and not all multiferroics with both magnetic and electric order show magnetoelectric effect, e.g., hexagonal  $\text{YMnO}_3$ . Nowadays, the term “magnetoelectric” broadly refers to any type of coupling between magnetic and electric properties [3].

Overall, multiferroics materials can be categorized into two types based on material constituents: single-phase and composite multiferroics. Most single-phase multiferroics exhibit multiferroic properties way below room temperature, and the magnetoelectric coupling behavior is weak due to the reciprocity relations that limit magnetoelectric susceptibilities [2]. Bismuth ferrite ( $\text{BiFeO}_3$ ) is one of the most-studied single-phase multiferroics since it is the only room temperature single-phase multiferroic material [4][5], with more than 10k publications to date on the material. In contrast, composite multiferroics containing two material constituents, such as a ferroelectric and a ferromagnetic, have emerged as a practical alternative. Such two-phase indirectly couples ferroelectric and ferromagnetic materials via strain. The two phases can be independently optimized to produce robust room-temperature multiferroics with strong magnetoelectric coupling between the layers, established by electric-field introduced strain.

## 1.2 Composite Multiferroics Heterostructures and Electric-field control of Magnetization

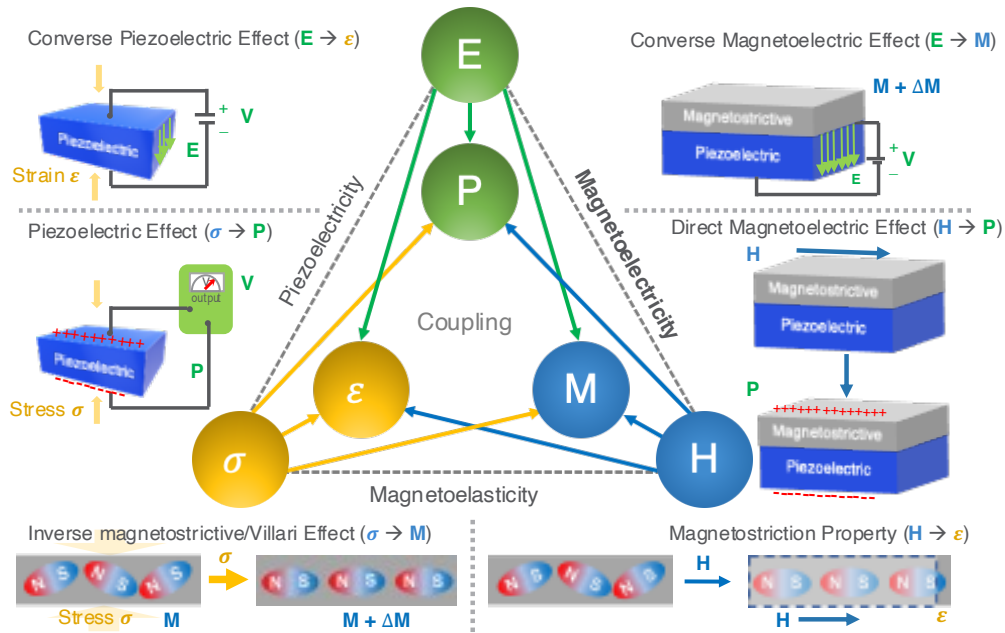
Unlike single-phase multiferroics, composite multiferroic heterostructures are particularly important for their larger magnetoelectric coupling effect, where coupling has been demonstrated via several methods, including elastic strain, exchange bias effect, and charge carrier density - all controllable by electric field [6]. Among these, using an electrical field to actuate strain-coupled multiferroic heterostructures has been widely demonstrated in the past

few years as an energy-efficient pathway for controlling magnetization in the ferromagnetic layer [7]–[11].

Composite multiferroic heterostructure combines ferromagnetic and ferroelectric materials to collectively achieve a robust magnetoelectric effect (**Figure 1.3**). The underlying working principle is the converse magnetoelectric effect which controls the magnetization in the magnetostrictive layer via the induced strain (elastic interaction) from the piezoelectric substrate. The induced strain causes a magnetization change in the magnetic material due to the inverse magnetostrictive effect, a.k.a. Villari effect [6], [12]. The converse magnetoelectric effect is defined as the product of the piezoelectric effect (mechanical  $\rightarrow$  electrical effect) in the ferroelectric phase and the magnetostrictive effect (magnetic  $\rightarrow$  mechanical effect) in the magnetic phase [13]:

$$\text{Converse ME effect} = \frac{\text{Electric}}{\text{Mechanical}} \times \frac{\text{Mechanical}}{\text{Magnetic}}. \quad (1-1)$$

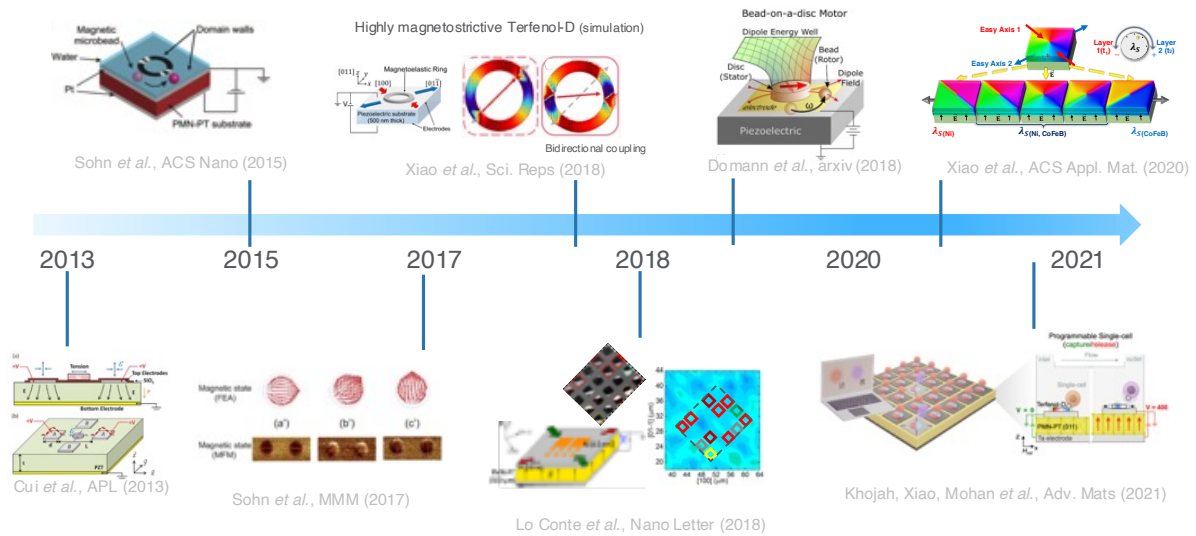
In our study, we utilize the magnetoelectric coupling behavior in composite multiferroics. Composite multiferroic heterostructures are particularly important for their larger ME coupling effect. Such coupling has been demonstrated via several methods, including elastic strain, exchange bias effect, and charge carrier density - all controllable by an electric field. In this dissertation, we are mainly interested in strain-coupled multiferroic heterostructures. An applied voltage across a ferroelectric substrate produces an electric field. The electrically-induced strain in the substrate coupled with the magnetic layer can be used to control magnetization orientation (i.e., magnetic anisotropy) in magnetic microstructures.



**Figure 1.3.** Schematics of coupling in multiferroic and magnetoelectric materials. The phase control diagram in the center has been adapted from [14].

### 1.3 Application of Multiferroics

The continuously increasing interest in micro- and nanoscale magnetic devices has encouraged researchers to develop new methods of controlling magnetism at the nanoscale. One such method involves artificial multiferroic heterostructures, where strain induced in piezoelectric materials is transferred to a magnetoelastic material layer to enable control of magnetism via an electric field. Compared to conventional electric current-control of magnetism, electric field-driven control of magnetism in multiferroic heterostructures has several advantages. For example, the multiferroic approach reduces power dissipation in small-scale applications and the accompanying potential for highly arrayed and localized device actuation. This multimodal control holds promise in the development of new energy-efficient applications, including nonvolatile memory devices [15], [16], actuators and transducers [17], and miniature antennae [18]. Furthermore, the potential of electric field-controlled magnetism in biomedical applications has been explored in manipulating magnetic particles [19].



**Figure 1.4.** Timeline of the recent strain-mediated multiferroic platforms developed at TANMS (Translational Applications of Nanoscale Multiferroic Systems) research center. Figures from [17], [19]–[24].

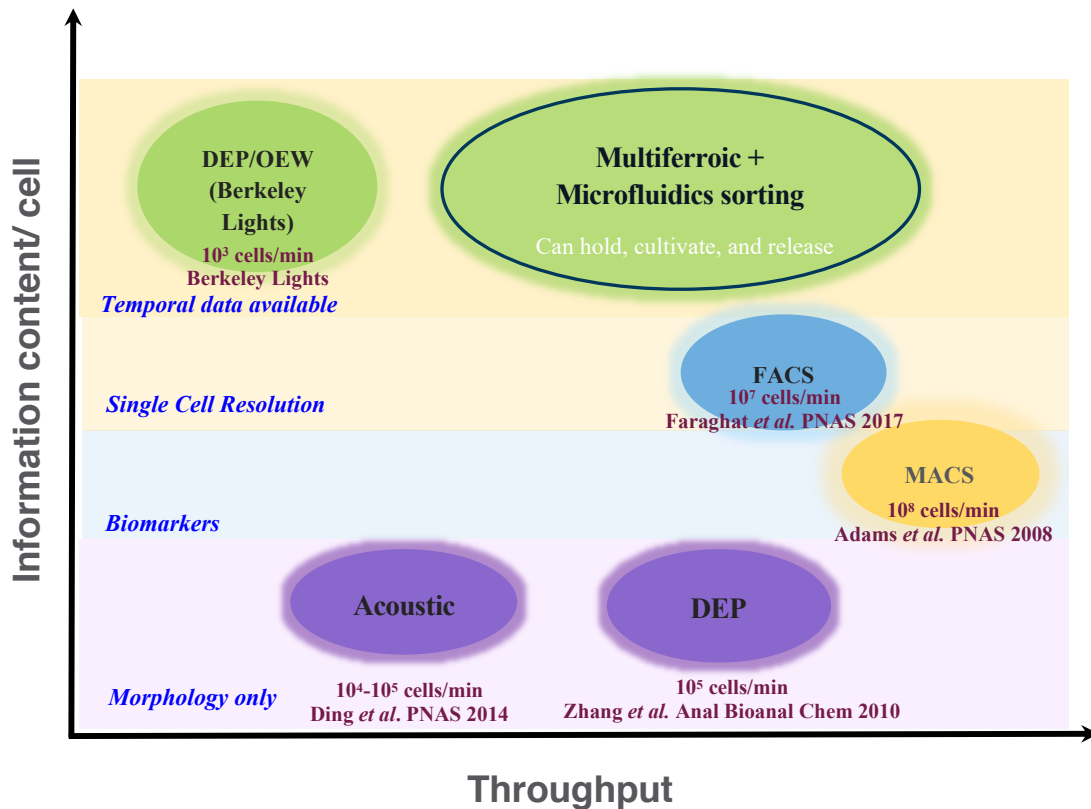
**Figure 1.4** shows a timeline of what has been done in TANMS research center in the area of strain-mediated magnetism control in micro- and nanostructures in the past few years [17], [19]–[24]. The team has worked on various prototypes of strain-mediated multiferroic heterostructure platforms to control magnetism at a small-scale. These strain-mediated composites employ the dipole coupling between multiferroic microstructures and external magnetic objects, such as superparamagnetic beads or magnetically-tagged cells for bio applications. The fundamental principles of these prototype devices are the same. As a voltage is applied to the piezoelectric substrate, the electric field could induce strain in the crystal through the converse piezoelectric effect. With sufficient mechanical strain, the magnetoelectric coupling between the magnetic and piezoelectric layer would reorient the magnetic moment in the microstructures. With proper design, material selection, experimentation, and testing, the magnetic stray fields from these microstructures could trap and move the external particles or interact with attached cells. Before 2018, a majority of the

work adopts Ni or FeGa as the magnetic layer. Microstructures with a size up to 4  $\mu\text{m}$  are used to generate the magnetic stray field. Magnetic reorientation occurs through magnetoelectric coupling and drives superparamagnetic beads with 1-2  $\mu\text{m}$  in diameter. However, these magnetic structures cannot sustain a large magnetic stray field sufficient enough to interact with magnetically tagged cells. This work looks into optimizing both the ferromagnetic and ferroelectric properties of the multiferroic systems. In particular, we opted for a highly magnetostrictive material, Terfenol-D, and examined its large magnetic single-domain with lateral size on par to the human cell, about 10-20  $\mu\text{m}$ , explained in Chapter 5.

#### 1.4 Cell sorting state-of-the-art

A white space chart for the cell sorting is presented in **Figure 1.5**. If one needs to sort cells based on cell morphology or shape, standing surface acoustic waves [25] or dielectrophoretic (DEP) sorting can be used, shown in the bottom level. In dielectrophoresis, a neutral particle (e.g., cell) experiences a DEP force due to the induced polarization. Depending on the properties of the medium and particles, including dimensions and morphologies, and the property of the electric field, the particles will experience either a negative or positive DEP force that repels or attracts cells to locations with high electric field gradients [26]. The magnetic-activated cell sorting (MACs) technique attaches superparamagnetic nanoparticles to the cells before separating them with permanent magnets. Though it has a high throughput, the response is binary since it cannot distinguish cells based on individual expression levels of the cell. Fluorescence-activated cell sorting (FACS) is commonly used to separate cells based on scattered light to get to single-cell resolution. On the top level, the methods can work on a single cell and provide temporal data so that one can measure the cell behavior over time. For example, Berkeley Lights, Inc. [27] uses an optofluidic method where non-invasive optoelectronic tweezers [28] with projected light are used to move individual cells and particles

in chips. On the upper right corner of **Figure 1.5**, our approach uses a magnetic stray field to control cells, microfluidics flow, and strain to release the cells. Next, an optical microscope is used to observe the behavior of cells in parallel. Finally, the combined multiferroics and microfluidics platform can capture, culture and realize controlled release of target cells.



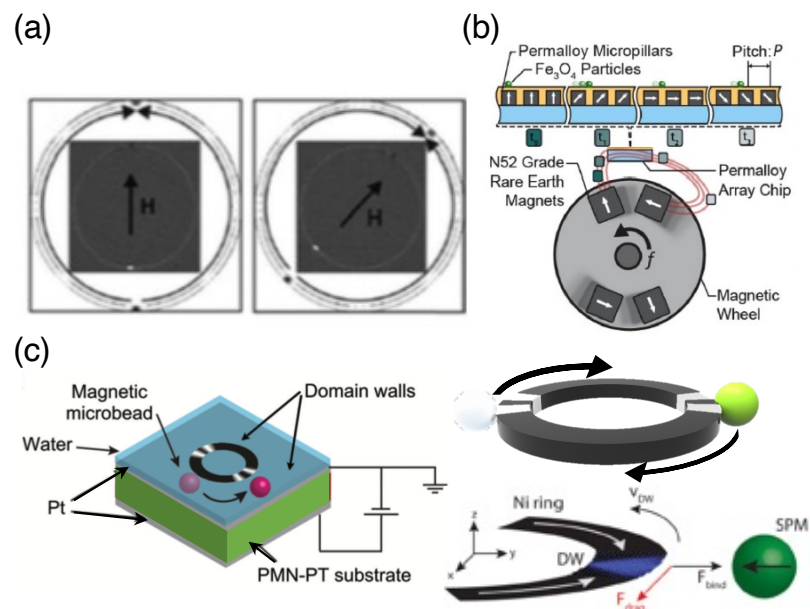
**Figure 1.5.** A white space chart for cell sorting state of the art. DEP: Dielectrophoretic sorting. MACs: Magnetic-assisted cell sorting. FACS: Fluorescence-assisted cell sorting. OEW: Optoelectronic tweezers.

The ability to control individual cells will be beneficial for developing personalized cell-based therapies where we need to select and individually release top-performing CAR-T cells, deeply characterize, map T-cell populations down to the single-cell level, and connect phenotype to gene expression.

### 1.4.1 Isolated functional cells and Immunotherapy

CAR T-cell therapy (chimeric antigen receptor) has been used in treating cancers in the past years; for example FDA approved its use for treating blood cancers: acute lymphoblastic leukemia and diffuse large B-cell lymphoma [29][30] in 2017. It first selects and genetically modifies a group of patients' T cells. Then it attaches receptors to these T cells, which can be infused back into the blood vessels, find cancer-causing cells based on specific proteins expressed on the surface and destroy them.

### 1.4.2 Magnetic-based magnetic particle control



**Figure 1.6.** (a)-(b) Conventional methods for controlling micromagnets at sub-micron-meter scale involve remote/bulky external magnets to generate a magnetic field. (a) Rotating magnetic field  $H$  from an external magnetic source displaces domain walls in a circular Py ring [31]. (b) A rotating magnetic wheel magnetizes micropillars to manipulate the magnetic potential energy landscape to move particles.



In the past two decades, magnetic-based cell separation has been proven to be an effective strategy for targeting single cells from sub-populations due to its non-destructive nature. In contrast to the current gold standard for bulk isolation of cells via the assistance of external magnetic fields, using micropatterned magnetic structures with tunable magnetization orientation is advantageous for its addressability on the microscale and at the individual magnetic particle/cell level. These recent advances in microstructure-assisted particle and cell manipulation still require a directionally cycled external magnetic field [32]. The presence of bulky permanent magnets or solenoids prevents real-time imaging from examining the cells' timely expression of phenotypic properties. In contrast, an electric-field-based control of magnetism in microstructures allows for a compact and scalable particle/cell sorting platform without the need for bulky external magnets. Compared to the current-based electrical control at the small scale, which suffers from Ohmic dissipation, an electric-field-based multiferroics system can lead to ultra-low-power and scalable particle/cell sorting platforms. The cell sorting system with multimodal control can be accomplished by combining strain-coupled multiferroic heterostructures with microfluidics channels.

#### *1.4.3 Microchannels for bead-based cell manipulation*

A standard method to control the fluids flow containing magnetically-labeled cells is to separately fabricate a polydimethylsiloxane (PDMS) layer with microchannels using soft lithography [33] techniques and attach it to the surface of the microfluidics device.

### **1.5 Ferromagnetic domains**

With applied voltage across ferroelectric substrates, we could induce changes in the magnetic domain configuration of ferromagnetic layers in the multiferroic composites. For

example, a ferromagnet exhibits spontaneous magnetization when there is no applied magnetic field.

Domains are formed to minimize the total magnetic energy of a ferromagnetic material. The following section examines various energy contributions to the total magnetic energy of a ferromagnet.

## 1.6 Magnetization Energy

### 1.6.1 Micromagnetics and Magnetic Energy

From the magnetic point of view, the time evolution of the normalized magnetization  $\mathbf{m}$  ( $|\mathbf{m}| = 1$ ) is determined by the micromagnetic relation that satisfies the Landau-Lifshitz-Gilbert equation (LLG). LLG describes the precessional dynamics and relaxation of the magnetization vector:

$$\frac{\partial \mathbf{m}}{\partial t} = -\mu_0 \gamma (\mathbf{m} \times \mathbf{H}_{eff}) + \alpha \left( \mathbf{m} \times \frac{\partial \mathbf{m}}{\partial t} \right), \quad (1-2)$$

where  $\mu_0$  is the vacuum permeability,  $\gamma$  is the gyromagnetic ratio and  $\alpha$  is the Gilbert damping constant. The damping factor is expected to affect the magnetization dynamics, including the speed with which the DW/domain will move and the time that will take for the magnetization to reach its stable state. However, it is not expected to affect the final state itself, which is determined by the minimization of total free energy.

The effective magnetic field  $\mathbf{H}_{eff}$  is taken as the partial derivative of the total magnetization energy with respect to the magnetic moment:

$$\mathbf{H}_{eff} = -\frac{1}{\mu_0 M_s} \frac{\partial E_{tot}}{\partial \mathbf{m}}, \quad (1-3)$$

where  $E_{tot}$  is the total energy density and  $M_s$  is the saturation magnetization of the material [34]. The total energy has contributions from the exchange energy ( $E_{ex}$ ), magnetostatic energy

( $\mathbf{E}_d$ ), Zeeman energy ( $\mathbf{E}_{ext}$ ), magnetocrystalline energy ( $\mathbf{E}_{mca}$ ), and magnetoelastic energy ( $\mathbf{E}_{me}$ ).

#### 1.6.1.1 Magnetostatic energy

As the principal driving force for magnetic domain formation and magnetization process, magnetostatic energy always exists in ferromagnetic materials. It is caused by the *demagnetization field*,  $\mathbf{H}_d$ , in the material. It is called the demagnetization field since the magnetic field created by the magnetic moment of the material will magnetize the material in the opposite direction from the magnetic moment. Magnetostatic energy is essentially the self-energy of a magnetic material in its own field and the interaction of the material with varying external magnetic fields [35]. The energy of a magnetic dipole  $\mathbf{m}$  in a magnetic field  $\mathbf{H}$  is expressed as:

$$E = -\mathbf{m} \cdot \mathbf{H}. \quad (1-4)$$

The demagnetization field  $\mathbf{H}_d$  is dependent on the shape. It can be expressed as:

$$\mathbf{H}_d = -N_d \mathbf{M}, \quad (1-5)$$

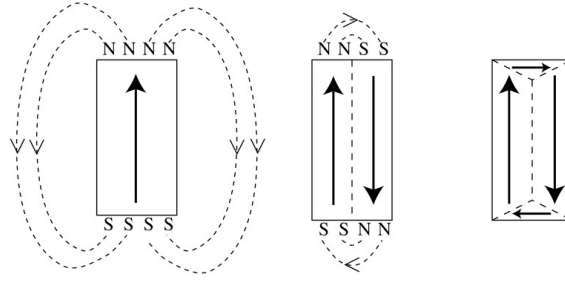
where  $N_d$  is the *demagnetiation factor dependent mainly on the shape anisotropy*.

$\mathbf{H}_d$  can also be determined from Maxwell's equations following Ampere's law and Gauss's law. It is related to the gradient of magnetic potential:

$$\mathbf{H}_d = -\nabla\phi. \quad (1-6)$$

The magnetostatic energy can be expressed as:

$$E_{ms} = -\frac{1}{2}\mu_0 \mathbf{M}_s \cdot \mathbf{H}_d. \quad (1-7)$$



**Figure 1.7.** Domain formation in a ferromagnet with reduced magnetoelastic energy from left to right. Figure from [36].

In **Figure 1.7**, from left to right, the magnetostatic energy is reduced as a result of reduced external demagnetization field and break into multiple domains to minimize magnetostatic energy. Note that the magnetic moments from the two domains are not parallel at the domain wall, resulting in increased exchange energy of the material. The rightmost figure is an ideal case of flux closure domain where the magnetostatic energy is zero.

### 1.6.1.2 Exchange energy

Arising from the exchange effect between adjacent electron spins, exchange energy provides a strong driving force to align neighboring electron spins, i.e., magnetic moments parallel to each other. A single domain such as one shown in **Figure 1.7** minimizes the contribution of exchange energy to the total energy. The exchange energy of each nearest-neighbor electron spins  $S_i$  and  $S_j$  is in the following form:

$$E_{ex} = -2A_{ex}\mathbf{S}_i \cdot \mathbf{S}_j \quad (1-8)$$

where  $A_{ex}$  is the exchange stiffness.

### 1.6.1.3 Magnetocrystalline energy

Magnetocrystalline anisotropy (MCA) describes the phenomenon where the magnetization prefers to align itself along certain crystallographic directions. Magnetic domains tend to form to align with the magnetic moments along the easy-axis direction.

In thin films, shape anisotropy typically dominates over magnetocrystalline anisotropy.

### 1.6.1.4 Magnetoelastic /Magnetostrictive energy

Magnetoelastic effect refers to the coupling between the mechanical strains and the magnetization direction. Magnetoelastic (a.k.a, Magnetostrictive) energy is the part of MCA that is relevant to strain. It essentially arises from the dimension change of a magnetic material upon magnetization. The induced strain is called the magnetostriction ( $\lambda = dl/l$ ), which is the fractional change in length. Though such length changes are typically relatively small, i.e., tens of parts per million (ppm), they are large enough to affect the magnetization and domain configurations.

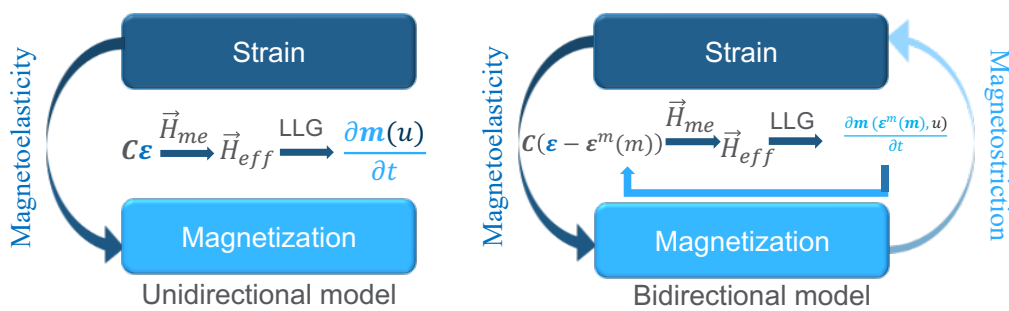
Magnetostriction arises mostly from spin-orbit coupling which is also responsible for crystal anisotropy. There are two types of magnetostriction: spontaneous magnetostriction and magnetic-field-induced magnetostriction [37]. Resistive strain gauges can be used to measure magnetostriction in bulk samples. Saturation magnetostriction  $\lambda_s$  represents the fractional change in length once a ferromagnetic sample transitions from a demagnetized state to a state where its magnetic moments are saturated along (aligning in parallel to) the applied magnetic field direction. For a material (e.g., Fe, Terfenol-D, CoFeB) that expands or elongates in the direction of magnetization, it has positive magnetostriction ( $\lambda_s > 0$ ). For a material (e.g., Ni) that contracts in the direction of magnetization, it is negatively magnetostrictive ( $\lambda_s < 0$ ).

## 1.7 Simulation of strain-mediated magnetic domain reorientation in magnetostrictive microstructures

Manipulation of magnetization via the strain-based approach has already been demonstrated experimentally in Ni [38], CoFeB [39], and FeGa [16] on piezoelectric substrates. Increasing interest in highly magnetoelastic materials, such as Terfenol-D ( $\text{Tb}_x\text{Dy}_{1-x}\text{Fe}_2$ ,  $x = 0.3$ ) with magnetostriction saturation  $\lambda_s = 1200 \times 10^{-6}$  [40], creates the need for a thorough understanding of the magnetization behavior inside these materials owing to their potential for enhanced strain-mediated magnetic moment rotation [41]. As a side note, maximizing magnetostriction is often a desirable pursuit, although there are cases where there are nuanced tradeoffs, and maximum magnetostriction is not necessarily a standalone objective. Much of the prior work that uses the unidirectional (UD) model has produced comparable results to the experimental observations, even though strain induced by the change in magnetization is generally ignored [42][43].

To address this growing interest in highly magnetostrictive thin film materials, we simulate the strain-induced magnetization change with two modeling methods: the commonly used unidirectional model and the recently developed bidirectional model. Unidirectional (UD) models account for magnetoelastic effects only, while bidirectional models (BD) account for both magnetoelastic and magnetostrictive effects. We found unidirectional models are on par with bidirectional models when describing the magnetic behavior in weakly magnetoelastic materials (e.g., Nickel), but the two models deviate when highly magnetoelastic materials (e.g., Terfenol-D) are introduced. These results suggest that magnetostrictive feedback is critical for modeling highly magnetoelastic materials instead of weaker magnetoelastic materials, where we observe only minor differences between the two methods' outputs [44].

Previously, we simulated the strain-induced magnetization change using both the BD and UD models. For both models, the micromagnetic and elastodynamic partial differential equations (PDEs) are implemented in the weak form and are solved using the finite element method. However, the two models differ because the BD model, differently from the UD model, incorporates stress-induced via magnetostriction, iterating between stress-induced changes in magnetization and magnetization-induced stress until a solution is found.



**Figure 1.8.** Description of the two simulation approaches: the unidirectional model only tracks inverse magnetostrictive effect, while the bidirectional model considers both the magnetostrictive and inverse magnetostrictive effects.

For weakly magnetostrictive Ni, the experimentally measured Gilbert damping factor  $\alpha$  is 0.038 [45], and for highly magnetostrictive Terfenol-D, it is  $0.06 \pm 0.02$  [46]. In our simulations, the primary goal is to compare the final static state after strain is applied, so  $\alpha$  is set to 0.5 to achieve equilibrium in a reasonable calculation time. The damping factor is expected to affect the magnetization dynamics, including the speed with which the DW/domain will move, and the time it takes for the magnetization to reach its stable state. However, it is not expected to affect the final state itself, which is determined by minimizing total free energy [39].

In the simulation, we induce a uniaxial magnetic anisotropy which will induce the magnetization to realign. This reorientation is expected to be fully deterministic if a magnetization rotation of an angle smaller than  $90^\circ$  is induced. Accordingly, we do not expect the larger damping factor to influence at all the final magnetic state induced by the applied strain via magneto-elastic coupling. The effective magnetic field  $H_{eff}$  is defined as:

$$\mathbf{H}_{eff} = -\frac{1}{\mu_0 M_s} \frac{\partial E_{tot}}{\partial \mathbf{m}}, \quad (1-9)$$

where  $\mathbf{E}_{tot}$  is the total energy density and  $M_s$  is the saturation magnetization.

In our model,  $\mathbf{H}_{eff}$  is expressed as the summation of the external field ( $H_{ext}$ ), exchange field ( $H_{ex}$ ), demagnetization field ( $H_d$ ) and magnetoelastic field ( $H_{me}$ ) as the magnetocrystalline anisotropy in amorphous and polycrystalline thin films is negligible. Among these fields, the magnetoelastic field  $H_{me}(\mathbf{m}, \boldsymbol{\varepsilon}^{tot})$  depends on both  $\mathbf{m}$  and the total strain  $\boldsymbol{\varepsilon}^{tot}$ . Solving these equations using the finite element method allows us to determine the final magnetization of the magnetic structure.

From the mechanical point of view, the displacement field  $\mathbf{u}$  obeys the elastodynamic equation:

$$\rho \frac{\partial^2 \mathbf{u}}{\partial t^2} = \nabla \cdot \boldsymbol{\sigma}, \quad (1-10)$$

where  $\rho$  and  $\boldsymbol{\sigma}$  denote the volumetric density and the stress tensor, respectively [47]. Thus, the constitutive relation between the stress tensor  $\boldsymbol{\sigma}$  and the elastic strain tensor  $\boldsymbol{\varepsilon}^{el}$  can be expressed as:

$$\boldsymbol{\sigma} = \mathbf{C} \boldsymbol{\varepsilon}^{el}, \quad (1-11)$$



where  $\mathbf{C}$  is the elastic stiffness tensor. In magnetoelastic materials that are also cubic crystals, the magnetoelastic strain tensor  $\boldsymbol{\varepsilon}^m$  is induced by  $\mathbf{m}$ :

$$\varepsilon_{ij}^m = \begin{cases} \frac{3}{2}\lambda_{100}(m_i^2 - \frac{1}{3}) & \text{for } i = j \\ \frac{3}{2}\lambda_{111}m_i m_j & \text{for } i \neq j \end{cases} \quad (1-12)$$

where  $\lambda_{100}$  and  $\lambda_{111}$  represent the magnetostriction constants in  $\langle 100 \rangle$  and  $\langle 111 \rangle$  directions, respectively.  $\boldsymbol{\varepsilon}^m$  also contributes to  $\boldsymbol{\varepsilon}^{tot}$ , namely  $\boldsymbol{\varepsilon}^{tot} = \boldsymbol{\varepsilon}^{el} + \boldsymbol{\varepsilon}^m$ .

The major difference between the BD and UD models originates from the way in which the strain is being treated. In the conventional UD model, elastic strain  $\boldsymbol{\varepsilon}^{el}$  is assumed to be the only strain contributing to the magnetoelastic effects, and is thus equivalent to the total strain  $\boldsymbol{\varepsilon}^{tot}$  (see **Figure 1.8**, left). Therefore, elastodynamics and micromagnetics are not fully coupled, as the magnetization is calculated in the following steps:

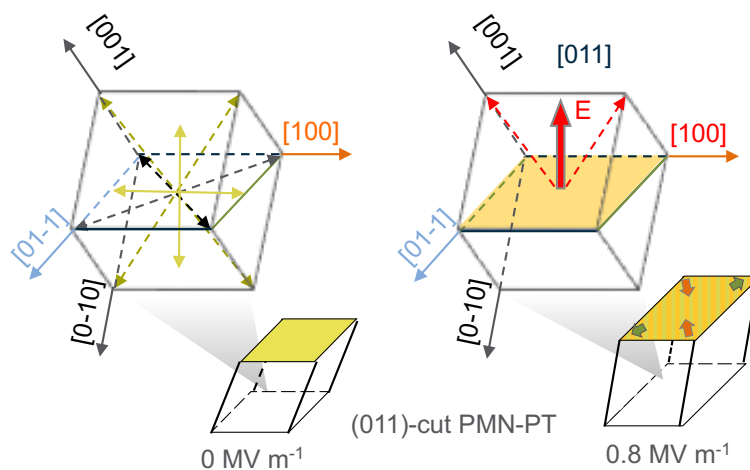
- a)  $\boldsymbol{\varepsilon}^{tot}$ , which equates to  $\boldsymbol{\varepsilon}^{el}$  in UD models, is calculated first by solving the elastodynamic equation,
- b)  $\boldsymbol{\varepsilon}^{tot}$  is incorporated into the LLG equation via  $\mathbf{H}_{me}$  to calculate  $\mathbf{m}$  in the magnetoelastic structure.

On the other hand, in the BD model, the total strain  $\boldsymbol{\varepsilon}^{tot}$  takes into account contributions from both the linear elastic strain and the magnetic strain. It solves the intrinsically coupled PDEs simultaneously: a)  $\boldsymbol{\varepsilon}^{tot}$ , which equates to  $\boldsymbol{\varepsilon}^{el} + \boldsymbol{\varepsilon}^m$ , is calculated from the elastodynamic equation, b)  $\boldsymbol{\varepsilon}^{tot}$  is incorporated into the LLG equation via  $\mathbf{H}_{me}$  to calculate  $\mathbf{m}$  as well as  $\boldsymbol{\varepsilon}^m$ , and c) the generated magnetic state is fed back into the elastodynamic equation and the above steps are repeated until reaching convergence. As shown in **Figure 1.8** (right), magnetization change causes change in strain by affecting  $\boldsymbol{\varepsilon}^m(\mathbf{m})$ , and hence  $\mathbf{H}_{me}$ . Consequently, the time-dependent distribution of magnetization vectors  $\mathbf{m}(\boldsymbol{\varepsilon}^m(\mathbf{m}), u, t)$  in

the magnetoelastic structure, which responds to both displacement field  $\mathbf{u}$  and recurring changes in effective strain imposed by  $\boldsymbol{\varepsilon}^m(\mathbf{m})$ , continue to modify  $\boldsymbol{\varepsilon}^m(\mathbf{m})$  and thus  $\mathbf{H}_{me}$  (as illustrated by the green arrow in **Figure 1.8**, right). This bidirectional model captures the bilateral communication/interaction between strain and magnetization via both Villari effect (inverse magnetostrictive effect) and magnetostrictive effect (see **Figure 1.8**).

By comparison, the BD model more fully captures the physics in the coupled magnetoelastic system. The decoupling in the UD model assumes that the magnetostriction coefficient is very small. Hence, the elastic strain is approximately equal to the total strain ( $\boldsymbol{\varepsilon}^{tot} \approx \boldsymbol{\varepsilon}^{el}$ ). However, when dealing with materials with high magnetostriction constants, the BD and UD models lead to drastically different results.

## 1.8 Common Piezoelectric Constituent in multiferroic heterostructures



**Figure 1.9.** Generates in-plane anisotropic strain with parallel-plate electrodes on (011)-cut PMN-PT

Single crystal  $[\text{Pb}(\text{Mg}_{1/3}\text{Nb}_{2/3})\text{O}_3]_{1-x}[\text{PbTiO}_3]_x$  (PMN-xPT,  $0 < x < 0.35$ ) and polycrystalline Lead Zirconate Titanate (PZT) are among the popular ferroelectric thin film and substrates

used in multiferroic heterostructures [20], [48]–[52]. **Figure 1.9** demonstrates a (011)-cut PMN-PT unit cell before and after electrically-poled along the [011] crystallographic direction. It experiences a compressive strain in [100] and tensile strain in [01-1] in-plane direction. The electrically-induced strain can change the magnetic anisotropy axis in the magnetostrictive layer due to the magnetoelectric coupling.

# Chapter 2 Characterization of Magnetoelectric Multiferroic Devices

## 2.1 Magnetic characterization

The following sections discuss some of the instruments and their working principles for measuring magnetization and characterizing magnetic properties of the ferromagnetic layer in magnetoelectric composite multiferroic devices.

### 2.1.1 SQUID Magnetometer

The Superconducting Quantum Interference Device (SQUID) contains two parallel Josephson junctions in which superconducting electrons can quantum-mechanically tunnel across very thin insulating layers positioned in between two superconductors. The device needs to be operated at low temperature jointly with a superconducting solenoid [37]. As one of the most sensitive magnetic field detectors [53], it can be used as a magnetometer to measure small magnetic fields with high sensitivity ( $10^{-14}$  T).

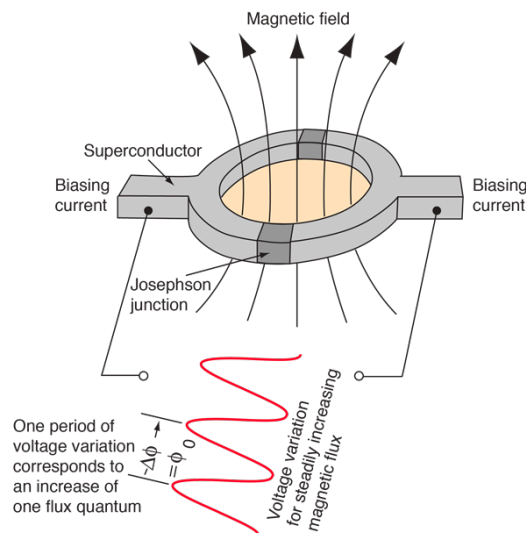
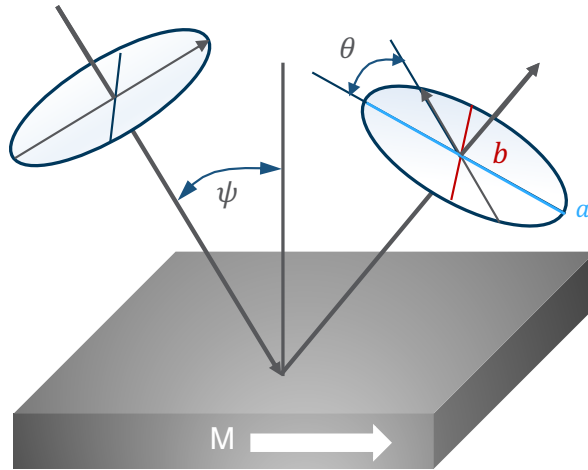


Figure 2.1. Schematics of a SQUID flux sensor. Figure from [54].

**Figure 2.1** shows the schematics of the device. A biasing current flows through two sides of the superconductor and passes through each of the two Josephson junctions. Due to changes in current at the two junctions, the magnetic flux through the ring structure changes. Based on Faraday's law, this change in magnetic flux results in a change in voltage measured at two ends of the device and induces a current in the ring. This induced current is parallel to the existing biasing current direction on one side of the device and antiparallel to the other side. Due to the wave nature of the superconducting circuit, there is a periodic resistance showing up in the device and a measurable voltage variation across the device [37]. The oscillation of the voltage is dependent on the change in the magnetic flux through the ring. In practice, the SQUID device is connected to a coil to measure the flux from a small sample (e.g., a 3mm \* 7mm surface area thin film in plastic straw) and hence its magnetization.

### 2.1.2 *Magneto-Optical Effect and Magneto-optic Kerr Effect (MOKE)*

In 1845, Faraday discovered that the angle of a linearly polarized light would change its angle of polarization after transmitting through optically transparent ferromagnetic material magnetized in a direction parallel to the light. When being incident on an opaque or metallic surface, the polarized light would change its angle of polarization  $\psi$  and ellipticity  $a/b$  based on the magnetization in the material. Such observed behavior in the reflected light affected by the ferromagnetic properties of the specimen is called the magneto-optic Kerr effect (MOKE) [55].

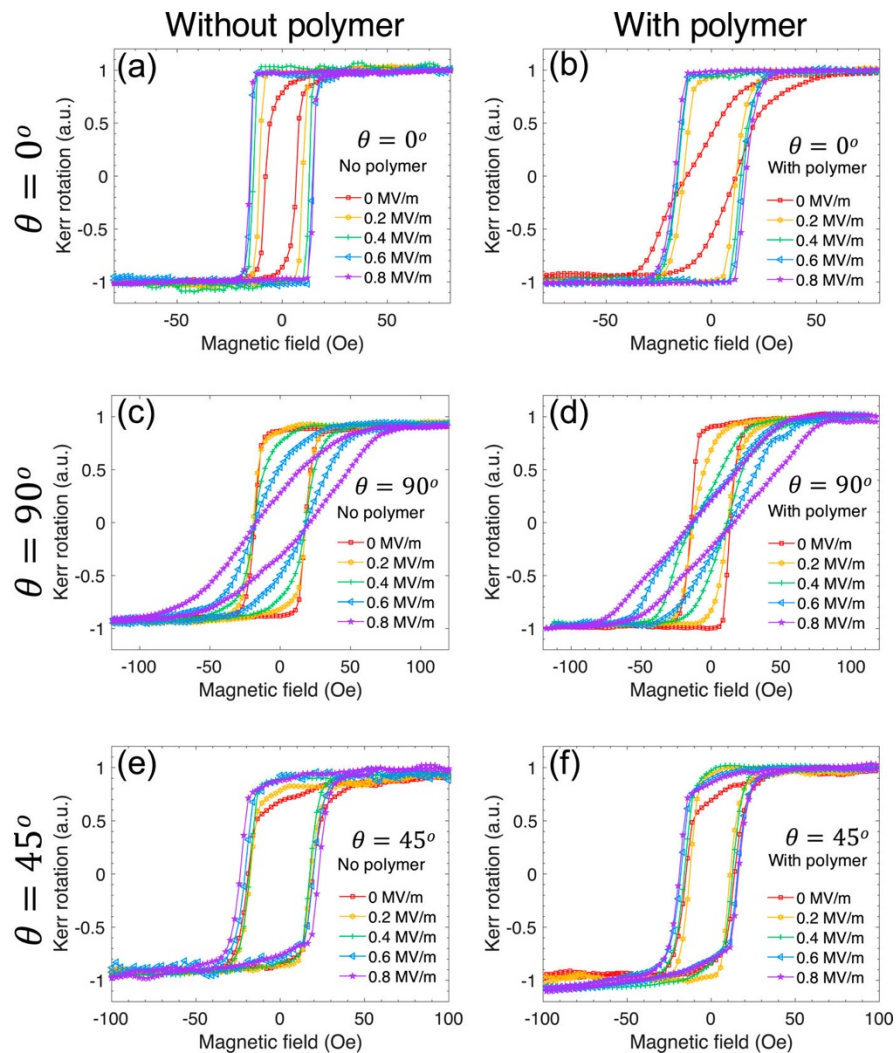


**Figure 2.2.** The polarized light angle rotates by  $\theta$  after reflection. The ellipticity of the reflected polarized light also changes with respect to magnetization  $M$ . Figure adapted from [56].

Investigating the MOKE in magnetic thin films provides various information on their magnetic properties, such as the extent of local magnetization, hysteresis loop (Kerr rotation vs. Magnetic field), and domain structure observation. It is important to note that the Kerr effect provides qualitative data on magnetization due to its relatively poor resolution [56] and is more sensitive to perpendicular magnetization [57].

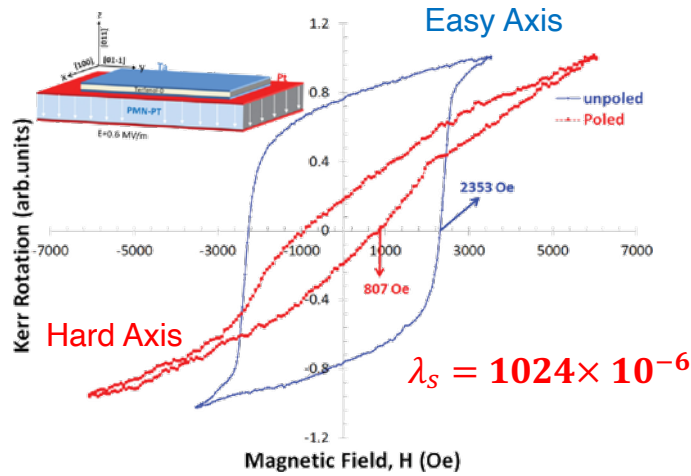
For example, **Figure 2.3** shows normalized Kerr rotation hysteresis curves measured for a previous study [58] of ferromagnetic Ni thin film on piezoelectric PMN-PT. Comparing **Figure 2.3** (a)-(b) of MOKE  $M$  vs.  $H$  curves for samples without and with polymer, respectively, we note that the presence of the planarization polymer in the multiferroics heterostructure increases the hard-axis anisotropy and thus reduces the remanence-saturation ratio  $M_r/M_s$  (normalized remanence). Though MOKE does not provide a quantitative measurement of saturation magnetization and remanence magnetization, we can still obtain the  $M_r/M_s$  ratio. For example,  $M_r/M_s$  measured at an electric field of 0 MV/m in the specimen without polymer

is greater than 0.85, while in the specimen with polymer, it is below 0.45. The almost two-fold increase in  $M_r/M_s$  ( $\theta$  of  $0^\circ$ ) before and after applying the electric field of 0.8 MV/m is adequate to show that the ME coupling between magnetic thin film and PMN-PT grows more robust due to the presence of the interposed polymer layer. The presence of the polymer layer smoothens the strain profile and planarizes the Ni layer, indicating an increased magnetoelastic effect. In another example, MOKE Kerr rotation measurement [59] is used to measure large coercivity change quantitatively in Terfenol-D thin film on PMN-PT substrate after electric-poling, as shown in **Figure 2.4**.



**Figure 2.3.** Example hysteresis loops of Ni thin film on PMN-PT [58]. Normalized magnetic Kerr rotation M-H curves measured at different electric fields with magnetic field parallel

to  $\theta = 0^\circ$ ,  $\theta = 45^\circ$  and  $\theta = 90^\circ$  directions, where  $\theta$  is the angle between in-plane magnetic field  $H$  and  $[100]$  direction of PMN-PT. (a)(c)(e) Without polymer. (b)(d)(f) With polymer.



**Figure 2.4.** A large coercivity change can be seen from the Kerr rotation vs Magnetic Field hysteresis loop of Terfenol-D thin film on PMN-PT after being poled at 0.6 MV/m. Figure adapted from [59]. Copyright © 2015 AIP Advances.

As shown, the MOKE technique is relatively simple for probing magnetic property. However, since it uses near-visible light with a rather long wavelength, MOKE is unsuitable for imaging the magnetic domain structures in sub-micron-scale elements [60]. In contrast, X-ray techniques can be informative in studying magnetization at a small scale (e.g., XMCD-PEEM), as discussed in Section 2.1.4.

### 2.1.3 Magnetic Force Microscopy

In an inhomogeneous magnetic field  $\mathbf{H}$ , the force  $\mathbf{F}$  experienced by a magnetic dipole  $\mathbf{m}$  is given by:

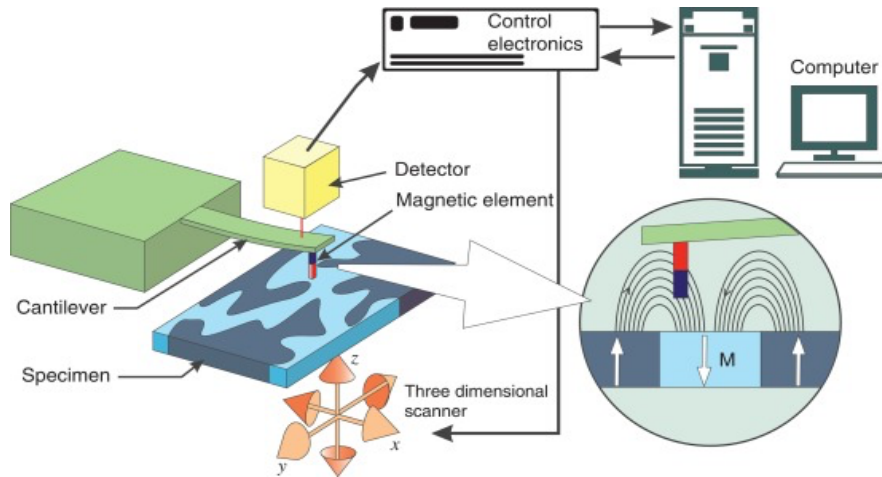
$$\mathbf{F} = \nabla(\mathbf{m} \cdot \mathbf{H}) [V A s m^{-1}]. \quad (2-1)$$

This force is the negative gradient of the energy. If the magnetic dipole is small, it can be written as the following based on the gradient operator:



$$\mathbf{F} = (\mathbf{m} \cdot \nabla)\mathbf{H} + \mathbf{H}(\nabla \cdot \mathbf{m}) \cong (\mathbf{m} \cdot \nabla)\mathbf{H}. \quad (2-2)$$

Therefore, a magnetic dipole aligned along the inhomogeneous magnetic field direction will tend to move towards the direction of increasing magnetic field [60].

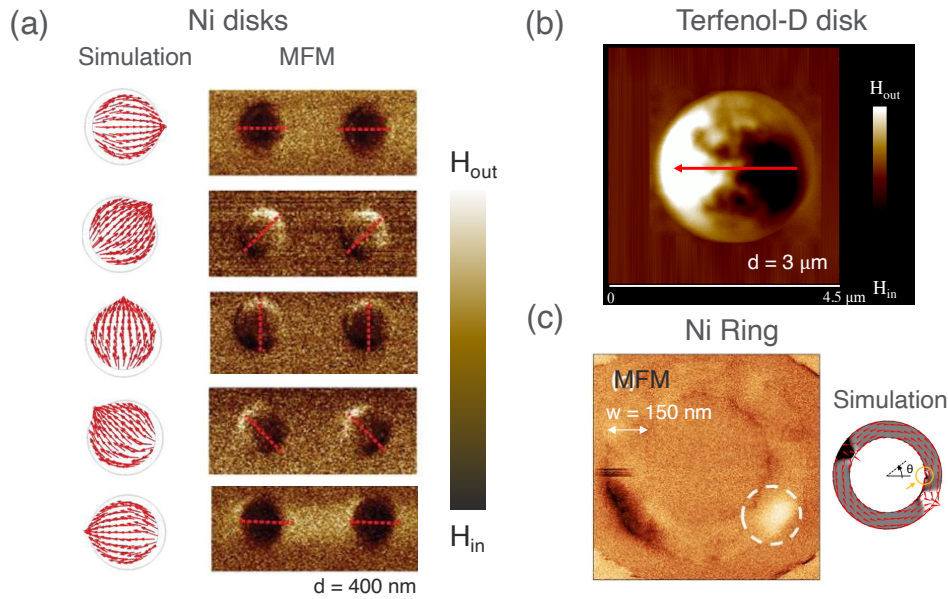


**Figure 2.5.** Working principle of Magnetic Force Microscopy (MFM). Figure from [61].

Magnetic Force Microscopy is an application of Equation 2-1. It has a very fine tip on the order of a few micrometers coated with a thin film of ferromagnetic material (e.g., Co) mounted onto a cantilever beam attached to a piezoelectric crystal. The magnetic moments of the electrons in the tip coupled with each other form a large magnetic moment aligning in the direction of the tip. When in an inhomogeneous magnetic field (i.e., the fringe field with field gradient), this magnetic moment of the tip would experience a measurable force, either attractive or repulsive. The spatial resolution of the MFM can be high enough to detect the stray fields from domain walls a few nanometers in width, and the magnetic force it can measure can also be as small as that from a single electron spin-flip [62]. The magnetic force acting on the magnetic tip can bend the tip. This force is calculated by monitoring using optical interferometry [63] the cantilever deflection due to the tip movement or oscillation amplitude of the cantilever beam, as shown in **Figure 2.5**.

Though MFM can be used to observe magnetic structures with very high resolution (i.e., 40 nm), better than MOKE Kerr microscopy, it suffers from several drawbacks: 1) the possibility of the tip perturbing highly mobile domain walls and domain states in some soft magnetic samples; 2) it is hard to directly calculate the magnetic stray field above the specimen based on the measured force on the tip due to the tip not being fully covered by the magnetic material [37]. Advantages of MFM include that vacuum is not necessary, the micrographs can be collected in magnetic fields, and the topographical information is separated from the magnetic information [63]. MFM is more sensitive to out-of-plane (mainly along the z-direction) stray fields from the sample and cannot clearly map out the in-plane magnetic domains. However, it can verify single domain micro- or nanomagnets by tracing the in-plane magnetic stray field on the edges.

Figure 2.6 shows a few MFM example results of magnetostrictive microstructures [64][65][66].  $H_{in}$  and  $H_{out}$  represent the stray field coming in and out of the magnetic structure. When the tip scanning direction aligns with the stray field direction, the sensitivity of the MFM tip is low, and vice versa. In (a), even though all the magnets exhibit single domain structure in the five micrographs, the overall contrast is higher (middle three images) when the stray field direction is at an angle with respect to the horizontal scanning direction than when the stray field direction aligns with the tip scanning direction (top and bottom images). Similarly, (b) demonstrates a single domain magnetic microstructure in Terfenol-D microdisk, with more detail in Chapter 5. Compared to MFM that potentially interacts and perturbs local magnetic state in the specimen, non-invasive magnetic imaging methods such as scanning electron microscopy with (spin) polarization analysis (SEMPA) and X-ray magnetic circular dichroism - photoemission electron microscopy (XMCD-PEEM) (Section 2.1.4) are more effective.



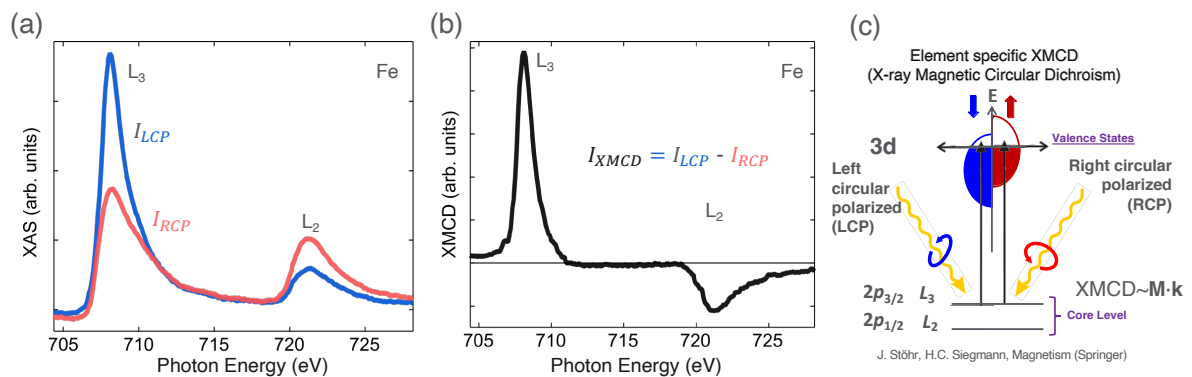
**Figure 2.6.** Magnetic Force Microscope is a helpful tool to characterize domain walls and stray-field in micro- and nanoscale magnetic structures. (a) Ni nanoscale disks on PZT substrate with a rotatable single domain. Figure adapted from [20]. (b) Single domain in Terfenol-D disk on Si wafer. Figure from [65]–[67].

#### 2.1.4 From X-ray Circular Dichroism to X-ray Photoemission Electron Microscopy (XMCD-PEEM)

The term “dichroism” describes the material property in which different polarizations are absorbed in different amounts. Circular Dichroism (e.g., X-ray magnetic circular Dichroism) has been used to study magnetic materials. The left and right circular polarization correspond to different spin angular momentum states, respectively.

In 1986, the magnetic x-ray dichroism effect was first discovered in LURE at Université Paris-Sud in France [68]. X-ray magnetic circular dichroism has since become a standard technique to characterize magnetic information of materials, including magnetic moments, magnetocrystalline energy, magnetostriction, magnetic hysteresis, coercivity, magnetization

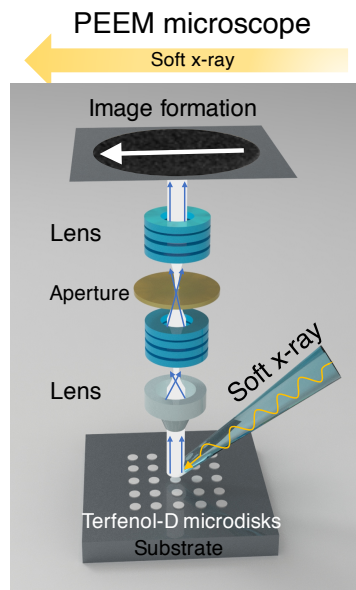
easy axis direction, etc. [69]. For magnetic materials, XMCD intensity refers to the difference between the x-ray absorption spectra, excited by left circularly polarized (LCP) X-ray and right-circularly polarized (RCP) X-ray beam in magnetic materials. This difference arises from the imbalance of empty valence states for excited electrons. The magnitude of XMCD is proportional to the magnetization component in the X-ray propagation direction (**Figure 2.7**).



**Figure 2.7.** Element-specific X-ray magnetic circular dichroism obtained at the absorption edge of the element of interest (e.g., for the L-edge absorption in Fe) provides magnetic information. (a) An example of X-ray absorption spectra taken with opposite circular polarizations for Fe. (b) XMCD is the difference between the LCP and RCP spectra. (c) Origin of XMCD, adapted from [60].

XMCD-PEEM images the XMCD signal taken on a 2D scale, with contrasts representing the in-plane magnetization direction. More experimental details and XMCD-PEEM images can be found in Chapter 4, Section 4.2.2. Alternative magnetic imaging methods such as MOKE discussed earlier in Section 2.1.2 have their resolution limited by the wavelength of visible light, and thus will fail to capture complex domain patterns at nanoscale resolution; for MFM, its potentially invasive character and small field of view prevent us from efficiently imaging an extensive range of structures. Furthermore, MFM will not be able to

capture with such efficiency, and MOKE will not capture the domain variation in detail. In other words, the instant mapping and the full-field nature of PEEM make it more advantageous compared to the MFM imaging with a raster scan. The XMCD-PEEM images shown later in this dissertation were collected by the PEEM-3 microscope [70] (**Figure 2.8**) at beamline 11.0.1, Advanced Light Source, Lawrence Berkeley National Lab.



**Figure 2.8.** Schematic of a PEEM microscope and image formation at CCD, based on PEEM-3 microscope at the Advanced Light Source, Berkeley National Lab.

## 2.2 Piezoelectric characterization – Strain

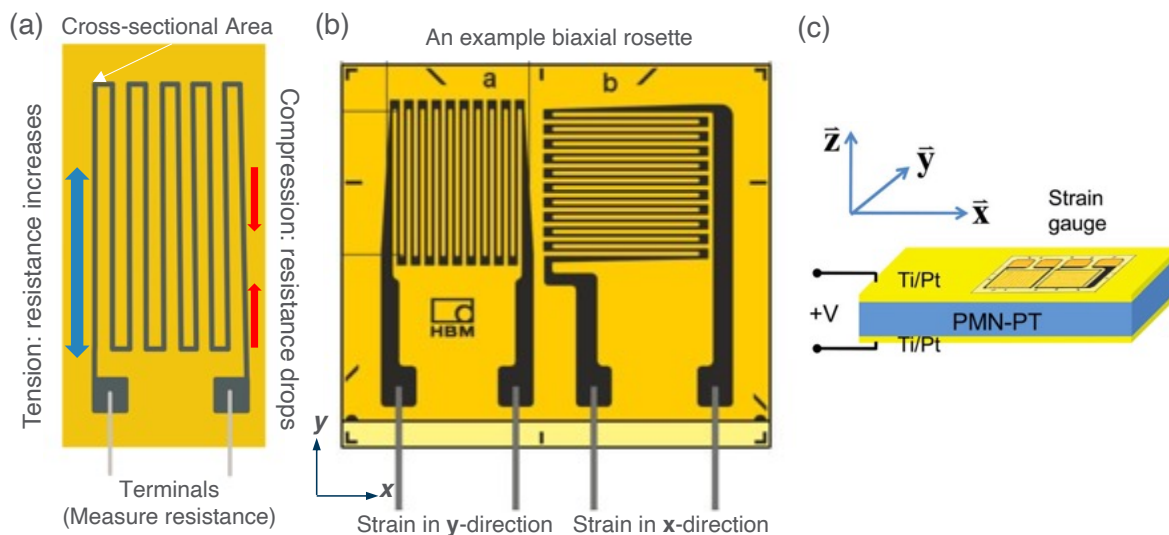
### 2.2.1 Metal Foil Strain Gauge

A commercialized metal foil strain gauge can be used to directly measure the macroscopic strain in the specimen of interest. It is cemented to the specimen using adhesive glue such as cyanoacrylate. A resistive strain gauge typically has a conductive strip following a zig-zag pattern of lines to prevent overheating versus a thin single-line geometry with equivalent resistance. The underlying working principle of a strain gauge is that when the

specimen it attaches to experience a tensile strain, it elongates the metal foil ( $\frac{\Delta l}{l} = \varepsilon$ ) and the cross-sectional area  $A_0$  of the metal lines decrease to  $(1-2\nu\varepsilon) A_0$ . As the dimension of the strain gauge changes, its resistance also change following:

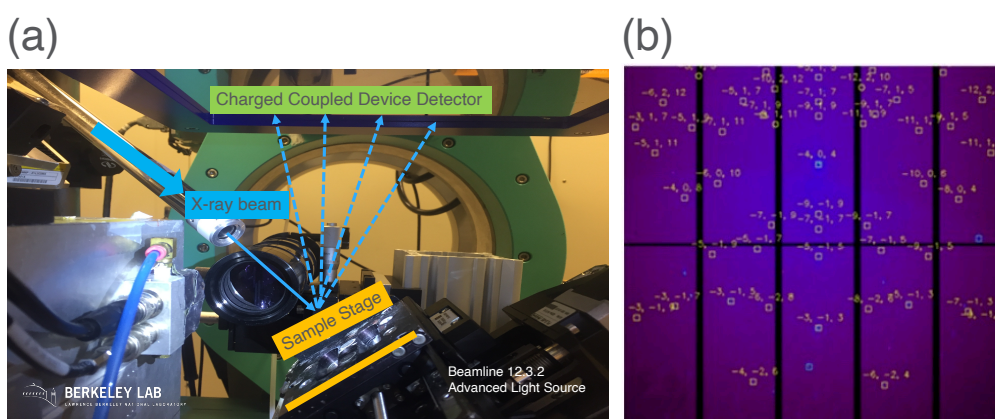
$$R = \frac{\rho l}{A} = \rho l_0(1 + \varepsilon) / (1-2\nu\varepsilon) A_0 \approx [1 + \varepsilon(1 + 2\nu)]R_0 . \quad (2-3)$$

Therefore, a change in resistance measurement of the strain gauge can be related to the macroscopic in-plane strain it experiences [63]. When the strain gauge is elongated in the direction parallel to the metallic lines, meaning it is under tensile strain, the cross-sectional area decreases, and the resistance increases. In contrast, when the strain gauge experiences compression along the direction parallel to the lines, the resistance decreases. Typically, a sensitive circuit with Wheatstone bridge configuration is used to measure this resistance change and hence the strain response of the specimen. The strain gauge measures uniaxial in-plane strain on a macroscopic level, taken as the average strain in the region (few mm in lateral dimension) covered by the strain gauge. To measure biaxial strain, a biaxial rosette with two strain gauges mounted parallel to each other can be used. For a bulk piezoelectric substrate, continuous top and bottom parallel plate electrodes are deposited before attaching the biaxial strain gauge to the top electrode (**Figure 2.9c**). The in-plane piezoelectric response with respect to applied voltage across a piezoelectric substrate can be obtained with the strain gauge measurements.



**Figure 2.9.** (a) Schematic of a resistive strain gauge. (b) An example biaxial rosette with two strain gauges mounted perpendicular to each other. Figure from [71], annotated. (c) Schematic of strain gauge glued to the top electrode on a bulk piezoelectric material PMN-PT to measure principal strains in both x and y directions. Figure from [11].

### 2.2.2 Laue X-ray Microdiffraction for probing strain at micron-scale



**Figure 2.10.** (a) Setup of the experimental area of the X-ray Microdiffraction beamline. A MAR 133 x-ray CCD camera placed in the 45 degree reflective geometry collects the diffracted x-ray from the sample. (Beamline 12.3.2, Advanced Light Source of Lawrence Berkeley

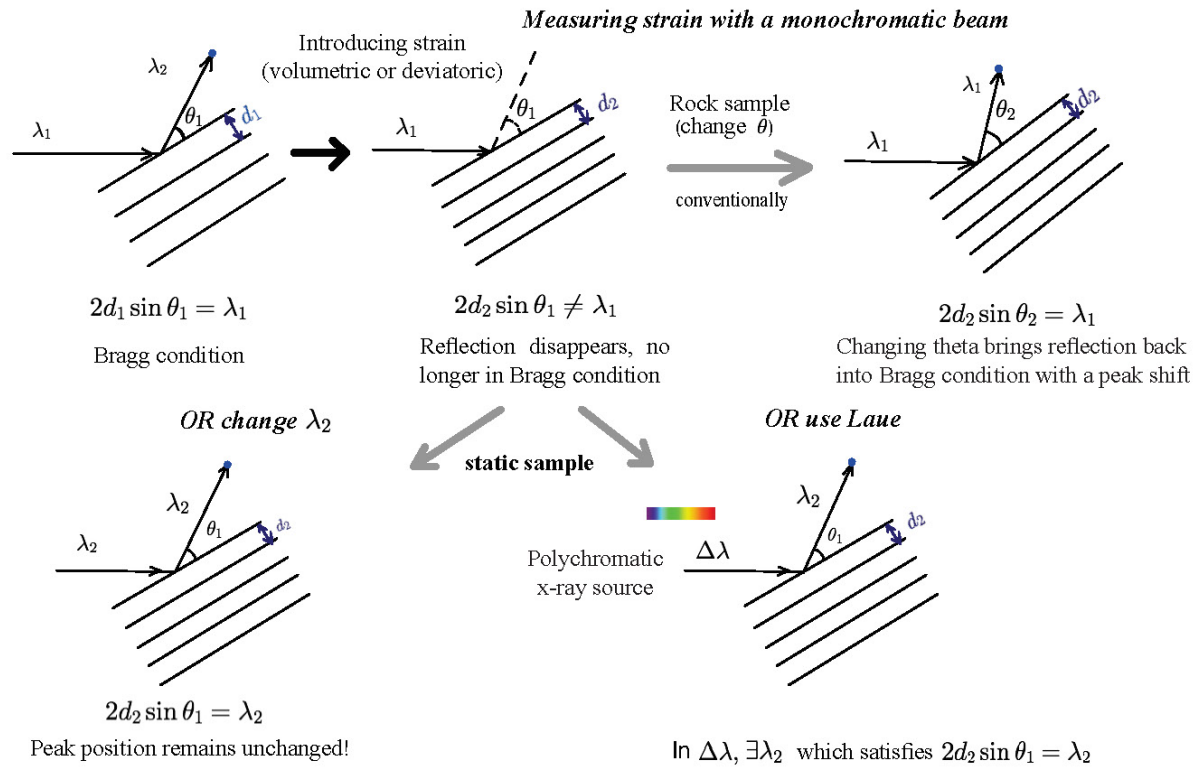
National Laboratory) (b) A Laue pattern with the most intense reflections indexed with  $hkl$  Miller indices. It can be used to obtain the deviatoric strain tensor. Figure from [72].

Different from metallic foil strain gauge measures macroscopic strain as discussed in the previous section, white-beam X-ray microdiffraction is an ideal tool to study the micron-scale local strain response in materials. Laue (polychromatic) X-ray microdiffraction can be used for investigating elastic strain distribution at the micron-scale [50], [73]. The X-ray microdiffraction [22], [74]–[76] facility used in this study (beamline 12.3.2, Advanced Light Source, Berkeley National Lab) uses an x-ray (energy range of the white beam: 5.5-14 keV) with wavelength in the range of 0.5 - 2Å with a beam size of 1.5  $\mu\text{m}$ , allowing measurements of the local strain at specific locations of the sample. **Figure 2.10** shows both the setup of the experimental area of the beamline and a sample Laue pattern. More information on the beamline design, layout and performance information can be found in Kunz *et al.*[77] . The beamline has two detectors, a MAR 133 x-ray Charged Coupled Device Detector (CCD) and a Si-drift detector. The CCD is used to detect both monochromatic and polychromatic diffraction patterns [77][78] and the Si-drift detector (Vortex-EM by SII Nanotechnology Inc.) can map x-ray fluorescence elemental mapping, which can be helpful for locating the focused x-ray to the desired locations on the sample. Previously in Lo Conte *et al.* [22], [79], x-ray fluorescence was used to map out the positions of patterned 2  $\mu\text{m}$  Ni squares on PMN-PT for subsequent x-ray microdiffraction measurements for the piezostain.

A focused X-ray beam with a diameter of 1.5  $\mu\text{m}$  (for experiment described in Chapter 6) is incident at 40° on the sample surface and scans along the sample directions of interest. While Laue microdiffraction along with monochromatic beam measurements provide information on the entire strain tensor [74], this dissertation mainly focuses on the experimentally-measured



in-plane deviatoric strain [78], [80], [81]. To measure the hydrostatic strain, a monochromatic beam with energy scanning in incremental steps will be needed [72], [78].



**Figure 2.11.** Schematics of Bragg’s law and difference between the two types of basic x-ray diffraction experiment: monochromatic method (top right) and Laue method (bottom right).

Figure 2.11 outlines the basic principles of measuring strain nondestructively with diffraction. For diffraction to occur, Bragg’s Law needs to be satisfied. Among the three principal parameters,  $\lambda$ ,  $d$  and  $\theta$ , two remains fixed while the third one is varied. In monochromatic mode, the wavelength of the beam is fixed, when strain leads to changes in the atomic planes distance in crystalline samples, the sample is rotated by rocking motion until Bragg’s Law is fulfilled again. Either volumetric or deviatoric strain could result in the diffraction peak or reflection position shift.

The illustration (**Figure 2.11**) is here to explain the measure of change in volume through change in interplanar spacings. Change in shape of the unit cell for deviatoric strain is not illustrated here but this should be straightforward without the need of illustrations. Distortion of the unit cell (shear) will result in tilt of the lattice planes, which would result in reflection shifts irrespective of the nature of the incoming beam (monochromatic or polychromatic).

In Laue (polychromatic) diffraction, the sample sits still and the varied parameter is the wavelength. The radiation is a combination of a full spectrum of wavelengths (white x-rays), among which there is some X-ray wavelength that satisfies the Bragg's Law. Considering different sets of planes will diffract X-ray at different wavelengths, with different diffracted directions ( $\theta$ ), the net diffraction result is a Laue pattern presented as a 2D image with different diffraction spots. Batch processing of Laue images using computational software can index and carry out strain refinement procedures. For our study, we used a specific software, XMAS, developed at the Advanced Light Source, Lawrence Berkeley National Laboratory [78].

When it comes to strain, the total strain tensor  $\varepsilon_{ij}$  can be broken into two components, the hydrostatic strain/ dilatational strain tensor  $\Delta$  due to volume change, and the deviatoric strain  $\varepsilon'_{ij}$  that accounts for the deformation at a constant volume [78]:

$$\varepsilon_{ij} = \varepsilon'_{ij} + \Delta_{ij},$$

$$\text{where } \varepsilon'_{ij} = \begin{bmatrix} \varepsilon'_{11} & \varepsilon'_{12} & \varepsilon'_{13} \\ \varepsilon'_{21} & \varepsilon'_{22} & \varepsilon'_{23} \\ \varepsilon'_{31} & \varepsilon'_{32} & \varepsilon'_{33} \end{bmatrix},$$

$$\Delta = \begin{bmatrix} \delta & 0 & 0 \\ 0 & \delta & 0 \\ 0 & 0 & \delta \end{bmatrix},$$

$$\delta = \frac{1}{3} \text{tr}(\varepsilon_{ij}).$$

The sum of the three normal strains  $\varepsilon_{11}$ ,  $\varepsilon_{22}$ ,  $\varepsilon_{33}$  is the volumetric strain  $\Delta V/V$ ; the average of the normal strains is the dilatational (or “hydrostatic”) strain  $\delta$ , and the deviatoric strains  $\varepsilon'_{ij}$  are obtained by subtracting  $\delta$  from each  $\varepsilon_{ii}$ .

With a volumetric strain, the reflection will not change position, but only the wavelength will change. With a deviatoric strain, the peak will shift both in angle and in wavelength. Changes at constant volume in the shape of the unit cell results in relative tilts of the lattice planes, leading to relative displacement of the Laue spots [82]. Meanwhile, changes in the volume of the unit cell cause changes in the interplanar distance, and thus shifting the reflection energy, but cause no shift in reflection position [78]. In other words, Laue diffraction without wavelength measurements, can only detect changes at constant volume in the shape of the unit cell, the deviatoric strain in the sample. Reflection indexing in the Laue pattern provides information on the shape and orientation of the unit cell. The reflection positions shift from the ideal “unstrained” position of the crystal can provide information on the elastic deformation state of the unit cell at constant volume, which can be represented by the deviatoric strains [78]. For the very same reasons as for volumetric strain, polychromatic beams cannot measure thermal expansion coefficients.

As the x-ray scans across the sample during the experiment, Laue diffraction patterns are obtained at each location. The indexing of the Laue patterns provides essential information on the crystals, including crystal structure, grain orientation, and unit-cell distortion (deviatoric strain). Therefore, the measured relative shift can provide information on the deviatoric elastic strains. The entire strain tensor can be derived along with the measured changes in the unit-cell volume (dilatational strain) via monochromatic beam [78]. Usually, measuring the dilatational strain component is not critical because the shear information needed for analyzing the

deformation state is included in the deviatoric strain measurements. For this work, we did not perform an energy (monochromator) scan at each point as it was found to be too time-consuming for this time-resolved experiment, requiring data collection at each voltage step. Therefore, this work focus on the in-plane relative strains by measuring the deviatoric component. The numerical results reported are the relative changes to the deviatoric strain when compared to an unstrained state. Finally, the in-plane deviatoric strains are denoted as  $\varepsilon'_{xx}$  and  $\varepsilon'_{yy}$ .

# **Chapter 3 Tunable magnetoelastic effect in voltage-controlled exchange-coupled composite multiferroic microstructures<sup>1</sup>**

## **3.1 Multiferroics systems with composite magnetic layer**

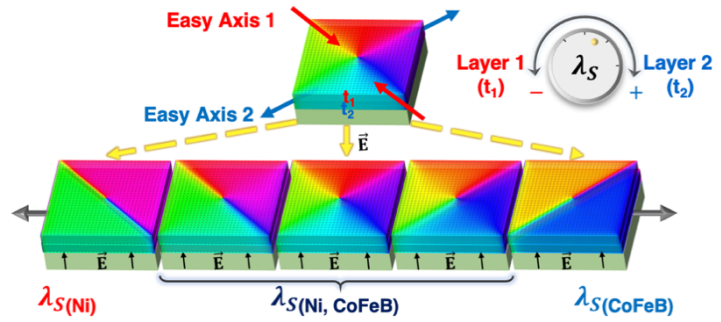
The ability to control magnetization through an electric field offered by such materials systems allows for an energy-efficient voltage-based approach to the control of on-chip magnetic nanostructures [15], [83], [84]. Accordingly, the development of efficient magnetoelectric systems with tunable properties is of great scientific as well as technological importance.

Magnetoelastic composite multiferroic systems [19]–[21], [85] are among the most promising magnetoelectric systems for spintronic devices. They rely on the combination of piezoelectric and magnetostrictive materials, where the electrically-generated strain in the piezoelectric layer is used to reorient the magnetization state of the magnetic layer [20], [38], [39]. So far, much work has been done on systems employing a single magnetostrictive material, with efforts focused on finding new magnetostrictive/piezoelectric heterostructures with large magnetoelastic coupling. However, this approach does not offer much flexibility for tuning the magnetoelastic coupling of a defined system.

---

<sup>1</sup> This chapter is adapted from previously published manuscript [65] with the same title.

In this chapter, we show that multiferroic systems with a composite magnetic layer can potentially offer much richer magnetoelectric properties, with



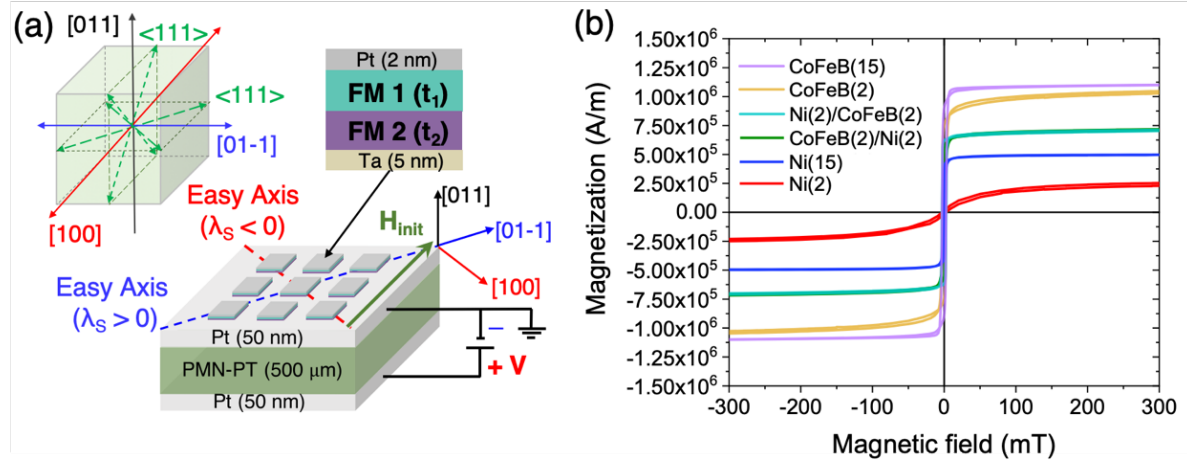
the possibility to tune such properties by tailoring the magnetic layer composition. Despite its high potential, this avenue has until now remained mostly unexplored.

We report an investigation of the magnetoelectric properties of model composite multiferroic systems consisting of a  $[\text{Pb}(\text{Mg}_{1/3}\text{Nb}_{2/3})\text{O}_3]_{1-x}-[\text{PbTiO}_3]_x$  (PMN-PT) [8], [58], [86] piezoelectric substrate and exchange-coupled Ni/CoFeB bilayers. The magnetoelastic coupling of these systems are studied by observing the electric field-induced magnetic reorientation in Ni/CoFeB microstructures by x-ray magnetic microscopy. The systems show a magnetoelastic effect that depends on the relative thickness of the two magnetic layers, offering a new degree of tunability. Micromagnetic simulations are used to better comprehend the magnetoelastic properties of the investigated systems, unveiling a behavior that cannot be described by simply combining the magnetoelastic responses of the two constituent magnetostrictive materials.

### 3.2 Experimental setup and magnetic characterization

The material systems of interest consist of Ni/Co<sub>40</sub>Fe<sub>40</sub>B<sub>20</sub> microstructures of different thickness combinations deposited on top of 500 μm-thick piezoelectric  $[\text{Pb}(\text{Mg}_{1/3}\text{Nb}_{2/3})\text{O}_3]_{0.69}-[\text{PbTiO}_3]_{0.31}$  (PMN-PT) single crystal substrates with both the top and the bottom surfaces covered by 50 nm-thick Pt electrodes. The piezoelectric substrates have the [011] pc (pseudo-cubic; in the following, this will be omitted for simplicity)

crystallographic direction pointing out of the surface plane, as in Figure 3.1(a), and are electrically pre-poled in this direction with the polarization pointing “up” before depositing and patterning the magnetic bilayer on top of it. The Ni/CoFeB microstructures are  $2 \mu\text{m} \times 2 \mu\text{m}$  in size.



**Figure 3.1** . (a) Sample schematic and crystallographic orientation of the PMN-PT crystal, with the surface normal along the [011] direction. After patterning, the magnetic microstructures were initialized by an external magnetic field,  $\mu_0 H_{init} = 300 \text{ mT}$ , applied as in the schematic. (b) SQUID magnetometry hysteresis loops for the different magnetic thin-films, before patterning, on PMN-PT investigated in this study (layers thickness in nm). The magnetic field was applied in-plane along the [01-1] direction.

A first hint of the emergent behavior of the investigated multiferroic systems is given by the magnetic properties of Ni/CoFeB thin-films, extracted through Superconducting Quantum Interference Device (SQUID) magnetometry measurements. As shown in Figure 3.1(b), the single-layer CoFeB thin films (purple and yellow curves in Figure 3.1(b)) are found to have the highest saturation magnetization value,  $M_s \approx 1.1 \times 10^6 \text{ A/m}$ , among the investigated samples. On the other hand, the samples with a 15 nm-thick Ni layer (blue curve in Figure 3.1(b)) shows a lower  $M_s$  of  $5 \times 10^5 \text{ A/m}$ . The  $M_s$  values for the aforementioned thin

films are close to previously reported ones, for CoFeB to be  $1 \times 10^6$  A/m [87], and for Ni to be  $4.8 \times 10^5$  A/m [88]. Finally, bilayer samples having a 2 nm-thickness for both CoFeB and Ni (cyan and green curves in Figure 3.1(b)) show an average  $M_S$  value of  $7.4 \times 10^5$  A/m, regardless of the stacking order. The shape of the bilayer MH loop combines the features of both Ni thin film and CoFeB thin film, indicating the magnetic properties of the bilayer result from the interplay between the two magnetic layers being coupled to each other. Even stronger evidence of the importance of the coupling between magnetic layers is given by the hysteresis loop obtained for the Ni (2 nm) sample (red line in Figure 3.1(b)). Compared to the 15 nm thick Ni with a square MH loop, the thin Ni (2 nm) loop indicates a superparamagnetic state, as shown by the very low saturation magnetization (at the maximum applied magnetic field), together with the absence of any significant remanence (see Figure 3.3(a) for more details) [89]. This finding is in accordance with a previous study showing superparamagnetism in ultrathin Ni film with thickness down to 2 nm[90]. However, the Ni (2 nm)/ CoFeB (2 nm) and CoFeB (2 nm)/ Ni (2 nm) samples both show an average  $M_S$  in between thick Ni (15 nm) and CoFeB, demonstrating the influence of ferromagnetic CoFeB on the thin Ni layer, resulting in the entire film stack being ferromagnetic (element specific hysteresis loops shown in Figure 3.3).

Though CoFeB (2 nm)/ Ni (2 nm) and Ni (2 nm)/ CoFeB (2 nm) films have the same  $M_S$ , a closer examination of the SQUID and x-ray magnetic spectroscopy data suggests the stacking order of the thin films plays a more subtle role in the bilayer's magnetic properties, such as coercive field (Section 3.2.3). From these initial results, we infer that parameters such as film thickness and stacking order have a significant impact on the magnetic properties and therefore on the magnetoelectric coupling in this artificial multiferroic composite, and to further explore the effects of these parameters we present magnetic imaging results below.



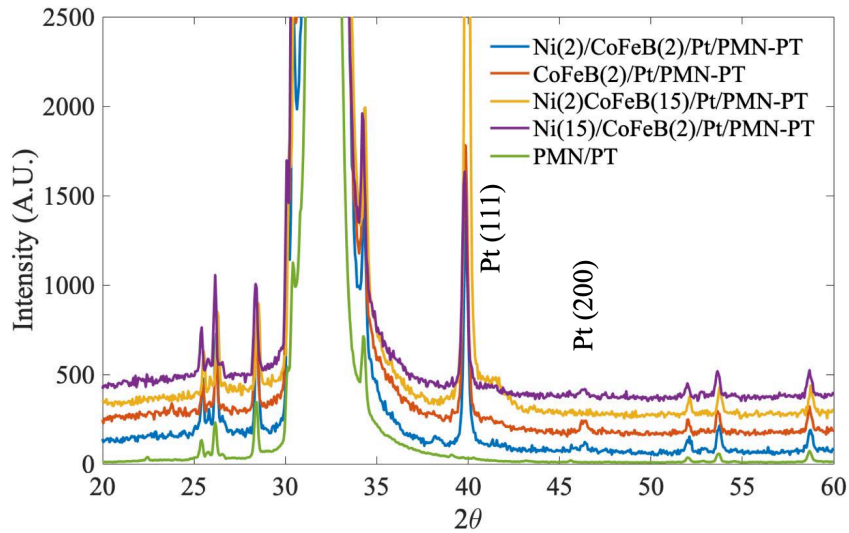
### 3.2.1 *Sample Preparation*<sup>2</sup>

After dicing the [011] cut polished  $[\text{Pb}(\text{Mg}_{1/3}\text{Nb}_{2/3})\text{O}_3]_{1-x}[\text{PbTiO}_3]_x$  (PMN-PT,  $x \approx 0.31$ ) single crystal into  $1 \text{ cm} \times 1 \text{ cm} \times 500 \text{ }\mu\text{m}$  thick pieces, we use a Matrix Plasma Asher to remove organic residues from the substrates with oxygen plasma. 5 nm Ti and 50 nm Pt thin films are deposited by e-beam evaporation via a CHA Solution electron beam evaporator on both surfaces of the PMN-PT substrate. Each film is deposited at a rate of  $0.3 \text{ \AA/s}$ . The Pt films serve as top and bottom electrodes so that the substrate can be actuated in a parallel plate capacitor geometry. Microstructures ranging from  $1 \text{ }\mu\text{m}$  to  $4 \text{ }\mu\text{m}$  in length are defined and written by electron beam lithography in the PMMA A2 resist coating the top Ti/Pt surface. Before CoFeB/Ni sputtering deposition, the PMN-PT is electrically prepoled with an electric field of  $0.4 \text{ MV/m}$  in the [011] direction of the PMN-PT to minimize the residual strain. Next, 5 nm Ta film and bilayers of CoFeB and Ni, each with a thickness of either 2 nm or 15 nm, are grown by magnetron sputtering with a base pressure of  $3 \times 10^{-8}$  Torr, capped with a 2 nm Pt layer to prevent oxidation. The roughness of the sample is measured with an atomic force microscope, showing an  $R_q$  of 0.6 nm. Then the magnetic patterns are lifted off using heated NMP solution at  $50^\circ\text{C}$ . The four corners of the samples are cut off to fit in the LCC while having the [100] and [01-1] crystal directions of the PMN-PT substrates pointing along the diagonal directions of the LCC. The reason for such alignment is to have the electrically-induced magnetoelastic easy axes of Ni and CoFeB along the diagonals of the PEEM micrographs for the ease of analysis. The devices are then wire-bonded such that the top surface is grounded and the bottom is connected to a bipolar voltage power supply. They are then magnetized by an initialization field  $H_{\text{init}}$  of 0.4 T applied in-plane along the direction bisecting [100] and [01-1] crystallographic directions of the PMN-PT.

---

<sup>2</sup> This section is adapted from [23].

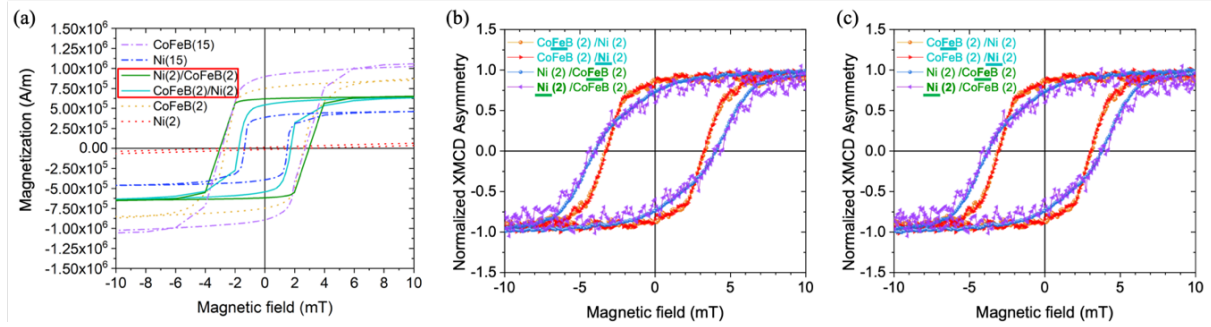
### 3.2.2 X-ray diffraction measurements of four thin film samples with varied thickness combinations



**Figure 3.2.** X-ray diffraction (XRD) measurements of four thin film samples on PMN-PT and a reference PMN-PT sample. The result shows no diffraction peak from the magnetic layer.

In order to characterize the deposited thin films from a structural point of view, XRD measurements are carried out on four samples with different thin film thickness combinations and the substrate PMN-PT for reference. The outcomes of the XRD characterization (Figure 3.2) shows no diffraction peaks associated with either of the magnetic layers. These results indicate an amorphous or nanocrystalline state for the deposited magnetic layers, which is not surprising for a DC sputtering deposition with no post-annealing.

### 3.2.3 Magnetic characterization of the exchange-coupled multiferroic heterostructures



**Figure 3.3.** (a) Zoomed-in SQUID magnetic hysteresis loops (from Fig. 1(b) from main text) of the corresponding magnetic thin films on PMN-PT investigated in the study. (b) Normalized x-ray magnetic circular dichroism hysteresis loops for Fe and Ni taken at room temperature in Ni (2 nm)/CoFeB (2 nm)/PMN-PT and CoFeB (2 nm)/Ni (2 nm)/PMN-PT (the element used for the measurement is underlined and indicated in bold). The magnetic field was applied at a grazing incidence of  $20^\circ$  with respect to the surface of the sample, with its in-plane component along the [01-1] direction. (c) Same as in (b), with magnetic field axis corrected by multiplying  $\cos(20^\circ)$  to reflect the amplitude of in-plane component of the applied magnetic field.

As shown by the SQUID magnetic hysteresis loops in Figure 3.3(a), the CoFeB (2 nm)/Ni (2 nm) and the Ni (2 nm)/CoFeB (2 nm) thin film on the PMN-PT substrate show the same saturation magnetization of  $\sim 7 \times 10^5$  A/m. However, the two systems show a different magnetic coercivities. The stack with a CoFeB (2 nm) layer in direct contact to the buffer layer shows a coercivity that is almost as twice as the one of the stack having the Ni (2 nm) layer at the interface with the buffer material.

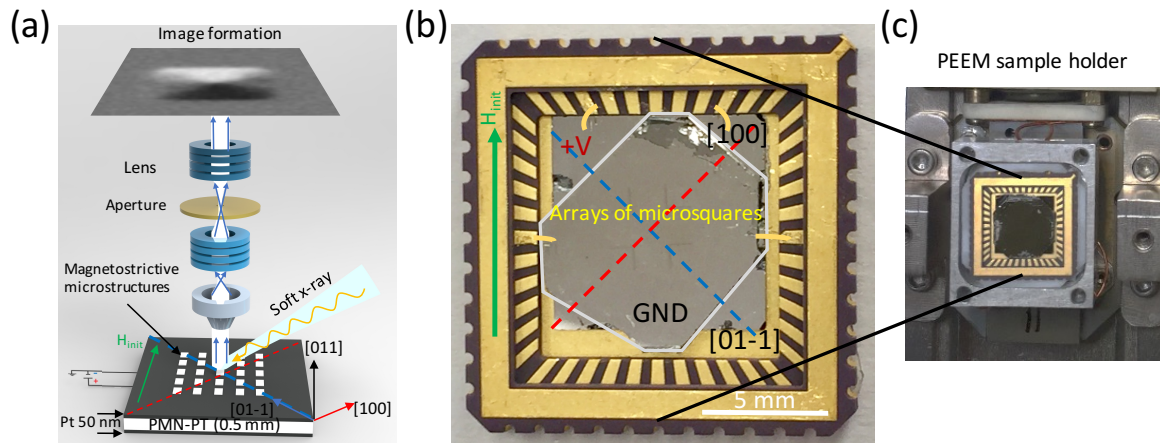
To further understand how the growth order affects the bilayer magnetic property reported above, x-ray magnetic circular dichroism (XMCD) is used to investigate the two thin film stacks. XMCD offers element-specific information on the magnetic property of the individual layers, thus the contributions to the magnetization from both CoFeB and Ni layer

can be separated. It could also provide direct evidence of the exchange coupling behavior. Figure 3.3(b) displays the Fe and Ni hysteresis loops from the Ni (2 nm)/ CoFeB (2 nm)/ Ta (5 nm)/ Pt (50 nm)/ Ti (5 nm)/ PMN-PT and CoFeB (2 nm)/ Ni (2 nm)/ Ta (5 nm)/ Pt (50 nm)/ Ti (5 nm)/ PMN-PT, at the x-ray incident angle of 20°. Figure 3.3(c) shows the MH loop with horizontal-axis being the component of the in-plane magnetic field. The overlapping of the Fe and Ni MH loops for each specific sample confirms that the two layers are exchange coupled. It also confirms that the coercivity of the bilayer depends on the growth order of the film. It is observed that when CoFeB serves as a seed layer in the case of Ni (2 nm)/ CoFeB (2 nm)/ Ta (5 nm)/ Pt (50 nm)/ Ti (5 nm)/ PMN-PT, the coercive field  $H_c$  is lower than when the Ni functions as a seed layer, in the case of CoFeB (2 nm)/Ni (2 nm)//Ta (5 nm)/Pt (50 nm)/PMN-PT. When CoFeB serves as the seed layer, the coercivity is close to that of CoFeB (2nm) film, and when Ni serves as the seed layer, the coercive field is close to that of Ni (15 nm) film.

#### 3.2.4 Magnetic contrast study by XMCD-PEEM

The magnetic properties of arrays of microscale magnetic square of CoFeB and Ni layers of different thickness combinations are investigated by XMCD-PEEM. XMCD-PEEM is an element-specific magnetic contrast imaging technique. It probes the secondary electrons emitted from the sample surface following the absorption of the incoming circularly polarized x-ray photons, known as the XMCD effect. Element specificity of the PEEM imaging makes it a powerful tool to investigate individual layers in a magnetic multilayer system. For this experiment, the magnetic domain visualization in each layer of the bilayer is achieved by separately probing at the photon energy of the Ni  $L_3$  edge for the Ni layer or the Fe  $L_3$  edge for the CoFeB layer. In this way the magnetic domains, as indicated by the magnetic contrast, in the two different material layers can be analyzed separately. **Figure 3.4(a)** is a schematic of the PEEM microscope and the position of the sample with respect to the incident x-ray and the

initialization magnetic field. **Figure 3.4(c)** shows the device (**Figure 3.4(b)**) mounted onto a PEEM sample holder that allows in-situ electric-field application.



**Figure 3.4.** (a) Schematic of the XMCD-PEEM imaging setup. The orientation of the device with respect to the incident x-ray beam is illustrated. Prior to imaging, an initialization magnetic field ( $H_{init}$ ) was applied. The crystallographic orientations of the [011]-cut PMN-PT are highlighted, with [100] being the compressive strain axis, and [01-1] being the tensile strain axis. (b) A completed device on an LCC with crystallographic directions of [011] cut PMN-PT and the orientation of the magnetic field for magnetization state initialization ( $H_{init}$ ) marked. The substrate is mounted on a piece of Si wafer of 0.3 mm thick so that the sample surface is at the proper height (0.8 mm from the LCC surface) for XMCD-PEEM imaging. The top surface of the multiferroic heterostructure is grounded (as indicated by “GND”, and the bottom is connected to a hot wire (as indicated by “+V”). (c) A device is mounted onto a PEEM-3 sample holder at beamline 11.0.1.1 of ALS, LBNL. Figure from [91]

### 3.3 In-operando magnetic imaging & Simulation

Following the initial characterization of the magnetic thin-films, the magnetoelastic properties of the systems are investigated through voltage-controlled magnetization

reorientation experiments in patterned microstructures. The magnetic state of the microsquares is imaged by x-ray magnetic circular dichroism - photoemission electron microscopy (XMCD-PEEM) [92]. Exploiting the probe depth of approximately 5 nm and the elemental sensitivity of x-ray absorption at the Fe and Ni  $L_3$ -edges [93]–[95], we are able to separately image the magnetic state in each magnetic layer and compare them with each other (See “Animation of the PEEM experiment setup for obtaining the magnetic contrast from the bilayers with the in situ electric field”<sup>3</sup>). As shown in Figure 3.3(a), the initial magnetic state observed in both sub-layers of the bilayer is the same, proving the presence of a strong exchange coupling at the CoFeB/Ni interface. Accordingly, from now on we will present only the XMCD-PEEM images referring to the CoFeB layer for simplicity, unless otherwise noted.

After magnetically initializing the samples by application of an external magnetic field  $\mu_0 H_{\text{init}} = 300$  mT as indicated in **Figure 3.5(a)**, many magnetic squares are observed to be in the Landau magnetic flux-closure [93] (subsequently referred to as the vortex state). However, the initialization yield is smaller than 100%, and in some of the images micro-squares are observed to be in a randomly oriented multi-domain state. This could be primarily due to domain wall pinning effects at structural imperfections, and also partially due to the inhomogeneous strain at sub-micron scale [96], which prevents those squares from relaxing to a vortex state after the magnetic field is removed. In this work, we focus on the behavior of the magnetic squares with an initial vortex state, such as the ones highlighted by the purple and

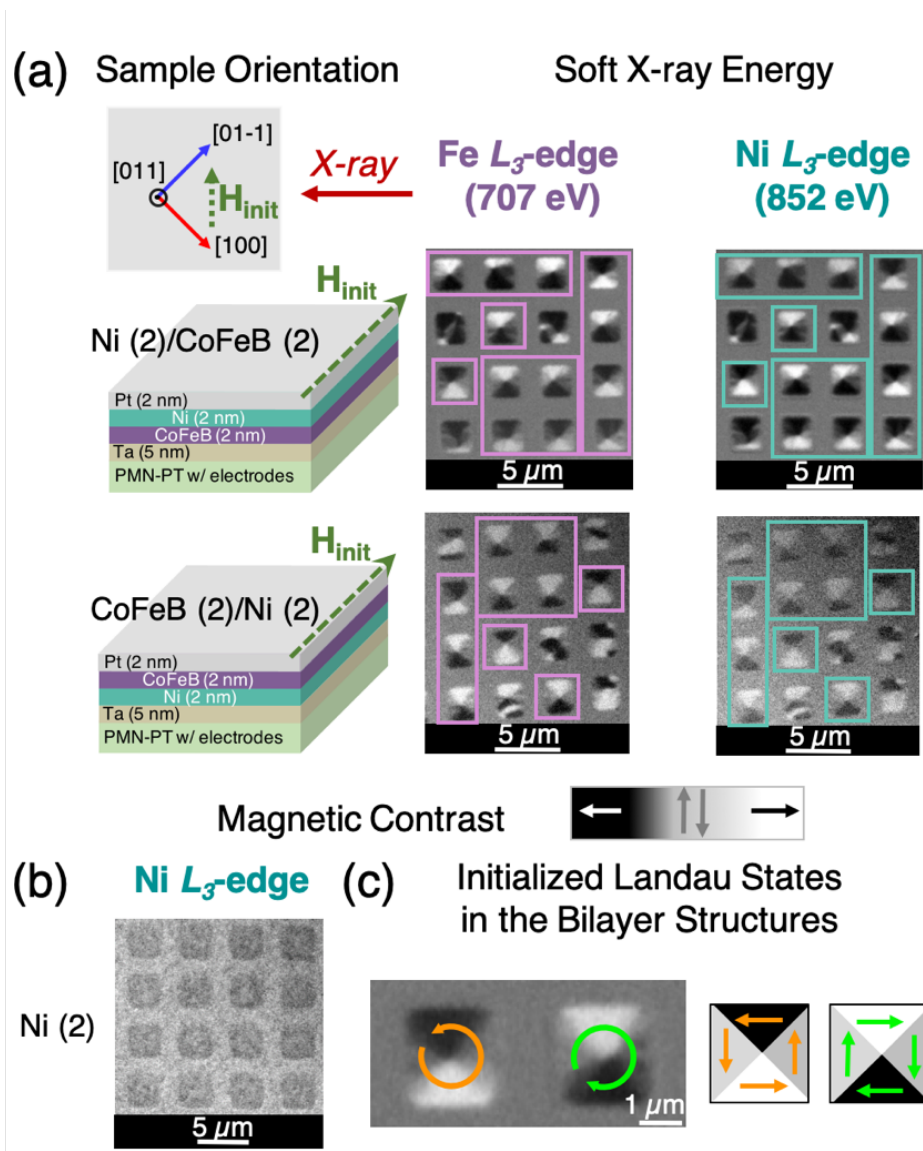
---

<sup>3</sup> Animation link : [https://pubs.acs.org/doi/suppl/10.1021/acsami.9b20876/suppl\\_file/am9b20876\\_si\\_002.mp4](https://pubs.acs.org/doi/suppl/10.1021/acsami.9b20876/suppl_file/am9b20876_si_002.mp4)

turquoise frames in Figure 3.5(a). The reason for investigating those squares is due to the high reliability of electric field-induced reorientation of magnetic vortex states [44], [97].

Schematics of XMCD-PEEM contrast that indicate vortex states of both chiralities are outlined in Figure 3.5(c). Further proof of the pivotal role played by the exchange coupling between the Ni and CoFeB layers is shown in Figure 3.5(a) and (b). The three sets of samples in Figure 3.5(a) and (b) show the magnetic state of three different samples: Ni (2 nm); CoFeB (2 nm)/ Ni (2 nm); and Ni (2 nm)/ CoFeB (2 nm). While no magnetic contrast is observed in the Ni (2 nm) squares, in both Ni-CoFeB samples the Ni layer shows a magnetic contrast, regardless of the stacking order. The probing depth is sufficient to measure through the entire thickness of the Ni (2 nm) film and shows that Ni (2 nm) alone is not ferromagnetic. Through interfacial exchange coupling with the adjacent CoFeB layer, the Ni layer as well becomes

ferromagnetic and the bilayer functions collectively as a single magnetic system, in agreement with the presented SQUID magnetometry measurements in Figure 3.1(b).



**Figure 3.5.** (a) XMCD-PEEM images at Fe and Ni  $L_3$  edges showing the initial magnetic state in bilayer microsquares. Note the similarity in magnetic state for each device in both the Fe  $L_3$ -edge and Ni  $L_3$ -edge, evidence of exchange coupling in this system. The purple and turquoise frames indicate where a Landau magnetic flux closure state is initially observed. The green arrows indicate the initializing magnetic field,  $\mu_0 H_{\text{init}} = 300$  mT. The grey scale bar with the arrows describes the contrast levels of magnetic orientation in the PEEM images. (b) Ni- $L_3$  edge XMCD-PEEM of Ni (2 nm) microsquares shows no magnetic contrast, as expected for a

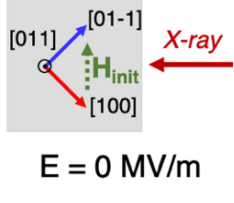
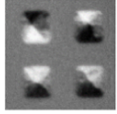
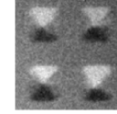
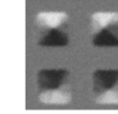
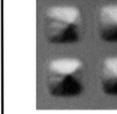
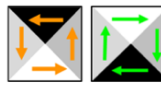

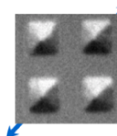
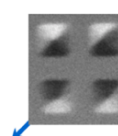
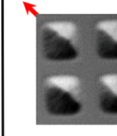


paramagnetic state. (c) Description of the two types of magnetic vortex states observed in the investigated samples. The schematics of squares in grey-scale describe the magnetic configurations in the PEEM images.

To study the electric field-driven magnetic reorientation in the initialized microsquares, we exploit the piezoelectric properties of the PMN-PT substrates. When an electric field is applied along the [011] crystallographic direction of the PMN-PT crystal, a piezo-strain is generated along the two main in-plane crystallographic directions - a compressive strain along the [100] direction, and a tensile strain along the [01-1] direction. This strain is transferred to the magnetic layers deposited on top of the PMN-PT substrate (Figure 3.1(a)), inducing a reorientation of the magnetic moments in the microstructures via inverse magnetostrictive effect [97]. Furthermore, the direction of the magnetic reorientation is dictated by the sign of the magnetostrictive constant of the specific magnetic material under investigation. We note that Ni has a negative magnetostriction constant, whereas CoFeB has a positive magnetostriction constant. Accordingly, the observation of an electrically driven reorientation of the magnetic state of the microsquares offers an unambiguous way to characterize the magnetoelastic coupling in these systems at the micron scale as well as to compare sign and strength of such coupling between the different investigated systems.

The initial ( $E = 0$  MV/m) and final ( $E = 0.8$  MV/m) magnetic states of the imaged microsquares are shown in Figure 3.6 for samples with different thicknesses of Ni and CoFeB layers. When an electric field is applied, a reorientation of the magnetic moments along one of the principal strain directions is induced, causing the transformation from a magnetic vortex towards a two-domain state. In the sample with a thick Ni layer we are able to observe a reorientation along the [100] compressive strain direction. In all other samples, the magnetic

moments reorient along the [01-1] direction of the substrate. **Table 3.1** summarizes the net in-plane magnetic anisotropy induced by the anisotropic piezo-strain in each of the samples. We also observe that the magnetic reorientation effect is weaker in the samples where an equal thickness for the two magnetic layers is chosen (Ni (2 nm); CoFeB (2 nm)) than in the samples with a large difference between the two thicknesses. We can conclude that when the magnetic layer volume is dominated by one of the two materials, the magnetoelastic effect is dictated by that material; while a more complex effect takes place when the magnetic volumes of Ni and CoFeB are similar.

 <p><math>E = 0 \text{ MV/m}</math></p>					<p>Bilayer Magnetic State</p> 
	<p><math>E = 0.8 \text{ MV/m}</math></p>				
<p>Easy Axis (EA)</p>	<p>[01-1]</p>			<p>[100]</p>	
	<p>EA CoFeB</p>			<p>EA Ni</p>	

**Figure 3.6.** Electric field-controlled magnetic reorientation in 2- $\mu\text{m}$  microsquares from four different Ni-CoFeB bilayer systems. The ratio between the Ni and CoFeB magnetic volumes controls the magnetoelectric effect in these multiferroic systems.

The behavior described above for non-symmetric samples can be explained by the magnetostrictive properties of the single magnetic materials. As mentioned above, Ni is known to be a negative magnetostrictive material, in which the magnetic moments prefer to align with the compressive strain direction, [100] (**Table 3.3** [98]). In contrast, CoFeB behaves as a positive magnetostrictive material, where the magnetic moments align along the tensile strain

direction, [01-1]. The effect of electric-field on the magnetic layer reorientation in microsquares of other lateral dimensions (see Section 3.3.1) confirm the same magnetoelastic behavior.

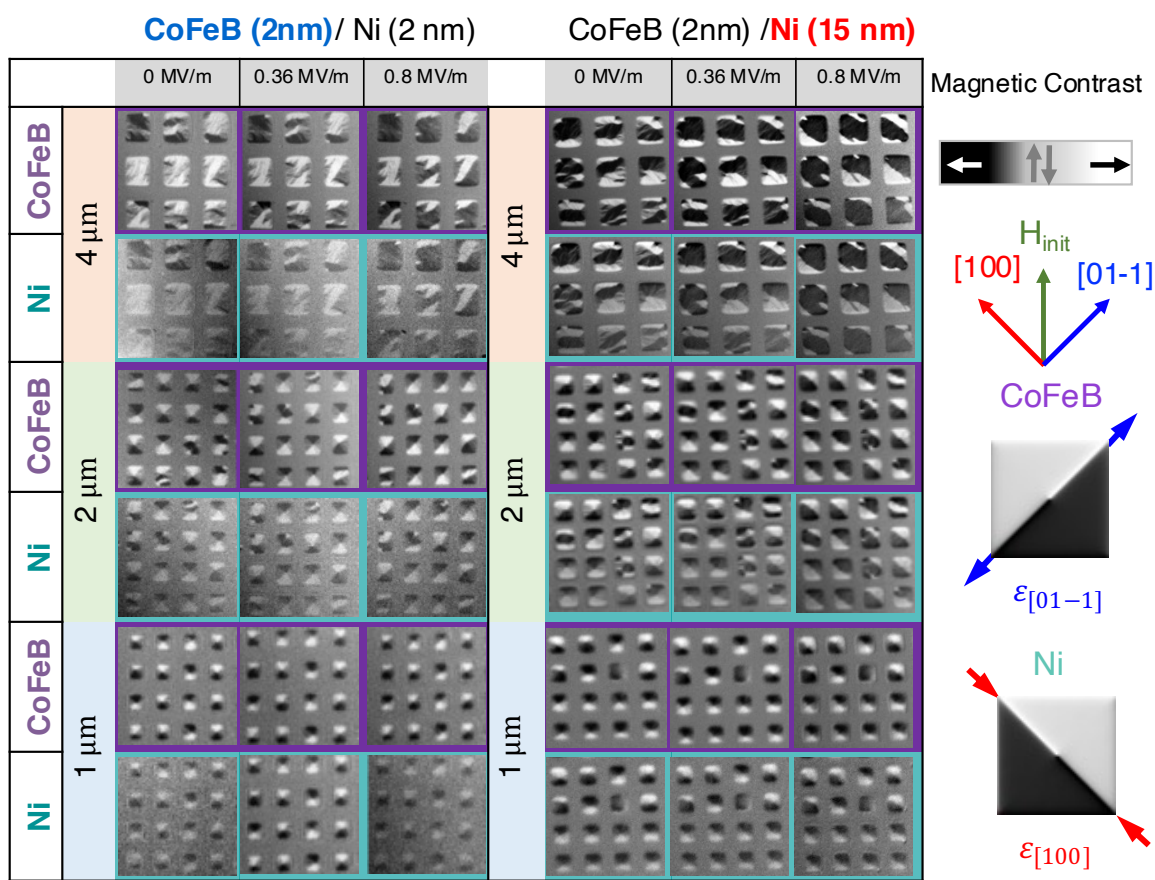
Sample	Material stack	Direction of new easy axis	Dominant Material
1	CoFeB (2nm) / PMN-PT	Tensile strain [01-1]	CoFeB
2	CoFeB (2nm) / Ni(2nm) / PMN-PT	Tensile strain [01-1]	CoFeB
3	Ni (2nm) / CoFeB (2nm) / PMN-PT	Tensile strain [01-1]	CoFeB
4	CoFeB (2nm) / Ni (15nm) / PMN-PT	Compressive strain [100]	Ni
5	Ni (2nm) / CoFeB (15 nm) / PMN-PT	Tensile strain [01-1]	CoFeB

**Table 3.1.** Magnetic easy axis reorientation direction upon applying electric field up to 0.8 MV/m. Table from [92].

### 3.3.1 Magnetic moment reorientation as a function of field in microstructures of different lateral dimensions

Figure 3.7 shows the strain-induced magnetic moment reorientation in the microsquare arrays as a function of the applied electric field. Here, microsquares with lateral dimensions of 4  $\mu\text{m}$ , 2  $\mu\text{m}$  and 1  $\mu\text{m}$  are shown. For all the applied electric fields, the magnetic contrast in the two constituent layers, Ni and CoFeB, is the same, suggesting that the bilayer microsquares are all exchange-coupled. In Figure 3.7, the microsquares with 1  $\mu\text{m} \times 1 \mu\text{m}$  and 2  $\mu\text{m} \times 2 \mu\text{m}$  in size mostly appear to be fallen into a vortex state at 0 MV/m after initialization, whereas the 4  $\mu\text{m} \times 4 \mu\text{m}$  ones form a more complex multidomain state, similar to the Z-domain state as reported in Sloetjes *et al.* [99], [100]. Regardless of the differences in the initial state, the magnetic moments in most of the microsquares tend to align with the tensile strain direction in CoFeB (2nm)/ Ni (2 nm) where CoFeB and Ni have the same volume, and towards the compressive strain direction in CoFeB (2 nm)/Ni (15 nm) where Ni has a much higher volume

than CoFeB. It is observed that the degree of magnetic reorientation increases as the microsquare size goes from  $1 \mu\text{m} \times 1 \mu\text{m}$ ,  $2 \mu\text{m} \times 2 \mu\text{m}$  to  $4 \mu\text{m} \times 4 \mu\text{m}$ , at the same electric field. Such difference in the extent of magnetic reorientation versus microsquare sizes is due to the variations in demagnetization energy density. As the microsquare increases in lateral size, demagnetization energy density becomes smaller during reorientation [101]. These domain reorientation results supplement the PEEM result discussion in the chapter.



**Figure 3.7.** XMCD-PEEM images of the microsquare arrays with different lateral dimensions, acquired at Fe- and Ni-  $L_3$  edges as a function of applied electric field ranging from 0 to 0.8 MV/m. (Left) CoFeB (2 nm)/ Ni (2 nm)/ PMN-PT microsquares with side length ranging from 1 to 4  $\mu\text{m}$ . CoFeB contributes more strongly to the observed magnetic domain reorientation. (Right) CoFeB (2 nm)/ Ni (15 nm)/ PMN-PT microsquares with side length ranging from 1 to

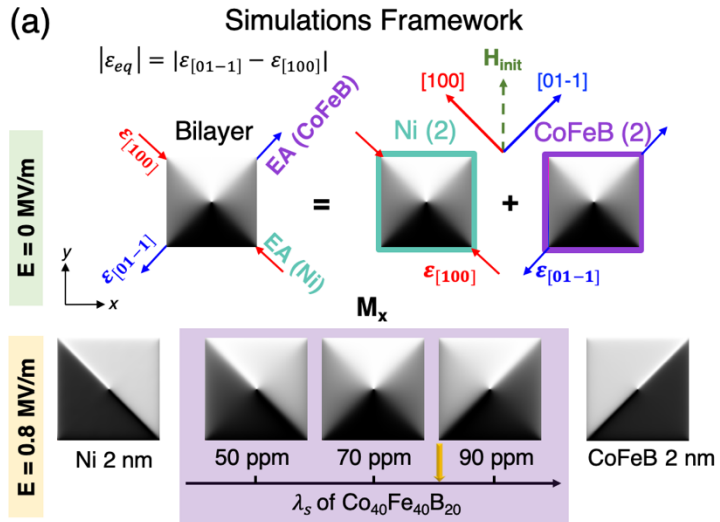
4  $\mu\text{m}$ . In both samples, the magnetic moments are exchange coupled in microsquares of all dimensions, at all electric fields.

The response observed for the symmetric bilayers calls for a closer investigation. First, the general behavior shows that the CoFeB layer contributes more strongly to the observed magnetoelastic effect than the Ni layer. Second, the effect itself is much weaker than what was observed for the asymmetric samples. Indeed, the magnetic reorientation effect is incomplete, generating a final state that is in between the vortex state and the two-domain state (see Figure 3.8 for more details), with a direction that tends toward the direction of tensile strain where CoFeB would have an easy axis. Accordingly, if the observed effect is accounted for by simply summing up the two magnetoelastic effects from the constituent magnetic layers, the interpretation is that the CoFeB layer has a slightly larger magnetoelastic effect than the Ni layer so as to generate the observed magnetic reorientation. However, in order to reach a deeper understanding of our experimental findings, we carry out micromagnetic simulations with the goal to reproduce the experimental findings described so far.

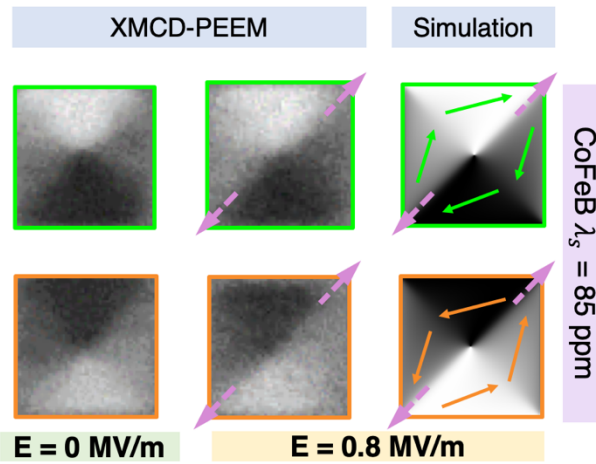
Micromagnetic simulations are carried out using the MuMax3 code [22], [97] (see Section 3.3.3 for more details). A  $2\ \mu\text{m} \times 2\ \mu\text{m}$  magnetic Ni-CoFeB square is simulated, where an initial vortex state is nucleated and subsequently modified by the application of a uniaxial anisotropy energy term. By using a phenomenological model to describe the magnetoelastic effect induced in this composite multiferroic system, the electrically controlled strain-induced uniaxial magnetoelastic anisotropy energy density can be evaluated through the following equation[102]:

$$U_{m.e.} = \frac{3}{2} \lambda_s Y (\varepsilon_{[01-1]} - \varepsilon_{[100]}) \sin^2 \theta_{[01-1]}, \quad (5.1)$$

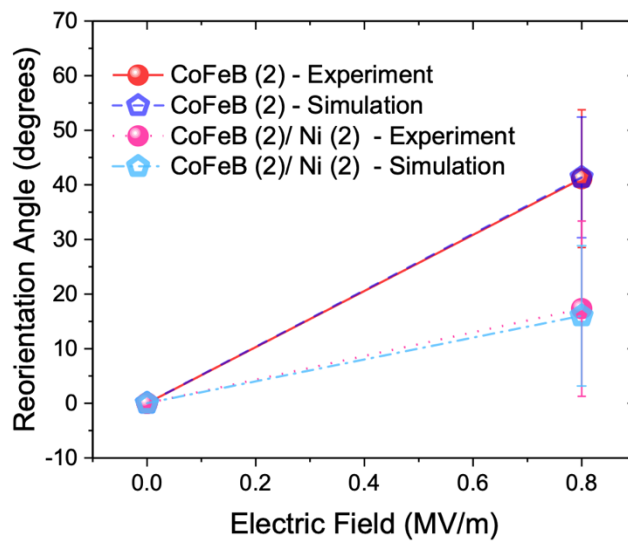
where  $\lambda_s$  is the saturation magnetostriction constant for Ni and CoFeB;  $Y$  is the average Young's modulus for the two magnetic layers;  $\theta_{[01-1]}$  is the angle between the magnetization direction and the tensile strain direction of the piezoelectric,  $[01-1]$ ; and  $\varepsilon_{[01-1]}$  and  $\varepsilon_{[100]}$  are the tensile and compressive piezo-strains, respectively. From Eq. (5.1) it is possible to define a magnetoelastic uniaxial anisotropy factor:  $K_{m.e.} = \frac{3}{2}\lambda_s Y \varepsilon_{eq}$ , with  $\varepsilon_{eq} = (\varepsilon_{[01-1]} - \varepsilon_{[100]})$ , which is a function of the electrically induced piezo-strain.



(b) Micromagnetic Simulations vs Experiments



(c) Electric-field induced Average Reorientation Angle



**Figure 3.8.** (a) Simulated bilayer micromagnetic system started from a vortex state 0 MV/m (top row), and 0.8 MV/m (bottom row). In the bottom row, the micromagnetic results of single layer Ni and CoFeB are included on both ends of the spectrum, where the magnetostrictive coefficient of CoFeB is tuned in the range of interest between 50 and 90 ppm. (b) Comparison between micromagnetic outcomes and experimental findings for the CoFeB (2 nm)/ Ni (2 nm) system indicate the suitable  $\lambda_s$  value of CoFeB to be 85 ppm. (c) Electric-field induced magnetic moment reorientation angles in CoFeB (2 nm)/ PMN-PT and CoFeB (2 nm)/ Ni (2 nm)/ PMN-PT samples, calculated from both experiment and simulation results.

The outcomes of the micromagnetic simulations are compared to the experimental observations in Figure 3.8. The simulations in which only the Ni or the CoFeB layer is modeled are able to reproduce the experimentally observed behavior. The simulations for the Ni square reproduce the experimentally observed magnetic reorientation effect in which the initial vortex state completely transforms in a two-domain state, with a final magnetization orientation along the compressive strain direction. The same holds for the simulation of the CoFeB square, except that the final magnetic state has magnetic moments aligned with the tensile strain direction. The reorientation angle at 0.8 MV/m is calculated to be  $41^\circ \pm 13^\circ$  from experiment and  $41^\circ \pm 8^\circ$  from simulation (Figure 3.8(c)). The uncertainty of the angles are deviations of the distribution of contrast values in the triangular domains defined for the analysis (explained in detail in Section 3.3.2 -Table 3.2). Those values are indeed indicating a full reorientation process, since the maximum achievable reorientation angle is  $45^\circ$  in the present experimental geometry. The error bars indicate the average standard deviation of the magnetic moment direction distributions in the four magnetic domains forming the initial Landau state. More detail on the domain angle analysis is described in Section 3.3.2.



### 3.3.2 Quantitative analysis of the magnetic moment direction from PEEM images

To obtain the quantitative analysis of magnetic moment reorientation in the magnetic domains within the microsquares, we calculated and compared the magnetization angle in individual domains based on the contrast variations of the XMCD-PEEM images. Similarly, the angles are calculated based on the simulation results before matching the experiment and simulation results.

Statistics of the XMCD-PEEM magnetic contrast intensity distribution provides quantitative information on the extent of magnetization reorientation. When the magnetic moment aligns parallel or anti-parallel to the x-ray propagation direction in-plane, the contrasts are the strongest, and the magnetic moment direction would correspond to  $0^\circ$  or  $180^\circ$ . We could normalize the magnetic image contrast to value denoted as “NC (normalized contrast)” between -1 and 1 after subtracting the background contrast in each domain at 0 MV/m. The average angle of the magnetic moment in an area could be calculated as  $\cos^{-1}(\text{NC})$ . As we ramp up the electric field, the overall range of the contrast value will decrease as observed in Figure 3.9.

Figure 3.9 (a)-(b) provides a detailed analysis of how image contrast varies before and after applying 0.8 MV/m (experiment) or 1000 ppm equivalent strain (simulation) to the system. The microsquares are divided into four triangular domains and color-coded for the analysis. These four regions of interest (ROIs) are named “Black” where the darkest contrast is observed (labeled in blue), “White” where the lightest contrast is observed (labeled in red), “Grey 1” and “Grey 2” whose contrast are in between that of “Black” and “White” (labeled in light green and dark green, respectively). For the PEEM image analysis, the mean contrast values and their standard deviations are obtained based on the averages of multiple microsquares. Then the

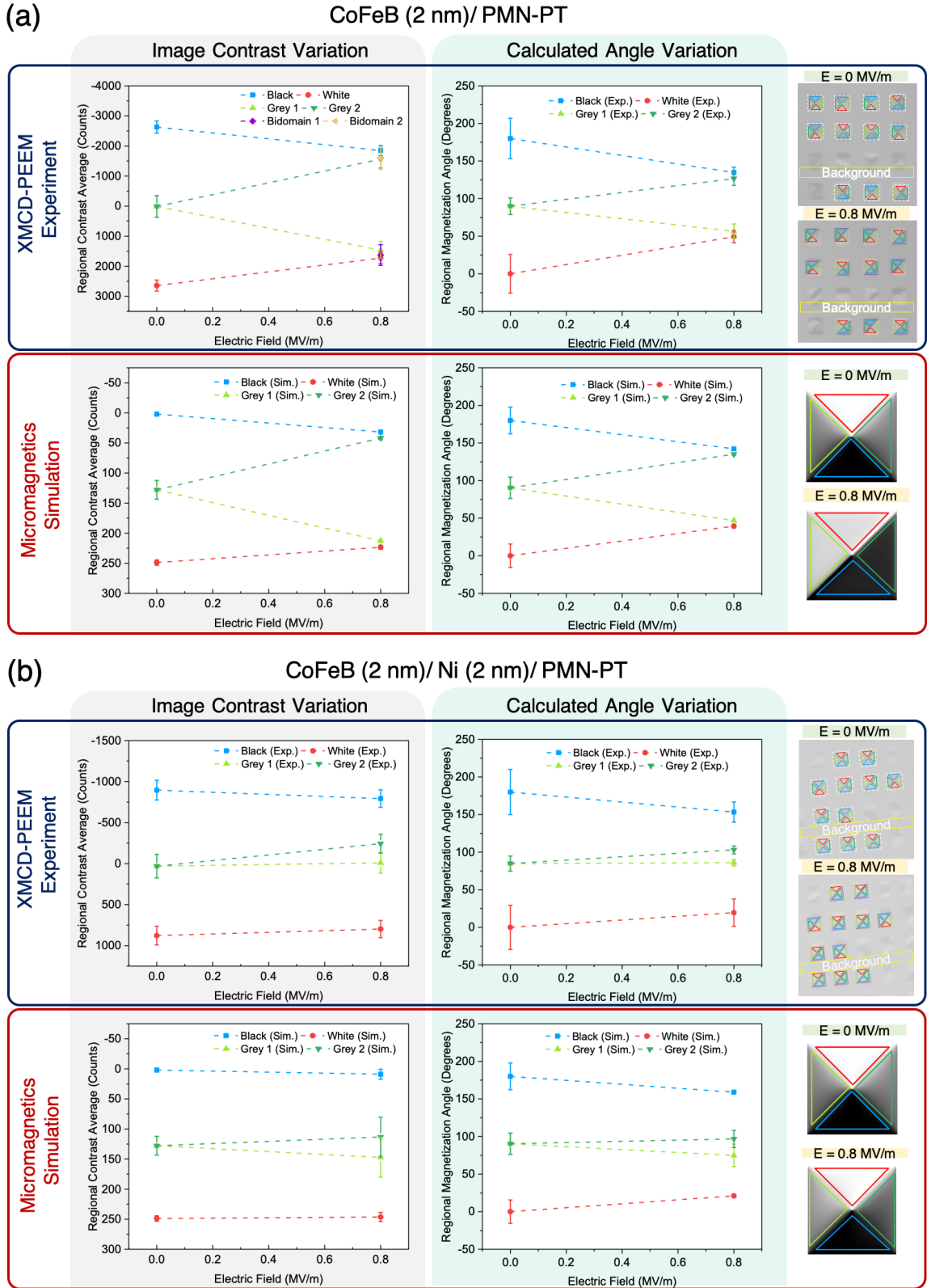
background contrast is subtracted to obtain the regional contrast average vs. electric field plot. For the micromagnetic simulation result analysis, similarly, the four ROIs are as labeled in the images. Figure 3.9(a) describes the image contrast variation and calculated angle variation in the four domains for the CoFeB (2 nm) on PMN-PT sample, while Figure 3.9(b) shows these of the bilayer CoFeB (2 nm)/ Ni (2 nm) on PMN-PT sample. The error bars in the plots arises from the distribution of magnetic moment orientation in the ROI indicated by the triangles. Additionally, for the experimental results, the uncertainty are the averages of the same ROI in multiple microstructures. In terms of the uncertainty in the reorientation angle reported in the main text, it is the average of standard deviations from each of the four triangle ROIs shown in Figure 3.9. Table 3.2 reports the angle and uncertainty calculated from individual ROIs for both experiment and simulation results.

(a)	CoFeB (2 nm)									
<b>Experiment</b>	$\theta_B$	$\theta_W$	$\theta_{G1}$	$\theta_{G2}$	$\bar{\theta}$	$\sigma_B$	$\sigma_W$	$\sigma_{G1}$	$\sigma_{G2}$	$\bar{\sigma}$
E = 0 MV/m	180.0	0.0	90.4	90.4		22.6	21.6	7.8	7.8	16.6
E = 0.8 MV/m	134.7	49.2	126.5	56.5		5.0	5.6	7.4	8.3	6.6
$\Delta\theta_{rot}$	-45.3	49.2	36.1	-33.9	<b>41.1</b>					<b>12.6</b>
<b>Simulation</b>	$\theta_B$	$\theta_W$	$\theta_{G1}$	$\theta_{G2}$	$\bar{\theta}$	$\sigma_B$	$\sigma_W$	$\sigma_{G1}$	$\sigma_{G2}$	$\bar{\sigma}$
E = 0 MV/m	180.0	0.0	89.1	89.1		12.2	15.5	7.2	7.2	11.1
E = 0.8 MV/m	142.2	39.4	135.0	46.8		1.9	2.3	1.7	1.1	1.8
$\Delta\theta_{rot}$	-37.8	39.4	45.9	-42.3	<b>41.1</b>					<b>7.9</b>

(b)	CoFeB (2 nm)/ Ni (2 nm)									
<b>Experiment</b>	$\theta_B$	$\theta_W$	$\theta_{G1}$	$\theta_{G2}$	$\bar{\theta}$	$\sigma_B$	$\sigma_W$	$\sigma_{G1}$	$\sigma_{G2}$	$\bar{\sigma}$
E = 0 MV/m	180.0	0.0	84.8	84.8		30.1	29.4	10.0	10.0	22.2
E = 0.8 MV/m	153.3	19.5	103.0	85.8		13.4	18.2	5.4	4.3	11.8
$\Delta\theta_{rot}$	-26.7	19.5	18.2	18.2	<b>16.4</b>					<b>16.1</b>

<b>Simulation</b>	$\theta_B$	$\theta_W$	$\theta_{G1}$	$\theta_{G2}$	$\bar{\theta}$	$\sigma_B$	$\sigma_W$	$\sigma_{G1}$	$\sigma_{G2}$	$\bar{\sigma}$
E = 0 MV/m	180.0	0.0	90.4	90.4		12.2	15.5	7.2	7.2	11.1
E = 0.8 MV/m	159.0	21.0	97.0	75.0		1.0	1.0	11.6	14.9	9.4
$\Delta\theta_{rot}$	-21.1	21.0	6.4	-15.5	<b>16.0</b>					<b>10.3</b>

**Table 3.2.** Calculation of reorientation angle ( $\Delta\theta_{rot}$ ) of both experiment and simulation results for (a) CoFeB (2 nm) and (b) CoFeB (2 nm)/ Ni (2 nm) reported in the main text. Here  $\theta_B$ ,  $\theta_W$ ,  $\theta_{G1}$  and  $\theta_{G2}$  denote the average angle of the magnetic moment in the ROI marked by black, white, grey 1 and grey 2, respectively.  $\bar{\theta}$  is the average of the reorientation angle at 0.8 MV/m when compared to at 0 MV/m. Similarly,  $\sigma_B$ ,  $\sigma_W$ ,  $\sigma_{G1}$  and  $\sigma_{G2}$  are standard deviation of the angles for each ROIs, and  $\bar{\sigma}$  is the average standard deviation.



**Figure 3.9.** Quantitative analysis of the magnetic contrast and magnetic moment direction variation in (a) CoFeB (2 nm)/ PMN-PT and (b) CoFeB (2 nm)/ Ni (2 nm)/ PMN-PT. The

mean and standard deviations of the color contrasts from four triangular domains before and after the electric field is applied (i.e., at both 0 MV/m and 0.8 MV/m) are used to calculate the extent of magnetic moment reorientation. The first row (in a blue box) in each table shows the analysis of the XMCD-PEEM experiment data, denoted by “(Exp.)” in the legends of the plots. The second row (in a red box) in each table presents the analysis of the micromagnetic simulation data, denoted by “(Sim.)” in the legends of the plots.

After validating our micromagnetic model, we investigate the behavior of CoFeB (2 nm)/Ni (2 nm) squares where we carefully modify the magnetostrictive coefficient of the CoFeB layer. What we learn from this modeling experiment is that in order to reproduce the experimental results (see Section 3.3.3 for more details on parameters) we must assume a magnetostrictive coefficient for the CoFeB ( $\lambda_s \approx 85$  ppm) that is more than twice as large, in magnitude, as that of Ni ( $\lambda_s = -33$  ppm)[103], from the experimental data we can extract a reorientation angle at 0.8 MV/m of  $16^\circ \pm 16^\circ$ . Choosing a  $\lambda_s$  for CoFeB of 85 ppm, the obtained reorientation angle by micromagnetic simulations is  $16^\circ \pm 10^\circ$  which agrees with the experimental value. Figure 3.8(c) shows the quantitative analysis of the average domain rotation angle at 0.8 MV/m when compared to at 0 MV/m for both the single layer and bilayer samples. The extracted value of  $\lambda_s$  for the CoFeB layer is in general agreement with what has been reported previously for Co<sub>50</sub>Fe<sub>50</sub>, where  $\lambda_s$  was found to be 70 ppm [103]–[105]. Co<sub>50</sub>Fe<sub>50</sub> is a very similar material to what is used in this work, where we have equal atomic concentration of Co and Fe in the Co<sub>40</sub>Fe<sub>40</sub>B<sub>20</sub> composition.

Even if the simulations and the experimental observations seem to agree when reasonable micromagnetic parameters are chosen for our modeling, what is surprising is that the global effect is not simply due to the sum of the two magnetoelastic effects in the two

ferromagnetic layers (Figure 3.10(a)-(c)). Indeed, using the phenomenological model described above to calculate the induced magnetoelastic anisotropy contributions from the two layers, we find that:

$$K_{m.e.}^{Ni} = \frac{3}{2} \cdot (33 \times 10^{-6}) \cdot (180 \times 10^9) \cdot (1 \times 10^{-3})/10^3 = 8.9 \text{ kJ/m}^3 \text{ and}$$

$$K_{m.e.}^{CoFeB} = \frac{3}{2} \cdot (85 \times 10^{-6}) \cdot (160 \times 10^9) \cdot (1 \times 10^{-3})/10^3 = 20.4 \text{ kJ/m}^3,$$

which allows us to calculate a ratio of  $\frac{K_{m.e.}^{CoFeB}}{K_{m.e.}^{Ni}} = 2.29$ . Here, the electrically induced strain of 1000 ppm was measured experimentally for the PMN-PT we used from the same growth batch[106] Accordingly, in order to have the observed incomplete magnetization in terms of the complete bidomain state, the magnetoelastic anisotropy energy density induced in the CoFeB layer needs to be more than twice as large as the one induced in the Ni layer. This is surprising, since for an incomplete reorientation only a slight difference between the two magnetoelastic effects would have been expected, as one would have anticipated from a simple *balancing effect* approach. This makes it clear that the exchange coupled magnetoelastic bilayer shows an emergent magnetic behavior, that is specific of the hybrid system and not simply the sum of the properties of its constituent. This finding has repercussions on our understanding of magnetoelastic systems and opens up a new avenue for the development of novel magnetoelectric materials with tunable functionalities, applicable in multiferroic-based memory, logic, sensor, microwave devices such as antennae [58] and even magnetic particle and cell sorting platforms [18].

To further understand how the exchange-coupled bilayer differs from the summation of two individual layers, the energy terms in different systems before and after applying the strain are reported and compared in Figure 3.10.

For the single layer Ni and CoFeB, Figure 3.10(a)-(b) shows the energy variation for exchange energy, demagnetization energy, anisotropy energy and total energy. Figure 3.10(c) reports the sum of the energy terms of the two individual layers Ni (2 nm) and CoFeB (2 nm) in (a) and (b).

On the other hand, Figure 3.10(d)-(f) reports the energetics for the exchange coupled bilayer system. Figure 3.10(d) and (e) show the energies in Ni and CoFeB layer, respectively, while Figure 3.10(f) reports the sum of each energy term from the two layers. Comparing Figure 3.10(c) with (f), we conclude that due to coupling between the bilayers, the energetics of the bilayer system is not a simple summation of the energy of the two single layers, and the effect of additional interactions on the magnetic energy needs to be considered.

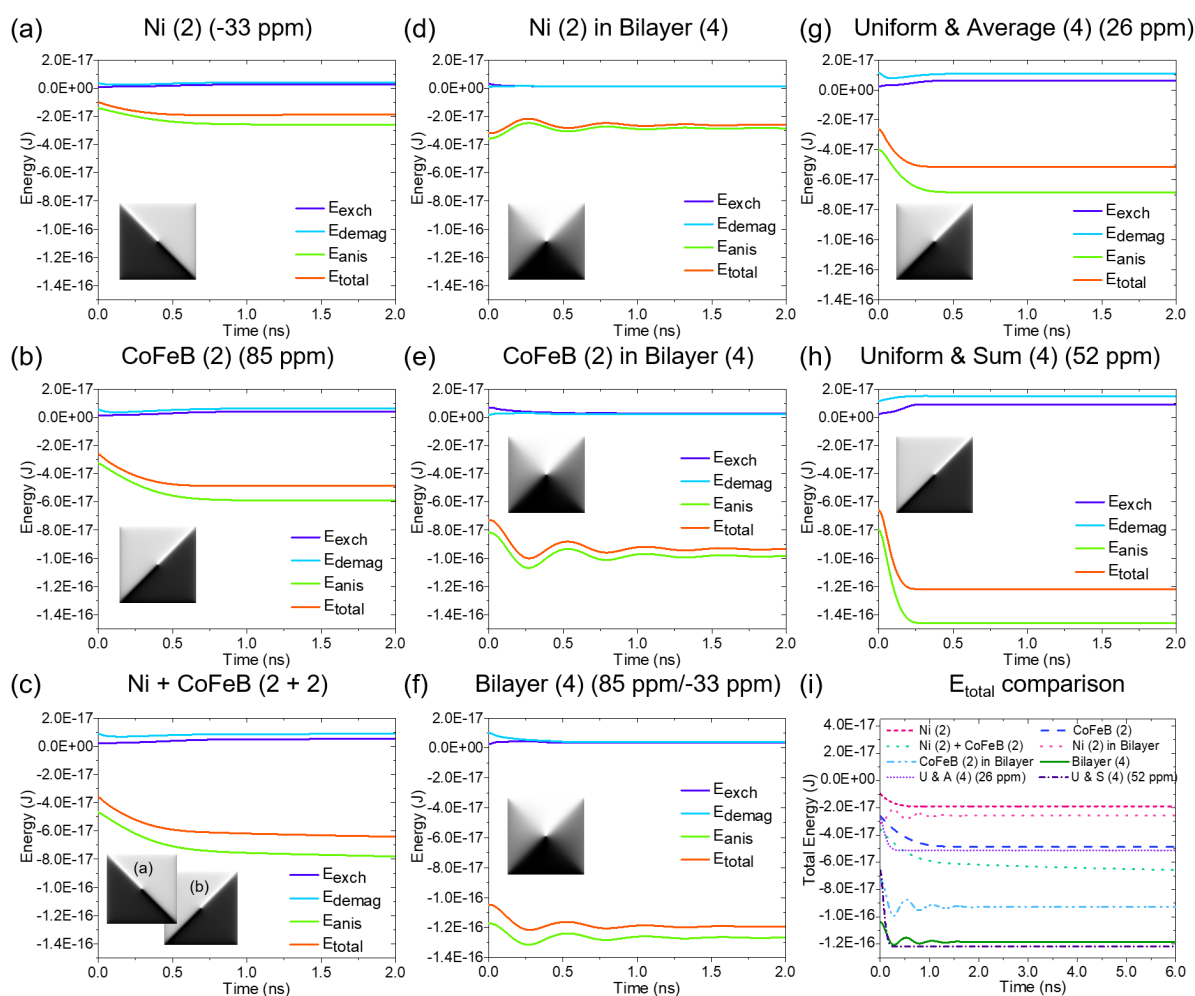
In order to reach a deeper understanding of the physics involved in the observed magnetoelastic effect, we simulated *ad hoc* virtual systems with tailored properties to compare with the actual bilayer system. We have investigated whether a single material with the desired saturation magnetostriction  $\lambda_s$  could replicate such bilayer system. Here, two virtual systems, called “Uniform & Average” and “Uniform & Sum”, are used to estimate the properties of the bilayer. The specifics of those systems are the following: The “Uniform & Average” system consists of a uniform layer of 4 nm in thickness, whose saturation magnetostriction  $\lambda_s = \frac{85 + (-33)}{2} = 26$  ppm, damping factor  $\alpha = 0.024$ , exchange stiffness  $A_{ex} = 1.525 \times 10^{-11}$  J/m, and Young’s Modulus  $Y = 170$  GPa are taken as the averages of those of Ni and CoFeB and whose saturation magnetization  $M_s = 7.25 \times 10^5$  A/m is the experimentally measured value (see Section 3.3.3 -Table 3.3 for more details). The “Uniform & Sum” system is identical to “Uniform & Average”, apart from its saturation magnetostriction  $\lambda_s = 85 + (-33) = 52$  ppm,

which is the sum of the saturation magnetostrictions of the two magnetic layers. What we find is that the *total magnetic energy* at equilibrium of the “average” system in Figure 3.10(g) is not the same as the one extracted for the bilayer system reported in Figure 3.10(f); while the “sum” system (see Figure 3.10(h)) is able to reproduce the energetics of the bilayer system even though it still does not produce the same magnetic configuration of the bilayer (same holds for the “average” system).

As a way to identify the importance of exchange coupling at the bilayer interface, which manifests clearly in the calculations of the magnetization dynamics, Figure 3.10(i) shows the total energy (of each of the aforementioned simulated systems) as a function of time, starting from the instant in which the initial vortex state begins its relaxation towards the uniaxial magnetoelastic anisotropy direction. Comparison of Ni and CoFeB layer in the bilayer (Figure 3.10(d)-(e)) with Ni, CoFeB single layer (Figure 3.10(a)-(b)) indicates the individual layers that become exchange coupled in the bilayer no longer behave as when they stand alone. On the one hand, the summation of the *total energies* of Ni and CoFeB single layer at equilibrium is close to the “Uniform & Average” (26 ppm) case which falls into a domain state similar to that of CoFeB. On the other hand, the *total energies* at equilibrium are very similar between the coupled bilayer and the “Uniform & Sum” (52 ppm) layer simulations. Nevertheless, the magnetic configurations in the final state (Figure 3.10 insets) after applying the strain still differ: with both the virtual cases having a two-domain state at equilibrium and the bilayer case still showing four distinct domains in distortion. This result implies that we obtained a synthetic material with tunable properties that is quite different from a single layer system with material properties given by simply averaging properties of the two layers. The simulation outcomes shine some more light on the complex behavior of the studied system, however further investigations are needed to reach a full comprehension of the observed phenomenon.



Finally, it is worth noting that in all the subplots in Figure 3.10, only the coupled bilayer case shows damped oscillations of its energy versus time (Figure 3.10(d)-(f)). Further investigation of the simulation setup indicates that the oscillation arises from the generation of spin-waves due to the interface between the two layers. However, the energies at equilibrium (which is the focus of this analysis) are not affected by such transient effects (Section 3.3.3).



**Figure 3.10.** Comparison of energy variations in different 2-μm microsquare systems using micromagnetic simulations, starting from vortex state until reaching an equilibrium state once the equivalent uniaxial anisotropy is applied. We report the variation of exchange energy, demagnetization energy, anisotropy energy and total energy in: (a) single 2 nm-thick Ni layer; (b) single 2 nm-thick CoFeB layer; (c) system whose energies are the sum of individual energy

terms from (a) and (b); **(d)** 2 nm-thick Ni layer from the CoFeB/Ni bilayer system; **(e)** 2 nm-thick CoFeB layer from the CoFeB/Ni bilayer system; **(f)** Ni(2 nm)\CoFeB(2 nm) bilayer system; **(g)** a 4 nm thick single layer that takes the averages of the magnetic properties of the CoFeB and Ni ( $M_s = 7.4 \times 10^5$  A/m,  $\lambda_s = 26$  ppm); and **(h)** a 4 nm thick single layer similar to that of (g), but with a  $\lambda_s$  of 52 ppm as the sum of  $\lambda_s$  from CoFeB and Ni. **(i)** The total energy variation in the eight aforementioned layers and systems. The micromagnetics parameters used for the simulation are reported in Section 3.3.3 -Table 3.3. At the top of each graph, the saturation magnetostriction coefficients (in ppm) used to model the layers are and the layer thicknesses are listed in the parentheses. Inset images are the magnetic configurations ( $m_x$ ) at the final equilibrium states.

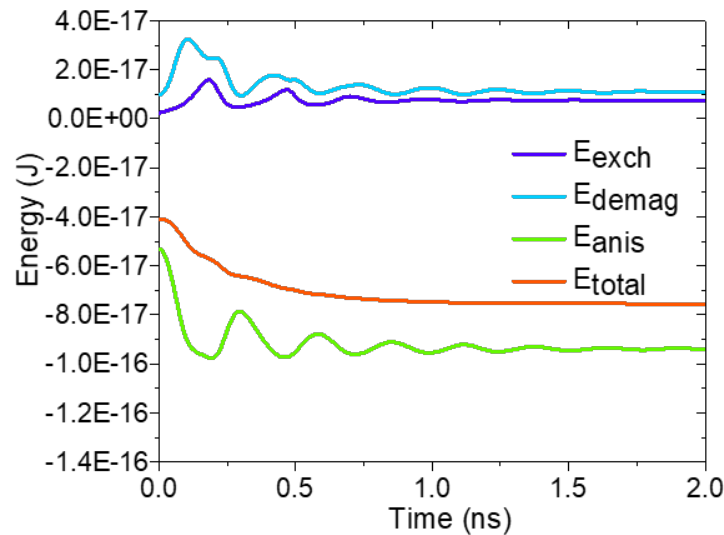
### 3.3.3 Micromagnetic simulations of magnetic energy variation in single layer and bilayer systems.

Thin film	$M_s$ (A/m)	$\lambda_s$ (ppm)	$\alpha$	$A_{ex}$ (J/m)	Y (GPa)
Ni	$4.8 \times 10^5$	-33	0.038	$1.05 \times 10^{-11}$	180
CoFeB	$1.0 \times 10^6$	85	0.01	$2.00 \times 10^{-11}$	160

**Table 3.3.** Intrinsic material dependent constants used for the micromagnetics simulation, where  $\lambda_s$  is the saturation magnetostriction coefficient,  $\alpha$  is the damping constant,  $A_{ex}$  is the exchange stiffness constant, and Y is the Young's modulus [107].

All of the material parameters used in the simulation are either taken from literature ( $\lambda_s$ ,  $\alpha$ ,  $A_{ex}$ , Y) or measured directly ( $M_s$ ,  $\epsilon_{eq}$ ). The micromagnetic simulation is initialized to be in a vortex state and the effect of electric-field applied strain is achieved by applying a uniaxial

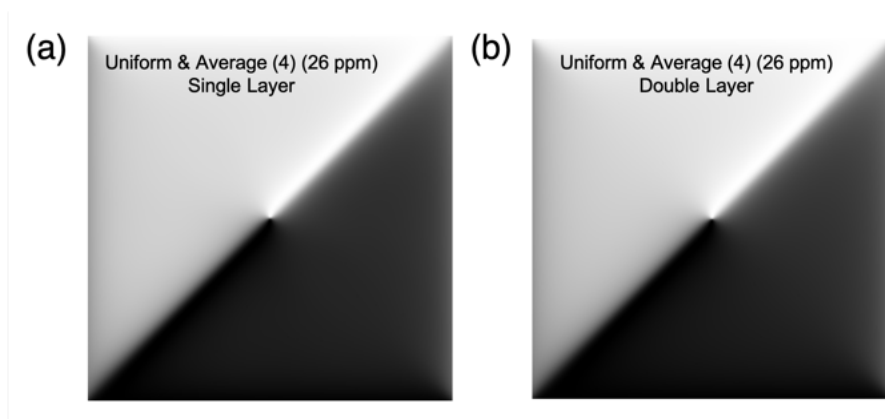
anisotropy term. We are mainly interested in the final energy of the systems, after reaching the new equilibrium ground states, as a function of time in the systems reported in Figure 3.10.



**Figure 3.11.** Oscillation of the energy vs. time profile in the simulation of bilayer system. The plot here shows the energy variation of a bilayer system that takes the average of Ni and CoFeB material parameters for individual layers, and with a saturation magnetostriction of 26 ppm.

Figure 3.11 shows oscillatory behavior of the energy profile during relaxation to equilibrium state while the uniaxial anisotropy is applied to the bilayer microsquare made up of 2 nm thick Ni and 2 nm thick CoFeB. To understand the origin of such oscillation, a bilayer system same as the “Uniform & Average (26 ppm)” case in Figure 3.10(g) is simulated. The only difference between the two simulations is that for the “Uniform & Average” case, the entire stack is treated as single layer, whereas the bilayer one here discussed comprises two 2 nm layers with the same property, but with an interface. It is thus concluded that the oscillation observed for the CoFeB/Ni bilayer system (Figure 3.10(f)) at the onset of the simulation originates from spin waves generated at the interface. The oscillation eventually fades away after about 1 ns (See “Micromagnetic simulation of the bilayer CoFeB/Ni system with the

applied in-plane total strain of 1000 ppm”<sup>4</sup>). Such interfacial effect does not affect the simulation outcome at the final magnetic state, proven by the two simulations reported in Figure 3.10(g) and Figure 3.12.



**Figure 3.12.** Final magnetic states of the bilayer stack for the “Uniform and Average” case from (a) when treated the bilayer as a single film stack and (b) when treated as a bilayer system are identical.

### 3.4 Concluding Remarks

In summary, the magnetoelastic properties of exchange coupled Ni-CoFeB magnetic microstructures on top of PMN-PT piezoelectric substrates are investigated as a function of the thickness of the two magnetic layers, through electric field-driven magnetic reorientation. On the one hand, when the ratio of the two magnetic thicknesses is significantly larger than one, the magnetoelastic properties of the system are dominated by those of the thicker layer. On the other hand, when the layers are the same thickness, the exchange-coupled microstructures exhibit a more complex behavior, which cannot be described by simply combining the magnetoelastic effects of the two constituent materials. The experimental observations are

---

<sup>4</sup> Animation link: [https://pubs.acs.org/doi/suppl/10.1021/acsami.9b20876/suppl\\_file/am9b20876\\_si\\_003.mp4](https://pubs.acs.org/doi/suppl/10.1021/acsami.9b20876/suppl_file/am9b20876_si_003.mp4)

reproduced by micromagnetic simulations, which support such interpretation. These results demonstrate the richness in magnetoelectric properties offered by exchange-coupled composite multiferroics, where the magnetoelastic effect is governed by the coupling between the two magnetic layers. Furthermore, the tunability of those magnetoelectric properties via magnetic layer composition and stacking order offers a path towards the development of new magnetoelectric systems that could access a richer space of material properties, which can be exploited in the development of new low-power magnetoelectric devices. This work is expected to motivate more experimental and theoretical studies focused on the magnetoelectric properties of composite multiferroic micro- and nano-structures with exchange-biased magnetic bilayers.

## **Chapter 4    Magnetic particle control via cytocompatible magnetostrictive microstructures<sup>5</sup>**

### 4.1 Magnetic particle control with magnetic stray field

Recently, manipulating magnetic particles with local magnetic fields has emerged as an appealing method for transporting bio-particles labeled with these magnetic beads [108], [109]. While extended exposure to dielectrophoretic traps [110] or optical tweezers [111] could damage cells, transport and trapping via magnetic particle manipulation is a non-destructive alternative. In addition, magnetic particle affinity to particular proteins, introduced through antibodies or other recognition elements conjugated to the particle surface, provides cell-type specificity to manipulations.

While using localized magnetic forces for manipulating magnetic microbead motion (e.g. magnetic tweezers [112]) allows remote control, the prevalent approaches for controlling the movement of magnetic beads along with bound bio-particles are not capable of operating with a large array of individually addressable elements. Previous approaches involve either external rotating magnetic fields or microfabricated electromagnets, with the former being bulky and de-localized and the latter posing problems such as on-chip heating [113]. On the other hand, using an electric field to control magnetic domain motion arises as a viable solution which not only benefits from magnetic force control with high precision, but also avoids problems such as joule heating and the need for bulky external magnets.

---

<sup>5</sup> This chapter is adapted from a previously published manuscript [107].

Moreover, it is of paramount importance to separate and manipulate cells and other bio-particles individually and in parallel for rapid biological analyses [114]. By employing magnetic domain walls whose motion is tunable via electric-field using multiferroic heterostructures and combining the device with microfluidics, ‘lab-on-chip’ devices can be developed that are capable of controlling the movement of detected entities with high precision, for downstream sorting, sequential reaction, and analysis. Controlling the coupling of the beads to the domain wall movement along with parallel optical imaging and analysis technologies [115] opens up opportunities to a myriad of applications for rapid cell analysis in sorting based on complex phenotypes [116]. Large arrays of individually addressable cells are particularly important for sorting rare cells in a population that may be useful diagnostically (e.g. antigen-specific T-cells, circulating tumor cells, etc.) or for selecting rare clones with useful properties for cell therapies or cell-based bio-manufacturing.

$[\text{Pb}(\text{Mg}_{1/3}\text{Nb}_{2/3})\text{O}_3]_{1-x}-[\text{PbTiO}_3]_x$  (PMN-PT) is one of the most commonly used ferroelectrics in such multiferroic heterostructures. PMN-PT with composition close to the phase boundary ( $x \approx 0.32-0.34$ ) will undergo a morphotropic phase transformation [117] with giant electromechanical response. Sohn *et al.* [19] have previously demonstrated strain-mediated deterministic domain wall motion in Ni rings on single crystal (011)-cut PMN-PT ( $x \approx 0.34$ ) with morphotropic phase transformation, which induces a large hysteretic strain jump at an electric field of  $\sim 0.5$  MV/m. Such strain change induces domain motion in the ring structures, which subsequently results in abrupt particle motion. Magnetolectric Ni/ (011) PMN-PT heterostructures with different compositions have been extensively researched [38], [58], [118] with magnetization reorientation controllable by electric-field, providing the groundwork for further optimization and applications. While Ni ( $\lambda_s(\text{Ni}) = -33 \times 10^{-6}$ ) has been a popular choice for the ferromagnetic component in these systems, FeGa with an order of

magnitude higher magnetostriction ( $\lambda_s(\text{FeGa}) = 350 \times 10^{-6}$ ) is attracting more attention due to the potential enhanced magneto-electric coupling figure of merit applicable to a broad range of uses, such as being a promising candidate for memory devices [16].

In this chapter, we first describe the fabrication process for magnetostrictive Ni and FeGa microstructures on piezoelectric PMN-PT. We chose Ni because it has been widely investigated in multiferroic systems in spite of the fact that it possesses only a moderate magnetostriction coefficient. We also include results on FeGa because its higher magnetostriction coefficient enables greater control of its magnetic state. We then demonstrate tuning of the magnetic state of nanoscale structures using electric fields, as shown by X-ray microscopy. The device behavior was also examined with nanoscale superparamagnetic beads, and the electric field-driven steady speed bead motion with response to the linear strain variation was captured by a high-speed camera.

Compared to the work of Sohn et al. [19] using PMN-PT with morphotropic strain transformation, this work features PMN-PT with a linear strain. The benefit of actuating the particle movement using PMN-PT with linear strain is that it allows us to operate in a regime where the particle displacement is proportional to the applied electric field. The domain motion is activated at a comparable smaller strain with the applied field in the range of 0.16 - 0.32 MV/m. While recent work has demonstrated the inhomogeneous nature of strain distribution in the single crystal PMN-PT [22], this response of the bead's continuous rotational behavior along the perimeter of the ring corresponds well to the linear macrostrain profile of the  $[\text{Pb}(\text{Mg}_{1/3}\text{Nb}_{2/3})\text{O}_3]_{0.69}\text{-}[\text{PbTiO}_3]_{0.31}$ . Localized capture of single particles with nm to  $\mu\text{m}$  diameters at the onion state domain wall of Ni and FeGa rings, and at the corners of squares with partial closure domain are observed by optical and fluorescence microscopy [119]. The



advantage of using these microstructures with localized domains is to enable single particle capture at specific locations rather than agglomerates of beads. In addition, a successful attempt to settle cells to the surface of the device were demonstrated, and cell viability under applied electric field from 0 to 0.8 MV/m was confirmed.

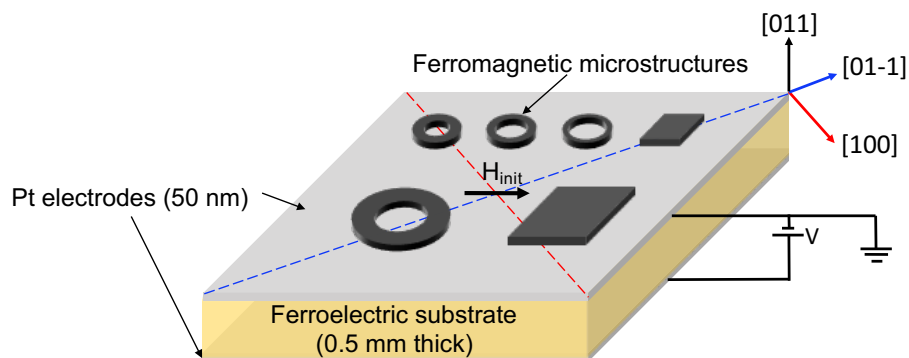
## 4.2 Experimental methods

### 4.2.1 *Fabrication of microstructures on piezoelectric substrate and magnetization state initialization*

The multiferroic heterostructure consists of a (011) cut  $[\text{Pb}(\text{Mg}_{1/3}\text{Nb}_{2/3})\text{O}_3]_{1-x}-[\text{PbTiO}_3]_x$  (PMN-PT,  $x \approx 0.31$ ) single crystal substrate (Atom Optics Co., Ltd, Shanghai, China). The piezoelectric coupling coefficient  $d_{33}$  of the substrates is between 800-1200 pC/N when poled in the [011] direction, and the  $d_{31}$  is -410 pC/N. 5 nm Ti and 50 nm Pt thin films are deposited on both sides of the  $1 \text{ cm} \times 1 \text{ cm} \times 500 \mu\text{m}$  thick substrate as electrodes to actuate the substrate in a parallel plate capacitor geometry. Electron beam lithography defines sub-micron features in PMMA A2 resist onto the Ti/Pt surface. Prior to deposition, the PMN-PT is electrically pre-poled in the out-of-plane direction with an electric field of 0.4 MV/m. A 5 nm Ti adhesion layer and a 15 nm polycrystalline Ni layer were deposited by e-beam evaporation using a CHA Solution electron beam evaporator, with a deposition rate of 0.3 Å/s. FeGa (20 nm) was deposited via magnetron sputtering using an Ulvac JSP 8000 (base pressure less than  $4 \text{ E-}7$  Torr) at 100 W and a sputtering pressure of 1.0 mTorr. Films were then patterned by a lift-off process, leaving a continuous Ti/Pt layer covering the PMN-PT substrate and sub-micron magnetic features defined on top of this metal layer.

Prior to applying an electric field through the substrate, magnetization states in the ring and square microstructures are initialized by applying and subsequently removing an in-plane

external magnetic field ( $H_{init}$ ) of 0.5 T. The magnetic field is applied in the direction bisecting the directions of the principal strain axes, [100] and [01-1] of the PMN-PT substrate. After the removal of  $H_{init}$ , the rings of interest will form “onion states” [19], [21], [120], [121] with the two onion state domains aligned along the direction of  $H_{init}$ , as a result of competition between exchange energy and demagnetization energy. Depending on the aspect ratio between the ring width and ring diameter, the stabilized onion state has two forms of domain walls: transverse or vortex [19]. On the other hand, the microsquares will fall into a full Landau state, or a partial Landau state due to physical imperfection [22], [97], [122]. The direction of  $H_{init}$  is so chosen in order to allow a  $45^\circ$  deterministic rotation of the initialized magnetic state, once the electric field is applied to the substrate [7], [22]. A schematic of the sample with its setup is shown in **Figure 4.1**.



**Figure 4.1.** Schematic of the sample and the relative orientations between the initial field direction and the PMN-PT principal strain axes. After the initialization field,  $H_{init}$ , is removed, an electric field is applied through the thickness of the ferroelectric PMN-PT via the top and bottom electrodes made of Pt thin films, inducing a differential in-plane strain.

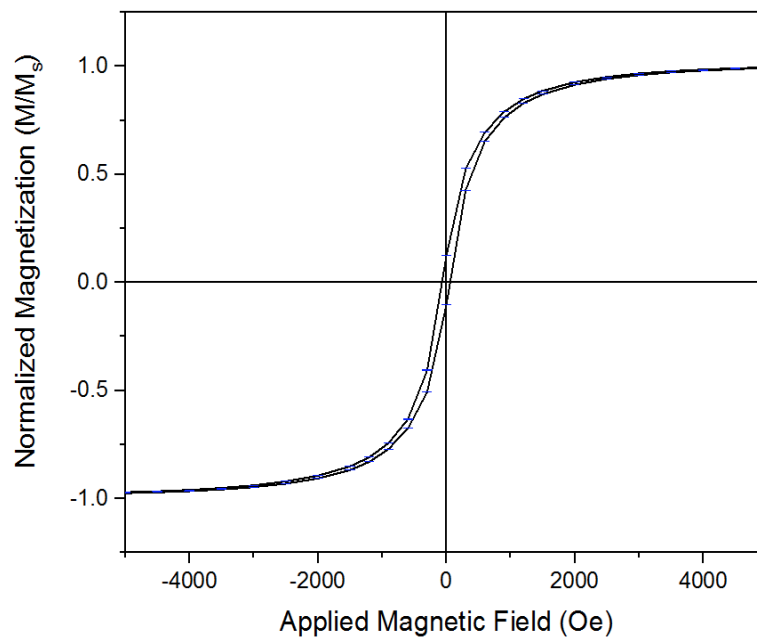
#### 4.2.2 XMCD-PEEM for magnetic domain imaging

X-ray magnetic circular dichroism-photoemission electron microscopy (XMCD-PEEM) at beamline 11.0.1.1 of the Advanced Light Source of the Lawrence Berkeley National

Laboratory is used to image the magnetization contrast in our magnetic structures. Apart from high resolution imaging, other advantages of XMCD-PEEM include element-specificity and non-invasiveness during electric-field sweeps [123]. For this study, XMCD-PEEM is mainly used to characterize the initialized magnetization states in the Ni and FeGa microstructures of different dimensions on PMN-PT at room temperature.

#### 4.2.3 Nano-magnetic particle preparation

Superparamagnetic (SPM) beads with diameter of 0.6  $\mu\text{m}$  and 2  $\mu\text{m}$  (Spherotech, Libertyville, IL) are suspended in distilled water in a 1.5 mL eppendorf tube. The surface of the superparamagnetic microbeads is functionalized with streptavidin to enable bioconjugation for future cell applications.



**Figure 4.2.** The magnetization hysteresis loop measured by SQUID magnetometry for a suspension of the superparamagnetic nanobeads ( $\sim 600$  nm in diameter) used for the fluorescent imaging.

As shown by this part of the study, using the micro- and nanoscale SPM beads is a powerful method to detect the location of the domain walls on a magnetostrictive microstructure based on the magnetic stray field emanating from it. When methods such as XMCD-PEEM are not easily accessible, this alternative method provides a lab-based tool to image the magnetic domain wall distribution in a straightforward manner. With fluorescent beads, this method allows for imaging with a large field of view where, in this case, arrays of microstructures can be imaged simultaneously. **Figure 4.2** shows the normalized magnetic hysteresis loop of the SPM beads 0.6  $\mu\text{m}$  in diameter, measured by superconducting quantum interference device (SQUID) magnetometry (Quantum Design MPMS 3). For preparation, a drop of beads suspended in the solution was dried on a plastic chip prior to the SQUID measurement.

#### *4.2.4 Trapping of superparamagnetic beads by stray field from Ni and FeGa microstructures*

Nanomagnetic particles provide a simple detection method of the magnetic stray field of microstructures. The surface of the nanoparticles is functionalized by different chemical groups to react with specific biological elements. In contrast to conventional methods to detect magnetic domain wall at the nanoscale such with XMCD-PEEM or magnetic force microscopy (MFM), this technique is highly accessible, non-invasive and compatible with in-vitro downstream applications.

SPM sub-micron sized beads were introduced to the patterned sample after passivating the surface with pluronic F-127 to prevent non-specific interactions. The beads were allowed to settle and sediment to the sample surface. Non-magnetically attached SPM beads (i.e., non-

specific adhesion) were washed off with low flow rates. In the experiments with electric-field induced strain in the PMN-PT, the SPM solution is applied at the center of the sample surface.

#### 4.2.5 *Electric field-driven particle motion*

Samples were initialized in an electromagnet and then mounted on a custom chip carrier, after which a droplet of fluid containing SPM beads was placed on the sample surface. Sedimentation and trapping of beads at magnetic domain walls was observed. Upon confirmation of the bead capture, the voltage was increased in steps of 40 V from 0 to 200 V, corresponding to a 0.0-0.4 MV/m electric field within the piezoelectric PMN-PT substrate. When an electric field is applied to the substrate, the induced strain will alter the magnetic energy landscape, which determines the preferential magnetization direction in either the Ni or FeGa. When a sufficient strain is applied, the magnetization states in both magnetostrictive materials will be modified. Since the magnetostriction coefficients,  $\lambda_s$ , of Ni and FeGa have opposite signs, the easy axis in Ni will be reoriented towards the compressive strain direction [100], while the easy axis in FeGa will be reoriented towards the tensile strain direction [01-1] of (011)-cut PMN-PT.

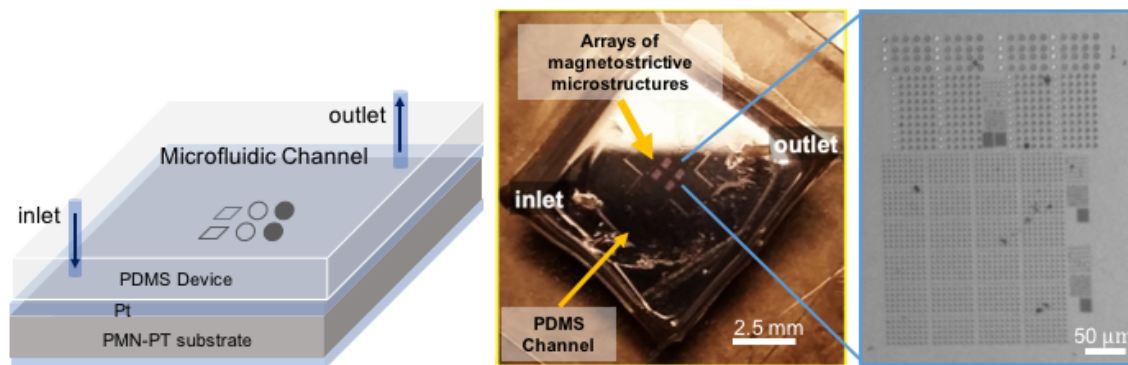
#### 4.2.6 *Optical microscope and Fluorescent microscope imaging and data analysis*

The device was viewed using an inverted microscope Nikon Ti-U (Nikon, Melville, NY) illuminated by a mercury arc lamp with 40 $\times$  and 100 $\times$  objectives. Fluorescent SPM nanobeads captured on a magnetic array were imaged with a CCD Coolsnap HQ2 camera (Roper Scientific, Evry, France). Images were processed by NIS Elements software (NIS-Elements Package Ver. 4.00, Nikon) to locate in high resolution the trapping location on the domain wall. High speed videos of microstructures to capture Brownian motion and electric

field-driven motion experiments were recorded using a Fastec IL3 high-speed camera at 1000 frames per second under bright field illumination.

#### 4.2.7 *Microfluidics Integration*

A PDMS device was fabricated with standard soft-photolithography to form a channel ( $H=100\ \mu\text{m}$ ,  $W=0.5\ \text{cm}$ ,  $L=0.5\ \text{cm}$ ), as shown in **Figure 4.3**. The master wafer was patterned with KMPR 1050 (Microchem Corp., Woburn, MA, USA). PDMS (Sylgard 184, Dow Corning, Midland, MI, USA) was mixed with a curing agent at a 10:1 weight ratio. The mixture was poured onto the master wafer and degassed to remove air bubbles. The PDMS was cured at  $100^\circ\text{C}$  overnight. Microchannel devices were cut out and aligned on the surface of Ni/(001)-PMN-PT and FeGa/(001)-PMN-PT multiferroic heterostructures after an inlet and outlet were punched connecting to upstream and downstream portions of the channel. The bonded microchannels are capable of steering the flow and perform washing steps to test multiple SPM bead trapping events on the same device.



**Figure 4.3.** Microfluidic chip integrated on the top surface of the magnetoelectric device. Arrays of magnetostrictive micropatterns are located at the center of the device, viewed by optical microscopy.

#### 4.2.8 *Cell viability test*

Jurkat leukemia cells (ATCC, Manassas, VA) were grown in RPMI 1640 media containing 10% fetal bovine serum (Invitrogen, Carlsbad, CA). Cells are cultured at 37°C in a humidified atmosphere of 5% CO<sub>2</sub>. Cell viability is determined by Calcein AM green fluorescence stain (Thermo Fisher, Waltham, MA).

## 4.3 Results and Discussion

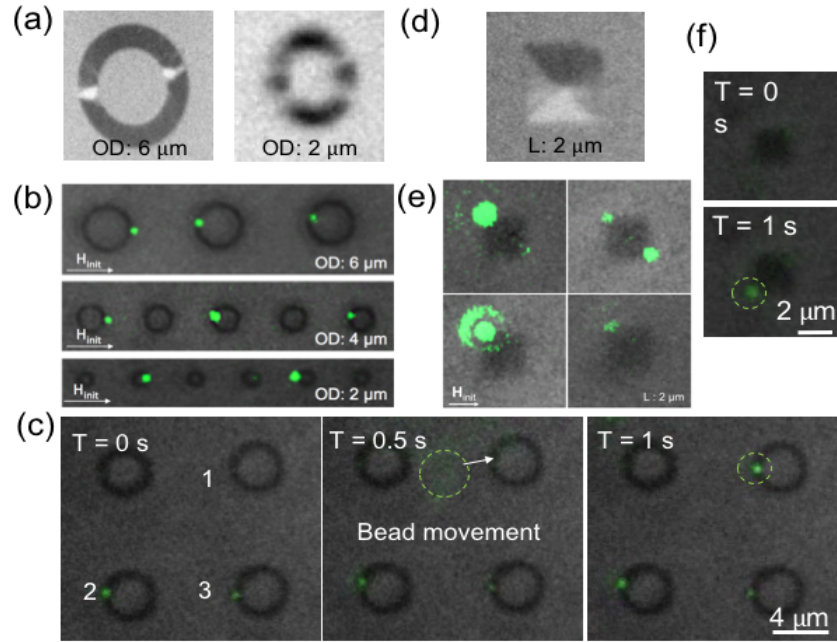
### 4.3.1 XMCD-PEEM imaging of the microstructure arrays and localized fluorescent bead trapping

Upon removal of the initializing magnetic field ( $H_{init}$ ), Ni and FeGa rings relaxed into onion state domains while squares relaxed into Landau states due to energy minimization between exchange and demagnetization contributions. XMCD-PEEM characterized the domain configuration in the microstructures by spatially resolving the magnetization contrast, where black and white indicate the magnetic orientation pointing to the right (0°) or to the left (180°), respectively, in the figures below.

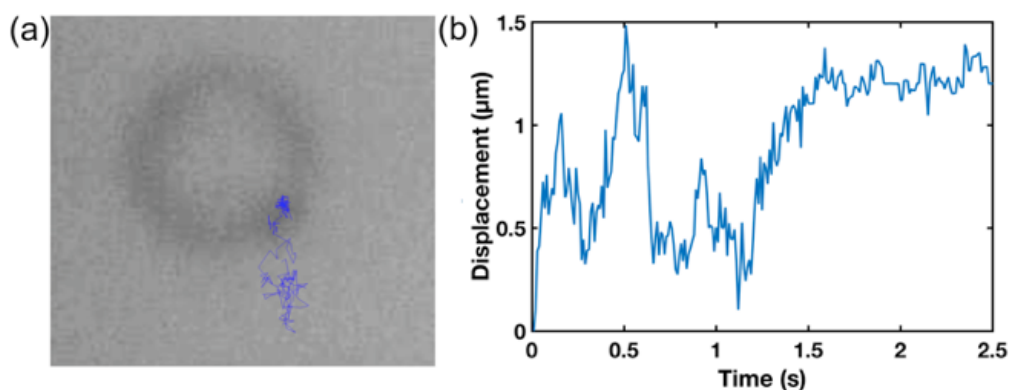
**Figure 4.4(a)** displays the XMCD-PEEM images of Ni microstructures at initialization, showing onion states in rings. Fluorescent SPM micro- and nanobeads are used to pinpoint the location of the onion state domain walls, which are local sources of magnetic stray field, and bead trapping locations using the same magnetic initialization protocol as used for the XMCD-PEEM samples. As an overlay of bright field and fluorescent microscope images, **Figure 4.4(b)** presents arrays of Ni rings of outer diameters 2  $\mu\text{m}$  - 6  $\mu\text{m}$  capture fluorescent beads at the DWs location of the onion state. A series of time lapse images of an array of Ni rings with OD of 4  $\mu\text{m}$ , and  $w$  of 350 nm capturing beads is shown in **Figure 4.4(c)**.

**Figure 4.4(d)** shows the XMCD-PEEM images of Ni square forming a Landau flux closure state with four triangular domains (magnetic vortex state [22]). Although the Landau state forms to minimize the demagnetization energy, the magnetization at the center of such vortex state points out of the plane to avoid drastic increase in exchange energy. Both Hall micromagnetometry and micromagnetics simulation studies on Landau state by Breitenstein *et al.* [124] suggested that the z-component of the stray field from the vortex core with a few nm in size becomes completely masked by the stray field from the domain walls from the four triangular domains at around 90 nm in their permalloy squares of 2  $\mu\text{m}$  in length and 20 nm in thickness. This helps to explain that with magnetic particles with diameter more than 0.5  $\mu\text{m}$ , the trapping by the vortex core with only a few nanometers in diameter and limited z-direction stray field range was not observed. Instead, consistent trappings occur at multiple corners of the squares (see **Figure 4.4(e)**), indicating the partial flux closure domain state produces high stray fields at the corners. Furthermore, according to a recent XMCD-PEEM study based on Ni microsquares on PMN-PT [22], the squares do not always form “perfect” flux-closure Landau state. **Figure 4.4(f)** shows the time lapse images of a square of 2  $\mu\text{m}$  in length capturing a bead at the corner. Combined with the bead trapping experiment, it can be observed that the initialized magnetic vortex state produces strong stray field at the corners of the squares. Such partial closure domain occurs due to several reasons: 1) physical imperfections of the fabricated micron scale structure with 15-20 nm in thickness, and 2) initial non-uniform magnetic uniaxial anisotropy could also contribute to the deviation from a perfect Landau state.



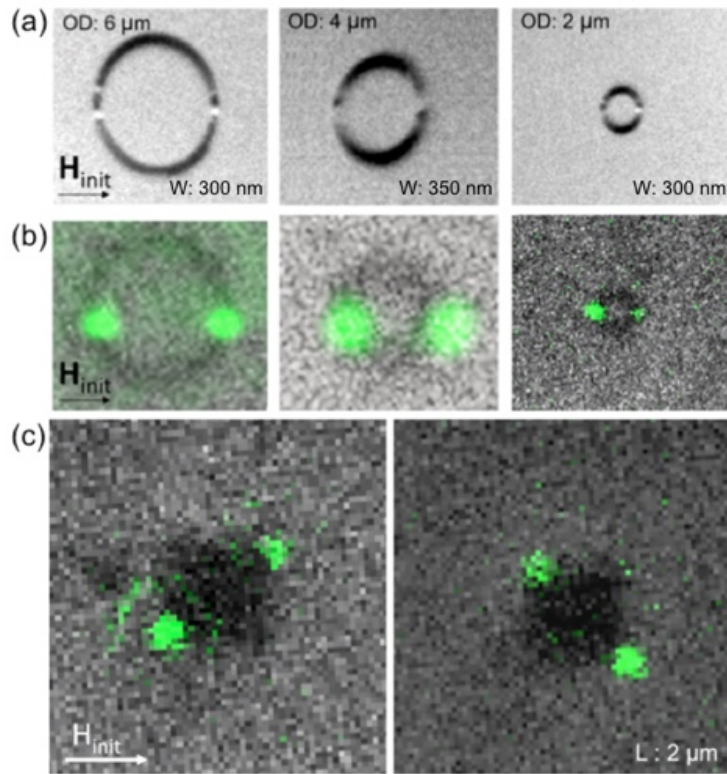


**Figure 4.4.** Fluorescent beads of  $0.6 \mu\text{m}$  (green) trapped and localized on the magnetic domain walls of the Ni microstructures. (a) XMCD-PEEM images of Ni rings. (b) Overlay of bright field and fluorescent microscope images of fluorescent beads coupled to rings of  $6 \mu\text{m}$ ,  $4 \mu\text{m}$ , and  $2 \mu\text{m}$  in diameter. (c) Time lapse images of  $4 \mu\text{m}$  Ni rings capturing fluorescent bead ( $0.6 \mu\text{m}$  in diameter) in the microfluidic channel, corresponding to the location of the DWs of Ni rings, as shown in the PEEM images. (d) XMCD-PEEM images of Ni squares with  $2 \mu\text{m}$  in length. (e) Overlay of bright field and fluorescent microscope images of fluorescent beads captures at the corners of  $2 \mu\text{m}$  squares. (f) Time lapse images of FeGa squares of  $2 \mu\text{m}$  in length capturing fluorescent bead at the corner. Dashed circle highlighted the position of the fluorescent bead.



**Figure 4.5.** (a) Representative particle trapping event in the absence of flow (1  $\mu\text{m}$  particle, 4  $\mu\text{m}$  diameter ring). Left: Particle path overlaid on image of 4  $\mu\text{m}$  Ni ring. (b) Particle displacement relative to position at time 0 (Euclidean distance) vs time over the course of the trapping event. Trapping occurs around 1.5 seconds and most random motion ceases.

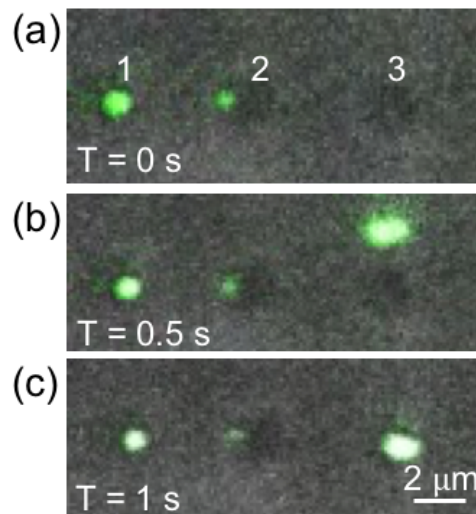
When no flow is applied and particles are simply allowed to sediment, high-speed camera footage of the trapping event shows that motion stops quickly upon interaction of the particle with the domain wall of a Ni ring, confirming the strong magnetic interaction between the bead at the domain wall that has sufficient energy to overcome thermal energy. In particular, prior to the moment of capture, the particle moves randomly (see **Figure 4.5**), suggesting that the observed motion is from Brownian diffusion and/or environmental vibration. The sudden decrease of the amplitude of this motion upon encountering the domain wall and its failure to reoccur thereafter must be from a localized pinning potential the particle experiences, in this case due to the magnetic field gradient from the domain wall.



**Figure 4.6.** (a) Initialized onion states in polycrystalline FeGa rings of varied width and diameter, with a thickness of 20 nm, observed by XMCD-PEEM. (b) Rings of various sizes in (a) trapping fluorescent nanoparticles via the magnetic stray field emanating from the onion state domain. (c) Squares of 2  $\mu\text{m}$  in length trapping fluorescent particles on the corners.

To investigate whether higher magnetostrictive FeGa microstructures follow similar paradigm of Ni microstructures, microstructures of similar dimensions are also examined. Figure 4.6(a) shows the XMCD-PEEM images of individual FeGa rings with outer diameters (OD) of 6  $\mu\text{m}$ , 4  $\mu\text{m}$ , and 2  $\mu\text{m}$ , and widths ( $w$ ) of 300 nm, 350 nm and 300 nm, respectively. With the desired onion states confirmed by XMCD-PEEM, fluorescent SPM micro- and nanobeads are used to confirm the one-to-one correspondence between the location of the onion state domains (see Figure 4.6(b)). For FeGa squares of 2  $\mu\text{m}$  in length, the beads are observed to be trapped on the corners, as shown in Figure 4.6(c). Figure 4.7 shows the time lapse images of an array of FeGa rings capturing beads, along with the process of bead

capturing by the rightmost No. 3 ring. The three rings shown here have a diameter of 2  $\mu\text{m}$  and width of 300 nm.

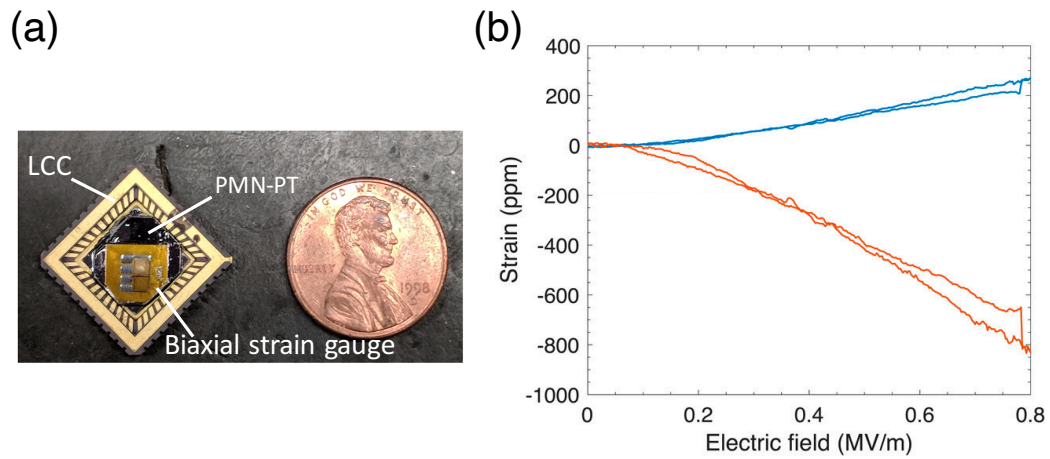


**Figure 4.7.** Time lapse images of 2  $\mu\text{m}$  ring (No.3) capturing a fluorescent bead in the microfluidic channel, corresponding to the location of the DWs of FeGa rings, as shown in the PEEM images. Ring No. 1 and No. 2 have captured beads prior to No. 3. All the three rings trapped beads locally along the x direction, in which  $H_{\text{init}}$  was applied.

#### 4.3.2 Strain profile characterization

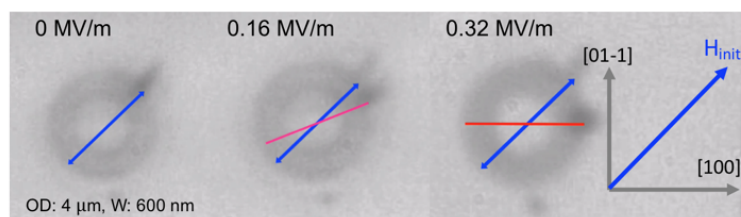
Previously, Sohn *et al.* [7] demonstrated the morphotropic transformation when PMN-PT transitioned from rhombohedral to orthorhombic in (011)-cut PMN-PT, inducing a large, nonlinear strain jump to the substrate at 0.5 MV/m . The transformation initiated abrupt particle motion to a full 45° rotation instantaneously. This study focuses on a PMN-PT with a different composition, resulting in a linear strain profile with electric field, as shown in **Figure 4.8**. The strain profile was measured by attaching a biaxial strain gauge onto the surface of the sample. As we apply electric field of various magnitudes, the induced strain will result in a change in the electrical resistance that is proportional to the strain magnitude. With a linear strain profile,

we expect a smoother modulation of the magnetic particle position along the perimeter of the ring as the electric field is applied across the substrate.



**Figure 4.8.** (a) Magnetolectric device is mounted on a leadless chip carrier (LCC), and a biaxial strain gauge is mounted on the surface of the device for strain profile characterization. (b) Linear strain response along the [01-1] and [100] directions of the PMN-PT substrate to the applied electric-field is measured using the strain gauge. Figure from [58].

### 4.3.3 Electric-field driven particle displacement



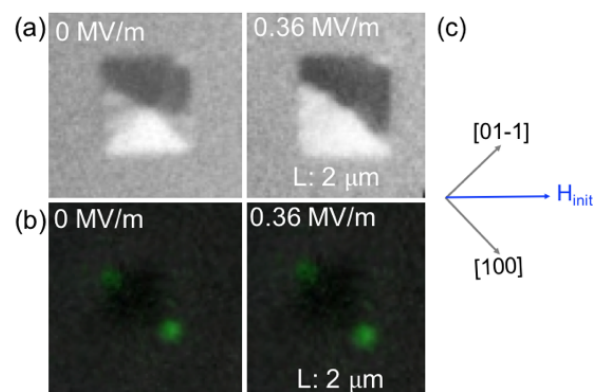
**Figure 4.9.** Continuous magnetic bead movement, driven by applied electric field to the PMN-PT with linear strain response, along the perimeter of the Ni ring, 4 μm in diameter and 600 nm in width, captured by optical microscope. The diameter of the bead is 1 μm.

Though electronically actuated particle motion in multiferroic heterostructures like these has been demonstrated previously using PMN-PT substrates with a nonlinear strain response [19], actuation using linear strain response is more desirable due to the potential for controllable, continuous particle motion. Due to the linear strain, within a certain range of applied fields the particle displacement is also expected to be proportional with respect to the electric field. However, as the magnitude of the strain response is lower in these linear strain samples, it was necessary to demonstrate that actuation of domain wall motion is still possible at non-destructive electric field strength. To this end, stepwise voltage was applied to PMN-PT substrate with Ni microstructures after particle trapping.

Successful, electrically driven continuous particle motion was observed for particles trapped on Ni rings, wherein a trapped magnetic particle rotated through several intermediate angles as the applied voltage was increased until aligned with the compressive strain axis [100] of the PMN-PT substrate (see **Figure 4.9**). No other motion of the trapped particles during this process was observed, including any reoccurrence of the random diffusive motion described above, suggesting that the particles remain trapped during the domain wall motion. This distinguishes these motions from the large, nonlinear strain-mediated displacements observed in Sohn et al. [7], in which the particles were moved in one step or even ejected from the domain wall due to the sudden DW rotation.

Interestingly, however, magnetic beads trapped at the corners of the squares of 2  $\mu\text{m}$ , either in Ni or FeGa, remain stationary after the application of electric field, with an example of a Ni square shown in **Figure 4.10**. Lo Conte et al. [22] has recently reported more details of electrical-field induced domain state change in Ni 2  $\mu\text{m}$  squares. One explanation is that as the magnetic vortex state (**Figure 4.10(a)** left) becomes a two-domain state whose domain wall

aligns with the compressive strain axis in  $[100]$ , the high energy density of the magnetic stray field still exists at the diagonal corners of the square. Taking into account the non-uniformly distributed strain in the substrate and imperfections from fabrication, the domain wall of the two-domain state does not always overlap perfectly with the diagonal of the square, leading to the locations of the bead trapping laying slightly away from the corner of the square. However, compared to the particle motion with respect to the ring, the particle captured by the corner of the square stabilizes at the same location. The different responses of magnetic particles to the two different geometries of the microstructures suggest a way to pattern various microstructures on the same device with different degrees of freedom for strain-mediated particle control, when compared to micropatterned magnetic arrays without such multiferroic control.

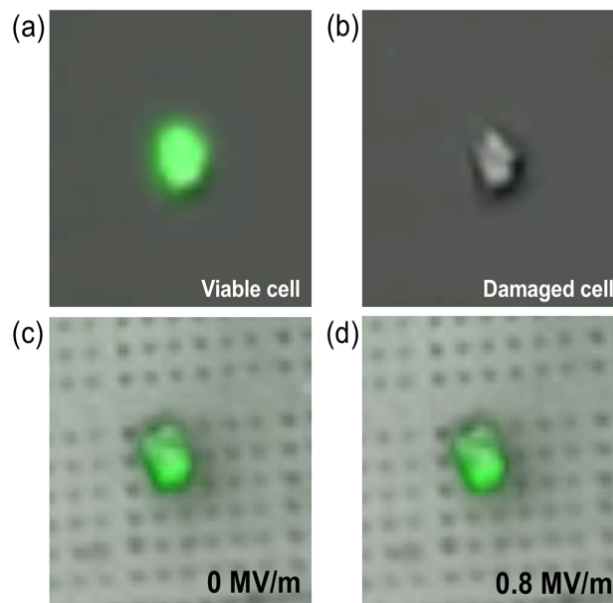


**Figure 4.10.** (a) XMCD-PEEM images of a Ni square with a magnetic vortex state at zero electric field, and evolves into a two-domain state at 0.36 MV/m, (b) a Ni square of 2 μm in length trapping fluorescent beads on the corners before and after applying voltage. (c) Sample orientation with respect to the initialization magnetic field direction.

#### 4.3.4 Cell viability on magnetoelectric devices

To investigate the cell viability [125] on the magnetoelectric devices with applied electric fields up to 0.8 MV/m, live Jurkat cells are stained with Calcein AM green fluorescent

dye. Cell membrane damage causes the green dye to escape, indicating cell death. Stained cells were settled on the Pt electrode covering the PMN-PT substrate. Cells remained viable when voltage was applied up to 400 V, corresponding to an electric field of 0.8 MV/m (**Figure 4.11**). This indicates cytocompatibility of the platform for in-vitro cell biomedical applications while actuating a magnetoelectric device with adequate packaging.



**Figure 4.11** - Viability test on multiferroic heterostructure platform using Calcein AM stain (a) stained viable cells (b) stain leakage of damaged cells. (c) before applying voltage (d) after ramping up the voltage to 400 V applied to the top and bottom electrodes, with corresponding electric field up to 0.8 MV/m, the cells are viable for downstream bio-applications.

#### 4.4 Concluding Remarks

In summary, we have demonstrated the trapping of submicron magnetic particles by magnetostrictive Ni and FeGa microstructures at specific locations, including onion state domain wall of the ring structures, and partial flux closure domain at the corner of squares. XMCD-PEEM shows the magnetic domains in both Ni and FeGa microstructures, while



optical and fluorescent microscope captures how the beads interact with the domain walls, highlighting an alternative nondestructive method of indirectly visualizing the domain wall locations in these magnetostrictive microstructures. The linear strain response when electric field is applied through the thickness of the PMN-PT substrate enables a steady and continuous translational movement of the magnetic bead to the newly electrically introduced magnetic easy-axis. The cytocompatible device provides a promising pathway to develop multiplex particle and cell manipulation platforms with sub-micron precision.

## **Chapter 5    Single-domain Multiferroic Array-addressable Terfenol-D (SMArT) Micromagnets for Cell Capture and Release<sup>6</sup>**

Chapter 4 presents magnetoelastic microstructures made of Ni and FeGa capturing superparamagnetic particles. It also shows that using optical and fluorescent microscope is a convenient way of visualizing how magnetic beads would interact with the magnetic stray field. Compared to using XMCD-PEEM to map out magnetic domain configurations in these sub-micron magnetic structures, optical and fluorescent microscope is nondestructive in visualizing the domain wall locations in these magnetostrictive microstructures. However, we also notice the magnetic stray field from these structures are not sufficient enough to robustly capture magnetically-labeled single cells in an array fashion. In this chapter, we explore the potential of highly magnetostrictive Terfenol-D microdisks when it comes to single-cell manipulation.

### **5.1 Overview of Terfenol-D based single-cell control**

Controlling magnetic fields at the microscale level programmatically can lead to automation at the scale of single cells  $\sim 10 \mu\text{m}$ . Most magnetic materials provide a consistent magnetic field over time but the direction or field strength at the microscale is not easily modulated. However, magnetostrictive materials, when coupled with ferroelectric material (i.e., strain-mediated multiferroics), can undergo magnetization reorientation due to voltage-induced strain, promising refined control of magnetization at the micron-scale.

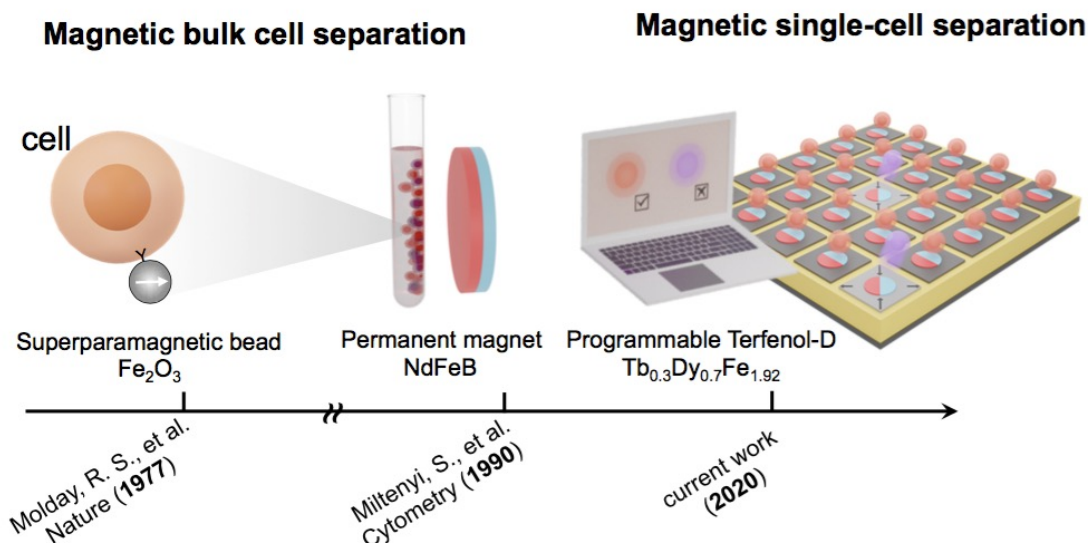
---

<sup>6</sup> This chapter is adapted from previously published manuscript [107], where the author was among the first co-authors. Some of the sections on Terfenol-D growth are adapted from K.Panduranga et al [67].

This chapter demonstrates the largest single-domain microstructures ( $20\ \mu\text{m}$ ) of Terfenol-D ( $\text{Tb}_{0.3}\text{Dy}_{0.7}\text{Fe}_{1.92}$ ), a material that has the highest magnetostrictive strain of any known soft magnetoelastic material. These Terfenol-D microstructures enabled controlled localization of magnetic beads with sub-micron precision. Magnetically-labeled cells were captured by the field gradients generated from the single-domain microstructures without an external magnetic field. The magnetic state on these microstructures were switched through voltage-induced strain, as a result of the strain-mediated converse magnetoelectric effect, to release individual cells using a multiferroic approach. These electronically addressable micromagnets pave the way for parallelized multiferroics-based single-cell sorting under digital control for biotechnology applications.

## 5.2 Magnetic cell separation: bulk and single-cell

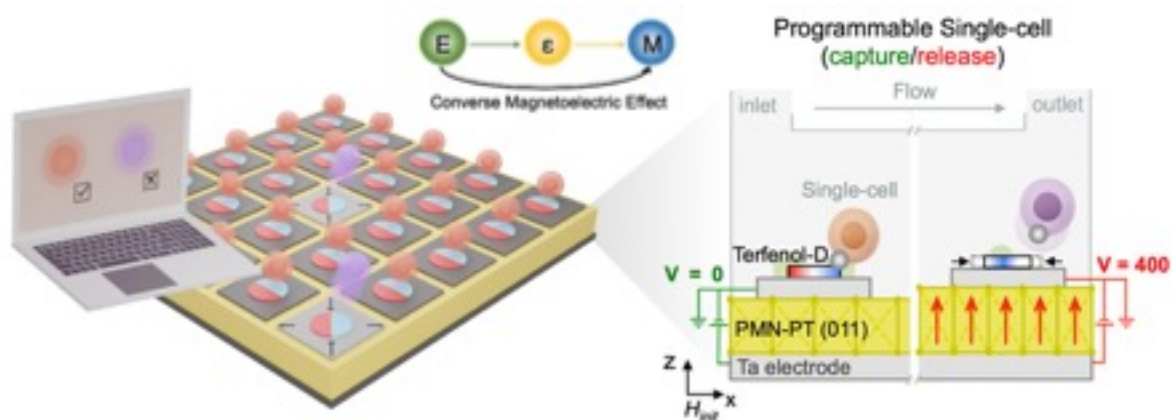
Programmable multiferroic materials can enable a technological transformation in magnetic cell separation, from bulk cell separation via coarsely applied external magnetic fields [32], [126], [127] to single-cell separation via localized and programmable magnetoelastic micromagnets [5], [128][3]. Over the past decades, magnetic cell separation has been widely used to separate cells in bulk by binding superparamagnetic beads to specific cell membrane proteins as shown in **Figure 5.1** [129]. Once the cell surface is functionalized with magnetic beads, an external magnetic field ( $H$ ) can direct the bulk migration of targeted cells in complex fluids (e.g. blood) [130], [131]. However, new advances in cell engineering for personalized therapies [30], [132], [133] can benefit from selection of individual cells based on their complex behaviors or time-dependent functions (e.g. cell-killing, secretion, motility) [134]–[137], which may not be directly correlated to cell surface protein expression. Therefore, a new generation of single-cell magnetic separation techniques is needed with precise and programmable cell capture/release that is scalable across massive arrays [138], [139].



**Figure 5.1.** An abbreviated view of technological development of magnetic cell separation. Three decades ago, permanent magnets were introduced to control cell on the bulk level. Since then, magnetic-based cell sorting has been among the popular commercialized cell sorting mechanisms. This work aims for single cell manipulation by combining a multiferroics platform with microfluidics channels.

The current landscape for magnetic cell separation consists of soft and hard magnetic materials [140]. Soft magnetic materials with a low coercive field ( $H_c$ ) lack sufficient fields to capture cells independently without an external inhomogeneous magnetic field ( $H$ ) [141]. On the other hand, hard magnetic materials with high  $H_c$  lack programmability to release target cells for downstream analysis [142]. The inability of prior techniques to change the intrinsic magnetic state nor modulate the magnetic amplitude locally prevents arrayed programmability at the microscale.

We propose the usage of a composite multiferroic platform that utilizes the converse magnetoelectric effect (see **Figure 1.3**) to control magnetoelastic materials with programmable and strain-tunable magnetization at the microscale. This approach presents an opportunity to increase magnetic separation resolution to the single-cell level [85], [143], [144].



**Figure 5.2.** Cross-sectional schematic of SMArT micromagnet for single-cell separation via strain-mediated multiferroics to turn on and off the capture and release of cells via voltage application to the device.

### 5.2.1 Domain structures in Magnetoelastic materials -- State of the Art

While magnetoelastic materials have been extensively studied in a range of energy efficient applications, including non-volatile memory [15], [145]–[148], actuators [149] and transducers [150], attempts towards cell manipulation have yet to be explored. Applying an initialization field ( $H_{init}$ ) to sufficiently small ( $<1 \mu\text{m}$ ) magnetoelastic nanostructures produces single magnetic domains with local stray fields ( $H_s$ ) that can replace inhomogeneous external magnetic fields ( $H$ ) for cell capture [97][151]. However, highly localized magnetic stray fields associated with typical single magnetic domain nanostructures ( $<1 \mu\text{m}$ ) are insufficient for cell capture alone [7], [107]. Scaling up the physical size of magnetoelastic nanostructures to the size of a single cell  $\sim 10 \mu\text{m}$  is required, but the larger soft magnetoelastic structures produce multi-domain magnetic states rather than single magnetic domains due to the energy competition between exchange energy and demagnetization energy [152]. These multi-domain states produce non-uniform magnetic stray fields, which is less effective for single cell capture/localization (**Figure 5.12**). Furthermore, the complexity of multi-domain structures

poses a challenge in reliably controlling the magnetic state for targeted cell release (**Figure 5.18**). Larger single-domain structures are needed for effective magnetic cell trapping and manipulation due to the single-domain strong stray fields (**Figure 5.10**). However, larger in-plane single domain structures have not been previously achievable with the current thin film magnetoelastic materials, such as Ni, CoFe, CoFeB or FeGa.

In this work, we were able to achieve large single-domain states ( $d = 20 \mu\text{m}$ ) that are capable of single-cell capture with single-domain multiferroic array-addressable Terfenol-D (SMArT) micromagnets, an intermetallic compound with the highest magnetostrictive strain of any known room temperature soft magnetoelastic material [153]. By coupling stress into these single-domain Terfenol-D structures, we were able to alter their magnetic state and achieve single-cell release (see schematics in **Figure 5.2**).

### 5.3 Fabrication of Terfenol-D thin film and microdisks

Magnetostrictive polycrystalline Terfenol-D thin films of 60 nm in thickness are deposited using a Direct Current (DC) magnetron sputtering process and a hybrid annealing approach [59]. It has been previously reported that a Terfenol-D thin film deposited on (011)-cut PMN-PT in such a manner exhibits a large coercivity reduction of 1546 Oe when PMN-PT is poled at 0.6 MV/m. The sputtered thin film is highly magnetoelastic [59]. In this section, we discuss the fabrication detail of the sputtered thin film and microstructures.

Terfenol-D thin films (60 nm) were produced by DC magnetron sputtering using a  $\text{Tb}_{0.3}\text{Dy}_{0.7}\text{Fe}_{1.92}$  alloy target obtained from TdVib LLC, USA. Different types of substrates were used for depositing the Terfenol-D films. Silicon wafers were used for determining the optimum properties of the Terfenol-D film [59], transparent Sapphire wafers were used for

XAS/XMCD studies in transmission mode, and PMN-PT substrates with top and bottom electrodes were used for inducing strain to the film through the application of voltage. The major sputtering process parameters used to produce the Terfenol-D thin films were 250 Watts of sputtering power, substrate-to-target distance of 5.5 cm, an Ar gas pressure of 5 mTorr and substrate temperature of 250 °C. Following this deposition, the film was post-annealed in-situ at 450 °C for 4 hours at a chamber pressure below  $5 \times 10^{-6}$  Torr to create polycrystalline films. For XMCD-PEEM imaging, we used finely polished PMN-PT [011] cut of 20 mm x 10 mm x 0.5 mm, with e-beam deposited 80 nm thickness of Al<sub>2</sub>O<sub>3</sub> on the top surface and Ti (5 nm)/Pt (50 nm) on bottom surface as a substrate to sputter deposit Ta/Terfenol-D (60 nm)/Ta multilayers.

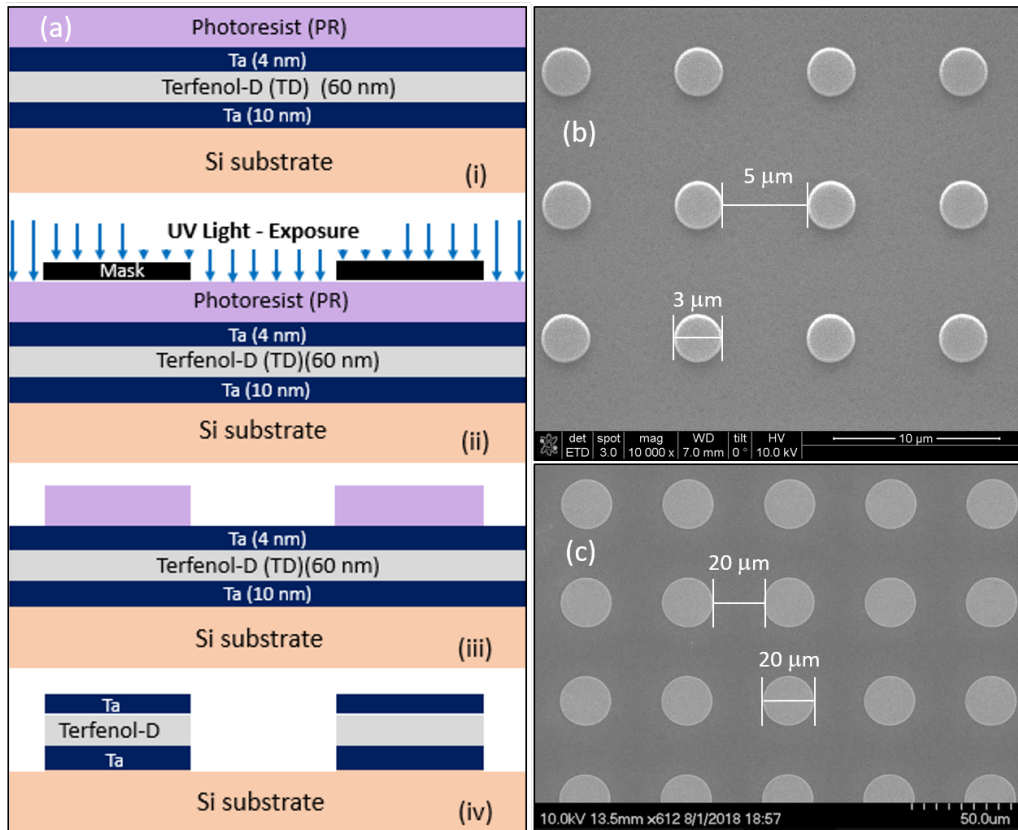
Terfenol-D micropatterns were fabricated using a conventional photolithographic method followed by Ar etching. The process consisted of spin coating of negative photoresist AZ nLOF 2020 onto the film surface followed by UV exposure using a Karl Suss mask aligner to transfer the pattern from the mask by hardening the photoresist. The film with transferred pattern was developed with AZ MIF 300 developer by dissolving the unexposed soft photoresist. After the photolithographic process the film with hardened photoresist was loaded into STS-AOE etcher to etch away the uncovered photoresist film region with Ar ions. The etched films were ultrasonicated in acetone to remove the photoresist. Finally, the microstructures were characterized and used for fabricating the single-cell sorting devices.

The structural and magnetic characterization of the films and their microstructures were carried out using several techniques. X-ray diffraction identified the film structure as face-centered cubic based on its diffraction pattern (**Figure 5.3a**). Terfenol-D films on 4" diameter silicon substrates were chosen to determine the residual stresses in the film using a wafer

curvature method. Crystallized Terfenol-D films showed a residual tensile stress of 70 MPa [59]. A SQUID magnetometer was used to determine the saturation magnetization  $M_s$ , coercivity  $H_c$  and remanence,  $M_r$  of the film as well as the microstructures. All the in-plane magnetization versus applied magnetic field plots obtained for films on Si, sapphire and PMN-PT substrates demonstrated squareness ( $M_r/M_s$ ) greater than 0.85 and  $M_s$  around 700 kA/m. The coercive field value of the films on Si and sapphire was  $H_c \sim 2300$  Oe, whereas the film on PMN-PT  $H_c \sim 3000$  Oe. The large coercivity and remanence values are largely attributed to the intrinsic residual stresses that arise during the deposition process. The residual stresses produce a large magnetoelastic induced in-plane easy axis producing both high coercivity and high remanence.

Scanning Electron Microscopy (SEM) imaging and Magnetic Force Microscopy (MFM) were used to characterize the morphology and magnetic states of the microstructures respectively. The spacing between 3 and 20  $\mu\text{m}$  diameter microdisks reduced strong dipole-dipole interactions between neighboring disks to enable the magnetic capture of single-cells to a single Terfenol-D microstructure (Figure 5.3b-c). The disk geometric variations were less than 5% based on optical inspection and measurement. The magnetic states of the 3  $\mu\text{m}$  diameter and 20  $\mu\text{m}$  diameter microdisks were imaged using MFM and XMCD-PEEM respectively. The details of XMCD-PEEM imaging are given in Section 5.4.2.





**Figure 5.3.** Fabrication process and characterization of Terfenol-D microstructures. (a) Fabrication process. (b) Scanning electron microscope (SEM) micrograph of (b)  $3\ \mu\text{m}$  diameter and (c)  $20\ \mu\text{m}$  diameter microdisks. Figure from [65].

## 5.4 Magnetic Property Characterization

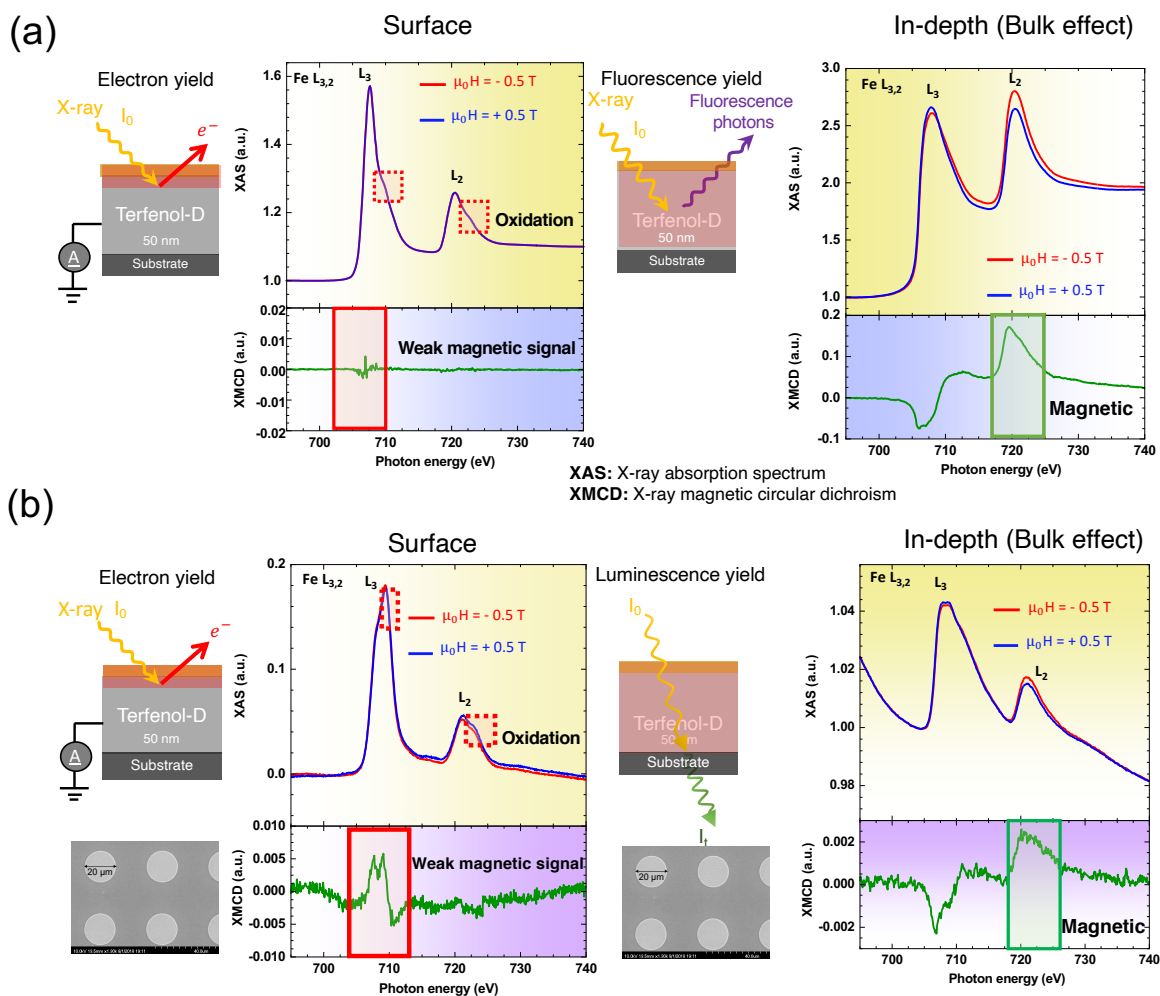
Once the film and microdisks are fabricated, we conduct several experiments to probe their magnetic property. We use X-ray Magnetic Circular Dichroism to examine the magnetic property of the film and patterned microdisks. Although the film and disks are overall magnetic, we notice some slight oxidation mainly at the sample surface. Room temperature SQUID Magnetometry Measurement over the course of three months is conducted to show stable magnetic film and disk quality. Magnetic Force Microscope images of 3 micron diameter Terfenol-D disks along with XMCD-PEEM images confirm the single magnetic domain configuration in the fabricated disks up to  $20\ \mu\text{m}$  in diameter. Additionally, superparamagnetic

beads are used to interact with these microdisks to further visualize the stray field from the single domain structures.

#### 5.4.1 *X-ray Absorption Spectra & X-ray Magnetic Circular Dichroism for Terfenol-D*

XMCD is used to understand the magnetic properties throughout the sample. Several different techniques are used to probe both at the surface and the bulk.

First of all, we study the patterned microdisks to see if patterning causes significant difference. To examine the surface, we use electron yield. For probing more of the bulk film behavior, fluorescence yield is used. Here, we are mainly interested in the XMCD taken at the Fe absorption edges  $L_3$  and  $L_2$ . At the surface, there is slight oxidation, according to the presence of both shoulders in XAS, and the weak magnetic signal from XMCD, as highlighted in red boxes (**Figure 5.4a**). However, more in-depth analysis of the film, with fluorescence yield, reveals little oxidation. Although the  $L_3$  signal is suppressed, the XMCD signal from  $L_2$  edge shows that the film is clearly magnetic. **Figure 5.4b** shows the XMCD for patterned microdots. The surface study reveals some oxidation to the Fe as well. For the entire microdisks, the study by luminescence yield shows desired magnetic state with little oxidation. Again,  $L_3$  edge is suppressed for luminescence yield, so we focus on  $L_2$ . XMCD of both film and disks confirm the oxidation occurs at the few nm surface, underneath the capping layer, yet not significant oxidation to the disks even when there are unprotected sidewall. This finding also helps explain the “wasp-waist behavior” seen in the magnetic hysteresis loop for arrays of both 20 and 3  $\mu\text{m}$  diameter disks, shown in Section 5.4.2.

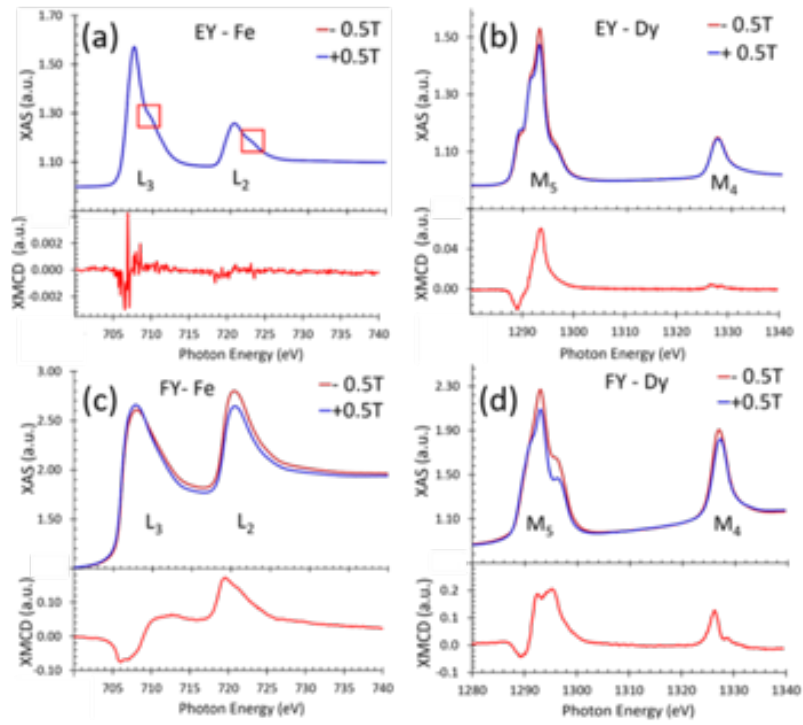


**Figure 5.4.** X-ray magnetic circular dichroism of Terfenol-D thin film and microdisks confirm the overall good magnetic quality of the film and etched microdisks. For the disks, a few nm of oxidation of Fe also occurs at surface below the 4 nm thick Ta capping.

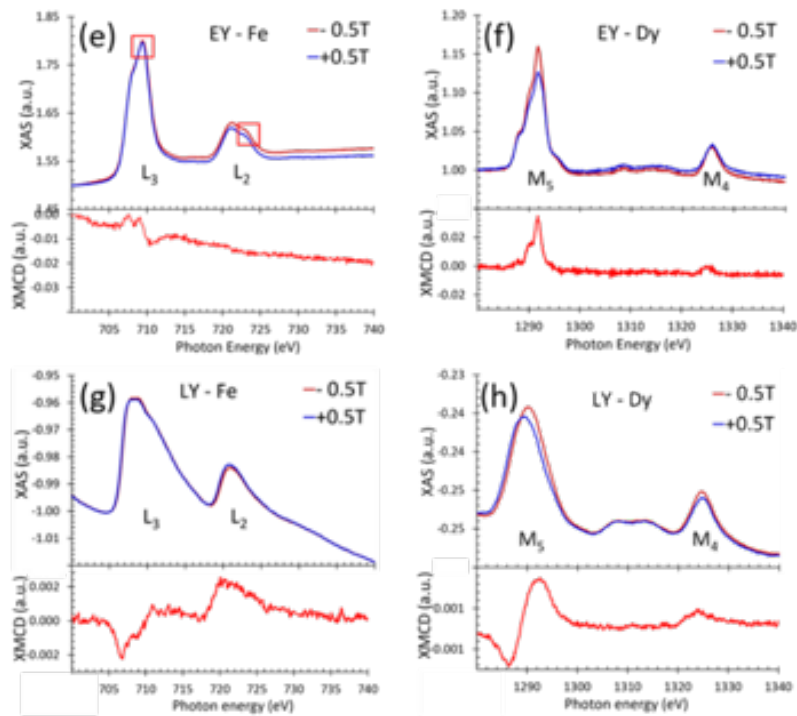
Having checked both XAS and XMCD spectroscopy of Fe, we also tune to the absorption edges of Dy and Tb. **Figure 5.5c** and **d** shows XAS and XMCD spectra of Fe  $L_{3,2}$  and Dy  $M_{5,4}$  edges measured with fluorescence yield (FY) mode for the continuous Terfenol-D thin film. The FY mode probes tens of nm deep to evaluate the energy states throughout the majority of the Terfenol-D film thickness as contrasted with the  $\sim 1$  nm depth of the EY mode. The Fe  $L_{3,2}$  edges shown in Figure 5c is similar to representative Fe  $L_{3,2}$  edges. However,

**Figure 5.5c** contains only metallic  $\text{Fe}^0$  state [29] indicating the oxidation is constrained to only the top  $\sim 1$  nm thickness. Furthermore, the observed strong XMCD signal (note ordinate axis scale) indicates magnetic  $\text{Fe}^0$  state as expected. **Figure 5.5d** shows the XAS and XMCD spectral line of the Dy  $M_{5,4}$  edges. Similar to **Figure 5.5b**, the XAS plot shows several shoulders in the  $M_5$  edge while only a single peak for the  $M_4$  edge. The corresponding XMCD spectra also shows strong magnetic signal suggesting negligible oxidation of Dy throughout the films thickness including the top 1 nm layer. These FY measurements combined with the EY measurements suggest the iron oxides is limited to the top  $\sim 1$  nm of the Terfenol-D thin film while the vast remainder of the film is oxide free. We believe that the top surface becomes oxidized during the deposition process prior to depositing the capping layer. Since the amount of oxygen is limited in the UHV sputtering system and the capping layer is deposited in a fairly short time period this particular oxidation is a self-limiting reaction. While this demonstrates that the continuous film is relatively free of oxidation it does not definitively conclude that the microdisks are also free from oxidation and for the later we conducted additional tests.

Continuous Terfenol-D Film



Patterned Terfenol-D Microdisk Arrays



**Figure 5.5.** XAS and XMCD spectra of Terfenol-D continuous film and micropatterned film

(a) electron yield measured with Fe L<sub>3,2</sub> edge for the continuous film (b) electron yield

measured with Dy M<sub>5,4</sub> edge for the continuous film (c) fluorescence yield measured with Fe

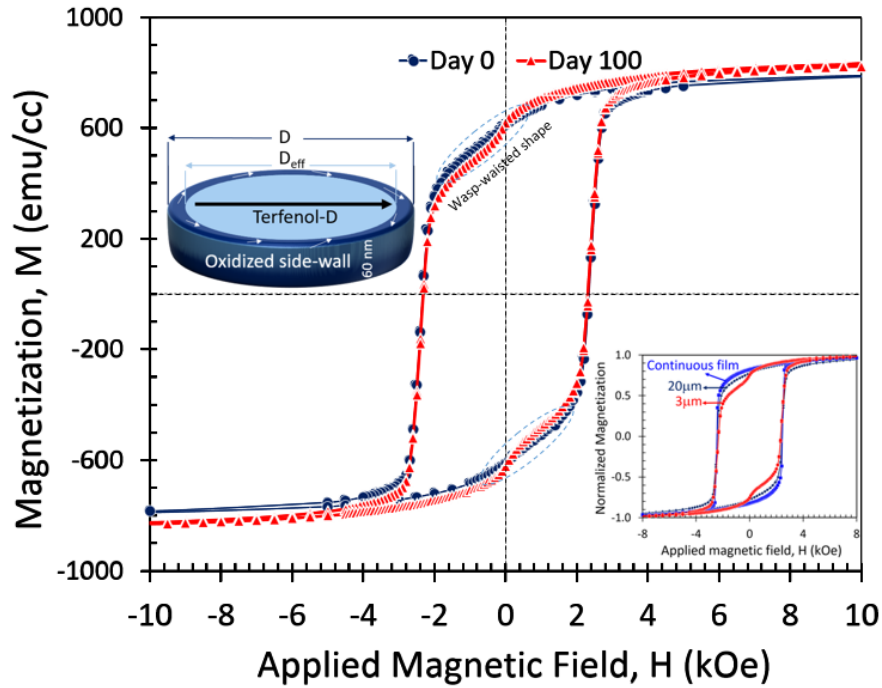
L<sub>3,2</sub> edge for continuous film (d) fluorescence yield measured with Dy M<sub>5,4</sub> edge for continuous film (e) electron yield measured with Fe L<sub>3,2</sub> edge for the micropatterned film (f) electron yield measured with Dy M<sub>5,4</sub> edge for the micropatterned film (g) luminescence yield measured with Fe L<sub>3,2</sub> edge for micropatterned film (h) luminescence yield measured with Dy M<sub>5,4</sub> edge for micropatterned film.

**Figure 5.5e** and **f** show the XAS and XMCD spectra of Fe L<sub>3,2</sub> and Dy M<sub>5,4</sub> measured with EY mode for the 20 μm diameter Terfenol-D microdisks. Here, the XAS and XMCD spectra provide absorption and magnetic information of the few nm deep film surface region as well as approximately 5 nm deep around the perimeter of the disk. The XAS absorption spectrum with Fe L<sub>3,2</sub> edges shown in **Figure 5.5e** displays prominent peaks at 710 eV and 723 eV, marked in red square boxes, corresponding to Fe<sup>3+</sup> state in contrast with the L<sub>3,2</sub> edges shown in **Figure 5.5a** (continuous film). The Fe<sup>3+</sup> peak intensities are stronger than that of the metallic Fe<sup>0</sup> indicating stronger oxidation in the probed region than the Fe<sup>3+</sup> shown in **Figure 5.5a**. This larger value is because in addition to probing the oxidized capped surface, the X-rays also penetrate the perimeter of the disk which is exposed to the ambient oxygen environment producing oxidation. This result combined with SQUID data suggest that Fe oxidation is only present around the perimeter of the disk. Furthermore, the corresponding XMCD spectra in **Figure 5e** shows a moderate magnetic signal due to the presence of some metallic Fe<sup>0</sup> in the probed region. We attribute this to the fact that the electron escaped beyond the surface oxide region and is interacting with metallic Fe<sup>0</sup> in the deeper region around the perimeter of the disk suggesting a potential self-limiting iron oxidized region. The EY absorption spectra with Dy M<sub>5,4</sub> edges (**Figure 5.5f**) shows strong peak at 1294 eV with multiple shoulders and another peak without shoulder at 1327 eV, similar to continuous film. The corresponding XMCD signals at the M<sub>5</sub> and M<sub>4</sub> edges are also stronger compared to the

continuous film indicating that the micro-disks are highly magnetic. These results indicate that the iron oxide forming around the perimeter of these micro-disks are a self-limiting reaction which does not continue to propagate throughout the disk volume. To further support this conclusion we conducted luminescence yield LY measurements on the microdisks.

**Figure 5.5g** shows XAS and XMCD spectra of Fe  $L_{3,2}$  edges of the 20  $\mu\text{m}$  diameter Terfenol-D disks measured with luminescence yield (LY) mode. The  $L_3$  and  $L_2$  edges with no shoulder indicate that the iron is in its metallic state in the probed region. This region shows negligible oxidation when the entire disk is probed. Similarly, **Figure 5.5h** shows the XAS and XMCD spectra of Dy  $M_{5,4}$  edges measured with LY mode. This also indicate strong magnetic signals at  $M_5$  and  $M_4$  edges. These results support the conclusion of the preceding paragraphs, i.e. the Fe oxide that forms around the perimeter is passivating. We believe that this occurs because of two primary features. The first feature is that the microdisks have a capping layer preventing oxygen from entering the Terfenol-D from the top surface. The second feature is that there is substantial in-plane residual tensile stresses in the film. We speculate that the in-plane stresses prevents crack formation as the Fe oxidizes. The elimination of cracks during the oxidation process prevents additional oxygen from entering the Terfenol-D microdisks. These residual stresses combined with the capping layer serve to prevent the stress corrosion cracking that drives oxygen to the interior of the Terfenol-D microdisks studied to date.

#### 5.4.2 *SQUID & MFM for magnetic microdisk property characterization*



**Figure 5.6.** M vs H plots of patterned Terfenol-D microdisks measured over the course of 100 days.

**Figure 5.6** shows representative SQUID M vs H plots for the 3  $\mu\text{m}$  diameter Terfenol-D disks measured over a 100 day period following fabrication, i.e., at day 0 and 100 presented. All magnetization plots measured during this time period show little changes including the  $M_r$  and  $H_c$  values following fabrication. The curves in **Figure 5.6** also exhibit a “wasp-waisted” step (labeled on the figure) like M vs H curves with anomalous magnetization changes as the magnetic field transitions through zero H field [154]. This “wasp-waisted” behavior originates either from superposition of hard and soft magnetic phases or oxidation of surface layers of a magnetically soft material. Such oxidation behavior can also be observed in the XMCD spectra discussed in Section 5.4.1. Therefore, this wasp-waisted region in the magnetic response is attributed to the presence of oxidation in the Terfenol-D microstructures, i.e. a second magnetic phase. Specifically, since the Terfenol-D film is capped and the continuous film (i.e. prior to fabrication of microdisks) does not exhibit this wasp-waisted behavior, we believe there exists



a small amount of side wall oxidation around the periphery (see schematic in top-right inset) creating a soft magnetic Iron oxide region due to the reaction of oxygen with surface iron atoms. This oxidation provides a slightly different magnetization response (i.e. combined oxidation along with Terfenol-D response) leading to this wasp-waisted M vs H curve. To better quantify the oxidation volume (i.e. the magnitude of  $D_{\text{eff}}$ ) in these micro-disks we provide the following information.

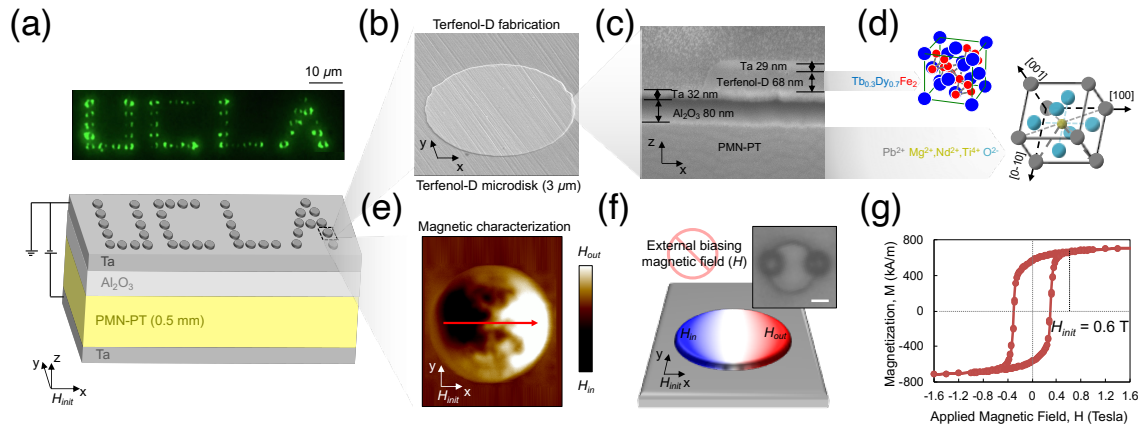
Since the Fe and rare-earth (Tb & Dy) atoms are antiferromagnetically coupled in Terfenol-D and the measured net magnetic moments are mostly from the rare-earth atoms [155], the loss of Fe atoms from the magnetic moments due to oxidation should also produce higher saturation magnetization. Specifically, the measured magnetization  $M_s \sim 800$  emu/cc is approximately 12% larger than that of the continuous film. The rare-earth rich region size around the disks perimeter is estimated by comparing the magnetization curves for the 3  $\mu\text{m}$  disks with the continuous film suggesting the wasp-waisted region (i.e. rare earth rich region) modifies the magnetic energy per volume by approximately 12% compared to the continuous film. Finally, the insignificant changes in the magnetization curves over the 100 day period suggests the oxide layer is passive and stable which is further addressed later in this manuscript discussing XAS and XMCD results. We attribute this micropatterned oxide passivation to the high relative residual stress state combined with the capping layer to prevent further crack opening during oxidation (i.e. stress corrosion cracking). The bottom-right inset of **Figure 5.6** shows M vs H hysteresis loops for a continuous Terfenol-D film, and arrays of 3  $\mu\text{m}$  and 20  $\mu\text{m}$  diameter Terfenol-D microdisks, respectively. As one can see, the M vs H loop of the 20  $\mu\text{m}$  diameter disks looks almost identical to the continuous film with  $M_s \sim 700$  emu/cc indicating negligible side-wall oxidation at the scale.

Top left inset of **Figure 5.6** shows the MFM and PEEM images of 3  $\mu\text{m}$  and 20  $\mu\text{m}$  diameter Terfenol-D disks, respectively. Prior to imaging, the microdisks are initialized by an in-plane magnetic field of 0.5 T. For the 3  $\mu\text{m}$  disk, the corresponding MFM image exhibits strong dipolar contrast and it indicates a “pseudo”-single domain state. The PEEM image shows overall uniform magnetization (in dark blue) in a large 20  $\mu\text{m}$  Terfenol-D disk taken at Dy  $M_5$  edge using XMCD-PEEM. The magnetic contrast is obtained from aligning and averaging the magnetic contrast of three PEEM images. The purpose of this step is to reduce the noise in the magnetic image as the magnetic signal observed at the Dy  $M_5$  edge is less intense than other edges. The three images are taken at a different azimuthal (in-plane) angle, including  $0^\circ$ ,  $90^\circ$  and  $180^\circ$ . The surface variation in contrast from the substrate surrounding the disk is attributed to the rough surface caused by the Argon etching process. The contrast blue here suggests that the magnetic moments are pointing horizontally in a single direction, and red suggests magnetic moments are pointing in the opposite ( $180^\circ$ ) direction. From the XMCD-PEEM image and associated strong blue contrast, we conclude that the Terfenol-D disks are pseudo-single domain even though their 20  $\mu\text{m}$  diameter and 70 nm in thickness would suggest a multi-domain state for this material. Single domain state in such a large size disk is unusual and is only possible because of the large residual tensile stress  $\sigma \sim 70$  MPa (measured with wafer curvature method [59]) induced during the Terfenol-D growth process producing large in-plane anisotropies and coercive fields. This large residual stress coupled with the materials large saturation magnetostriction  $\lambda_s \sim 880$  ppm produces an effective magnetoelastic anisotropy  $\lambda_s\sigma$  much larger than that required to form closure domains producing the observed pseudo-single domain state [156] represented in the images of Figure 4 upper left.

Next, to investigate the magnetoelastic properties of Terfenol-D microstructures for strain induced cell capture/release, experiments are carried out on sputter-deposited Ta (23 nm)/Terfenol-D (68 nm)/Ta(32 nm) multilayer thin films on PMN-PT  $[\text{Pb}(\text{Mg}_{1/3}\text{Nb}_{2/3})\text{O}_3]_{1-x}[\text{PbTiO}_3]_x$  ( $x \approx 0.34$ , PMN-PT) [011]-cut piezoelectric substrate. Electron-beam evaporated  $\text{Al}_2\text{O}_3$  (80 nm) is deposited between the PMN-PT and Terfenol-D to prevent oxygen diffusion into the Terfenol-D. The Terfenol-D is patterned by optical lithography followed by Ar etching (**Figure 5.7(a-d)**). Terfenol-D thin films exhibit a relatively large coercive field ( $H_c$ ) of 0.3T, saturation ( $M_s$ ) and remanent ( $M_r$ ) magnetization of 710 and 600  $\text{kA m}^{-1}$ , respectively, measured by superconducting quantum interference device (SQUID) (**Figure 5.7g**). A strong dipolar contrast is observed in 3  $\mu\text{m}$  Terfenol-D disks indicating single-domain states imaged by magnetic force microscopy (MFM) following the application of an in-plane magnetic field ( $H_{\text{ini}}$ ) of 0.5 T (**Figure 5.7e**). A single domain state in these large disks (3  $\mu\text{m}$ ) is possible due to the large residual tensile stress of 70 MPa [59] developed during the Terfenol-D annealing process, which also produces large in-plane anisotropies and coercive fields. This large residual stress coupled with the material's large saturation magnetostriction  $\lambda_s \sim 880$  ppm produce an effective magnetoelastic anisotropy sufficient to produce a pseudo-single domain state in these micropatterned disks [156]. Following initialization, and in the absence of an external magnetic field, magnetic beads were uniformly captured at the magnetized poles as illustrated in (**Figure 5.7a and f**, Movie S1 [157]<sup>7</sup>). To find out if the single magnetic domain can persist beyond 3  $\mu\text{m}$ , we fabricated substantially larger microstructures with diameter of 20  $\mu\text{m}$  and beyond and image the magnetic domain with a more efficient and non-invasive magnetic imaging method – XMCD-PEEM.

---

<sup>7</sup> Supplementary Movie 1 [67] located at: <https://onlinelibrary.wiley.com/doi/full/10.1002/adma.202006651>

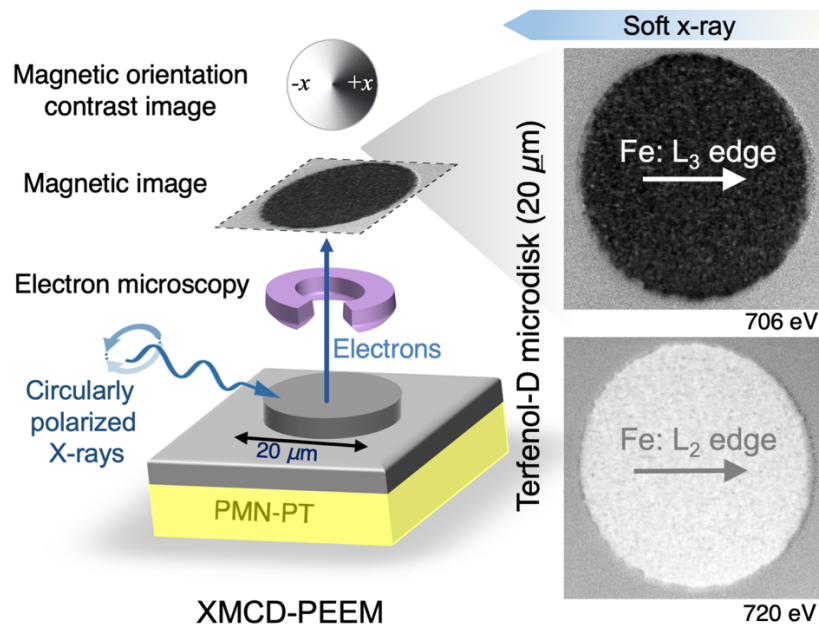


**Figure 5.7.** Fabrication and characterization of single-domain Terfenol-D microstructures. (a) Schematic of the SMArT device and microscope image showing magnetic bead capture (green) on Terfenol-D single-domain micropatterns on a PMN-PT substrate without the use of an external magnet. (b) Scanning electron microscope (SEM) image of a  $3\ \mu\text{m}$  Terfenol-D disk and (c) cross sectional cut by focused ion beam (FIB) showing (d) Terfenol-D microstructure on PMN-PT. (e) Magnetic force microscopy image of the  $3\ \mu\text{m}$  disk reveals a single domain configuration (f) that enables strong and precise magnetic trapping of magnetic beads on the magnetized poles (scale bar,  $1\ \mu\text{m}$ ). (g) Magnetic hysteresis loop of the Terfenol-D disks shows a large saturation magnetization of  $780\ \text{kA m}^{-1}$  and a coercivity of  $0.3\ \text{T}$ , as measured by SQUID. A large fraction of the magnetization is retained upon the removal of the saturation magnetic field.

#### 5.4.3 XMCD-PEEM imaging of single-domain and multi-domain magnetoelastic microstructures

We also used X-ray magnetic circular dichroism–photoemission electron microscopy (XMCD-PEEM) to image the magnetic domains at the absorption edges of individual elements in Terfenol-D microstructures (Figure 5.9a). According to the PEEM images taken at the Fe  $L_2$  and  $L_3$  absorption edges, a majority of the magnetic moments point in a single horizontal

direction, thus the entire disk functions collectively as a single domain (**Figure 5.8**). The black contrast indicates the local magnetization is pointing along the  $+x$  direction; the white indicates the magnetization is pointing in the  $-x$  direction. At Fe  $L_2$  and  $L_3$  absorption edges, the XMCD has opposite signs of magnetic dichroism and both rare earth elements Dy and Tb at  $M_5$  edge shows the same magnetic contrast as Fe at  $L_2$  edge, providing evidence that the Fe and rare-earth atoms (Tb and Dy) are antiferromagnetically coupled (**Figure 5.9a-d**) [65]. The PEEM images acquired at these two absorption edges show opposite magnetic contrast, confirming that the observed image contrast is magnetic-related and the structure exhibits a net single domain configuration.

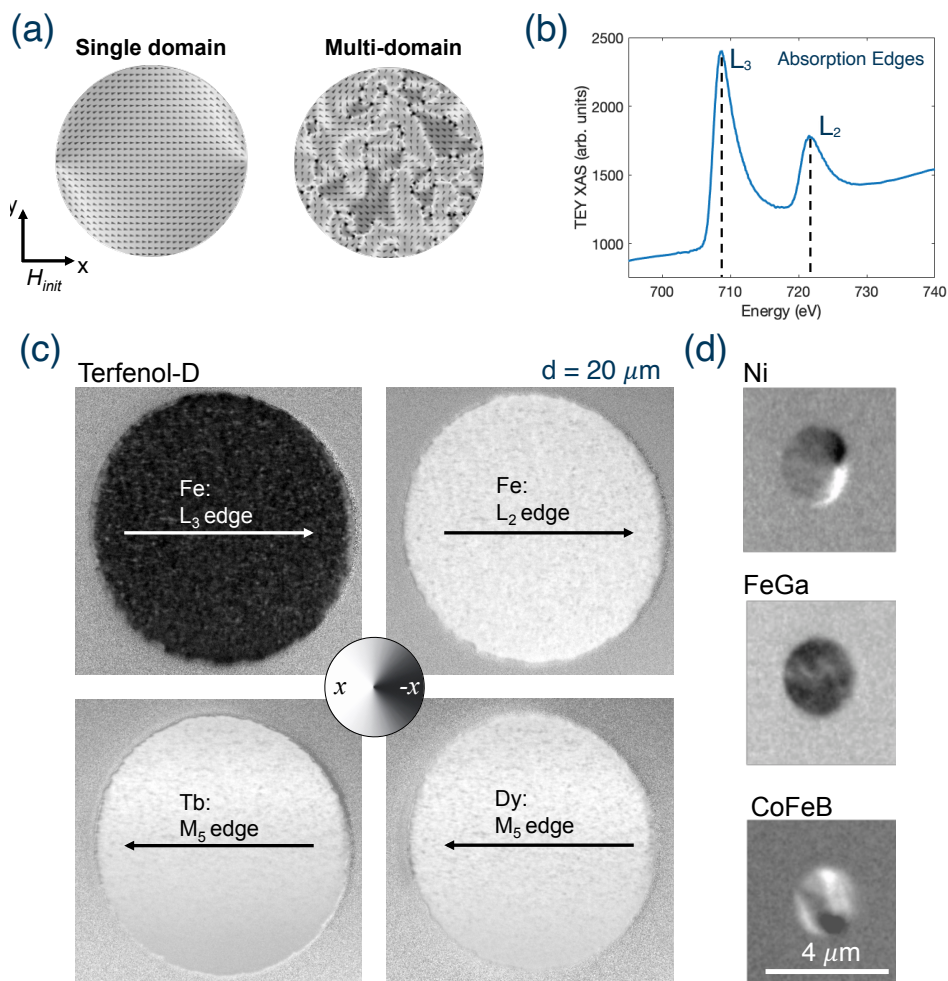


**Figure 5.8.** XMCD-PEEM imaging is used to image the magnetic domain state of Terfenol-D micromagnets of 20 μm in diameter. Magnetic contrast in a 20 μm disk at the elemental absorption edges of Fe, where white contrast indicates the magnetization is pointing in the  $-x$  direction and the black contrast indicates the magnetization is pointing in the  $+x$  direction. The opposite contrast of XMCD-PEEM images taken at two absorption edges of Fe confirms the effective single-domain magnetic configuration without an external magnetic field.

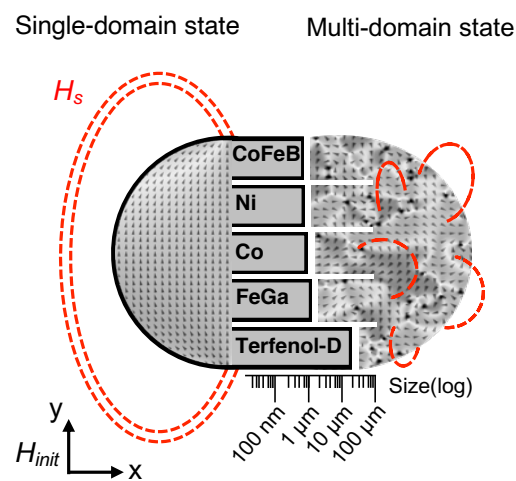
The experiment was conducted with PEEM-3 photoemission electron microscope at beamline 11.0.1.1. of the Advanced Light Source. Prior to imaging, the sample was loaded into the high vacuum etching chamber for Ar ion sputter cleaning to remove the 4 nm thick Ta capping layer and the top few nm of Terfenol-D. After sample preparation, the sample was transferred into the PEEM chamber at a pressure of  $3E-8$  Torr. The X-ray absorption spectrum (XAS) of Fe was examined to check if the sample surface was oxidized. In Figure 5.9b, the XAS taken with a photon energy between 695 and 730 eV did not show a multiplet signature which could indicate the presence of an oxidation state. The measured XAS matched that of unoxidized Fe, implying that the Ta capping layer protected well the reactive Terfenol-D microstructures. To image the magnetic domain at the Fe absorption edges, the X-ray energies were then tuned to the energies of Fe  $L_3$  (706.9 eV) and  $L_2$  (719.9 eV) absorption edges, respectively to excite the electron  $2p \rightarrow 3d$  transition with circularly polarized x-ray. The secondary electrons emitted from the magnetic sample were then accelerated from the sample to the objective lens via a strong electric field. After passing through a series of lens, the images taken at two x-ray polarities were recorded (Figure 5.9c).

The difference between the two XAS images is the XMCD-PEEM image showing the magnetic contrast. Due to the opposite sign of the spin-orbit coupling in  $2p_{3/2}$  and  $2p_{1/2}$  states, the XMCD effects at the two absorption energies will have opposite sign. It is thus expected that the magnetic contrasts be opposite to each other when taken at the two edges. Two images were taken for the same microstructure at each absorption edge energy by left and right circularly polarized x-rays. Pixel-by-pixel difference of the two images yielded the XMCD-PEEM image with magnetic contrast, revealing the ferromagnetic domain in the microstructure. XMCD images from Fe  $L_3$  and  $L_2$  edges, as shown in Figure 5.9c, with opposite contrast confirming the presence of an effective single magnetic domain up to  $20 \mu\text{m}$  in diameter. In

addition, the XMCD-PEEM images were also taken at the energy of Tb and Dy  $M_5$  edge to confirm the coupling behavior between the elements and ferrimagnetic behavior of Terfenol-D. Figure 5.9d shows the experimental results from PEEM with some of the most studied magnetoelastic microdisks patterned on PMN-PT. The microdisks of Ni, FeGa, and CoFeB revealed a multi-domain state at remanence with 15 nm in thickness and 2  $\mu\text{m}$  in diameter as a result of the energy competition between exchange energy and demagnetization energy. However, Terfenol-D showed an effective single domain at remanence state an order of magnitude larger than the rest. Thus, enabling Terfenol-D micromagnet programmability at the scale of a single cell with 10-20  $\mu\text{m}$  in diameter.



**Figure 5.9. XMCD-PEEM imaging of single domain and multi-domain magnetoelastic microstructures.** (a) An example of single domain and multi-domain states in disks at relaxation, simulated by mumax3 micromagnetics modeling, a 2D plane on the surface of microstructure [102]. (b) X-ray absorption spectrum (XAS) image of the magnetic domain at Fe absorption edges. The X-ray energies were then tuned to the energies of Fe  $L_3$  (706.9 eV) and  $L_2$  (719.9 eV) absorption edges, respectively to excite the electron  $2p \rightarrow 3d$  transition with circularly polarized x-ray demonstrated in the (c) XMCD-PEEM images of the magnetic contrast at the elemental absorption edges of all three elements (Tb, Dy, Fe) in the Terfenol-D confirm the single domain configuration in the  $20 \mu\text{m}$  Terfenol-D microstructures. The black contrast indicates the magnetization is pointing along the  $+x$  direction; the white indicates the magnetization is pointing in the  $-x$  direction. The entire disk functions nearly as a magnet with a single domain. (d) XMCD-PEEM images of Ni, FeGa, and CoFeB disks with  $2 \mu\text{m}$  in diameter grown on PMN-PT reveal multi-domain configurations at remanence.



**Figure 5.10. Comparison of length scales for single-domain states in different materials.** Single-domain states in magnetoelastic Terfenol-D at remanence are observed for order of magnitude higher length scales ( $20 \mu\text{m}$ ), while other magnetoelastic micromagnets (CoFeB, Ni, FeGa) switch to a multi-domain state around  $1\text{-}2 \mu\text{m}$  in diameter as observed in XMCD-PEEM after magnetic-field removal (**Figure 5.9**).



Therefore, in contrast to other soft magnetoelastic materials, the fabricated polycrystalline thin-film Terfenol-D shows anomalously large single-domain structures an order of magnitude larger in dimension than previously thought possible. More importantly for this application, the domain sizes are on par with single human cell sizes, which have diameter approximately  $10\ \mu\text{m}$  (illustration of comparison in **Figure 5.10**). This large single domain magnetoelastic structure discovery promises a new scale of micromagnetic capture that is sufficiently large to localize and capture a single cell without an externally applied magnetic field. In addition, the magnetoelastic properties of the single domain structures enable strain mediated multiferroic programmability for single-cell release following magnetic capture.

#### 5.4.4 *In-situ mapping of the magnetic domain capture regions via fluorescently-labeled magnetic beads (FMBs)*

While MFM and XMCD-PEEM are useful for characterizing magnetic domain configurations, they are limited in characterizing the magnetic capture performance of the initialized magnetic stray field ( $H_s$ ) in a viscous medium. Here, we developed an *in-situ* high-throughput approach to map and measure magnetic capture and release of magnetic materials using Terfenol-D multiferroic microstructures in a microfluidic channel in real-time.

PDMS microfluidic channels were fabricated with standard soft photolithography. A mixture of PDMS (Sylgard 184, Dow Corning, Midland, MI, USA) base and curing agent with 10:1 weight ratio was poured over the master wafer and degassed for one hour to remove air bubbles before cured at  $65\ ^\circ\text{C}$  overnight. The microchannels sizing (L) 1 cm x (W) 6 mm x (H)  $500\ \mu\text{m}$  were aligned to overarch the Terfenol-D micropatterns. Permanent bonding was formed by applying a thin layer of uncured PDMS on the interface followed by a 2-hour incubation at  $65\ ^\circ\text{C}$ . All surfaces were passivated with surfactant Pluronic F127 (Sigma-

Aldrich, St. Louis, MO) to prevent non-magnetic binding or adhesion. We used small fluorescently-labeled magnetic beads (FMB) (Spherotech, Libertyville, IL) of 0.5-1  $\mu\text{m}$  in diameter to increase the spatial resolution of the mapped magnetic capture regions.

After Terfenol-D micropatterns were magnetically initialized with a saturating field of  $H_{init} = 0.5$  T, a microchannel was bonded to the surface of PMN-PT substrate to introduce FMBs at a low flow rate (**Figure 5.11a** and **Figure 5.12a**).

To visualize FMB capture locations on Terfenol-D microstructures, we used an inverted microscope Nikon Ti-U (Nikon, Melville, NY) illuminated by a mercury arc lamp with 4 $\times$ -100 $\times$  objectives and recorded via a CCD Coolsnap HQ2 camera (Roper Scientific, Evry, France) (**Figure 5.12a**) [158].

Terfenol-D microstructures are detected and converted to grayscale where white pixels represent FMBs. With no external magnetic field applied, all of the initialized Terfenol-D microstructures captured suspended FMBs on the magnetized poles (**Figure 5.11b**). Micromagnetic trapping regions were mapped with high-resolution fluorescence imaging (0.16  $\mu\text{m}/\text{pixel}$ ) (**Figure 5.12b**). In addition to PMN-PT substrates, FMB capture were reproducible on Terfenol-D microstructures that were patterned on silicon and sapphire substrates (**Figure 5.12a**).

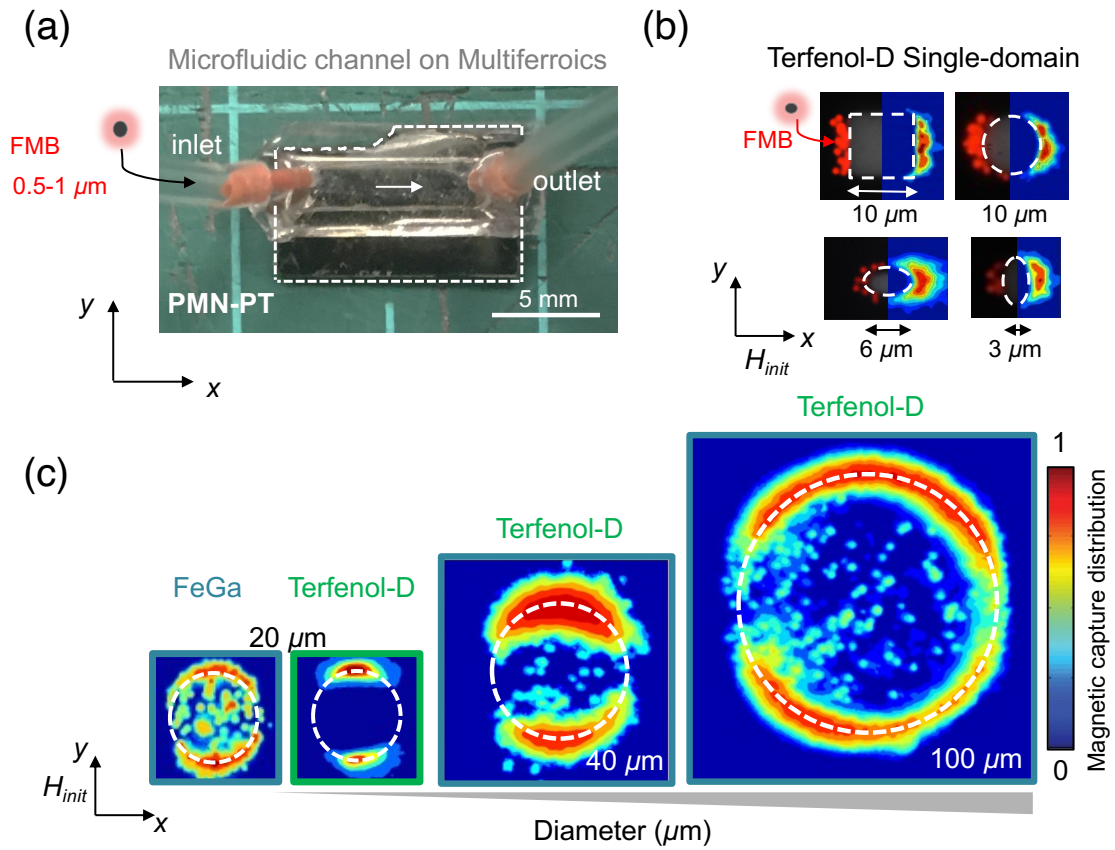
An in-house MATLAB code was developed to overlay images and normalize pixel intensity to generate a heat map of the bead distribution from a number ( $n$ ) of Terfenol-D microdisks in a large array (**Figure 5.12b**). Single-domain Terfenol-D microstructures consistently demonstrated uniform magnetic binding regions on the magnetized poles.

However, larger Terfenol-D microstructures demonstrated scattered magnetic bead binding regions between the magnetized poles (**Figure 5.12c**). Based on the heat map of the magnetic capture regions we were able to identify single-domain and multi-domain states in magnetoelastic microstructures.

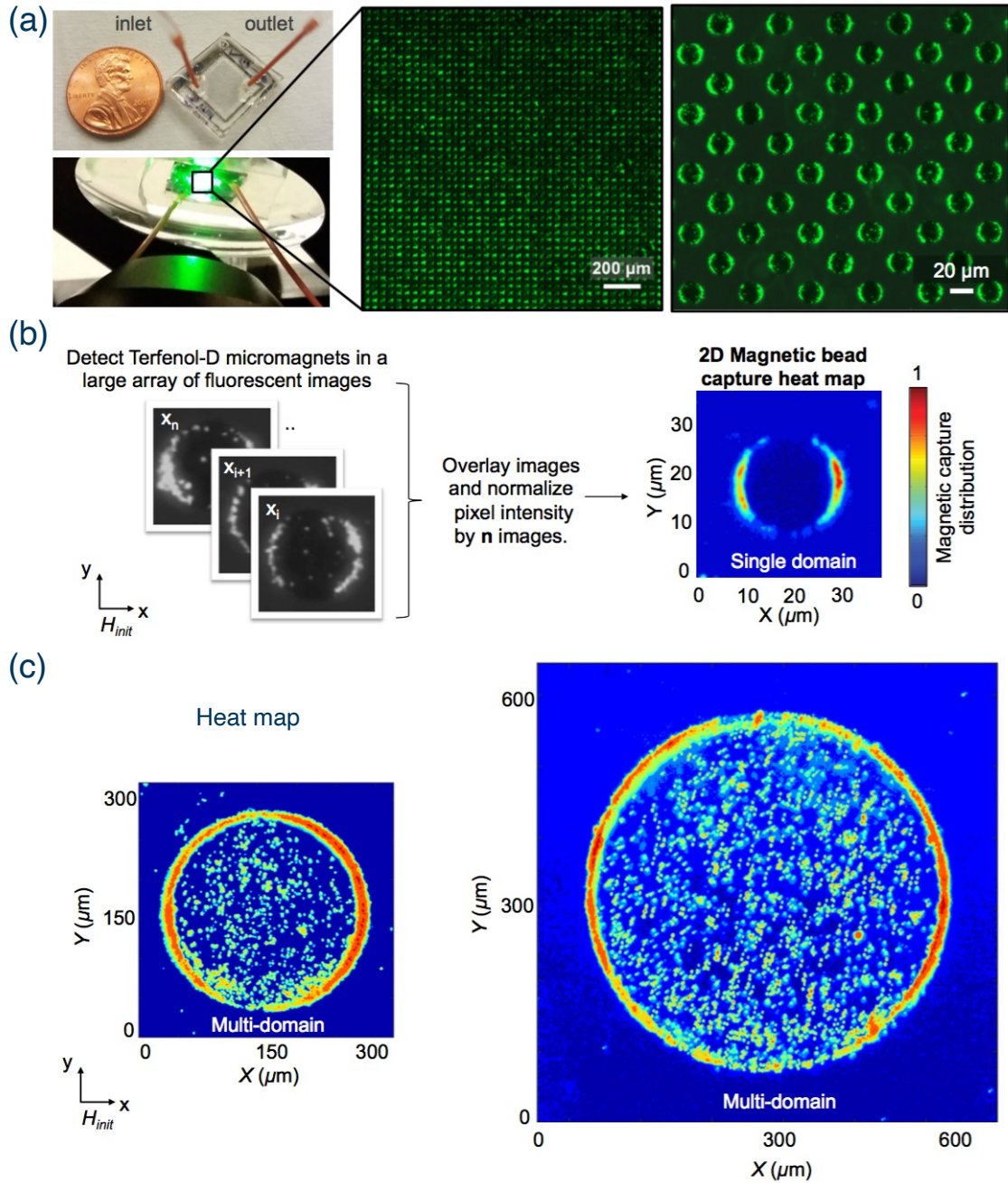
Analysis shows that Terfenol-D structures with a diameter ranging from 3 to 20  $\mu\text{m}$  in size exhibit precise FMB capture based on highly localized fields in the magnetically initialized single-domain poles regardless of their shape anisotropy, as demonstrated in previous PEEM results (Movie S2 [157]<sup>8</sup>). Interestingly, 20  $\mu\text{m}$  structures composed of FeGa, with the second largest magnetostriction among soft magnetic materials, result in multi-domain states (**Figure 5.11c**). Terfenol-D microdisks larger than 40  $\mu\text{m}$  begin to transition into a multi-domain state where FMBs were captured in a scattered pattern associated with the smaller domains' stray fields in between the magnetized poles (**Figure 5.11c** and **Figure 5.12b-c**). Although this method of FMB capture in fluid does not identify local magnetic spin orientation, it enables magnetic state characterization and magnetic bead capture evaluation for single-domain and multi-domain microstructures in a general microfluidic set-up.

---

<sup>8</sup> Supplementary Movie 2 [67] located at: <https://onlinelibrary.wiley.com/doi/full/10.1002/adma.202006651>.



**Figure 5.11.** Magnetic capture performance of single-domain Terfenol-D microstructure arrays. (a) Optical photograph of the microfluidic/multiferroic device (scale bar, 5 mm). (b) Mapping the magnetic capture distribution of fluorescently labeled magnetic beads on single-domain Terfenol-D microstructures. (c) FeGa structures of the same size transition into a multi-domain state, while Terfenol-D structures of less than 40  $\mu\text{m}$  in diameter remain single-domain.



**Figure 5.12.** High-throughput imaging of magnetic bead capture regions on magnetoelastic microstructures in a large array. (a) Microfluidic device integration on top of Terfenol-D micropatterns fabricated on sapphire (top) and silicon (bottom). Fluorescence microscopy images of the large array were acquired after introducing fluorescently labeled magnetic beads (FMB) to a number of  $n$  magnetoelastic microstructures. Uniform magnetic bead capture were observed across a massive array of magnetically initialized Terfenol-D single-domain microstructures. (b) Image analysis software was used to quantify measurements and

generate heatmaps of the magnetic bead capturing regions, where pixels with higher intensity correspond to the magnetic bead locations. Single-domain Terfenol-D microstructures demonstrated uniform magnetic bead capture locations on the magnetized poles. (c) Heat maps of multi-domain microstructures 250  $\mu\text{m}$  and 500  $\mu\text{m}$  in diameter demonstrated scattered bead capture locations between the magnetized dipoles.

## 5.5 Magnetic force landscape

To further investigate the magnetic force ( $F_m$ ) landscape of the mapped micromagnetic bead binding regions, we incrementally increased the counteracting hydrodynamic drag force defined by Faxén's correction to the Stokes drag force:

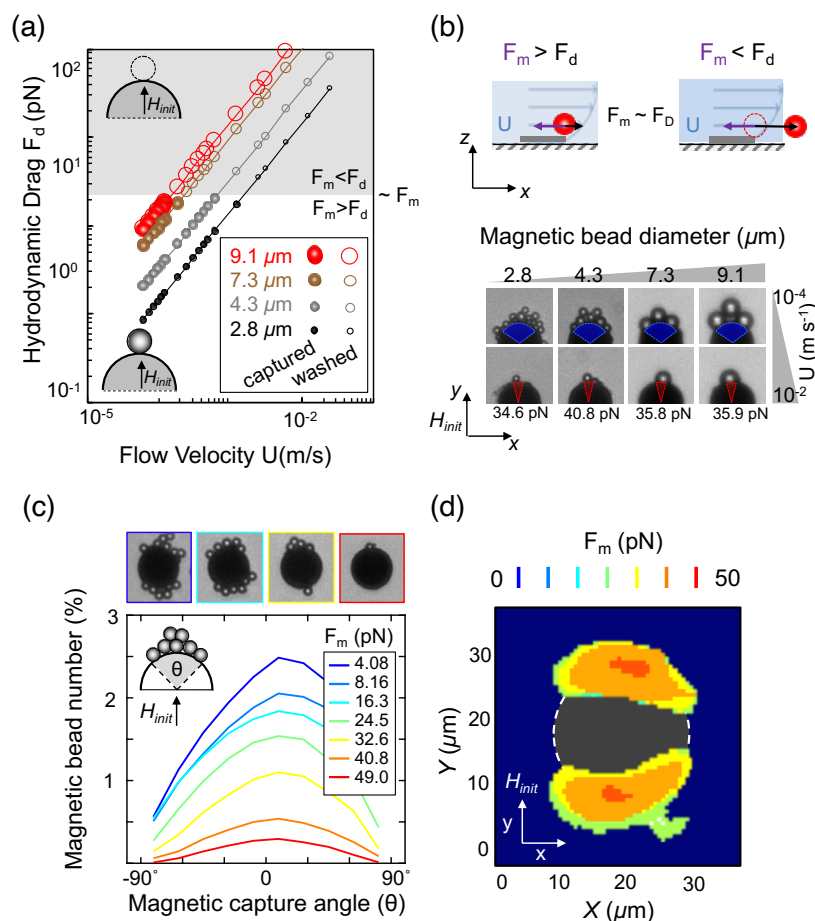
$$F_d = 6\pi\eta UD\xi \quad (5-1)$$

We explored a range of flow velocities ( $U = 0.001 - 0.1 \text{ m s}^{-1}$ ) and magnetic bead diameters ( $D = 2.8 - 9.1 \mu\text{m}$ ), where we kept the following two properties constant: fluid viscosity ( $\eta$ ), the near-surface correction factor ( $\xi$ ), which modifies Stokes drag for magnetic beads in close proximity to the surface of the Terfenol-D microstructures (see Section 5.5.1) [159], [160]. The drag force was then recalculated by 3D numerical simulation to include the Terfenol-D microdisk under the bead, which was in good agreement with the theoretical drag force (marked in solid lines) (**Figure 5.14**). Under continuous flow, we estimated the magnetic binding force by increasing the flow rate (and corresponding hydrodynamic drag force,  $F_d$ ) to the point where the drag force overcomes the magnetic capture force,  $F_m$ , causing release of the particle (**Figure 5.11b**, Movie S3 [157]<sup>9</sup>). Since the captured beads of different sizes are magnetically coated with similar thicknesses, larger magnetic beads were released at lower flow rates due to drag force linearly increasing with bead diameter (**Figure 5.14b** and c). However, all of the

---

<sup>9</sup> Supplementary Movie 3 [67] located at: <https://onlinelibrary.wiley.com/doi/full/10.1002/adma.202006651>

magnetically coated beads with different sizes were released at similar  $F_d \sim 36$  pN, which serves to validate the average magnetic binding force measurements across different micropatterns (**Figure 5.11b**, also see Section 5.5.1). Locally on the Terfenol-D microdisk, we mapped the magnetic force gradient as a function of the magnetization-easy axis angle ( $\theta$ ) where  $F_{m(\theta=0)} = 49$  pN (**Figure 5.11c**). As expected for single-domain Terfenol-D magnets, the stray field ( $H_s$ ) gradient decays away from the magnetization angle ( $\theta = 0^\circ$ ) in the 2D magnetic binding force map (**Figure 5.13a** and **Figure 5.15**). Also, a single bead can be captured and arrayed in each micromagnet to probe the strain-induced change in the easy axis angle.



**Figure 5.13.** (a) Optimized magnetic capture ( $F_m > F_d$ ) and release ( $F_m < F_d$ ) flow conditions to map the magnetic capture behavior of Terfenol-D micromagnets in-situ with different

magnetic beads sizes (2.8-9.1  $\mu\text{m}$ ) illustrated in bright field images in (b) with the governing forces: magnetic binding force  $F_m$  and hydrodynamic drag  $F_d$ . The solid lines are the theoretical Faxén drag correction force given by Eq (1). (c) The magnetic binding force ( $F_m$ ) is measured as a function of magnetization angle ( $\theta$ ) on single-domain Terfenol-D 20  $\mu\text{m}$  microdisks via a range of flow velocities to increase the spatial resolution of the 2D magnetic force map illustrated in (d).

### *5.5.1 In-situ high-throughput measurement of the magnetoelastic stray field ( $H_s$ ) magnetic binding force in a viscous medium*

To program magnetic capture and release of single-domain magnetoelastic microstructures in a large array in viscous medium, we need to have a measurable magnetic binding force for suspended magnetic beads in microchannels. Other conventional magnetic force measurement methods like fluxgate-MFM [161], scanning hall probe microscope (SHPM) [162] and scanning SQUID microscope achieve measurements at high spatial resolution (10 nm), but they are not scalable for a large array of thousands of magnetoelastic microstructures. In addition, these methods do not factor other non-magnetic external forces in viscous medium in a microfluidic set-up that compete with the magnetic binding force ( $F_m$ ) and influence magnetic bead capture/release. Therefore, we have developed an in-situ high-throughput method to achieve multiple measurements of the magnetic binding force of magnetically initialized Terfenol-D microstructures in large numbers using fluorescence imaging and image analysis methods described in Section 5.4.4.

Magnetic beads of different sizes were introduced to magnetically initialized Terfenol-D microstructures at different flow rates. Each flow rate exerts an external competing hydrodynamic drag force ( $F_d$ ) that counteracts the local magnetic binding force ( $F_m$ ) of the



Terfenol-D stray field ( $H_s$ ) across a large microstructure array. The magnetic bead interactions are tracked on many microstructures at the same time and same flow condition to get multiple measurements of the magnetic field landscape of each Terfenol-D microstructure. We observed three magnetic bead interactions with magnetized Terfenol-D microstructures, bead capture, tumbling and release. (i)- magnetic beads are captured or maintained on Terfenol-D microdisks when the magnetic binding force dominates over the hydrodynamic drag force ( $F_m > F_d$ ). (ii)- At higher flow rates, magnetic beads are released but then tumble or jump between Terfenol-D trapping regions. Given the temporary binding or release of the magnetic beads from the micromagnet, we assume the magnetic binding force and hydrodynamic drag are similar ( $F_m \sim F_d$ ) in this condition. (iii)- Lastly, when the hydrodynamic drag dominates over the magnetic binding force ( $F_m < F_d$ ), magnetic beads are released instantly with limited stray field ( $H_s$ ) influence from the downstream neighboring disks in the Terfenol-D micropattern array.

To calculate the counteracting hydrodynamic drag force in each condition, we first considered Faxén's correction to Stoke's drag force (eq 4-1), since the captured bead is located near the Terfenol-D surface under a Stokes flow regime with limited inertia [159], [160], [163]. The hydrodynamic drag ( $F_d$ ) was defined as

$$F_d = 6\pi\eta UD\xi, \quad (5-2)$$

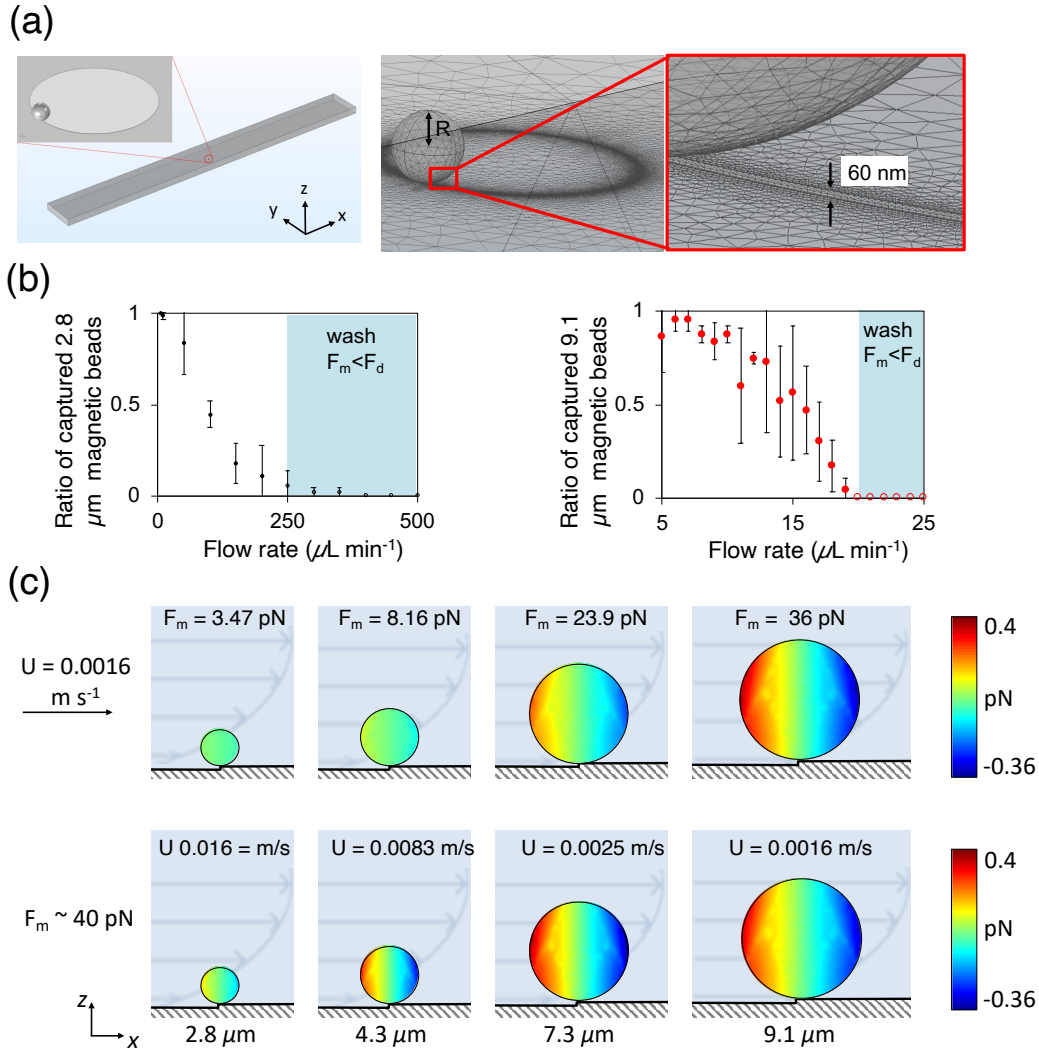
where  $D$  is the bead diameter,  $\eta$  is the viscosity of the suspending liquid,  $U$  is the average fluid velocity at the center of the bead, and  $\xi$  is the near surface correction factor defined by the power series expansion of the ratio of the bead radius ( $a$ ) to the distance from the wall surface ( $l$ ). In this study we used the three term power series of Faxén correction to the translational drag force parallel to the wall [52], [160], [164], defined as

$$F_d = \frac{6\pi\eta UD}{1 - \left(\frac{9}{16}\right)\left(\frac{a}{l}\right) + \left(\frac{1}{8}\right)\left(\frac{a}{l}\right)^3}, \quad (5-3)$$

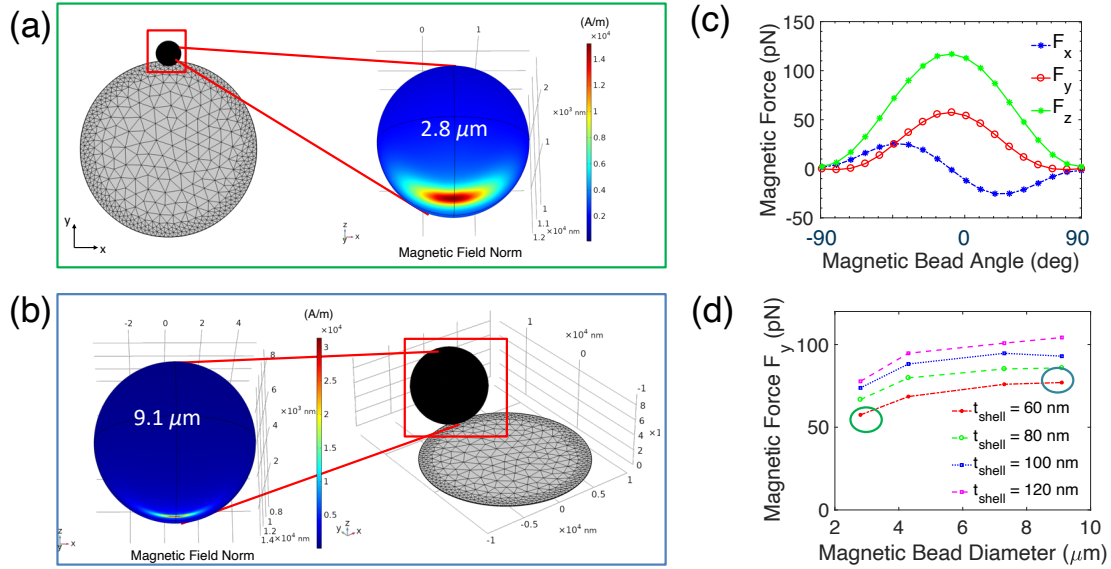
We then matched the theoretical drag force calculation with Finite Element Method (FEM) COMSOL Multiphysics software to simulate 3D fluid-particle interaction in the experimental conditions. The channel geometry was modeled using dimensions of the experimental channel (L: 10000  $\mu\text{m}$  x W: 1000  $\mu\text{m}$  x H: 200  $\mu\text{m}$ ), as illustrated in **Figure 5.14a**. A thin disk represents the Terfenol-D microdisk geometry in which the bead is trapped on its surface and 60 nm away from the substrate wall. A no-slip boundary condition is applied to the channel walls, microdisk, and bead. The inlet flow rate (5-2000  $\mu\text{L}/\text{min}$ ) and the particle diameter (2.8 - 9.1  $\mu\text{m}$ ) were set using a parametric sweep. The drag force on the particle was calculated by integrating the total stress over the surface of the particle in the x-axis parallel to the flow. **Figure 5.14b** shows the resulting total drag force ( $F_d$ ) parallel to the flow direction and opposite to the magnetic force ( $F_m$ ) at different flow velocities. To estimate the magnetic binding force ( $F_m$ ), we compared the calculation of ( $F_d$ ) of different size beads ( $D = 2.8, 4.5, 7.4$  and  $9.1 \mu\text{m}$ ) in the tumbling stage where ( $F_m \sim F_d$ ). The magnetically coated beads of different sizes were released at similar hydrodynamic drag force  $\sim 36$  pN, which validates the numerical drag force calculation method (**Figure 5.14c**).

To verify that similar magnetic forces ( $F_m$ ) are experienced by magnetically coated beads of different sizes, we used COMSOL Multiphysics software to simulate the magnetic force of captured beads on effective single domain Terfenol-D disk of 20  $\mu\text{m}$  in diameter initialized along the y-axis [165]. The magnetic beads used in the experiments consist of a polystyrene core and a thin magnetic iron oxide coating with thickness ranging from 60 to 120 nm, according to the vendor. We thus simulated magnetic beads of different sizes ( $D = 2.8, 4.5, 7.4$  and  $9.1 \mu\text{m}$ ) with four different iron oxide shell thicknesses ( $t_{\text{shell}} = 60, 80, 100, 120$  nm). The magnetic field norm distribution (A/m) on the surface of the magnetic beads decays toward zero several micrometers away from the disk (**Figure 5.15a-b**). This observation helps

explain why the magnetic forces experienced by the magnetic beads do not scale proportionally to the bead size, but are in a close range instead. As observed in the experiment, the total magnetic force experienced by the bead is at its largest when the bead is located at the magnetization angle ( $\theta = 90^\circ$ ) along the  $y$ -direction (**Figure 5.15b**). Thus we examine the magnetic forces along  $y$ -direction of the beads of different size and shell thickness combinations when they are positioned at the magnetization angle (**Figure 5.15c**). The in-plane magnetic force  $F_y$  of different magnetic bead sizes with the same magnetic shell thickness shows similar magnetic force from the magnetic disk. Since the exact magnetic shell thickness of the same type of beads may vary according to the vendor, the forces from the simulation are a-proof-of-concept rather than an accurate reflection of the exact magnetic forces experience by individual beads. Therefore, the in-situ high-throughput experimental measurement method uses one type of magnetically coated beads to average the magnetic binding force from thousands of Terfenol-D microstructures.



**Figure 5.14.** High-throughput in-situ measurement of the magnetic binding force for Terfenol-D microstructures in a large array. (a) Hydrodynamic drag force for different bead diameters were computed numerically using experimental flow rates, microfluidic channel dimensions and the Terfenol-D microstructure geometry. (b) The fraction of magnetic beads released increases at higher flow rates. (c) Under the same flow rates, 2.8, 4.3, 7.3 and 9.1  $\mu\text{m}$  beads experience different hydrodynamic drag forces. At the magnetic bead release flow condition, the hydrodynamic drag force measurement is estimated to equal the magnetic binding force  $\sim 36 \text{ pN}$  for different bead diameters.

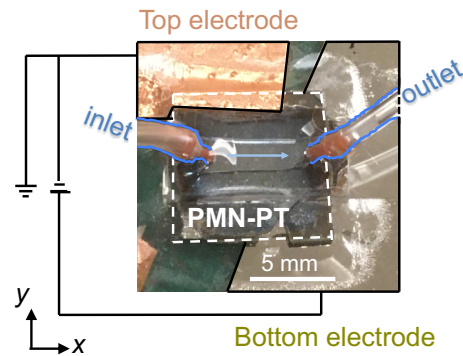


**Figure 5.15.** (a)-(b) Surface distribution of magnetic field norm of both 2.8  $\mu\text{m}$  and 9.1  $\mu\text{m}$  beads with a magnetic shell thickness of 60 nm. The magnetic field norm decays toward zero a few  $\mu\text{m}$  away from the beads. (c) Angle dependence of magnetic force components on the 2.8  $\mu\text{m}$  bead with shell thickness of 60 nm. The magnitude of total magnetic force reaches the highest when the bead is located along the magnetization  $y$ -axis ( $\theta = 0^\circ$ ). Here  $F_y$  and  $F_z$  are pointing in the  $-y$  and  $-z$  directions. (c) Finite Element simulation result of magnetic force  $F_y$  on the magnetically coated beads with different combinations of bead diameter and magnetic coat thickness. The beads are located at the magnetization axis, as shown in the schematics, corresponding to the experimental observation.

## 5.6 Electric-field-driven single cell release from Terfenol-D microdisk

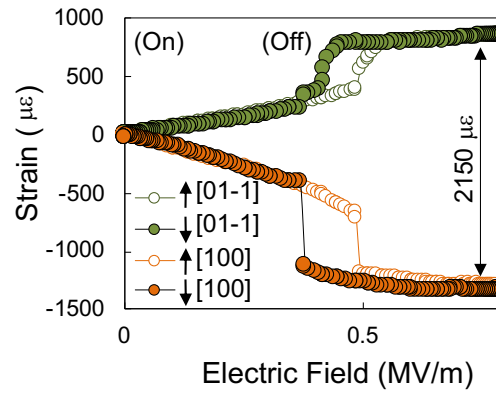
Our results demonstrate Terfenol-D magnetoelastic coupling leads to localized magnetic capture in single-domain micromagnets. We further investigated magnetoelastic coupling with voltage-induced microstrain to reprogram the micromagnetic Terfenol-D state for magnetic release. We imaged in real-time the microfluidic/multiferroic device to investigate the magnetic bead capture and release behavior before and after applying a voltage induced

strain to PMN-PT [011]-cut piezoelectric substrates in the optimized stable flow capture condition (**Figure 5.16**. Microfluidic/Multiferroic SMArT device set up., Movie S4 [157], and Section 5.6.1).

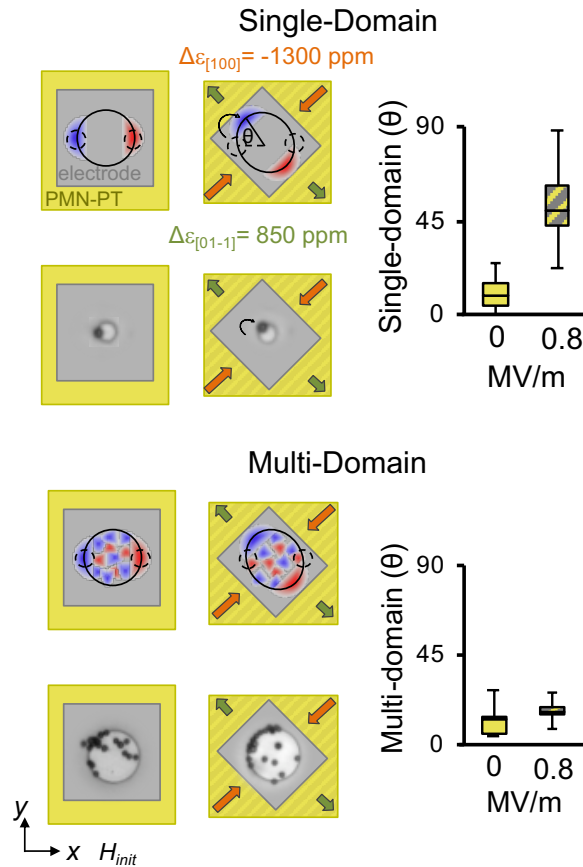


**Figure 5.16.** Microfluidic/Multiferroic SMArT device set up. The blue arrow indicates the flow direction of the microfluid in the channel.

An electric field of  $0.8 \text{ MV m}^{-1}$  induces a compressive strain of 1300 ppm along the [100] direction and a tensile strain of 850 ppm along [01-1] direction (**Figure 5.17**). The resulting differential strain of 2150 ppm creates a new minimum in the energy landscape, rotating the direction of magnetization in the Terfenol-D disk (**Figure 5.20**). Consequently, the trapping angle for the magnetic bead shifts by  $\Delta\theta = 40^\circ$  after applying the electric field (**Figure 5.18**). Originally, the bead is trapped in a direction at an angle  $45^\circ$  relative to both [01-1] and [100] strain axis, as indicated in Figure 4d. The electric-field induced easy-axis along [01-1] direction results in this shift in bead capture location. However, in multi-domain microstructures, no substantial change in the magnetic reorientation was observed after applying strain due to the heterogeneous magnetic capture regions (**Figure 5.20**).



**Figure 5.17.** Strain response of the PMN-PT substrate along [100] and [01-1] crystallographic directions with respect to the out-of-plane electric field, measured by a biaxial strain gauge. Applying a 0.8 MV/m electric field induces compressive strain of 1300 ppm along the [100] direction and tensile strain of 850 ppm along [011], illustrated in the PMN-PT crystal structure in **Figure 1.9**.

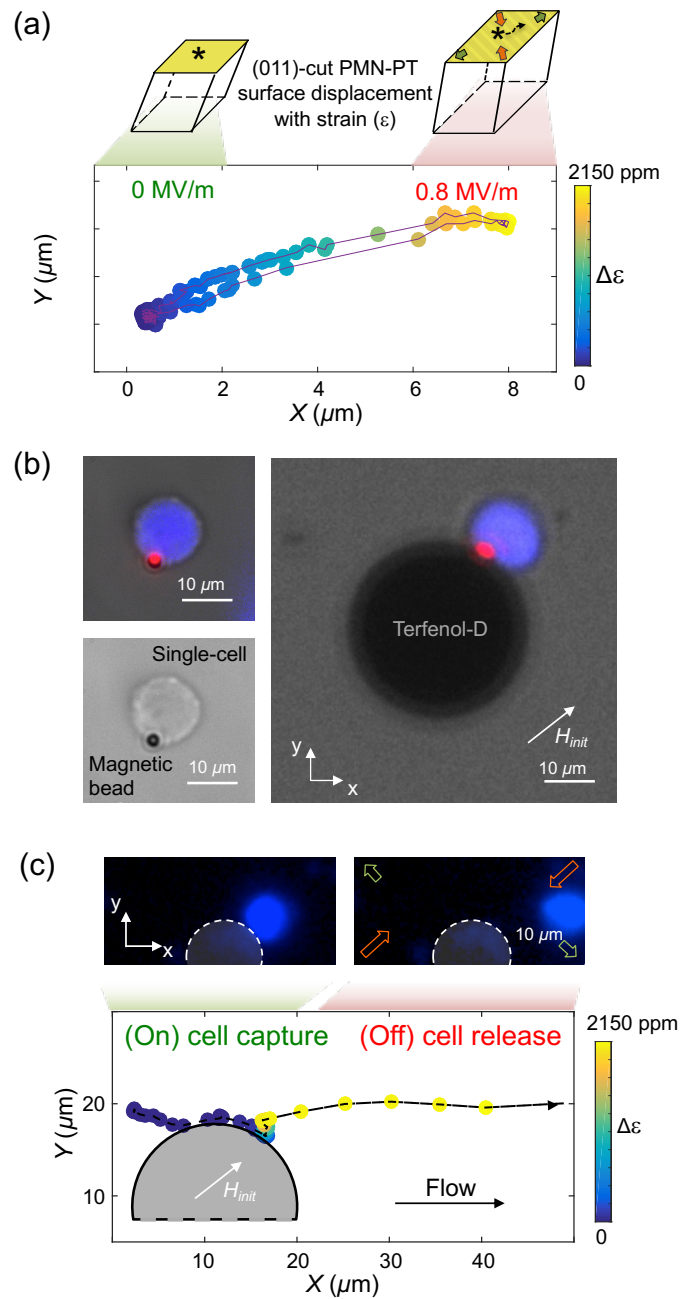


**Figure 5.18.** A total strain of 2150 ppm induced by an electric field of 0.8 MV/m perturbs the single domain state due to magnetoelastic coupling, reorients the magnetic domain  $\sim 40$  degrees to the electrically-induced easy axis (along [01-1] direction). In contrast, multi-domains rearrange in a manner that has little impact on the net direction of magnetization.

Leveraging this magnetization reorientation shift, magnetic beads and magnetically labeled single cells were captured on single-domain Terfenol-D microdisks then subsequently released after applying a voltage induced strain (**Figure 5.19b-c** and Movie S5 [157]). We tracked the displacement of the PMN-PT surface as a function of the voltage-induced strain to proportionally assign the strain value while recording the capture/release of magnetically-labeled cells (**Figure 5.19a** and Section 5.6.1). As the magnetic domain stray field reorients towards the newly strain-induced easy axis ([01-1] direction of PMN-PT) at  $\Delta\varepsilon = 2150$  ppm



(marked in yellow), the cells were released due to the decline of the stray magnetic field  $x$ -component counteracting the drag force, which is parallel to the flow direction. Trapped cells in the device were viable for cell culture and expansion for downstream applications (**Figure 5.21**).

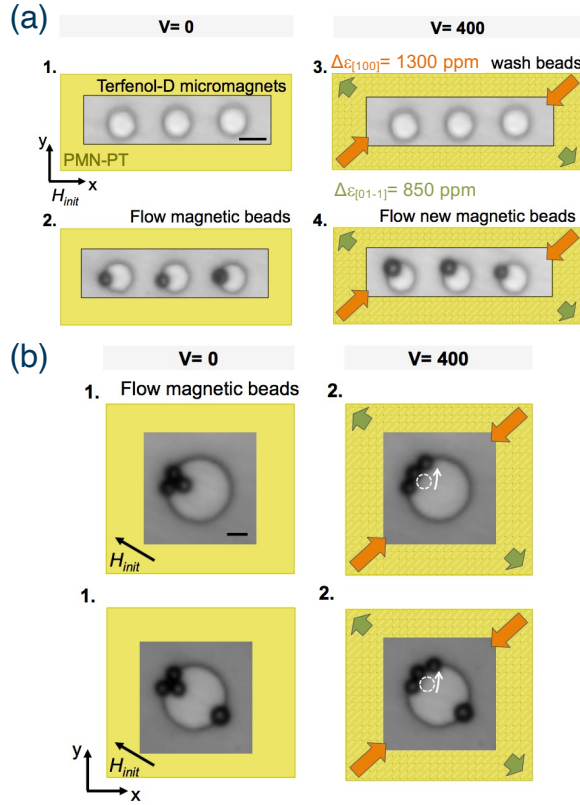


**Figure 5.19.** (a) Real-time tracking of the displacement on the surface due to strain in the PMN-PT substrate (reference location labeled with \*). (b) Bright field and fluorescent images

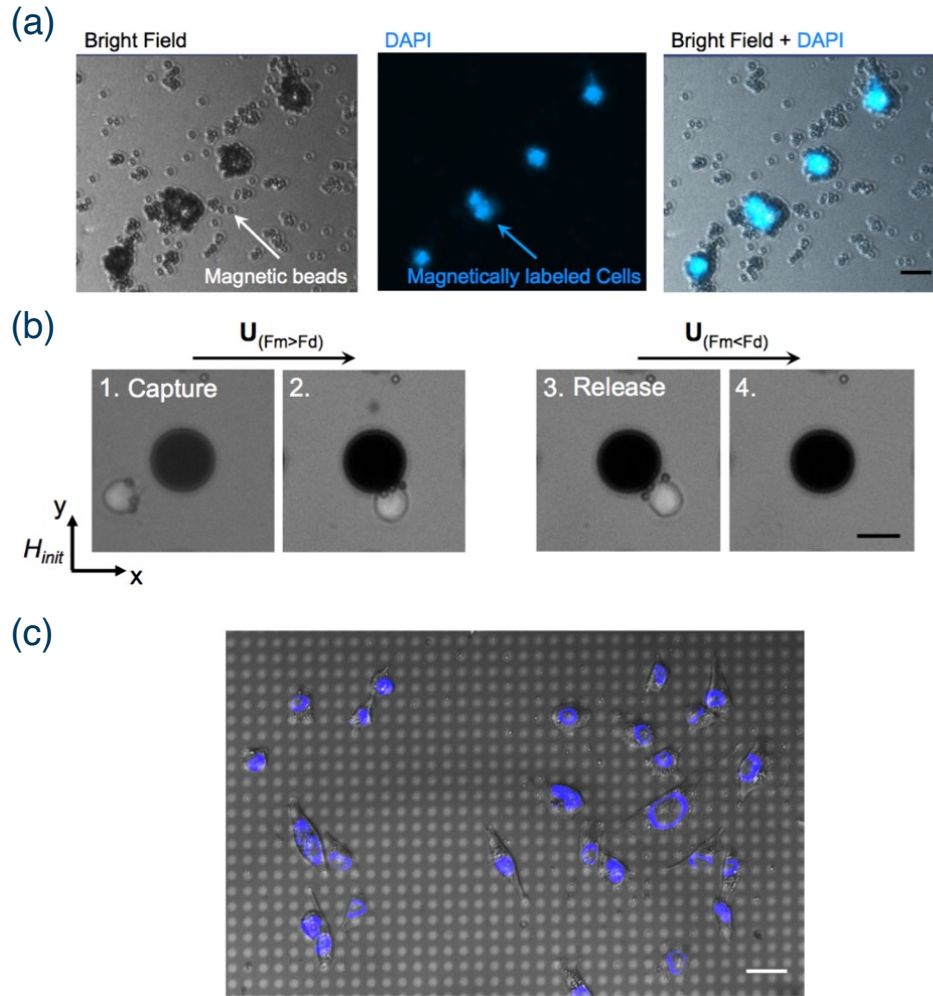
of a magnetically labeled and fluorescently labeled single cell. (c) When subjected to electrically-induced strain, individual magnetically labeled single cells were released from the Terfenol-D micromagnets to the outlet of the microchannel.

### 5.6.1 *Effect of strain on Terfenol-D microstructures and cells*

To study the effect of strain on Terfenol-D single-domain and multi-domain microstructures, we tracked the magnetic bead capture regions before and after applying strain on the PMN-PT substrate. **Figure 5.20** demonstrates the experimental steps of using magnetic beads to locate the newly induced magnetic easy axis angle after applying strain. In addition, we noticed beads attached near the Terfenol-D microdisks dislocate to a new magnetization angle after applying strain. To track in real-time the release of captured magnetically labeled cells associated with strain, we tracked the movement of the PMN-PT surface that is near a Terfenol-D microstructure (labeled with \*) while applying voltage. We used stationary beads on the PMN-PT surface that are not attached to the Terfenol-D microstructures for the image analysis tracking code. The maximum strain value from **Figure 5.17** was used to correspond to the PMN-PT maximum surface displacement. Then the PMN-PT displacement values in between were assigned proportionally to the strain values. The bead translated an average distance of  $6.5 \mu\text{m}$  with the PMN-PT surface from 0 ppm (blue) to maximum strain of 2150 ppm (yellow) (**Figure 5.19a**). Measuring the PMN-PT surface displacement while recording magnetically labeled cells capture and release events enabled synchronization of the strain with shift in magnetization and resulting cell release.



**Figure 5.20.** Experimental procedure for tracking the change in magnetization pole reorientation of Terfenol-D microstructures after applying strain on PMN-PT substrate (yellow). (a) First, we image the Terfenol-D microstructures before introducing beads or applying beads or strain. Second, we flow beads in a microfluidic channel on the PMN-PT substrate and image the Terfenol-D microstructures. Third, we wash away the beads then apply voltage-induced strain on the PMN-PT substrate. Fourth, we flow new magnetic beads and image their locations after strain. We noticed the beads settle on a newly induced magnetic easy axis in the Terfenol-D microstructure. (b) We repeat the same procedure but without the washing step (3) on larger microstructures that capture more than one bead on their magnetized pole. We noticed beads that are not directly attached to the magnetized pole dislocate to the new magnetization angle after applying strain. Scale bar,  $5 \mu\text{m}$ .



**Figure 5.21.** Magnetically labeled cell preparation for capture and release via voltage induced strain. (a) Fluorescently stained cells coated with magnetic beads are imaged with bright field and fluorescence microscopy. (b) Microchannel flow conditions were optimized for cell capture at a flow velocity  $U_{(F_m > F_d)}$  and release at  $U_{(F_m < F_d)}$  on Terfenol-D microstructures. (c) Terfenol-D microstructures were cytocompatible for cell growth and expansion for downstream applications. Scale bar, 20  $\mu\text{m}$ .

Jurkat cells (average diameter  $\sim 15 \mu\text{m}$ ) were cultured in RPMI 1640 medium supplemented with 10% (v/v) fetal bovine serum and 1% penicillin-streptomycin and maintained  $\sim 10^6$  cells/mL density. To magnetically label Jurkat cells, streptavidin-coated magnetic beads (Spherotech, Libertyville, IL) were washed with PBS and conjugated with 5

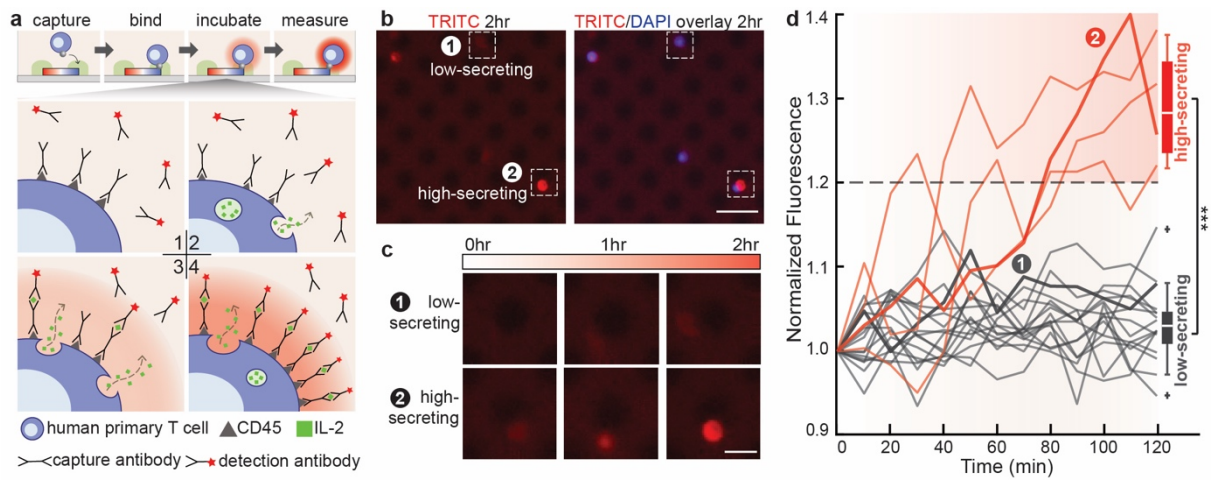
$\mu\text{g/mL}$  biotin anti-human CD45 Antibody (clone HI130: #304003; BioLegend) before added to a suspension of Jurkat cells at a 1:10 cell to bead ratio in culture medium for labeling. The labeling was performed at room temperature with gentle mixing for an hour. Magnetically labeled Jurkat cells were captured on the Terfenol-D single-domain microstructures under a low flow velocity condition of  $5 \mu\text{L/min}$  where  $F_d < 36 \text{ pN}$ . Single magnetically labeled cells remained captured on the Terfenol-D microdisk until strain was applied with an electric field of  $0.8 \text{ MV/m}$  as discussed elsewhere. To test Terfenol-D cytocompatibility for adherent cells, we incubated MCF-7 cells on Terfenol-D microstructures at  $37^\circ\text{C}$  in a humidified atmosphere with  $5\% \text{ CO}_2$  for a week. Cells grew and expanded on the surface of the Terfenol-D microstructures (**Figure 5.21**).

### 5.7 Time-dependent measurement of single-cell secretion

We further explored applying Terfenol-D micromagnet arrays to dynamic single-cell phenotyping assays by evaluating functional and time-dependent cell properties, specifically the heterogeneous secretion of interleukin-2 (IL-2), a critical cytokine signaling molecule that regulates T cell proliferation and differentiation [166], from single primary human T cells. An immunoaffinity assay (**Figure 5.22a**) was performed to allow a secreted IL-2 molecule immobilized onto the cell membrane via a capture antibody fused against both IL-2 and the CD45 cell surface biomarker. The captured IL-2 subsequently bind to an anti-IL-2 detection antibody labeled with PE fluorophores. As IL-2 molecules are continuously secreted over a 2-hour incubation, ample PE-labeled detection antibodies are enriched on the cell membrane, forming a ring-shaped fluorescent signal (**Figure 5.22b-c**) whose intensity indicates the cell's secretion level. By tracking the intensity of the fluorescent secretion signals on an array of magnetically trapped single T cells over 2 hours (**Figure 5.22d**), we observed the divergence of two sub-populations of T cells based on their secretion levels ( $p < 0.001$ ), the high-secreting

cells reaching a  $29.1 \pm 7.0\%$  increase of signal intensity at the end of 2 hours ( $n_1=4$ ), while the low-secreting cells averaging a  $3.3 \pm 4.5\%$  signal increase ( $n_2=17$ ).

For a proof-of-concept demonstration of dynamic cell profiling on Terfenol-D micromagnet arrays, we performed an adapted IL-2 Secretion Assay (Miltenyi Biotec, 130-090-487) on a trapped array of human primary T cells (average diameter  $\sim 8 \mu\text{m}$ ). The human primary T cells were isolated from whole blood using EasySep™ Human T Cell Isolation Kit (STEMCELL Technologies, 17951) and stimulated with ImmunoCult™ Human CD3/CD28 T Cell Activator (STEMCELL Technologies, 10971) when needed. The cell culture was maintained at  $\sim 10^6/\text{mL}$  in RPMI 1640 medium supplemented with 10% (v/v) fetal bovine serum, 1% penicillin-streptomycin, and 50 U/mL IL-2. Prior to experiment, the human primary T cells were activated for cytokine production by 25 ng/mL PMA (Sigma-Aldrich, P1585) and 1  $\mu\text{g}/\text{mL}$  Ionomycin (Sigma-Aldrich, 407951) for 6 hours at  $10^7$  cells/mL. The activated cells were thoroughly washed, stained with Hoechst to locate nuclei, labeled with magnetic beads and IL-2 Catch Reagent following vendor's protocol. The labeled cells were resuspended at  $\sim 10^6/\text{mL}$  in RPMI 1640 containing 0.1% (v/v) phycoerythrin (PE) labeled IL-2 Detection Antibody, and immediately injected into the microfluidic channel of a SMArT device staged on a Nikon Ti-E fluorescence microscope. A set of DAPI (100 ms exposure) and TRITC (1 second exposure) images were taken every 10 minutes for 2 hours and analyzed using Image J. Magnetically trapped cells were located by matching the nuclei staining in DAPI with the Terfenol-D microdisk patterns, and their secretion signals were quantified by the maximum TRITC fluorescence intensity within each area of interest.



**Figure 5.22. Time-dependent secretion measurement of magnetically captured single cells.** (a) Schematics of the adapted immunoaffinity assay to measure IL-2 secretion from single human primary T cells. (b) Fluorescent images of IL-2 secretion signals (TRITC) from human primary T cells (DAPI) at the end of a 2-hour incubation (scale bar, 50  $\mu\text{m}$ ). One representative low-secreting cell (cell ①) and one high-secreting cell (cell ②) are identified, and their secretion signals at 0, 1 and 2 hours are magnified in (c) (scale bar, 20  $\mu\text{m}$ ). (d) Single-cell IL-2 secretion signals tracked every 10 minutes for 2 hours. Sub-populations of high-secreting cells ( $n_1 = 4$ ) are characterized from low-secreting cells ( $n_2 = 17$ ) by a threshold of normalized fluorescence  $> 1.20$  at the end of 2 hours. The highlighted lines ① and ② signify the time-dependent IL-2 secretion signals from the two identified cells in (b) and (c). \*\*\* $P < 0.001$  using two-tailed Student's t-test.

## 5.8 Concluding Remarks

Smart programmable single-domain magnetoelastic materials provide an autonomous and tunable micromagnetic platform for single-cell manipulation. Coupling strain-mediated multiferroic control into these platforms via voltage-induced strain enables high-throughput single-cell separation and enrichment of specific magnetically labeled cells across an electronically addressable array. Therefore, multiferroics present an opportunity to automate

single-cell selection based on functional and time-dependent properties, which remains a fundamental challenge for biotechnology and the development of optimal cell therapies. Furthermore, such array-addressable control of magnetic components could be used in practical applications such as magnetoelectric storage devices [167], magnetic sensors [168], and voltage-tunable RF/microwave devices [18], [169].



## **Chapter 6    Localized Strain Profile in Surface Electrode Array<sup>10</sup>**

### **6.1 Patterned Surface Electrodes and Induced-Strain**

Using voltage-generated strain to control magnetism in miniaturized devices is an energy-efficient alternative to the conventional current-driven approach due to the Joule heating suppression. Such devices are based on a class of materials--magnetolectric multiferroics. Recent advances in multiferroic magnetolectric composites [105], [170]–[172] have brought us closer to applying fundamental research discoveries to a broad range of applications, including data-storage devices [150], probabilistic computing platforms [15], [144], [173], voltage-tunable radio-frequency microwave devices [174],[169], artificial neural networks [175],[176], and microfluidic particle and cell sorting platforms [177]. For multiferroic heterostructures, understanding the strain coupled into the magnetoelastic structures is necessary, especially any variation in strain with length scales similar to the magnetic element size.

To date, researchers have extensively studied the electric-field control of magnetism in a variety of mechanically-coupled composite multiferroic heterostructures, where strain from a piezoelectric material [67], [107], [158] governs magnetism in an adjacent magnetoelastic material [48], [178], [179] due to the converse magnetolectric effect. To drive a desirable magnetoelastic response, instead of optimizing the material properties of magnetoelastic and piezoelectric constituents, one could use patterned surface electrodes to engineer the strain.

---

<sup>10</sup> This chapter is a slightly modified version of “Localized strain profile in surface electrode array for programmable composite multiferroic devices” published in Applied Physics Letters and has been reproduced here with the permission of the copyright holder.

With surface electrodes, the in-plane strain is generated locally between the electrodes, with the strain profile defined by the electrodes' location and orientation.

In this chapter, we focus on examining the induced strain distribution in the single-crystal piezoelectric  $\text{Pb}(\text{Mg}_{1/3}\text{Nb}_{2/3})\text{O}_3]_{0.69}\text{-}[\text{PbTiO}_3]_{0.31}$  (PMN-PT) with surface electrodes. As opposed to piezoelectrics fully covered with electrodes, which rely on piezoelectric coefficients  $d_{31}$ ,  $d_{32}$  for in-plane anisotropic strain [11], [51], [180], the surface electrode design can provide more freedom in strain control due to the adjustability of the electrode arrangement. This work could serve as a roadmap/reference for designing compact, programmable electrode arrays for multiferroics applications.

Many multiferroic devices based on PMN-PT adopt a design that uses a single pair of electrodes across the entire surface. In particular, (011)-cut PMN-PT generates in-plane anisotropic strain to alter the magnetic domain in the coupled magnetic layer [181]. A tensile strain is induced along [01-1], and a compressive strain is generated along [100]. (001)-cut PMN-PT is another popular substrate choice, especially when the magnetic films require epitaxial growth, such as  $\text{La}_{0.7}\text{Sr}_{0.3}\text{MnO}_3$  (LSMO) [7], [22], [23], [182], [183] or  $\text{Fe}_{(1-x)}\text{Ga}_x$  alloys [184], with a lattice match to PMN-PT [185]. With an applied electric field, the substrate typically undergoes isotropic, in-plane compressive strain [186]. With this approach of a single pair of electrodes across the entire substrate, there is little control over the direction of strain, and no ability to control strain for different magnetic elements individually.

Alternatively, surface electrodes can be used to engineer the direction and magnitude of strain with local control. Surface electrode pairs patterned on piezoelectrics (PMN-PT [50], [73],  $\text{Ba}_{1-x}\text{Sr}_x\text{TiO}_3$  (BST) [187], PZT [175]) have shown local magnetoelectric control of Ni

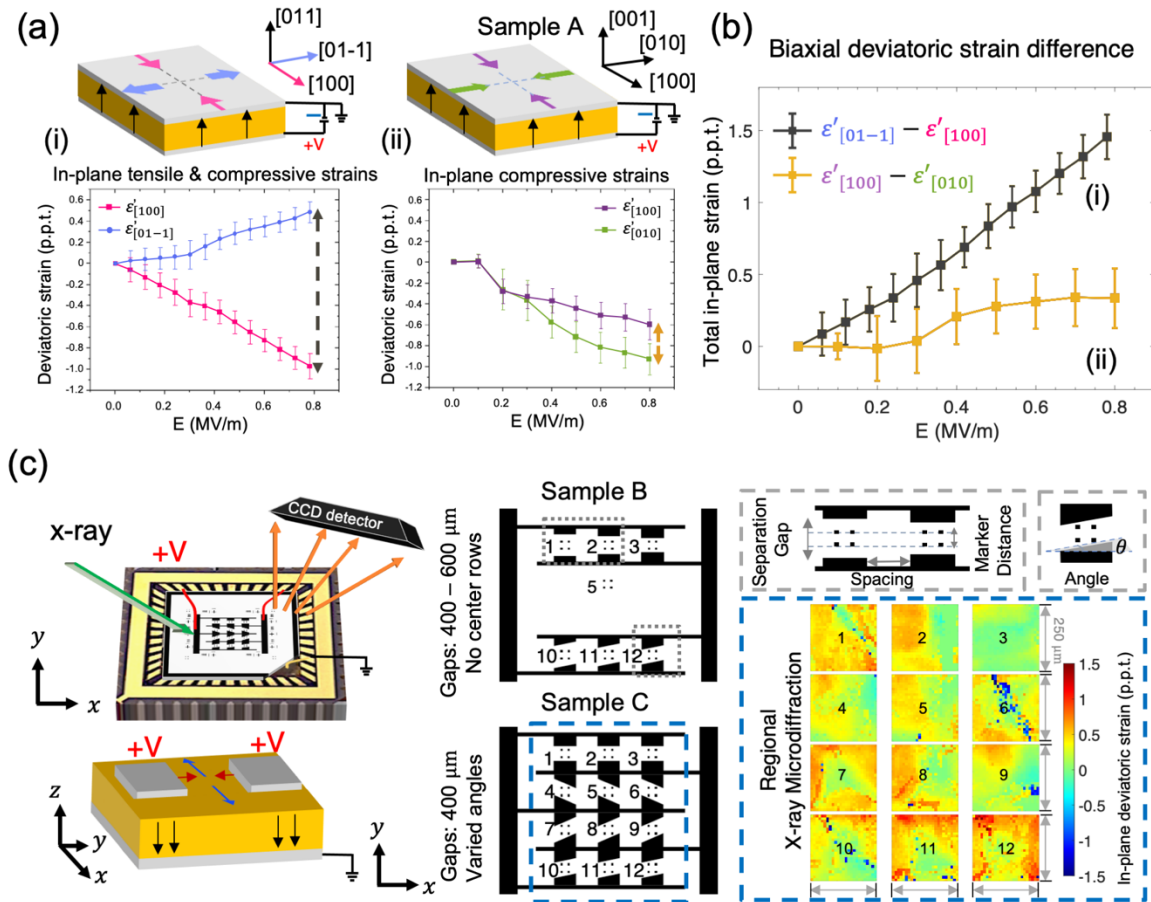
or FeGa elements [52], [64], [188]. These device prototypes have provided experimental evidence on the local strain-mediated behavior of a few micromagnets patterned between a set of electrode pairs a few hundreds of microns apart.

So far, little has been done to characterize the impact of neighboring electrode pairs on strain experimentally. In this work, we focus on characterizing the deviatoric strain (more detail in Section 2.2.2) distribution between surface electrode pairs arranged in arrays on (001)-cut PMN-PT using synchrotron-based scanning X-ray microdiffraction [189]. The goal is to understand the role of electrode arrangement on the local strain distribution between the electrodes, which will provide insight into how dense electrode arrays can be packed while maintaining control of each magnetic element. We analyze the average local axial deviatoric strain along [100] and [010] directions, in the region between the surface electrode pairs. The local strain is compared with the axial strain generated by the parallel plate electrodes, which is expected to be compressive in-plane [78]. Furthermore, we examine the effect on strain from electrode pair arrangement and interactions among neighboring surface electrode pairs. Finite element simulations are used to interpret the varied regional strain behavior better.

## 6.2 Single crystal PMN-PT substrates with different electrode configurations

In the experiment, the three (001)-cut PMN-PT samples ( $1\text{ cm} \times 1\text{ cm} \times 500\text{ }\mu\text{m}$  (thickness)), TRS Technologies, Inc., State College, PA, USA) under investigation are Sample A with parallel plate electrodes as a reference (**Figure 6.1a**), Samples B and C with 6 and 12 surface electrode pairs, respectively (**Figure 6.1c**). All of the electrodes consist of a 5 nm Ti and a 50 nm Pt layer. In Sample A, both the top and bottom surfaces are uniformly covered by an electrode. For Sample B and C, arrays of electrode pairs are patterned on the top surface,

while the bottom surface is covered uniformly by an electrode. The samples are wire bonded to leadless chip carriers (**Figure 6.1c**) before being mounted on to a printed circuit board.

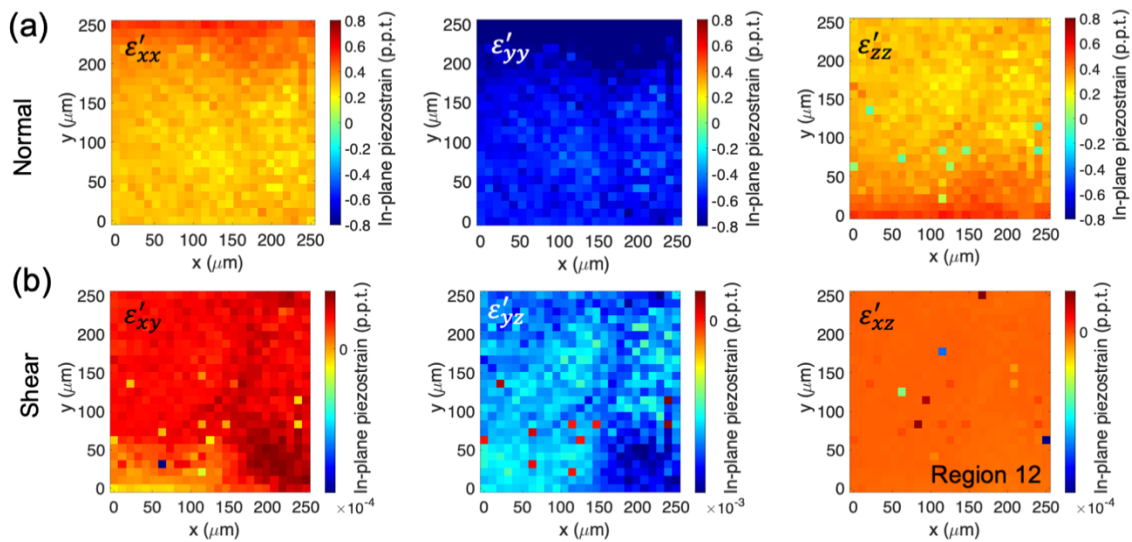


**Figure 6.1.** (a) Schematics of PMN-PT with parallel-plate electrodes. (i) (top) (011)-cut exhibits a strong in-plane anisotropic strain; (bottom) X-ray microdiffraction results confirm the presence of a negative compressive deviatoric strain along [100] and a positive tensile deviatoric strain along [01-1] when voltage is applied. (ii) (top) (001)-cut with in-plane compressive strains when voltage is applied; (bottom) X-ray microdiffraction results show compressive deviatoric strain along both [100] and [010] directions. (b) Total in-plane strain (difference between deviatoric strains in the directions highlighted in (a)) vs electric field. Error bars represent the standard deviation of the pixel-wise micron-scale strain. (c) (Left) Schematics of X-ray microdiffraction with *in situ* voltage applied. Surface electrode arrays on

(001)-cut PMN-PT. (Middle) Samples B and C have varied electrode pair distances, spacing and angle arrangements. In each region, four dot squares serve as location reference points. (Right) A demonstration of the reconstructed regional strain maps ( $\varepsilon'_{xx}$ ) of the 12 dotted regions from Sample C.

### 6.2.1 Deviatoric strain tensor

The calculated deviatoric strain tensor at each spatial location (pixel) results from the measured lattice distortion of PMN-PT relative to the reference unstrained PMN-PT unit cell. From the X-ray microdiffraction, we obtain deviatoric strains including normal and shear components. **Figure 6.2** shows the strain maps of different deviatoric strain components in Region 12, Sample B.



**Figure 6.2.** Strain maps showing different deviatoric strain components in Region 12, Sample B. The strain values reflect the difference between deviatoric strains taken at 400 V and 0 V.

(a) Normal components of deviatoric strain tensor:  $\varepsilon'_{xx}$ ,  $\varepsilon'_{yy}$ ,  $\varepsilon'_{zz}$ ; (b) Shear components of deviatoric strain tensor:  $\varepsilon'_{xy}$ ,  $\varepsilon'_{yz}$ ,  $\varepsilon'_{xz}$ .

**Table 6.1** reports the magnitude of average deviatoric strain components in the region along with the standard deviations.

Deviatoric Strain	Strain Component	Mean (p.p.t.)	Standard Deviation
Normal	$\varepsilon'_{xx}$ (in-plane)	0.3259	0.0699
	$\varepsilon'_{yy}$ (in-plane)	-0.6521	0.1398
	$\varepsilon'_{zz}$ (out-of-plane)	0.3222	0.0808
Shear	$\varepsilon'_{xy}$	4.40E-04	2.11E-04
	$\varepsilon'_{yz}$	-1.56E-05	2.70E-05
	$\varepsilon'_{xz}$	-0.0026	5.44E-04

**Table 6.1.** Regional deviatoric strain components in Sample B, Region 12.

### 6.3 Experimental details for electrically-induced deviatoric strain calculation

Recently, Lo Conte *et al.* used X-ray microdiffraction to map out the electrically-induced axial strain distribution in (011)-oriented PMN-PT with parallel plate electrodes [74], [78], achieving micron-scale resolution at the locations with patterned magnetic microstructures (**Figure 6.1a(i)**). During the microdiffraction scanning, individual diffraction pattern is collected stepwise from a grid point (an x-y position) to provide information on lattice strain and crystal orientation. For this work, the electrically-induced deviatoric strain is calculated for each step, as represented by a  $10 \times 10 \text{ } \mu\text{m}^2$  pixel in the constructed 2D strain maps (**Figure 6.1c**), by taking the deviatoric strain difference of extracted strain at a non-zero voltage and at zero voltage.

In Sample A, the X-ray performs a raster scan with an area of  $500 \times 500 \text{ } \mu\text{m}^2$  at the center of the sample. In Sample B and C, the X-ray scans multiple  $250 \times 250 \text{ } \mu\text{m}^2$  areas.

The location of each scanned region during the microdiffraction experiment is dictated by four Pt square markers. The location of each scanned region during the microdiffraction experiment is dictated by four Pt square markers, each 20  $\mu\text{m}$  long. Prior to X-ray microdiffraction, the coordinates of both the top left and the bottom right corners for each square region are determined by Pt  $L\alpha$  micro X-ray fluorescence [22] and recorded. At each voltage step, the X-ray scans are repeated at the same regions marked by these coordinate pairs.

This work mainly focuses on the experimentally-measured in-plane deviatoric strain components [190],  $\varepsilon'_{xx}$  and  $\varepsilon'_{yy}$ , measured by Laue method, as they are the driving mechanism for in-plane magnetization rotation or switching in numerous studies [78]. In the remaining part of this paper, we will refer to deviatoric strain as strain.

Before examining the regional strain profile generated by the surface electrode pairs, we conduct X-ray microdiffraction on two prepoled PMN-PT samples with parallel plate electrodes and apply voltages up to 400 V, as shown in **Figure 6.1a**. The first one (**Figure 6.1a(i)**), a (011)-cut PMN-PT studied in Lo Conte *et al.* generates in-plane anisotropic strain along the main crystallographic directions [100] and [01-1] as a function of the voltage. The second one (Sample A, above **Figure 6.1a(ii)**) is a (001)-cut PMN-PT, which would ideally exhibit isotropic compressive strain on a macroscopic level along the [100] and [010] directions [22], [44], [64], [188]. For the first sample, the average induced in-plane strain is compressive along [100] and tensile along [01-1]. For the second, the average axial strains are both compressive. Interestingly, the axial strains between nominally equivalent [100] and [010] directions are close in magnitude but not identical when the strain is examined at the microscale. The error bars in the strain-voltage plot in **Figure 6.1a** also suggest that the axial strain exhibits spatial variation in the scanned regions for both PMN-PT samples. In **Figure 6.1b**, we show

the difference between the average of two deviatoric strains as total (in-plane) strain from both samples. This difference is the driver for controlling magnetization (i.e., strain-induced magnetoelastic uniaxial anisotropy) in previously reported strain-coupled thin-film magnetic nanostructures [50], [73]. For the (011)-cut PMN-PT, it is obvious that a large strain difference is induced at 400 V, whereas for the (001)-cut, the strain difference is much lower. Ideally, we expect this strain difference to be zero, but the local inhomogeneity of strain [22], [85] and ferroelectric domains [22] likely account for the non-zero average in the biaxial strain difference magnitude.

Next, we obtain regional microdiffraction scans in Samples B and C for two voltage cycles from 0 V to 400 V, where the first one poles the samples (See effect of poling in Section 6.3.1). During the microdiffraction experiment, a positive voltage is applied to the top surface electrodes, and the bottom is grounded (**Figure 6.1c**). The regions of interest are each marked by four markers and labeled numerically for ease of reference. **Figure 6.1c** (Right) also demonstrates the zoomed-in reconstructed deviatoric strain maps from Sample C. When a voltage is applied to the surface electrode pairs, to satisfy the compatibility conditions of strain [51], an in-plane compressive strain is produced at the surface of the PMN-PT along the  $y$ -direction (i.e., the direction of the electrode pair), and a tensile strain is generated along the  $x$ -direction.

### *6.3.1 Effect of poling to the local deviatoric strain distribution*

For the X-ray microdiffraction, the samples were poled prior to the experiment. A voltage of 400 V is applied to the top and bottom surface of the PMN-PT (0.8 MV/m) for 15 min at room temperature to pole the sample in air prior to the X-ray microdiffraction measurements. One challenge with poling in air is arching may occur, although it wasn't observed in our



samples. Other alternative poling methods include poling in silicone oil bath at an elevated temperature [191].

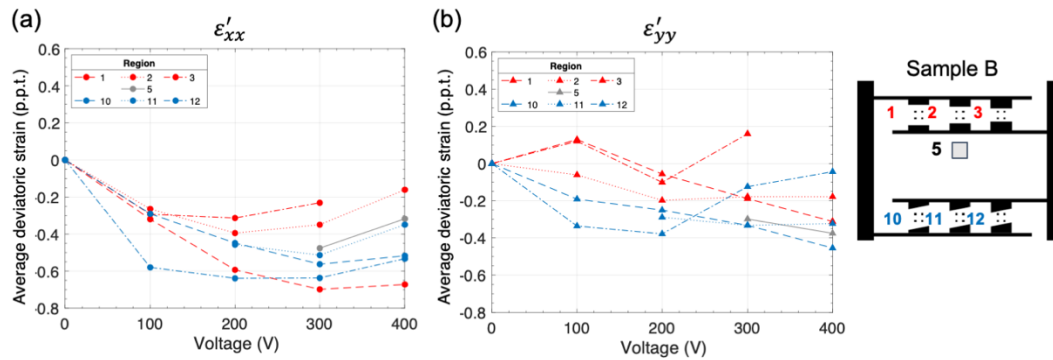


Figure 6.3. Plots of average regional axial deviatoric strain vs voltage in the unpoled Sample B differ largely from these in the prepoled Sample B.

X-ray microdiffraction results of regional deviatoric strain between the surface electrode pairs show clear evidence of the effect of poling on the physical state of the PMN-PT substrate on a micron-scale level. In the unpoled state, the regional strain variations from different regions do not share the same trend and for each region, the strain magnitude does not increase monotonically with respect to the applied voltage (**Figure 6.5c**). However, in the prepoled sample, we observe a clear increasing trend in axial strain for all the regions as we ramp up the voltage. The regional strain is tensile along the  $x$ -direction and compressive along the  $y$ -direction.

The major difference between samples B and C is the density of electrode array pairs, where C has two more rows of electrode pairs than B and thus is more densely packed. In Sample B, regions 1-3 are in the top row, region 5 is not between a closely packed electrode pair and regions 10-12 are in the bottom row. For the top and bottom row with electrode pairs, the

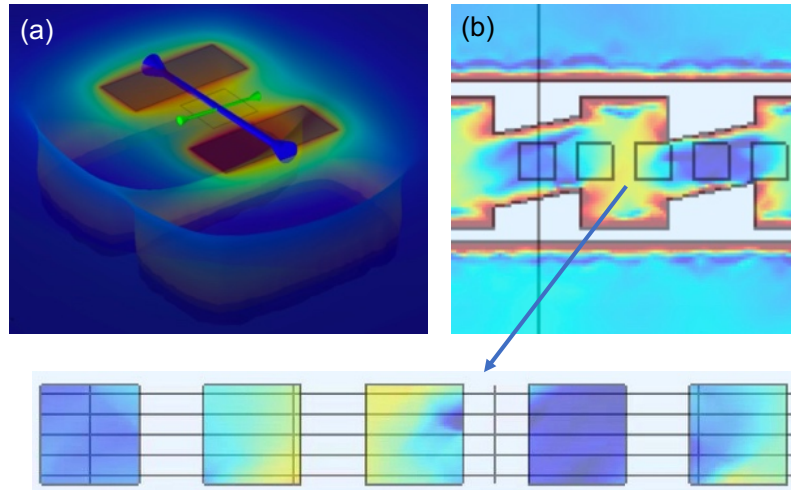
electrode pair separation distances are 600  $\mu\text{m}$ , 500  $\mu\text{m}$  and 400  $\mu\text{m}$ . On the bottom row, the electrode pairs are placed at an angle of  $11.25^\circ$  with respect to the [010] crystallographic direction. In Sample C, regions 1-12 are scanned, where all the electrode pairs are separated by 400  $\mu\text{m}$ , and the electrode pair angles are  $0^\circ$ ,  $11.25^\circ$ ,  $-22.5^\circ$  and  $22.5^\circ$  for each row, respectively.

Two electrode pairs located at regions 3 and 12 in both samples share the same electrode pair configuration, where the electrode pairs are separated by 400  $\mu\text{m}$ . Previous simulation studies have shown that at such a length scale, the surface electrode pair on a PZT could produce a highly localized strain field in regions smaller than  $1 \times 1 \text{ mm}^2$  [192]. Since the separation distance between surface electrodes is on the order of a few hundred microns, it becomes impossible to characterize the strain by a strain gauge. Hence, X-ray microdiffraction is crucial for characterizing the spatial strain profile as a result of varied surface electrode array configuration, including pair density, separation distance between electrode pairs, and angle of the electrodes with respect to substrate crystallographic direction.

From X-ray microdiffraction data, we extract the electric-field induced deviatoric strains  $\varepsilon'_{xx}$  and  $\varepsilon'_{yy}$  for individual regions. **Figure 6.5a** shows an example of the 2D map of induced strain. As expected, the local induced strain is tensile along the  $x$ -direction and compressive along the  $y$ -direction. However, from the micron-scale mapping, the strain is not uniform at the micrometer scale.

A finite element simulation using COMSOL Multiphysics with the same electrode setup as in Sample B also shows local anisotropic axial strain as in the experiment.

For the simulations, (001)-cut PMN-PT with the same geometry ( $1\text{ cm} \times 1\text{ cm} \times 500\text{ }\mu\text{m}$ ) is built. A thin layer of polymer material ( $50\text{ }\mu\text{m}$  thick) is incorporated into the simulation to mimic the colloidal silver paste (TED PELLA, INC.) used in the experiments for attaching the bottom electrode to the leadless chip carrier. The interface is grounded and the bottom surface of the PMN-PT is fixed. Strain-charge form matrix (TRS Technologies, Inc., State College, PA, USA) is used to calculate the piezoelectric effect. The mesh size is defined as  $2\text{ }\mu\text{m}$  around electrodes in order to ensure the accuracy. The strain distribution is then calculated with a series of electrode distances and angles (Figure 6.3(a)). From the 2D  $\varepsilon'_{yy}$  map below (Figure 6.3(b)), a relatively large strain gradient is pronounced around the electrode edges or between sets of pairs, as highlighted in the horizontal square regions. A related work by Zhao *et al.* [188] using high-energy X-ray diffraction on the ferroelectric patterned with partial-electrode (“electrode edge scan”) along with the finite element analysis (FEA) reveal high electric field concentrations near the electrode edge. A similar work using nanocomposite electrode on PMN-PT [193] also reported through the FEA non-uniform electric field near the edge of the patterned electrode grating. Though the electrode configurations and experimental scanning direction in our study differ from the two aforementioned studies, it is important to note the inhomogeneity in polarization or strain profile in the vicinity of the electrode is observed in all cases. While in the center zone between any set of electrodes, the variation in strain is relatively small and thus the strain distribution is more uniform. In addition, the strain magnitudes are higher than in the regions outside of the electrode pairs. This property of localized strain makes such a design prototype applicable to practical applications where the ability to actuate local magnetic microstructures (e.g., in the region between the electrode pairs) is desired.



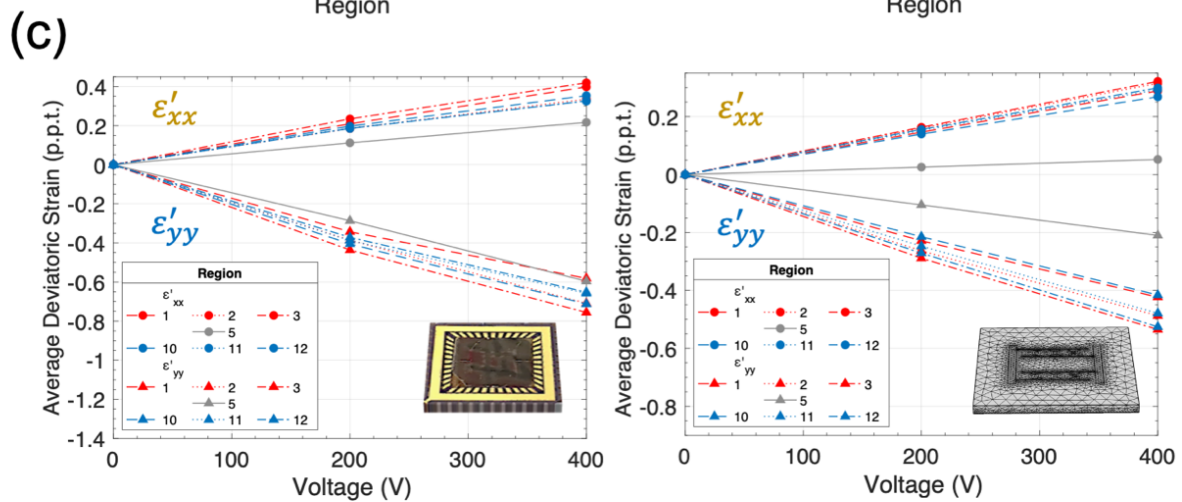
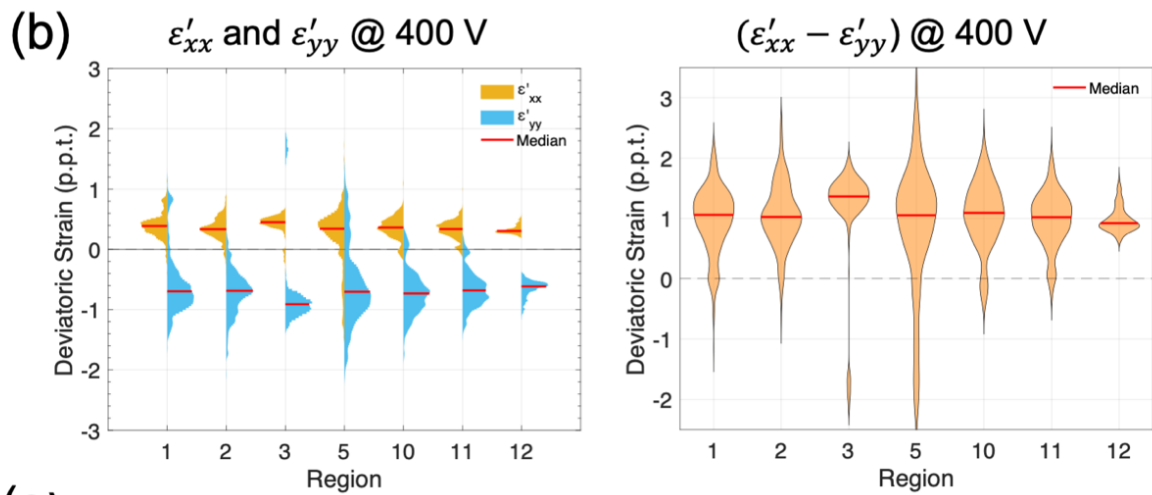
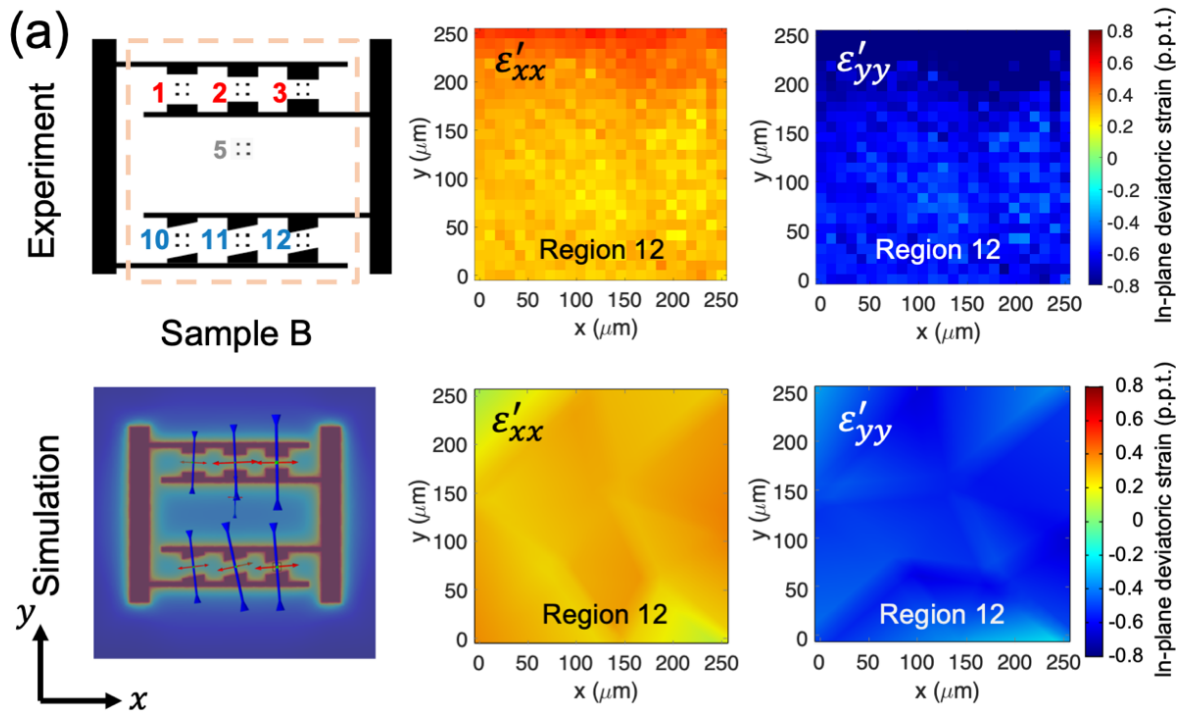
**Figure 6.4.** (a) A 3D zoomed-in view of an electrode pair on PMN-PT with an applied voltage, with axial strains illustrated by arrows. (b) From simulation, strain distribution in between electrode pairs and outside of electrode pairs. Each highlighted box has a size of  $250 \times 250 \mu\text{m}^2$ .

The simulated induced strain mapping is shown in **Figure 6.5a**. For the simulation, we do not consider nonuniform strain and ferroelectric domains present in the experimental system, as suggested by the strain distribution in Sample A (**Figure 6.1a(ii)**), so the strain variation is less pronounced.

### 6.3.2 Experiment vs Simulation results

Indeed, while the simulation captures the polarity (tensile vs compressive) and the magnitude of the strain components, there are discrepancies between the experiment and simulation results in terms of micron-scale level strain magnitude and strain variation in individual regions. The simulation assumes ideal condition of the PMN-PT sample with no ferroelectric domain or intrinsic crystal property variation across the sample. Reasons for these discrepancies could include the inhomogeneity of strain in the actual sample, as previously reported by Lo Conte *et al.* [194], residual stress after poling, possible compositional variation

crystal property in PMN-PT due to imperfect growth condition with Bridgman technique, and the presence of micron-scale wide ferroelectric domains [22] and different domain configurations [51], [186] in the PMN-PT sample. Specifically, the poling direction is along  $\langle 001 \rangle$  while the ferroelectric polarizations are energized along the four  $\langle 111 \rangle$  directions of PMN-PT. The polarization could be distributed among these four degenerate variants, resulting in variation in strain states at different locations in the sample. With surface electrodes adding in-plane polarization, ferroelectric domains could also be moved, adding more complexity and variations to the actual sample as compared to the simulated strain states.



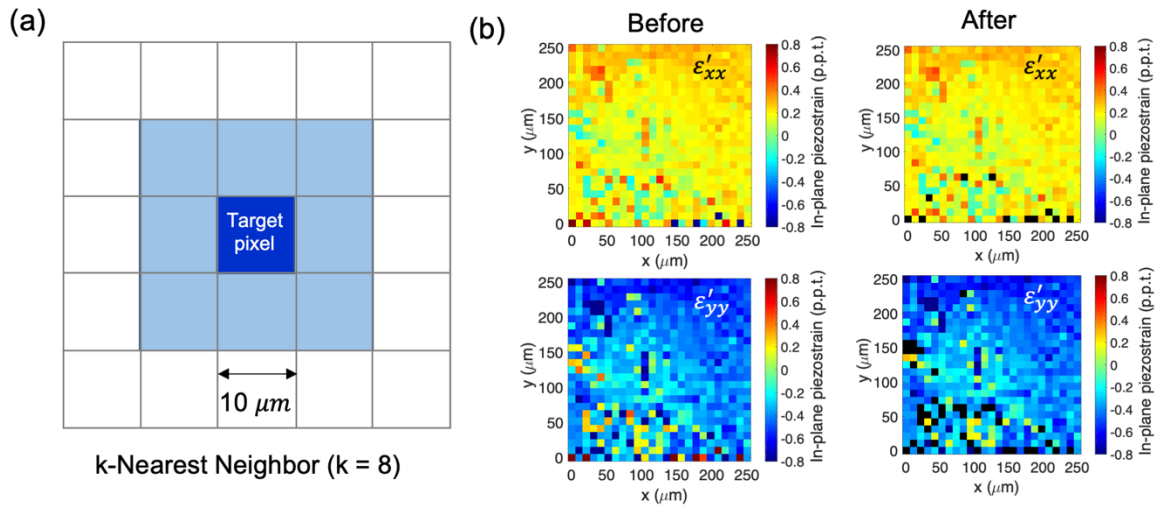
**Figure 6.5.** (a) X-ray microdiffraction scans are conducted locally with an area of  $250 \times 250 \mu\text{m}^2$  in 7 regions on Sample B. The electrode gap distance decreases from 600 to 400  $\mu\text{m}$  in 100  $\mu\text{m}$  decrements for regions 1-3, and 10-12. Reference region 5 is outside of the individual electrode pairs. (Top) 2D strain map for region 12, in both  $x$ - and  $y$ - directions. Each pixel has a size of  $10 \times 10 \mu\text{m}^2$ . (Bottom) Simulation results. (b) Violin plot with the distribution of (Left) the induced strains along  $x$ - and  $y$ - directions ( $\varepsilon'_{xx}$  and  $\varepsilon'_{yy}$ , respectively) and (Right) the in-plane biaxial strain difference. (c) Average axial strain vs. voltage for all regions in Sample B (Left) from experiment and (Right) simulation.

To evaluate the experimental strain distribution and variation for the 625 pixels, we created violin plots [195] (**Figure 6.5b**) for both the axial deviatoric strains and their difference,  $\varepsilon'_{yy} - \varepsilon'_{xx}$ . To account for the experimental noise during X-ray microdiffraction scanning, apart from fitting Laue peaks with the XMAS software, we adopt the nearest neighbor technique (see Section 6.3.3) for outlier removal with less than 0.6% of the pixels removed for any image.

### 6.3.3 *Outlier removal for strain mapping*

The strain mapping originates from pixelated scanning of Laue diffraction. Due to the random errors in peaking fitting that translate into error in strain values, some recovered pixels in the strain map do not closely reflect the deviatoric strain values at the corresponding locations and are treated as outliers. Such errors from peak fitting mainly occur when back reflections deviate largely from an ideal Lorentzian or Gaussian peak profile [196]. To find these outliers and safely remove them for following strain distribution analysis, we adopt the  $k$ -nearest neighbor method, where  $k = 8$  for our calculation (**Figure 6.6(a)**), by comparing the difference in a pixel's strain value and the median of these neighbors. We first calculate the

standard deviations of the entire regional strain map with 625 pixels. If the difference is more than 2 standard deviations, we marked the pixel as an outlier. In **Figure 6.6(b)**, we show the before and after strain maps following the outlier removal process from both  $\epsilon'_{xx}$  and  $\epsilon'_{yy}$  from region 11, Sample B.



**Figure 6.6.** (a) Remove outliers by comparing the strain value of each pixel to its k-nearest neighbors ( $k = 8$ ). (b) Example of outlier removal for Region 11 in Sample B. Data collected when the applied voltage is 200V.

To reduce noise in the strain map, there are two steps involved. The first step uses X-ray microdiffraction analysis software (XMAS) [197] at beamline 12.3.2, Advanced Light Source to fit the Laue peaks. The peak profiles are fitted with a 2D Gaussian or Lorentzian function in a box delineated around the peak maxima. To obtain the Laue peak positions, the software first separates pixels above certain intensity from those below it. The threshold is adjusted automatically to account for the beam intensity fluctuation. Pixels in clusters with intensities above the threshold and values higher than any of their eight closest neighbors, namely maxima, are defined as possible peak positions. These maxima are fitted with a



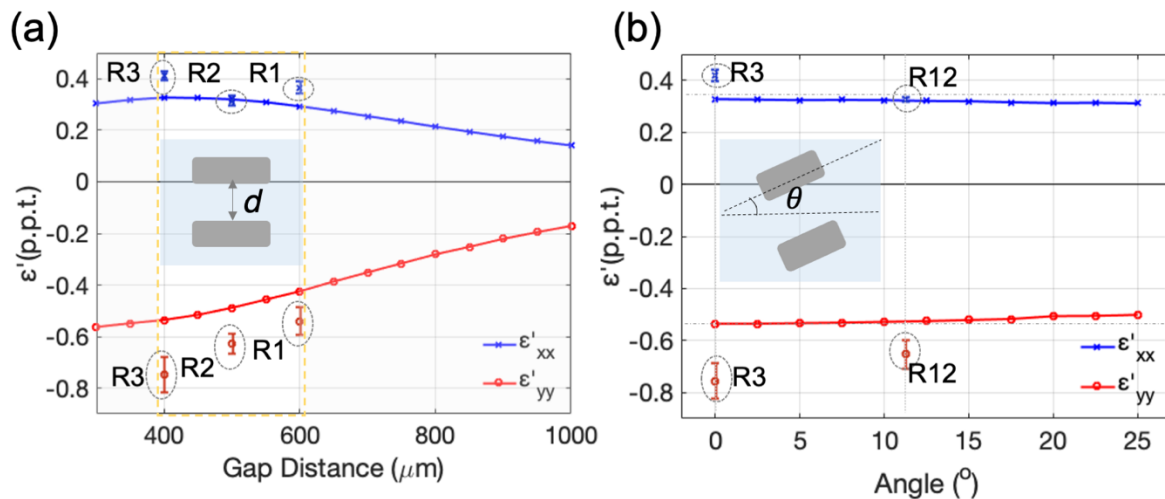
Lorentzian, Gaussian or Pearson function [78]. To separate real Laue reflections from the noise or artifacts, the XMAS software imposes various constraints on the intensities, peak widths and chi-square factor. The second step is to remove salt-and-pepper type of noise in the strain map itself where the nearest-neighbor technique is employed.

Another robust method for fitting Bragg peaks from the diffraction data involves using the distribution moments calculated from a local window around the peak, and conducting a least-squares fit based on the distribution moments. More detail can be found in this well-developed Matlab Peak Fitting GUI for diffraction data: LIPRAS: Line-Profile Analysis Software [78] (<https://github.com/SneakySnail/LIPRAS>)

Additionally, we report the regional average strain in **Figure 6.5c** from both experiment and simulation. The differential deviatoric strain achieved in localized regions on (001)-cut PMN-PT using the surface electrodes in this work is similar to that of the global anisotropic strain profile in (011)-cut PMN-PT from **Figure 6.1a(i)**. However, with the locally-controllable strain of our surface electrodes, one could, for example, actuate individual microscale magnetic components. Furthermore, the surface electrodes can be used to engineer the differential deviatoric strain, as opposed to the case of **Figure 6.1a(i)**, which relies on having the appropriate material and crystalline cut, thus limiting the set of material choices.

Also observed from **Figure 6.5b** and **Figure 6.5c**, the average strain for each direction and the strain difference vary by region. Such differences in local strain profile suggest a collective effect from the electrode pair separation distances (400 – 600  $\mu\text{m}$ ), the electrode pair rotation of  $11.25^\circ$  in the bottom row and the location of the region in the sample. Next, we resort to simulation for providing additional insight on the effect of separation gap distance and

angle using parametric sweeps. The simulation results in **Figure 6.7a** present the biaxial deviatoric strain difference as a function of electrode pair separation gap distance  $d$ . For the ranges studied experimentally, the simulations show decreasing strain in both  $x$ - and  $y$ -directions as the gap distance narrows. The corresponding axial strains measured experimentally for regions 1-3 in Sample B are marked in **Figure 6.7a**. In terms of the strain variation with electrode angles, an increase in the electrode pair tilting angle with respect to the  $x$ -direction slightly decreases the strain along the  $[100]$  and  $[010]$  directions, as shown in **Figure 6.7b**.



**Figure 6.7.** A parametric sweep study using finite element simulation shows the effect on the induced deviatoric strain from electrode gap distance and angle. Corresponding average strain values obtained experimentally from regions 1-3 (labeled R1-R3, respectively) in Sample B are highlighted in circles with error bars representing 95% confidence intervals. **(a)** Gap distance between the electrode pairs affects the axial strain magnitudes. For the range explored experimentally, an increase in gap distance leads to a decrease in strain (highlighted by a dotted circle). **(b)** Role of electrode angle (with respect to the  $[010]$  crystallographic direction). In Sample B, as the angle increases from  $0^\circ$  to  $11.25^\circ$ , the deviatoric strains decrease slightly.

We also compare the local strain results to the anisotropic axial strain generated globally in parallel plate (011)-cut PMN-PT substrate (**Figure 6.1b**). It is observed that the locally induced strain in the 6 regions (1-3, 10-12) are similar in magnitude as in the (011)-cut PMN-PT, a significant increase from the nearly isotropic compressive strain in Sample A with parallel plate electrodes.

We use axial deviatoric strain ratio [198] ( $\varepsilon'_{yy}/\varepsilon'_{xx}$ ) to compare the strain behavior across different regions in a sample and similar regions across samples. Different ratios reflect variations in regional piezoelectric coefficients which allow one to access a diverse range of strain responses at a given applied voltage.

First, we compare the axial strain ratio in all regions in Sample B (see Section 6.3.4) to conclude that the strain is not strictly confined between electrode pairs; rather, it can affect the strain distribution outside of the region. Next, we compare the axial strain ratio to see how the variation of the electrode pair density affects the strain behavior in local regions. In particular, we compare the axial strain ratio in regions 3 and 12 from Sample B and C since those regions have identical electrode designs (i.e., same gap distance and angle).

#### 6.3.4 Voltage-induced axial deviatoric strain ratio $\varepsilon'_{yy}/\varepsilon'_{xx}$

Although region 5 is outside of any closely packed electrode pair, it still exhibits a non-zero *biaxial* deviatoric strain difference. In **Table 6.2**, we report the  $\varepsilon'_{yy}/\varepsilon'_{xx}$  ratio for all seven regions in Sample B at 200 V and 400 V. Region 5 has a ratio of 2.7 compared to other regions with a ratio ranging from 1.6 to 2.0, indicating that along the  $y$ -axis, the strain from the neighboring electrode pairs is not localized and is contributing to the strain. Its strain distribution is less concentrated than the other regions probed in the experiment partly due to

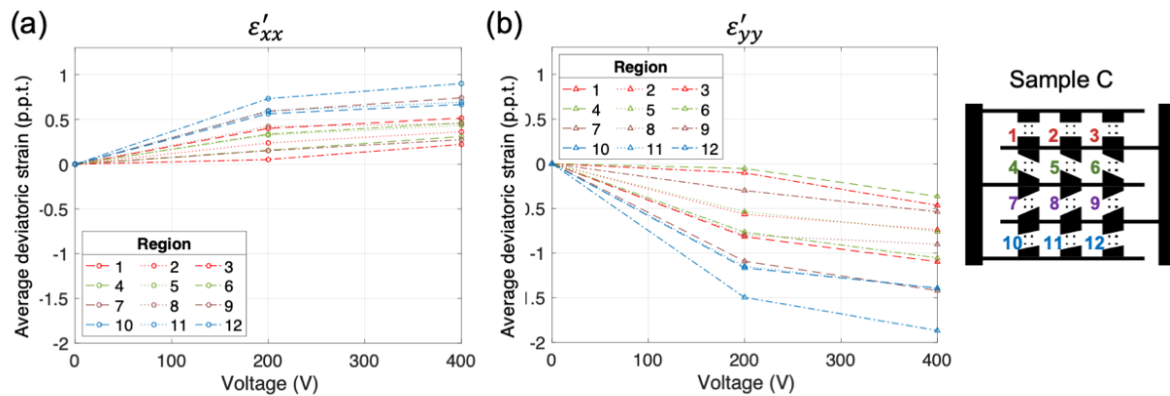
it not being confined between a closely placed electrode pair. This finding suggests that the presence of electrode pairs with separation distance on par with the substrate thickness can contribute to more localized, comparably more homogeneous strain. It could also open up avenues to further exploration such as to investigate the neighboring effect of surrounding electrode pairs as well as the global effect of electrode pads on the side used for wire bonding or connection purposes.

**Table 6.2.** Regional  $\varepsilon'_{yy}/\varepsilon'_{xx}$  in Sample B

	Region 1	Region 2	Region 3	Region 5	Region 10	Region 11	Region 12
200V	1.6	2.1	1.8	2.7	2.0	2.0	2.0
400V	1.6	2.1	1.9	2.6	2.0	2.1	2.0

Among all 7 probed regions in Sample B, region 5 is the only region that is not directly sandwiched between two surface electrode pairs. Apart from still showing measurable induced deviatoric strain, region 5 also shows the highest axial deviatoric strain ratio among all while with a large variation in magnitude. This finding suggests that the electrode pairs along the vertical direction ( $y$ -direction), in particular, region 2 and region 11, when subject to an applied voltage, could still affect the strain profile beyond the regions they predominantly control. These two regions are closer to region 5 along the  $y$ -direction versus distances between region 5 and the two vertical side electrode bars positioned along the  $x$ -direction. As a result, on a global level, region 5 receives larger strain along the  $y$ -direction versus the  $x$ -direction when compared to other regions located at the center of their electrode pairs. Therefore, we would expect to see a higher strain ratio from region 5.

It is worth noting that from sample to sample, we observed variations in strain magnitudes which most likely results from the intrinsic material properties of PMN-PT samples provided by TRS<sup>11</sup>.

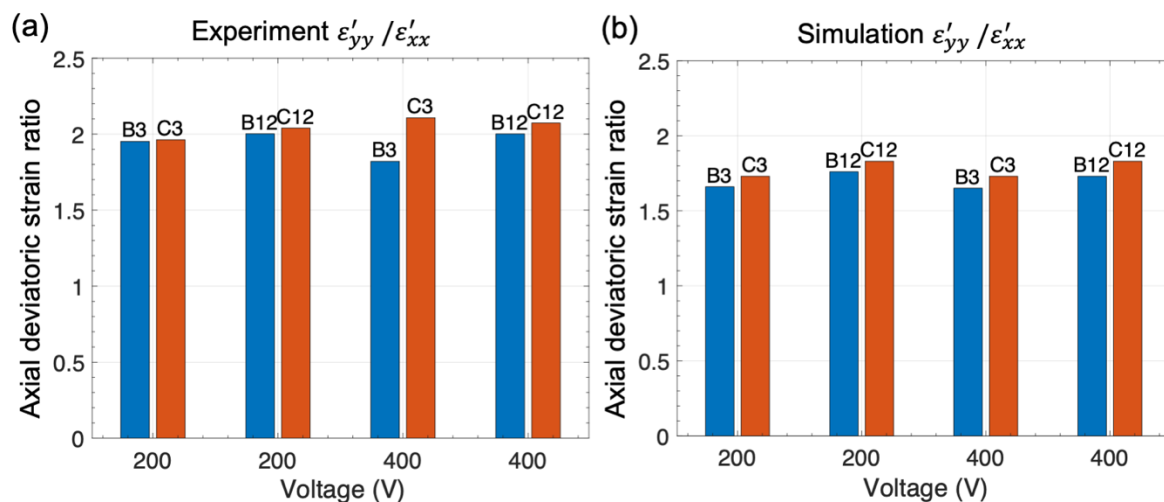


**Figure 6.8.** Average regional induced deviatoric strain vs applied voltage in Sample C. (a) Tensile strain along the  $x$ -direction. (b) Compressive strain along the  $y$ -direction.

The variation between PMN-PT samples (**Figure 6.8**) is partially due to the fact that these materials are grown using a Bridgman Crystal Growth method producing samples with small variations in composition depending upon where they were taken from the grown rod or if they were taken from different rods. The PMN-PT samples are also extremely sensitive to compositions since they are near a morphotropic phase boundary (MPB) with some compositions providing a large strain jump (i.e. phase change) with an applied field [199]. Therefore, we attribute the strain modifications we observe due to these compositional variations. While some strain variations were observed, it is important to point out the deviatoric strain vs. voltage plots across different regions and samples provided similar trends but small differences in strain magnitudes. To quantitatively compare the regional strains measured from Samples B and C in this study we thus used an axial deviatoric strain ratio ( $\epsilon'_{yy}/\epsilon'_{xx}$ ) between the two.

<sup>11</sup> <http://www.trstechnologies.com/Materials/High-Performance-PMN-PT-Piezoelectric-Single-Crystal>

Similar to Sample B, the voltage-induced axial strain profile from prepoled Sample C shows tensile and compressive strain along the  $x$ - and  $y$ - directions, respectively.



**Figure 6.9.** Comparison of axial deviatoric strain ratios  $\varepsilon'_{yy}/\varepsilon'_{xx}$  in regions 3 and 12 at 200 V and 400 V. From both (a) experiment and (b) simulation results, the ratios are higher in both regions from Sample C than those from Sample B, implying the additional electrodes in sample C couple with their neighbors and lead to increased anisotropic strain.

From both the experimental and simulation results (**Figure 6.9**), the  $\varepsilon'_{yy}/\varepsilon'_{xx}$  ratio from Sample C is higher than that in Sample B. This observation implies that the presence of additional rows of electrode pairs in the middle in Sample C versus Sample B leads to a higher axial strain ratio. It suggests the presence of denser electrode pairs along the  $y$ -direction plays a non-negligible role in making the regional strain profile more anisotropic along the  $y$ - versus  $x$ - directions. Overall, the X-ray microdiffraction results on the micron-scale level reveal that the local strain can be affected collectively by the three factors investigated in this work: local electrode separation distance, angle of placement with respect to the crystallographic directions, and closeness to neighboring electrodes. With the current surface electrode design, the samples generate localized strain with tunable axial strain magnitudes.

## 6.4 Concluding Remarks

In conclusion, X-ray microdiffraction provides a distinct opportunity to map out the local deviatoric strain in ferroelectric PMN-PT in the areas of interest between surface electrodes with micron-scale resolution. An in-depth understanding of the spatial distribution of regional strain is crucial, particularly for driving arrays of strain-coupled magnetic microstructures in multiferroic systems. We characterize and analyze the strain profile in PMN-PT resulting from both parallel plate electrodes and patterned electrode arrays. The results highlight the effect of electrode geometry on both the local and global scales. In particular, we examined local strain in multiple regions from (001)-cut PMN-PT samples with surface electrodes, and the average axial strain response is consistent with predictions from piezoelectric simulations. This systematic study also highlights the influence of electrode pair geometry, including separation distance of the pair, angle of the pair, and neighboring electrode pair compactness on the local and regional strain.

## Chapter 7 Conclusions

Multiferroics with both ferromagnetic (FM) and ferroelectric (FE) properties have attracted substantial interest in recent years owing to the strong magnetoelectric (ME) coupling behavior between these two ferroic orders. Researches in the room-temperature composite multiferroics materials with strong magnetoelectric coupling behavior have paved the way to applications in different application domains, including but not limited to magnetoelectric random access memory, sensors and actuators, magnetic antennae, and biomedical devices.

Motivated by the scalability and energy efficiency of voltage-controlled multiferroics and the usage of magnetism in the biotechnological domain, this work studies properties of composite multiferroics with a particular focus on the potential of array-addressable particle and cell control with multiferroics.

The first two chapters present both the background and state of the art in multiferroics and cell sorting, before moving on to more details on different characterization methods used for analyzing the properties of multiferroics.

Chapter 3 utilizes the element-specific magnetic imaging method mentioned in Section 2.1.4 to explore the tunable magnetostrictive effect in bilayer ferromagnetic layers. The primary purpose of this work is to show the versatility of composite multiferroics engineering. It investigates magnetoelectric properties of exchange-coupled Ni-CoFeB-based composite multiferroic microstructures. The strength and sign of the magnetoelastic effect are strongly correlated with the ratio between the thicknesses of the two magnetostrictive materials. In cases where the thickness ratio deviates significantly from one, the magnetoelastic behavior of the



multiferroic microstructures is dominated by the thicker layer, which contributes more strongly to the observed magnetoelastic effect. More symmetric structures with a thickness ratio equal to one show an emergent interfacial behavior which cannot be accounted for simply by summing up the magnetoelastic effects occurring in the two constituent layers. This new aspect is clearly visible in the case of ultrathin bilayers, where the exchange coupling drastically affects the magnetic behavior of the Ni layer, making the Ni/CoFeB-bilayer a promising new synthetic magnetic system entirely. This chapter demonstrates the richness and high tunability of composite multiferroic systems based on coupled magnetic bilayers compared to their single magnetic layer counterparts. Furthermore, due to the compatibility of CoFeB with present magnetic tunnel junction-based spintronic technologies, the reported findings on this materials-related study are also expected to be of great interest for the development of ultra-low-power magnetoelectric memory devices.

Chapter 4 and Chapter 5 switch gear to examine the potential of a multiferroics platform for particle and cell sorting. While Chapter 4 confirms that the multiferroics platform can control magnetically-labeled particles and cytocompatibility of such platform, its scale is not prepared for cell control. Chapter 5 then examines programming magnetic fields with microscale control to enable automation at the scale of single cells  $\sim 10 \mu\text{m}$ . Most magnetic materials provide a consistent magnetic field over time, but the direction or field strength at the microscale is not easily modulated. However, when coupled with ferroelectric material (i.e., strain-mediated multiferroics), magnetostrictive materials can undergo magnetization reorientation due to voltage-induced strain, promising refined control of magnetization at the micron-scale. This work demonstrates the largest single-domain microstructures ( $20 \mu\text{m}$ ) of Terfenol-D ( $\text{Tb}_{0.3}\text{Dy}_{0.7}\text{Fe}_{1.92}$ ), a material with the highest magnetostrictive strain of any known soft magnetoelastic material. These Terfenol-D microstructures enabled the controlled localization

of magnetic beads with sub-micron precision. Magnetically-labeled cells were captured by the field gradients generated from the single-domain microstructures without an external magnetic field. Due to strain-mediated converse magnetoelectric effect, the magnetic state on these microstructures was switched through voltage-induced strain to release individual cells using a multiferroic approach. These electronically addressable micromagnets pave the way for parallelized multiferroics-based single-cell sorting under digital control for biotechnology applications.

Chapter 6 investigates localized in-plane strains on the microscale, induced by arrays of biased surface electrodes patterned on piezoelectrics. Particular focus is given to the influence that adjacent electrode pairs have on one another to study the impact of densely packed electrode arrays. We present a series of X-ray microdiffraction studies to reveal the spatially-resolved micron-scale strain distribution. The strain maps with micron-scale resolution highlight how the local strain profile in square regions up to  $250 \times 250 \mu\text{m}^2$  in size is affected by the surface electrodes that are patterned on ferroelectric single-crystal  $\text{Pb}(\text{Mg}_{1/3}\text{Nb}_{2/3})\text{O}_3$ - $[\text{PbTiO}_3]_{1-x}$  (PMN-PT). The experimental measurements and simulation results show the influence of electrode pair distance, positioning of the electrode pair, including the angle of placement, and neighboring electrode pair arrangements on the strength and direction of the regional strain. Our findings are relevant to the development of micro-architected strain-mediated multiferroic devices. The electrode arrays could provide array-addressable localized strain control for applications including straintronic memory, probabilistic computing platforms, microwave devices, and magnetic-activated cell sorting platforms.

## Appendix A Fabrication Notes

### A-1 Recipe for Ni rings on top/bottom electrodes PMN-PT samples

- Obtain 1cm \* 2cm\* 0.5mm PMN-PT substrate
- Clean sample (ultrasonic in acetone) →
- Matrix Asher PR strip @240C, 3 min →
- Deposit Ti/Pt layer with NanoLab old CHA (Ti 10 nm/Pt 40 nm), deposition rate: 0.5A/sec for Ti, 0.5A/sec for Pt →
- CHA deposition again on the other side of the substrate (Ti/Pt) →
- Layers of the sample up to now: Pt (40)/Ti (10)/PMN-Pt/Ti (10)/Pt(40) (nm)
- Cut PMN-PT samples in half with a diamond cutter after CHA, mark [100] (compression, direction, along 2 cm axis) and [01 1̄0] (tension direction, along 1cm axis direction)
  - \*Can deposit Ti/Au as the bottom layer in Nanolab (more economical)
- Clean with Matrix Asher only top layer (240C)
- Spin coat on Pt:
  - AP3000 adhesion promotor spin rate 3000rpm (30 sec) → bake@110C for 5 min
    - Step 1: (0.5 sec) 50 rpm, ramp: 300 rpm/sec
    - Step 2: (5 sec), 500 rpm, ramp: 100 rpm/sec
    - Step 3: (30 sec), 3000 rpm, ramp: 300 rpm/sec
    - Step 4: (0.5sec), 0 rpm, ramp: 300 rpm/sec →
  - BCB polymer (thickness: 10um) 5000rpm → bake @100C for 1 min (in the meantime, open the vacuum over chamber to cool down from default temp 100/150C, change the temperature to 50C for vacuum oven)
    - Step 1: (0.5 sec) 50 rpm, ramp: 300 rpm/sec
    - Step 2: (5 sec), 500 rpm, ramp: 300 rpm/sec
    - Step 3: (30 sec), 5000 rpm, ramp: 300 rpm/sec
    - Step 4: (25sec), 15 rpm, ramp: 300 rpm/sec (EBR: edge bead removal)
    - Step 5: (0.5sec), 0 rpm, ramp: 300 rpm/sec
- BCB(10um)/AP3000/Pt (40 nm)/Ti (10 nm)/PMN-Pt/Ti 10 nm)/Pt(40 nm)
- Wrap an Al foil around a metal block and mount the sample on top to let the sample cool down

- Vacuum oven set to @255C bake for 3 hours (including 90 min for ramping temp):  
put in samples first, close the door, vacuum, raise temperature afterwards
- Dehydrate on hot plate at 100 C
- Deposit Ti/Pt on top of BCB →  
Pt(40)/Ti(10)-prevent discharge during peem/BCB(10um)/AP3000/Pt  
(40)/Ti (10)/PMN-Pt/Ti (10)/Pt(40)→
- Clean sample with 100 C matrix asher + acetone+methnol+IPA (no  
ultrasonification) →
- Ebeam lithography Prep:
  - MAA EL-6 Spin coat → spin rate 3000 rpm/sec, soft bake 5 mins (@170  
C), cool to RT →
  - PMMA950 A2 Spin coat → spin rate 3000 rpm/sec soft bake 5 min (@170  
C):
  - Spin coating: Select recipe 4
    - Recipe Clear-4 (delete previous recipe)
    - Step 1: (0.5 sec) 50 rpm, ramp: 300 rpm/sec
    - Step 2: (5 sec), 500 rpm, ramp: 300 rpm/sec
    - Step 3: (45 sec), 3000 rpm, ramp: 300 rpm/sec
    - Step 4: (0.5sec), 0 rpm, ramp: 300 rpm/sec →
- E-beam exposure: (GDSII file, reserve one week in advance) Right after spin coat  
→
- Development:
  - MIBK: IPA = 1:3
  - 1 min without agitation
  - rinse with IPA for 5 sec (not too long!) →
  - Check pattern with optical microscope→
- Poling (after development) pole in ISNC, ramp up to 200 V, bottom electrode 200  
V (use Cu tape) →
- ISNC CHA deposition right after poling→ Ni on top of PMN-PT: Ti(5nm)/Ni(15,  
30nm) 0.3A/sec (Ti) and 0.5A/sec (Ni) →
- Lift-off: Right after deposition: Heated NMP for lift-off (50 C), use magnetic bar  
for stirring @ 500 rpm overnight→Rinse with Acetone, Met & IPA

- Don't dry the NMP on the sample until seeing the lift-off results with optical microscope looks good (otherwise harder for further lift-off)
- Check with optical microscope (don't use SEM before PEEM)
- Cut sample, wire bonding on to a LCC carrier

## A-2 Recipe for Ni rings on surface electrode PZT samples

CHA deposition Ti/Pt (5 nm, 40 nm) on one surface (bottom side) of PZT

- Photolithography Mask 1 (for electrodes):

Set hotplate to 115 C

Solvent Cleaning Acetone+Metanol+IPA

O2 cleaning Matrix Asher @ 240 C

PR spin coat PR: SPR 220-3.0

Step 1:	50 rpm	300 rpm/sec	2 sec
Step 2:	500 rpm	300 rpm/sec	5 sec
Step 3:	3000 rpm	300 rpm/sec	30 sec
Step 4:	15 rpm	300 rpm/sec	15 sec (EBR)
Step 5:	0 rpm	500 rpm/sec	0.5 sec

Soft bake 115 C time: 1'30''

Karl-Suss Exposure Hard-contact, 12 sec exposure time for PZT

Relaxation 10 min relaxation time for SPR 220-3.0

Develop MF-26A time: 1'00''

→ Rinse with DI water

CHA evaporation Ti/Au/Al (5 nm/ 80 nm/ 10 nm) deposition rate 0.5A/sec for all (Process # 43)

Lift-off In NMP @80 C overnight

Descum Matrix Asher (for removing remaining SPR 220-3.0)

BCB polymer:

Set up hotplates, 110 C for AP3000, 100 C for BCB

Open vacuum oven, set temp to 50 C

AP3000

Step 1:	(0.5 sec) 50 rpm, ramp: 300 rpm/sec
Step 2:	(5 sec), 500 rpm, ramp: 100 rpm/sec
Step 3:	(30 sec), 3000 rpm, ramp: 300 rpm/sec
Step 4:	(0.5sec), 0 rpm, ramp: 300 rpm/sec

Soft Bake 110 C time 5'00''

1<sup>st</sup> BCB coating (BCB 32) (2 um thick)

Step 1: (0.5 sec), 50 rpm, ramp: 300 rpm/sec

Step 2: (5 sec), 500 rpm, ramp: 300 rpm/sec  
 Step 3: (30 sec), 5500 rpm, ramp: 300 rpm/sec  
 Step 4: (25sec), 15 rpm, ramp: 300 rpm/sec (EBR)  
 Step 5: (0.5sec), 0 rpm, ramp: 300 rpm/sec

Soft bake 100 C time 1'00''  
 Vacuum bake 210 C time 1 hr (from when it reaches 210, PZT  
 ~2hr total)

Slow ramping

2<sup>nd</sup> BCB coating, soft bake

Vacuum bake 255 C time 1 hr 30 min (~2hr 30 min  
 total after putting the sample into the oven)

- Mask 2 (making via through the BCB polymer):

\*Nanoscope (ISNC)→measuring BCB thickness

Spin coat PR: SPR 220-7.0 (RPM 3000)

Step 1: 50 rpm 300 rpm/sec 2 sec  
 Step 2: 500 rpm 300 rpm/sec 5 sec  
 Step 3: 3000 rpm 300 rpm/sec 30 sec  
 Step 4: 15 rpm 300 rpm/sec 15 sec (EBR)  
 Step 5: 0 rpm 500 rpm/sec 0.5 sec

Exposure Hard-contact, 12 sec exposure time for PZT  
 Relax time 20 min  
 Develop MF-26A time: 1'00''→ rinse with DI water  
 Fluorine etcher BCB fast 12 min

- Mask 3 (ground plane and ebeam alignment markers):

- Set hotplate to 115 C
- Solvent Cleaning Acetone+Metanol+IPA
- O2 cleaning Matrix Asher @ 50
- PR spin coat PR: SPR 220-3.0
  - Step 1: 50 rpm 300 rpm/sec 2 sec

- Step 2: 500 rpm      300 rpm/sec      5 sec
- Step 3: 3000 rpm      300 rpm/sec      30 sec
- Step 4: 15 rpm 300 rpm/sec      15 sec (Edge Bead Removal)
- Step 5: 0 rpm 500 rpm/sec      0.5 sec
- Soft bake      115 C      time: 1'30''
- Karl-Suss Exposure      Hard-contact, 12 sec exposure time for PZT
- Relaxation      10 min relaxation time for SPR 220-3.0
- Develop      MF-26A      time: 1'00''
- Rinse with DI water
- Optical Microscope check film quality
- CHA evaporation      Al/Ti/Pt (5nm/ 50 nm)      ~1.8g      Pt  
(process #46)
- Lift-off      NMP @ 50 C overnight
- Descum      Matrix Asher

- Ebeam lithography (MMA EL-6, 950 PMMA A2)

Sputter a thin layer of Au before e-beam to avoid charging problem during electron beam (EB) writing

After ebeam, remove surface Au with gold etchant (5 sec) and rinse with DI water

- Development
- Use probe to scratch electric via to the gold electrodes
- Wire bond sample to a leadless chip carrier (LCC)



### A-3 Recipe for surface electrodes on (001) PMN-PT samples

- Set hotplate to 115 °C
- Clean sample with solvent (ultrasonic in acetone) → (not too long in case the backside Pt electrode got removed)
- *Matrix Asher PR strip/O2 cleaning @240°C, 3 min → to remove organic residue (on the side without Pt) if there is any (can skip)*
- Photoresist Spincoat SPR 220-3.0 (can substitute)
  - Step 1: 50 rpm    300 rpm/sec    2 sec
  - Step 2: 500 rpm    300 rpm/sec    5 sec
  - Step 3: 3000 rpm    300 rpm/sec    30 sec
  - Step 4: 15 rpm    300 rpm/sec    15 sec (Edge Bead Removal)
  - Step 5: 0 rpm    500 rpm/sec    0.5 sec
  - Soft bake    115 C    time: 1'30''
- Karl-Suss Mask Aligner Exposure    Hard-contact, 12 sec exposure time
  - There are 3 different patterns on the mask, each pattern on one sample (4 samples + 2 backup; 2 samples in each box). Four samples have backside Pt film.
  - For the two backup 1cm\*1cm samples that are transparent, no Pt has been deposited onto either side. If using this two samples, either side for exposure is fine. If possible, deposit Ti/Au or Ti/Pt to the backside as electrode prior to the process.
  - The side to expose is the side without Pt
  - The smallest critical feature size is the 40um\*40um square. There are alignment markers with size 2-10 um which may be useful for later processes and study but are not critical, and won't be used for the upcoming beamtime.
  - The pattern will be exposed in the direction such that the y axis of the sample has a rough outline for the transparent sample, or is parallel to the longer side of a long rectangular area with no Pt (covered by tape earlier) on the backside.
- PR Relaxation    10 min relaxation time for SPR 220-3.0
- Development    MF-26A    time: 1'00''
  - Rinse with DI water
- Ebeam evaporator (Ti 5 nm/Pt 50 nm), deposition rate: 0.5A/sec for Ti, 0.5A/sec for Pt → (The surface roughness of PMN-PT is between 2-10 nm, so a thicker Ti adhesion layer maybe helpful)
  - During deposition, cover up the four sides by Kapton tape to avoid deposition on the side of the sample.
- Lift-off -- In NMP @80 C overnight
- *Descum Matrix Asher (for removing remaining PR) (can skip this step)*
- *Wire bond sample on a leadless chip carrier*

## A-4 Recipe for Terfenol-D Microdisks

1. Heat up two hotplates to 90 °C and 110 °C
2. Solvent clean wafer/PMN-PT substrate with IPA and Acetone (ultrasonic clean)
3. Dehydration bake 90 °C for 10 min (time and temperature not critical for this step)
4. Cool down before spin coat
5. Spincoat negative photoresist AZ nLOF 2020:
  - Step 1: speed = 1000 rpm ramp = 500 rpm/sec 3s
  - Step 2: speed = 3000 rpm ramp = 1000 rpm/sec 45s
  - Step 3: speed = 0 rpm ramp = 500 rpm/sec 0s
6. Soft bake: 110 °C for 1 min
7. Exposure: 3.5 s Hard Contact mode, gap = 30 um (Mercury lamp power at 12 mW/cm<sup>2</sup>)
  - Terfenol-D feature dimensions: 3um and 20um disks
8. Post exposure baking: 110 °C for 1 min
9. Develop in AZ300MIF for 1 min and check under the optical microscope
10. Rinse with DI water and N<sub>2</sub> dry
11. Ar ion etching (Recipe AOE PZT4\_4) – needs calibration every once in a while for etch thickness.

**Note:** One could also use positive photoresist AZ 5214 to get the same result, except for step 6 to 10:

6. Softbake: 100 °C for 1 min
7. Exposure: 8 s Hard Contact mode, gap = 30 um (Mercury lamp power at 12 mW/cm<sup>2</sup>)
8. Develop (no post-exposure bake needed)
9. Develop in diluted AZ400K (AZ 400 K : DI water = 1: 4) for 25 sec
10. Rinse in DI water and N<sub>2</sub> dry

## References

- [1] W. Eerenstein, N. D. Mathur, and J. F. Scott, “Multiferroic and magnetoelectric materials,” *Nature*, vol. 442, no. 7104, pp. 759–765, 2006, doi: 10.1038/nature05023.
- [2] W. F. Brown, R. M. Hornreich, and S. Shtrikman, “Upper Bound on the Magnetoelectric Susceptibility,” *Phys. Rev.*, vol. 168, no. 2, pp. 574–577, 1968, doi: 10.1103/PhysRev.168.574.
- [3] M. Fiebig, T. Lottermoser, D. Meier, and M. Trassin, “The evolution of multiferroics,” *Nat. Rev. Mater.*, vol. 1, no. 8, 2016, doi: 10.1038/natrevmats.2016.46.
- [4] G. Catalan and J. F. Scott, “Physics and applications of bismuth ferrite,” *Adv. Mater.*, vol. 21, no. 24, pp. 2463–2485, 2009, doi: 10.1002/adma.200802849.
- [5] N. A. Spaldin and R. Ramesh, “Advances in magnetoelectric multiferroics,” *Nat. Mater.*, vol. 18, no. 3, pp. 203–212, 2019, doi: 10.1038/s41563-018-0275-2.
- [6] J. Ma, J. Hu, Z. Li, and C. W. Nan, “Recent progress in multiferroic magnetoelectric composites: from bulk to thin films,” *Adv Mater*, vol. 23, no. 9, pp. 1062–1087, 2011, doi: 10.1002/adma.201003636.
- [7] H. Sohn *et al.*, “Electrically driven magnetic domain wall rotation in multiferroic heterostructures to manipulate suspended on-chip magnetic particles,” *ACS Nano*, vol. 9, no. 5, pp. 4814–4826, 2015, doi: 10.1021/nn5056332.
- [8] T. H. E. Lahtinen, K. J. a. Franke, and S. van Dijken, “Electric-field control of magnetic domain wall motion and local magnetization reversal,” *Sci Rep*, vol. 2, p. 258, 2012, doi: 10.1038/srep00258.
- [9] A. Morelli, F. Johann, S. R. Burns, A. Douglas, and J. M. Gregg, “Deterministic Switching in Bismuth Ferrite Nanoislands,” 2016, doi: 10.1021/acs.nanolett.6b02311.
- [10] N. D’Souza, M. S. Fashami, S. Bandyopadhyay, and J. Atulasimha, “Experimental Clocking of Nanomagnets with Strain for Ultralow Power Boolean Logic,” *Nano Lett.*,

- vol. 16, no. 2, pp. 1069–1075, 2016, doi: 10.1021/acs.nanolett.5b04205.
- [11] T. Wu *et al.*, “Domain engineered switchable strain states in ferroelectric (011) [Pb(Mg<sub>1/3</sub>Nb<sub>2/3</sub>)O<sub>3</sub>](1-x)-[PbTiO<sub>3</sub>]<sub>x</sub> (PMN-PT, x≈0.32) single crystals,” *J. Appl. Phys.*, vol. 109, no. 12, p. 124101, 2011, doi: 10.1063/1.3595670.
- [12] E. Villari, “Change of magnetization by tension and by electric current,” *Ann. Phys. Chem.*, vol. 126, pp. 87–122, 1865.
- [13] C. W. Nan, “Magnetoelectric effect in composites of piezoelectric and piezomagnetic phases,” *Phys. Rev. B*, vol. 50, no. 9, pp. 6082–6088, 1994, doi: 10.1103/PhysRevB.50.6082.
- [14] N. Spaldin and M. Fiebig, “The Renaissance of Magnetoelectric Multiferroics,” *Science* (80-. ), vol. 309, no. July, pp. 391–392, 2005.
- [15] M. Bibes and A. Barthélémy, “Multiferroics-Towards-a-magnetoelectric-memory,” *Nat. Mater.*, vol. 7, no. June, pp. 425–426, 2008.
- [16] H. Ahmad, J. Atulasimha, and S. Bandyopadhyay, “Reversible strain-induced magnetization switching in FeGa nanomagnets: Pathway to a rewritable, non-volatile, non-toggle, extremely low energy straintronic memory,” *Sci Rep*, vol. 5, p. 18264, 2015, doi: 10.1038/srep18264.
- [17] J. Cui *et al.*, “A method to control magnetism in individual strain-mediated magnetoelectric islands,” *Appl. Phys. Lett.*, vol. 103, no. 23, p. 232905, 2013, doi: 10.1063/1.4838216.
- [18] Z. Yao, Y. E. Wang, S. Keller, and G. P. Carman, “Bulk Acoustic Wave-Mediated Multiferroic Antennas: Architecture and Performance Bound,” *IEEE Trans. Antennas Propag.*, vol. 63, no. 8, pp. 3335–3344, 2015, doi: 10.1109/tap.2015.2431723.
- [19] H. Sohn *et al.*, “Electrically driven magnetic domain wall rotation in multiferroic heterostructures to manipulate suspended on-chip magnetic particles,” *ACS Nano*, vol.

- 9, no. 5, pp. 4814–4826, 2015, doi: 10.1021/nm5056332.
- [20] H. Sohn *et al.*, “Deterministic multi-step rotation of magnetic single-domain state in Nickel nanodisks using multiferroic magnetoelastic coupling,” *J. Magn. Magn. Mater.*, vol. 439, pp. 196–202, 2017, doi: 10.1016/j.jmmm.2017.04.077.
- [21] Z. Xiao *et al.*, “Bi-directional coupling in strain-mediated multiferroic heterostructures with magnetic domains and domain wall motion,” *Sci Rep*, vol. 8, no. 1, p. 5207, 2018, doi: 10.1038/s41598-018-23020-2.
- [22] R. Lo Conte *et al.*, “Influence of Nonuniform Micron-Scale Strain Distributions on the Electrical Reorientation of Magnetic Microstructures in a Composite Multiferroic Heterostructure,” *Nano Lett.*, vol. 18, no. 3, pp. 1952–1961, 2018, doi: 10.1021/acs.nanolett.7b05342.
- [23] Z. Xiao *et al.*, “Tunable Magnetoelastic Effects in Voltage-Controlled Exchange-Coupled Composite Multiferroic Microstructures,” *ACS Appl. Mater. Interfaces*, vol. 12, no. 5, pp. 6752–6760, 2020, doi: 10.1021/acsami.9b20876.
- [24] R. Khojah, R. Stoutamore, and D. Di Carlo, “Size-tunable microvortex capture of rare cells,” *Lab Chip*, vol. 17, no. 15, pp. 2542–2549, 2017, doi: 10.1039/c7lc00355b.
- [25] X. Ding *et al.*, “Cell separation using tilted-angle standing surface acoustic waves,” *Proc. Natl. Acad. Sci. U. S. A.*, vol. 111, no. 36, pp. 12992–12997, 2014, doi: 10.1073/pnas.1413325111.
- [26] C. Zhang, K. Khoshmanesh, A. Mitchell, and K. Kalantar-Zadeh, “Dielectrophoresis for manipulation of micro/nano particles in microfluidic systems,” *Anal. Bioanal. Chem.*, vol. 396, no. 1, pp. 401–420, 2010, doi: 10.1007/s00216-009-2922-6.
- [27] “Berkeley Lights.” .
- [28] M. C. Wu, P. Y. Chiou, and A. T. Ohta, “Optoelectronic Tweezers? Optical Manipulation using LEDs and Spatial Light Modulators,” pp. 12–13, 2015, doi:

- 10.7567/ssdm.2006.b-7-1.
- [29] National Cancer Institute, “CAR T-Cell Therapy Approved for Some Children and Young Adults with Leukemia,” 2017. .
- [30] S. Rafiq, C. S. Hackett, and R. J. Brentjens, “Engineering strategies to overcome the current roadblocks in CAR T cell therapy,” *Nat. Rev. Clin. Oncol.*, vol. 17, no. 3, pp. 147–167, 2020, doi: 10.1038/s41571-019-0297-y.
- [31] M. Donolato *et al.*, “On-chip manipulation of protein-coated magnetic beads via domain-wall conduits,” *Adv. Mater.*, vol. 22, no. 24, pp. 2706–2710, 2010, doi: 10.1002/adma.201000146.
- [32] P. Tseng *et al.*, “Flexible and stretchable micromagnet arrays for tunable biointerfacing,” *Adv Mater*, vol. 27, no. 6, pp. 1083–1089, 2015, doi: 10.1002/adma.201404849.
- [33] G. M. Whitesides, E. Ostuni, X. Jiang, and D. E. Ingber, “Soft lithography in Biology,” *Annu. Rev. Biomed. Eng.*, vol. 3, pp. 335–73, 2001.
- [34] T. L. Gilbert, “Classics in Magnetism A Phenomenological Theory of Damping in Ferromagnetic Materials,” *IEEE Trans. Magn.*, vol. 40, no. 6, pp. 3443–3449, 2004, doi: 10.1109/tmag.2004.836740.
- [35] J. M. D. Coey, *Magnetism and Magnetic Materials*. Cambridge University Press, 2009.
- [36] N. A. Spaldin, *Magnetic Materials: Fundamentals and Applications*, 2nd ed. Cambridge University Press, 2011.
- [37] D. Jiles, *Introduction to Magnetism and Magnetic Materials*. 1991.
- [38] J. L. Hockel, A. Bur, T. Wu, K. P. Wetzlar, and G. P. Carman, “Electric field induced magnetization rotation in patterned Ni ring/Pb(Mg<sub>1/3</sub>Nb<sub>2/3</sub>O-3)((120.32))-[PbTiO<sub>3</sub>](0.32) heterostructures,” *Appl. Phys. Lett.*, vol. 100, no. 2, 2012, doi: Artn 022401 10.1063/1.3675458.
- [39] S. Zhang *et al.*, “Giant electrical modulation of magnetization in

- Co<sub>40</sub>Fe<sub>40</sub>B<sub>20</sub>/Pb(Mg<sub>1/3</sub>Nb<sub>2/3</sub>)<sub>0.7</sub>Ti<sub>0.3</sub>O<sub>3</sub>(011) heterostructure,” *Sci Rep*, vol. 4, p. 3727, 2014, doi: 10.1038/srep03727.
- [40] S. Dong, J. Cheng, J. F. Li, and D. Viehland, “Enhanced magnetoelectric effects in laminate composites of Terfenol-D/Pb(Zr,Ti)O<sub>3</sub> under resonant drive,” *Appl. Phys. Lett.*, vol. 83, no. 23, p. 4812, 2003, doi: 10.1063/1.1631756.
- [41] G. Dewar, “Effect of the large magnetostriction of Terfenol-D on microwave transmission,” *J. Appl. Phys.*, vol. 81, no. 8, p. 5713, 1997, doi: 10.1063/1.364646.
- [42] R. P. . P. Beardsley D. E.; Zemen, J.; Bowe, S.; Edmonds, K. W.; Reardon, C.; Maccherozzi, F.; Isakov, I.; Warburton, P. A.; Campion, R. P.; Gallagher, B. L.; Cavill, S. A.; Rushforth, A. W., “Effect of lithographically-induced strain relaxation on the magnetic domain configuration in microfabricated epitaxially grown Fe<sub>81</sub>Ga<sub>19</sub>,” *eprint arXiv:1609.02930*, 2016.
- [43] M. M. A.-R. Dhritiman Bhattacharya Noel D’Souza, Supriyo Bandyopadhyay, Jayasimha Atulasimha, “Incoherent magnetization dynamics in strain mediated switching of magnetostrictive nanomagnets,” 2015, doi: 10.1088/0957-4484/28/1/015202.
- [44] Z. Xiao *et al.*, “Bi-directional coupling in strain-mediated multiferroic heterostructures with magnetic domains and domain wall motion,” *Sci. Rep.*, vol. 8, no. 1, p. 5207, 2018, doi: 10.1038/s41598-018-23020-2.
- [45] J. Walowski, M. D. Kaufmann, B. Lenk, C. Hamann, J. McCord, and M. Münzenberg, “Intrinsic and non-local Gilbert damping in polycrystalline nickel studied by Ti : sapphire laser fs spectroscopy,” *J. Phys. D. Appl. Phys.*, vol. 41, no. 16, p. 164016, 2008, doi: 10.1088/0022-3727/41/16/164016.
- [46] D. B. Gopman, J. W. Lau, K. P. Mohanchandra, K. Wetzlar, and G. P. Carman, “Determination of the exchange constant of Tb<sub>0.3</sub>Dy<sub>0.7</sub>Fe<sub>2</sub> by broadband

- ferromagnetic resonance spectroscopy,” *Phys Rev B*, vol. 93, no. 6, 2016, doi: 10.1103/PhysRevB.93.064425.
- [47] C. Y. Liang *et al.*, “Modeling of magnetoelastic nanostructures with a fully coupled mechanical-micromagnetic model,” *Nanotechnology*, vol. 25, no. 43, p. 435701, 2014, doi: 10.1088/0957-4484/25/43/435701.
- [48] P. Duran and C. Moure, “Piezoelectric ceramics,” *Mater. Chem. Phys.*, vol. 15, no. 3–4, pp. 193–211, 1986, doi: 10.1016/0254-0584(86)90001-5.
- [49] T. Wu *et al.*, “Domain engineered switchable strain states in ferroelectric (011) [Pb(Mg<sub>1/3</sub>Nb<sub>2/3</sub>)O<sub>3</sub>]<sub>(1-x)</sub>-[PbTiO<sub>3</sub>]<sub>x</sub>(PMN-PT, x≈0.32) single crystals,” *J. Appl. Phys.*, vol. 109, no. 12, p. 124101, 2011, doi: 10.1063/1.3595670.
- [50] J. Irwin *et al.*, “Magnetoelectric Coupling by Piezoelectric Tensor Design,” *Sci. Rep.*, vol. 9, no. 1, p. 19158, 2019, doi: 10.1038/s41598-019-55139-1.
- [51] Y. Ba *et al.*, “Spatially Resolved Electric-Field Manipulation of Magnetism for CoFeB Mesoscopic Discs on Ferroelectrics,” *Adv. Funct. Mater.*, vol. 28, no. 11, p. 1706448, 2018, doi: 10.1002/adfm.201706448.
- [52] C. Chen *et al.*, “Voltage manipulation of magnetic particles using multiferroics,” *J. Phys. D. Appl. Phys.*, vol. 53, no. 17, p. 174002, 2020, doi: 10.1088/1361-6463/ab7038.
- [53] J. Clarke, “SQUIDS,” *Sci. Am.*, vol. 271, no. 2, pp. 46–53, 1994.
- [54] N. R, “SQUID Magnetometer.” [Online]. Available: <http://hyperphysics.phy-astr.gsu.edu/hbase/Solids/Squid.html>.
- [55] P. N. Argyres, “Theory of the Faraday and Kerr effects in ferromagnetics,” *Phys. Rev.*, vol. 97, no. 2, pp. 334–345, 1955, doi: 10.1103/PhysRev.97.334.
- [56] S. Tumanski, *Handbook of Magnetic Measurements*. CRC Press, 2011.
- [57] S. D. Bader and J. L. Erskine, “Magneto-Optical Effects in Ultrathin Magnetic Structures,” in *Ultrathin Magnetic Structures II: Measurement Techniques and Novel*



- Magnetic Properties*, B. Heinrich and J. A. C. Bland, Eds. Berlin, Heidelberg: Springer Berlin Heidelberg, 1994, pp. 297–325.
- [58] Z. Xiao *et al.*, “Enhanced magnetoelectric coupling in a composite multiferroic system via interposing a thin film polymer,” *AIP Adv.*, vol. 8, no. 5, p. 55907, 2018, doi: 10.1063/1.5007655.
- [59] K. P. Mohanchandra, S. V Prikhodko, K. P. Wetzlar, W. Y. Sun, P. Nordeen, and G. P. Carman, “Sputter deposited Terfenol-D thin films for multiferroic applications,” *AIP Adv.*, vol. 5, no. 9, p. 97119, 2015, doi: 10.1063/1.4930602.
- [60] J. S. H. C. Siegmann, *Magnetism from fundamental to dynamics*, vol. 152. 2006.
- [61] L. Abelmann, “Magnetic Force Microscopy,” in *Encyclopedia of Spectroscopy and Spectrometry (Third Edition)*, Third Edit., J. C. Lindon, G. E. Tranter, and D. W. Koppenaal, Eds. Oxford: Academic Press, 2017, pp. 675–684.
- [62] H. J. Mamin, D. Rugar, B. W. Chui, and R. Budakian, “Single spin detection by magnetic resonance force microscopy,” *Nature*, vol. 430, pp. 329–332, 2004.
- [63] R. C. O’Handley, *Modern Magnetic Materials*, vol. 13, no. 4. John Wiley & Sons, Inc., 2000.
- [64] H. Sohn *et al.*, “Deterministic multi-step rotation of magnetic single-domain state in Nickel nanodisks using multiferroic magnetoelastic coupling,” *J. Magn. Magn. Mater.*, vol. 439, pp. 196–202, 2017, doi: 10.1016/j.jmmm.2017.04.077.
- [65] M. K. Panduranga *et al.*, “Single magnetic domain Terfenol-D microstructures with passivating oxide layer,” *J. Magn. Magn. Mater.*, vol. 528, no. January, 2021, doi: 10.1016/j.jmmm.2021.167798.
- [66] J. Cui *et al.*, “Generation of localized strain in a thin film piezoelectric to control individual magnetoelectric heterostructures,” *Appl. Phys. Lett.*, vol. 107, no. 9, 2015, doi: 10.1063/1.4930071.

- [67] R. Khojah *et al.*, “Single-Domain Multiferroic Array-Addressable Terfenol-D (SMArT) Micromagnets for Programmable Single-Cell Capture and Release,” *Adv. Mater.*, p. 2006651, 2021, doi: 10.1002/adma.202006651.
- [68] G. Van Der Laan *et al.*, “Experimental proof of magnetic x-ray dichroism,” *Phys. Rev. B*, vol. 34, no. 9, pp. 6529–6531, 1986, doi: 10.1103/PhysRevB.34.6529.
- [69] G. Van Der Laan, “Applications of soft x-ray magnetic dichroism,” *J. Phys. Conf. Ser.*, vol. 430, no. 1, 2013, doi: 10.1088/1742-6596/430/1/012127.
- [70] “PEEM-3 at the ALS: X-ray Photoemission Electron Microscopy.” [Online]. Available: <http://xraysweb.lbl.gov/peem2/webpage/Home.shtml>.
- [71] “Biaxial Strain Gauge.” [Online]. Available: [https://img.directindustry.com/images\\_di/photo-g/6017-12173179.jpg](https://img.directindustry.com/images_di/photo-g/6017-12173179.jpg).
- [72] H. A. S. Shin *et al.*, “Microstructure evolution and defect formation in Cu through-silicon vias (TSVs) during thermal annealing,” *J. Electron. Mater.*, vol. 41, no. 4, pp. 712–719, 2012, doi: 10.1007/s11664-012-1943-7.
- [73] C. Thiele, K. Dörr, O. Bilani, J. Rödel, and L. Schultz, “Influence of strain on the magnetization and magnetoelectric effect in  $\text{La}_{0.7}\text{A}_{0.3}\text{MnO}_3$  PMN-PT (001) (A=Sr,Ca),” *Phys. Rev. B - Condens. Matter Mater. Phys.*, vol. 75, no. 5, p. 054408, 2007, doi: 10.1103/PhysRevB.75.054408.
- [74] N. Tamura *et al.*, “Scanning X-ray microdiffraction with submicrometer white beam for strain/stress and orientation mapping in thin films,” *J. Synchrotron Radiat.*, vol. 10, no. 2, pp. 137–143, 2003, doi: 10.1107/S0909049502021362.
- [75] P. A. Lynch, A. W. Stevenson, D. Liang, D. Parry, S. Wilkins, and N. Tamura, “A laboratory based system for Laue micro x-ray diffraction,” *Rev. Sci. Instrum.*, vol. 78, no. 2, p. 023904, 2007, doi: 10.1063/1.2437777.
- [76] M. Goiriena-Goikoetxea *et al.*, “Influence of dislocations and twin walls in  $\text{BaTiO}_3$  on

- the voltage-controlled switching of perpendicular magnetization,” *Phys. Rev. Mater.*, vol. 5, no. 2, p. 24401, 2021, doi: 10.1103/physrevmaterials.5.024401.
- [77] M. Kunz *et al.*, “A dedicated superbend x-ray microdiffraction beamline for materials, geo-, and environmental sciences at the advanced light source,” *Rev. Sci. Instrum.*, vol. 80, no. 3, 2009, doi: 10.1063/1.3096295.
- [78] N. Tamura, “XMAS: A Versatile Tool for Analyzing Synchrotron X-ray Microdiffraction Data,” in *Strain and Dislocation Gradients from Diffraction: Spatially-Resolved Local Structure and Defects*, R. Barabash and G. Ice, Eds. Imperial College Press: London, 2014, pp. 125–155.
- [79] Z. Xiao, “Controlling magnetization and strain at the micron-scale and below in strain-mediated composite multiferroic devices,” UCLA, 2017.
- [80] L. E. Levine, C. Okoro, and R. Xu, “Full elastic strain and stress tensor measurements from individual dislocation cells in copper through-Si vias,” *IUCrJ*, vol. 2, pp. 635–642, 2015, doi: 10.1107/S2052252515015031.
- [81] T. Q. Phan *et al.*, “Synchrotron X-ray microbeam diffraction measurements of full elastic long range internal strain and stress tensors in commercial-purity aluminum processed by multiple passes of equal-channel angular pressing,” *Acta Mater.*, vol. 112, pp. 231–241, 2016, doi: 10.1016/j.actamat.2016.04.035.
- [82] I. C. Noyan and J. B. Cohan, *Residual Stress Measurement by Diffraction and Interpretation*. Springer, 1987.
- [83] K. L. Wang, J. G. Alzate, and P. Khalili Amiri, “Low-power non-volatile spintronic memory: STT-RAM and beyond,” *J. Phys. D: Appl. Phys.*, vol. 46, no. 8, 2013, doi: 10.1088/0022-3727/46/7/074003.
- [84] V. Novosad *et al.*, “Novel Magnetostrictive Memory Device,” *J. Appl. Phys.*, vol. 87, no. 9, pp. 6400–6402, 2000, doi: 10.1063/1.372719.

- [85] M. Buzzi *et al.*, “Single domain spin manipulation by electric fields in strain coupled artificial multiferroic nanostructures,” *Phys Rev Lett*, vol. 111, no. 2, p. 27204, 2013, doi: 10.1103/PhysRevLett.111.027204.
- [86] S. Zhao, J. Wan, M. Yao, J. Liu, F. Song, and G. Wang, “Flexible Sm–Fe/Polyvinylidene Fluoride Heterostructural Film with Large Magnetoelectric Voltage Output,” vol. 97. *Appl. Phys. Lett.*, p. 212902, 2010.
- [87] A. J. Schellekens, A. van den Brink, J. H. Franken, H. J. Swagten, and B. Koopmans, “Electric-field control of domain wall motion in perpendicularly magnetized materials,” *Nat Commun*, vol. 3, p. 847, 2012, doi: 10.1038/ncomms1848.
- [88] Y. Bai, N. Jiang, and S. Zhao, “Giant Magnetoelectric Effects in Pseudo 1–3 Heterostructure Films with FeGa Nanocluster-assembled Micron-scale Discs embedded into Bi<sub>5</sub>Ti<sub>3</sub>FeO<sub>15</sub> Matrices,” vol. 10. *Nanoscale*, 2018, doi: 10.1039/c7nr09652f.
- [89] Z. Xiao *et al.*, “Electric-field controlled magnetic reorientation in exchange coupled CoFeB/Ni bilayer microstructures,” *Journal of Physics: Conference Series*, vol. 1407. 2019, doi: 10.1088/1742-6596/1407/1/012024.
- [90] E. Klokholm and J. Aboaf, “The saturation magnetostriction of thin polycrystalline films of iron, cobalt, and nickel,” *J. Appl. Phys.*, vol. 53, no. 3, pp. 2661–2663, 1982, doi: 10.1063/1.330930.
- [91] I. A. O. Thomas Tsakalakos Asuri K. Vasudevan, Ed., *Nanostructures: Synthesis, Functional Properties and Applications*. Springer Science & Business Media.
- [92] Z. Xiao *et al.*, “Electric-field controlled magnetic reorientation in exchange coupled CoFeB/Ni bilayer microstructures,” *J. Phys. Conf. Ser.*, vol. 1407, no. 1, 2019, doi: 10.1088/1742-6596/1407/1/012024.
- [93] D. J. Sellmyer and Z. S. Shan, “Magnetic Hysteresis in Novel Nanostructured Films,” in *Magnetic Hysteresis in Novel Magnetic Materials*, G. C. Hadjipanayis, Ed. Dordrecht:

- Springer Netherlands, 1997, pp. 419–451.
- [94] C. A. Neugebauer, “Saturation Magnetization of Nickel Films of Thickness Less Than 100 Å,” *Phys. Rev.*, vol. 116, no. 6, pp. 1441–1446, 1959, doi: 10.1103/PhysRev.116.1441.
- [95] C. T. Chen *et al.*, “Experimental Confirmation of the X-Ray Magnetic Circular-Dichroism Sum-Rules for Iron and Cobalt,” *Phys. Rev. Lett.*, vol. 75, no. 1, pp. 152–155, 1995, doi: DOI 10.1103/PhysRevLett.75.152.
- [96] G. Schönhense, “Imaging of magnetic structures by photoemission electron microscopy,” *J. Phys. Condens. Matter*, vol. 11, no. 9517, 1999.
- [97] R. S. Alex Hubert, *Magnetic Domains: The Analysis of Magnetic Microstructures*. Berlin: Springer, 1998.
- [98] J. Ryu, S. Priya, K. Uchino, and H. E. Kim, “Magnetolectric effect in composites of magnetostrictive and piezoelectric materials,” *J. Electroceramics*, vol. 8, no. 2, pp. 107–119, 2002, doi: Doi 10.1023/A:1020599728432.
- [99] J. L. Hockel, A. Bur, T. Wu, K. P. Wetzlar, and G. P. Carman, “Electric field induced magnetization rotation in patterned Ni ring/Pb(Mg<sub>1/3</sub>Nb<sub>2/3</sub>)O<sub>3</sub>[(1–0.32)-[PbTiO<sub>3</sub>]<sub>0.32</sub> heterostructures,” *Appl. Phys. Lett.*, vol. 100, no. 2, p. 022401, 2012, doi: 10.1063/1.3675458.
- [100] J. Chen, Y. Bai, C. Nie, and S. Zhao, “Strong Magnetolectric Effect of Bi<sub>4</sub>Ti<sub>3</sub>O<sub>12</sub>/Bi<sub>5</sub>Ti<sub>3</sub>FeO<sub>15</sub> Composite Films,” vol. 663. *Journal of Alloys and Compounds*, pp. 480–486, 2016, doi: <https://doi.org/10.1016/j.jallcom.2015.12.088>.
- [101] S. D. Sloetjes *et al.*, “Interplay between bulk and edge-bound topological defects in a square micromagnet,” *Appl. Phys. Lett.*, vol. 112, no. 4, p. 42401, 2018, doi: 10.1063/1.5010166.
- [102] A. Vansteenkiste, J. Leliaert, M. Dvornik, M. Helsen, F. Garcia-Sanchez, and B. Van

- Waeyenberge, “The design and verification of MuMax3,” *AIP Adv.*, vol. 4, no. 10, p. 107133, 2014, doi: 10.1063/1.4899186.
- [103] M. I. Bichurin, V. M. Petrov, and G. Srinivasan, “Theory of low-frequency magnetoelectric coupling in magnetostrictive-piezoelectric bilayers,” *Phys. Rev. B*, vol. 68, no. 5, 2003, doi: ARTN 054402 10.1103/PhysRevB.68.054402.
- [104] C. Jin, J. H. Liu, and C. B. Jiang, “Magnetic domain characterisation of high magnetic field treated FeGa single crystal,” *Mater. Res. Innov.*, vol. 18, no. sup4, pp. S4-597-S4-600, 2014, doi: 10.1179/1432891714z.000000000745.
- [105] E. W. Lee, “Magnetostriction and Magnetomechanical Effects,” *Reports Prog. Phys.*, vol. 18, pp. 184–229, 1955, doi: Doi 10.1088/0034-4885/18/1/305.
- [106] D. Hunter *et al.*, “Giant magnetostriction in annealed Co(1-x)Fe(x) thin-films,” *Nat Commun*, vol. 2, p. 518, 2011, doi: 10.1038/ncomms1529.
- [107] Z. Xiao *et al.*, “Cytocompatible magnetostrictive microstructures for nano- and microparticle manipulation on linear strain response piezoelectrics,” *Multifunct. Mater.*, vol. 1, no. 1, p. 014004, 2018, doi: 10.1088/2399-7532/aae4d7.
- [108] W. M. Stefan Miltenyi Walter Weichel, and Andreas Radbruchyl, “High Gradient Magnetic Cell Separation With MACs,” *Cytom. J. Int. Soc. Anal. Cytol.*, no. 11, pp. 231–238, 1990.
- [109] C. Murray *et al.*, “Quantitative Magnetic Separation of Particles and Cells Using Gradient Magnetic Ratcheting,” *Small*, vol. 12, no. 14, pp. 1891–1899, 2016, doi: 10.1002/sml.201502120.
- [110] A. Rosenthal and J. Voldman, “Dielectrophoretic traps for single-particle patterning,” *Biophys J*, vol. 88, no. 3, pp. 2193–2205, 2005, doi: 10.1529/biophysj.104.049684.
- [111] K. C. Neuman and A. Nagy, “Single-molecule force spectroscopy: optical tweezers, magnetic tweezers and atomic force microscopy,” *Nat Methods*, vol. 5, no. 6, pp. 491–

- 505, 2008, doi: 10.1038/nmeth.1218.
- [112] I. De Vlaminck and C. Dekker, “Recent advances in magnetic tweezers,” *Annu Rev Biophys*, vol. 41, pp. 453–472, 2012, doi: 10.1146/annurev-biophys-122311-100544.
- [113] B. Lim, P. Vavassori, R. Sooryakumar, and C. Kim, “Nano/micro-scale magnetophoretic devices for biomedical applications,” *J. Phys. D. Appl. Phys.*, vol. 50, no. 3, p. 33002, 2017, doi: 10.1088/1361-6463/50/3/033002.
- [114] P. Sajeesh and A. K. Sen, “Particle separation and sorting in microfluidic devices: a review,” *Microfluid. Nanofluidics*, vol. 17, no. 1, pp. 1–52, 2013, doi: 10.1007/s10404-013-1291-9.
- [115] A. Greenbaum *et al.*, “Wide-field computational imaging of pathology slides using lens-free on-chip microscopy,” *Sci. Transl. Med.*, vol. 6, no. 267, p. 267ra175, 2014, doi: DOI: 10.1126/scitranslmed.3009850.
- [116] C. Brasko *et al.*, “Intelligent image-based in situ single-cell isolation,” *Nat Commun*, vol. 9, no. 1, p. 226, 2018, doi: 10.1038/s41467-017-02628-4.
- [117] J. A. Gallagher, J. Tian, and C. S. Lynch, “Composition dependence of field induced phase transformations in [0 1 1] C PIN–PMN–PT relaxor ferroelectric single crystals with d<sub>322</sub> piezoelectric mode,” *Acta Mater.*, vol. 81, pp. 512–523, 2014, doi: 10.1016/j.actamat.2014.06.062.
- [118] T. Wu *et al.*, “Electrical control of reversible and permanent magnetization reorientation for magnetoelectric memory devices,” *Appl. Phys. Lett.*, vol. 98, no. 26, p. 262504, 2011, doi: 10.1063/1.3605571.
- [119] S. Knowlton, A. Joshi, P. Syrrist, A. F. Coskun, and S. Tasoglu, “3D-printed smartphone-based point of care tool for fluorescence- and magnetophoresis-based cytometry,” *Lab Chip*, vol. 17, no. 16, pp. 2839–2851, 2017, doi: 10.1039/c7lc00706j.
- [120] M. Kläui *et al.*, “Switching processes and switching reproducibility in ferromagnetic

- ring structures,” *Appl. Phys. Lett.*, vol. 84, no. 6, pp. 951–953, 2004, doi: 10.1063/1.1640451.
- [121] M. Klaui, C. A. F. Vaz, L. Lopez-Diaz, and J. A. C. Bland, “Vortex formation in narrow ferromagnetic rings,” *J. Physics-Condensed Matter*, vol. 15, no. 21, pp. R985–R1023, 2003.
- [122] M. Foerster *et al.*, “Direct imaging of delayed magneto-dynamic modes induced by surface acoustic waves,” *Nat Commun*, vol. 8, no. 1, p. 407, 2017, doi: 10.1038/s41467-017-00456-0.
- [123] X. M. Cheng and D. J. Keavney, “Studies of nanomagnetism using synchrotron-based x-ray photoemission electron microscopy (X-PEEM),” *Rep Prog Phys*, vol. 75, no. 2, p. 26501, 2012, doi: 10.1088/0034-4885/75/2/026501.
- [124] L. Breitenstein, P. Lendেকে, S. Bohlens, G. Meier, and U. Merkt, “Stray field of a Landau magnetization pattern,” *J. Appl. Phys.*, vol. 104, no. 8, p. 83909, 2008, doi: 10.1063/1.3000479.
- [125] M. J. Stoddart, *Cell viability assays: introduction." Mammalian Cell Viability*. Humana Press, 2011.
- [126] B. Lim *et al.*, “Magnetophoretic circuits for digital control of single particles and cells,” *Nat Commun*, vol. 5, p. 3846, 2014, doi: 10.1038/ncomms4846.
- [127] G. Vieira *et al.*, “Magnetic Wire Traps and Programmable Manipulation of Biological Cells,” *Phys. Rev. Lett.*, vol. 103, no. 12, pp. 16–19, 2009, doi: 10.1103/PhysRevLett.103.128101.
- [128] M. Fiebig, “Revival of the magnetoelectric effect,” *J. Phys. D. Appl. Phys.*, vol. 38, no. 8, 2005, doi: 10.1088/0022-3727/38/8/R01.
- [129] S. Miltenyi, W. Muller, W. Weichel, and A. Radbruch, “High Gradient Magnetic Cell Separation With MACS,” *Cytometry*, vol. 11, no. 2, pp. 231–238, 1990, doi:



<https://doi.org/10.1002/cyto.990110203>.

- [130] A. H. Talasz *et al.*, “Isolating highly enriched populations of circulating epithelial cells and other rare cells from blood using a magnetic sweeper device,” *Proc. Natl. Acad. Sci. U. S. A.*, vol. 106, no. 10, pp. 3970–3975, 2009, doi: 10.1073/pnas.0813188106.
- [131] R. S. Molday, S. P. S. Yen, and A. Rembaum, “Application of magnetic microspheres in labelling and separation of cells,” *Nature*, vol. 268, no. 5619, pp. 437–438, 1977, doi: 10.1038/268437a0.
- [132] M. Albert, M. Franchin, T. Fischbacher, G. Meier, and H. Fangohr, “Domain wall motion in perpendicular anisotropy nanowires with edge roughness,” *J Phys Condens Matter*, vol. 24, no. 2, p. 24219, 2012, doi: 10.1088/0953-8984/24/2/024219.
- [133] A. Aijaz *et al.*, “Biomanufacturing for clinically advanced cell therapies,” *Nat. Biomed. Eng.*, vol. 2, no. 6, pp. 362–376, 2018, doi: 10.1038/s41551-018-0246-6.
- [134] Z. L. Chang, P. A. Silver, and Y. Y. Chen, “Identification and selective expansion of functionally superior T cells expressing chimeric antigen receptors,” *J. Transl. Med.*, vol. 13, no. 1, pp. 1–16, 2015.
- [135] T. R. Mosmann and R. L. Coffman, “Heterogeneity of Cytokine Secretion Patterns and Functions of Helper T Cells,” vol. 46, F. J. Dixon, Ed. Academic Press, 1989, pp. 111–147.
- [136] M. Hölzel, A. Bovier, and T. Tüting, “Plasticity of tumour and immune cells: A source of heterogeneity and a cause for therapy resistance?,” *Nat. Rev. Cancer*, vol. 13, no. 5, pp. 365–376, 2013, doi: 10.1038/nrc3498.
- [137] E. R. Jerison and S. R. Quake, “Heterogeneous T cell motility behaviors emerge from a coupling between speed and turning in vivo,” *Elife*, vol. 9, p. e53933, 2020.
- [138] A. D. Fesnak, C. H. June, and B. L. Levine, “Engineered T cells: The promise and challenges of cancer immunotherapy,” *Nat. Rev. Cancer*, vol. 16, no. 9, pp. 566–581,

- 2016, doi: 10.1038/nrc.2016.97.
- [139] N. M. Mount, S. J. Ward, P. Kefalas, and J. Hyllner, “Cell-based therapy technology classifications and translational challenges,” *Philos. Trans. R. Soc. B Biol. Sci.*, vol. 370, no. 1680, 2015, doi: 10.1098/rstb.2015.0017.
- [140] B. D. C. and C. D. Graham, *Introduction to Magnetic Materials*. Hoboken, NJ, USA: John Wiley & Sons, Inc., 2008.
- [141] M. Poudineh *et al.*, “Tracking the dynamics of circulating tumour cell phenotypes using nanoparticle-mediated magnetic ranking,” *Nat. Nanotechnol.*, vol. 12, no. 3, pp. 274–281, 2017, doi: 10.1038/nnano.2016.239.
- [142] P. Chen, Y. Y. Huang, K. Hoshino, and J. X. Zhang, “Microscale magnetic field modulation for enhanced capture and distribution of rare circulating tumor cells,” *Sci Rep*, vol. 5, p. 8745, 2015, doi: 10.1038/srep08745.
- [143] Y.-H. Chu *et al.*, “Electric-field control of local ferromagnetism using a magnetoelectric multiferroic,” *Nat Mater*, vol. 7, no. 6, pp. 478–482, Jun. 2008.
- [144] S. Manipatruni, D. E. Nikonov, and I. A. Young, “Beyond CMOS computing with spin and polarization,” *Nat. Phys.*, vol. 14, no. 4, pp. 338–343, 2018, doi: 10.1038/s41567-018-0101-4.
- [145] A. Ney, C. Pampuch, R. Koch, and K. H. Ploog, “Programmable computing with a single magnetoresistive element,” *Nature*, vol. 425, no. 6957, pp. 485–487, 2003, doi: 10.1038/nature02014.
- [146] Z. Luo *et al.*, “Current-driven magnetic domain-wall logic,” *Nature*, vol. 579, no. 7798, pp. 214–218, 2020, doi: 10.1038/s41586-020-2061-y.
- [147] A. K. Biswas, S. Bandyopadhyay, and J. Atulasimha, “Complete magnetization reversal in a magnetostrictive nanomagnet with voltage-generated stress: A reliable energy-efficient non-volatile magneto-elastic memory,” *Appl. Phys. Lett.*, vol. 105, no. 7, 2014,

- doi: 10.1063/1.4893617.
- [148] S. Manipatruni *et al.*, “Scalable energy-efficient magnetoelectric spin–orbit logic,” *Nature*, vol. 565, no. 7737, pp. 35–42, 2019, doi: 10.1038/s41586-018-0770-2.
- [149] G. Youssef, S. Newacheck, M. Lopez, and R. Stampfli, “Triaxial Magnetic Flux Emanation in Response to Uniaxial Electric Field in Magnetoelectric Composite Cylinder Structure,” *Phys. Status Solidi Appl. Mater. Sci.*, vol. 217, no. 15, pp. 1–7, 2020, doi: 10.1002/pssa.202000177.
- [150] C. W. Nan, M. I. Bichurin, S. Dong, D. Viehland, and G. Srinivasan, “Multiferroic magnetoelectric composites: Historical perspective, status, and future directions,” *J. Appl. Phys.*, vol. 103, no. 3, p. 031101, 2008, doi: 10.1063/1.2836410.
- [151] W. Gong, H. Li, Z. Zhao, and J. Chen, “Ultrafine particles of Fe, Co, and Ni ferromagnetic metals,” *J. Appl. Phys.*, vol. 69, no. 8, pp. 5119–5121, 1991, doi: 10.1063/1.348144.
- [152] P. Fischer *et al.*, “Study of magnetic domains by magnetic soft x-ray transmission microscopy,” *J. Phys. D. Appl. Phys.*, vol. 35, no. 19, pp. 2391–2397, 2002, doi: 10.1088/0022-3727/35/19/310.
- [153] T. A. Duenas and G. P. Carman, “Large magnetostrictive response of Terfenol-D resin composites (invited),” *J. Appl. Phys.*, vol. 87, no. 9 II, pp. 4696–4701, 2000, doi: 10.1063/1.373133.
- [154] T. Magno De Lima Alves *et al.*, “Wasp-waisted behavior in magnetic hysteresis curves of CoFe<sub>2</sub>O<sub>4</sub> nanopowder at a low temperature: Experimental evidence and theoretical approach,” *RSC Adv.*, vol. 7, no. 36, pp. 22187–22196, 2017, doi: 10.1039/c6ra28727a.
- [155] J. C. Parlebas, K. Asakura, A. Fujiwara, I. Harada, and A. Kotani, “X-ray magnetic circular dichroism at rare-earth L<sub>23</sub> absorption edges in various compounds and alloys,” *Phys. Rep.*, vol. 431, no. 1, pp. 1–38, 2006, doi: 10.1016/j.physrep.2006.05.002.

- [156] R. T. M. Jun Ye, “Residual stress and domain structure,” *J. Geophys. Res.*, vol. 100, no. B6, pp. 9995–10002, 1995.
- [157] R. Khojah *et al.*, *Supplementary Movies on Single-Domain Multiferroic Array-Addressable Terfenol-D Micromagnets*. 2021.
- [158] Y. C. Hsiao *et al.*, “Capturing magnetic bead-based arrays using perpendicular magnetic anisotropy,” *Appl. Phys. Lett.*, vol. 115, no. 8, p. 082402, 2019, doi: 10.1063/1.5085354.
- [159] J. Happel and H. Brenner, *Low Reynolds number hydrodynamics: with special applications to particulate media*, vol. 1. Springer Science & Business Media, 2012.
- [160] J. Leach *et al.*, “Comparison of Faxén’s correction for a microsphere translating or rotating near a surface,” *Phys. Rev. E - Stat. Nonlinear, Soft Matter Phys.*, vol. 79, no. 2, pp. 1–4, 2009, doi: 10.1103/PhysRevE.79.026301.
- [161] R. Proksch *et al.*, “Quantitative magnetic field measurements with the magnetic force microscope,” *Appl. Phys. Lett.*, vol. 69, no. 17, pp. 2599–2601, 1996, doi: 10.1063/1.117712.
- [162] G. Shaw, R. B. G. Kramer, N. M. Dempsey, and K. Hasselbach, “A scanning Hall probe microscope for high resolution, large area, variable height magnetic field imaging,” *Rev. Sci. Instrum.*, vol. 87, no. 11, 2016, doi: 10.1063/1.4967235.
- [163] S. Kim and S. J. Karrila, *Microhydrodynamics: principles and selected applications*. Courier Corporation, 2013.
- [164] C. Hurth *et al.*, “Biomolecular interactions control the shape of stains from drying droplets of complex fluids,” *Chem. Eng. Sci.*, vol. 137, pp. 398–403, 2015, doi: 10.1016/j.ces.2015.06.059.
- [165] P. Reith, X. Renshaw Wang, and H. Hilgenkamp, “Analysing magnetism using scanning SQUID microscopy,” *Rev. Sci. Instrum.*, vol. 88, no. 12, 2017, doi: 10.1063/1.5001390.
- [166] S. H. Ross and D. A. Cantrell, “Signaling and function of interleukin-2 in T

- lymphocytes,” *Annu. Rev. Immunol.*, vol. 36, pp. 411–433, 2018.
- [167] S. R. Burns, O. Paull, J. Juraszek, V. Nagarajan, and D. Sando, “The Experimentalist’s Guide to the Cycloid, or Noncollinear Antiferromagnetism in Epitaxial BiFeO<sub>3</sub>,” *Adv. Mater.*, 2020, doi: 10.1002/adma.202003711.
- [168] G. Sreenivasulu, P. Qu, V. M. Petrov, H. Qu, and G. Srinivasan, “Magneto-electric interactions at bending resonance in an asymmetric multiferroic composite: Theory and experiment on the influence of electrode position,” *J. Appl. Phys.*, vol. 117, no. 17, 2015, doi: 10.1063/1.4919818.
- [169] W. Peng, B. Howe, and X. Yang, “Multiferroic RF/microwave devices,” in *Integrated Multiferroic Heterostructures and Applications*, 2019, pp. 157–174.
- [170] C.-Y. Liang *et al.*, “Modeling of magnetoelastic nanostructures with a fully coupled mechanical-micromagnetic model,” *Nanotechnology*, vol. 25, no. 43, p. 435701, 2014, doi: 10.1088/0957-4484/25/43/435701.
- [171] S. Zhang *et al.*, “Giant electrical modulation of magnetization in Co<sub>40</sub>Fe<sub>40</sub>B<sub>20</sub>/Pb(Mg<sub>1/3</sub>Nb<sub>2/3</sub>)<sub>0.7</sub>Ti<sub>0.3</sub>O<sub>3</sub>(011) heterostructure,” *Sci Rep*, vol. 4, p. 3727, May 2014, doi: 10.1038/srep03727.
- [172] T. Wu *et al.*, “Giant electric-field-induced reversible and permanent magnetization reorientation on magnetoelectric Ni/(011) [Pb(Mg<sub>1/3</sub>Nb<sub>2/3</sub>)O<sub>3</sub>]<sub>(1-x)</sub>–[PbTiO<sub>3</sub>]<sub>x</sub> heterostructure,” *Appl. Phys. Lett.*, vol. 98, no. 1, p. 12504, 2011, doi: 10.1063/1.3534788.
- [173] A. A. Bukharaev, A. K. Zvezdin, A. P. Pyatakov, and Y. K. Fetisov, “Straintronics: a new trend in micro- and nanoelectronics and material science,” *Physics-Uspekhi*, vol. 61, no. 12, pp. 1175–1212, 2018, doi: 10.3367/ufnr.2018.01.038279.
- [174] M. T. McCray, M. A. Abeed, and S. Bandyopadhyay, “Electrically programmable probabilistic bit anti-correlator on a nanomagnetic platform,” *Sci. Rep.*, vol. 10, no. 1, p.

- 12361, 2020, doi: 10.1038/s41598-020-68996-y.
- [175] A. B. Ustinov *et al.*, “Dynamic electromagnonic crystal based on artificial multiferroic heterostructure,” *Commun. Phys.*, vol. 2, no. 1, p. 137, 2019, doi: 10.1038/s42005-019-0240-7.
- [176] A. K. Biswas, J. Atulasimha, and S. Bandyopadhyay, “The straintronic spin-neuron,” *Nanotechnology*, vol. 26, no. 28, p. 285201, 2015, doi: 10.1088/0957-4484/26/28/285201.
- [177] S. Boyn *et al.*, “Learning through ferroelectric domain dynamics in solid-state synapses,” *Nat Commun*, vol. 8, p. 14736, 2017, doi: 10.1038/ncomms14736.
- [178] H. Uršič, M. Santo Zarnik, and M. Kosec, “Pb(Mg 1/3 Nb 2/3 )O 3 –PbTiO 3 (PMN-PT) Material for Actuator Applications,” *Smart Mater. Res.*, vol. 2011, p. 452901, 2011, doi: 10.1155/2011/452901.
- [179] M. Acosta *et al.*, “BaTiO<sub>3</sub>-based piezoelectrics: Fundamentals, current status, and perspectives,” *Appl. Phys. Rev.*, vol. 4, no. 4, p. 041305, 2017, doi: 10.1063/1.4990046.
- [180] J. J. Yang *et al.*, “Electric field manipulation of magnetization at room temperature in multiferroic CoFe<sub>2</sub>O<sub>4</sub>/Pb(Mg<sub>1/3</sub>Nb<sub>2/3</sub>)<sub>0.7</sub>Ti<sub>0.3</sub>O<sub>3</sub> heterostructures,” *Appl. Phys. Lett.*, vol. 94, no. 21, p. 212504, 2009, doi: 10.1063/1.3143622.
- [181] J. Ryu *et al.*, “Ubiquitous magneto-mechano-electric generator,” *Energy Environ. Sci.*, vol. 8, no. 8, pp. 2402–2408, 2015, doi: 10.1039/c5ee00414d.
- [182] M. Ghidini *et al.*, “Shear-strain-mediated magnetoelectric effects revealed by imaging,” *Nat. Mater.*, vol. 18, no. 8, pp. 840–845, 2019, doi: 10.1038/s41563-019-0374-8.
- [183] H. Xu *et al.*, “Strain-mediated converse magnetoelectric coupling in  $\text{La}_{0.7}\text{Sr}_{0.3}\text{MnO}_3/\text{Pb}(\text{Mg}_{1/3}\text{Nb}_{2/3})\text{O}_3\text{-PbTiO}_3$  multiferroic heterostructures,” *Cryst. Growth Des.*, vol. 18, no. 10, pp. 5934–5939, 2018, doi: 10.1021/acs.cgd.8b00702.
- [184] A. Herklotz, J. D. Plumhof, A. Rastelli, O. G. Schmidt, L. Schultz, and K. Dörr,

- “Electrical characterization of PMN-28%PT(001) crystals used as thin-film substrates,” *J. Appl. Phys.*, vol. 108, no. 9, p. 094101, 2010, doi: 10.1063/1.3503209.
- [185] D. Seguin, M. Sunder, L. Krishna, A. Tatarenko, and P. D. Moran, “Growth and characterization of epitaxial Fe<sub>0.8</sub>Ga<sub>0.2</sub>/0.69PMN-0.31PT heterostructures,” *J. Cryst. Growth*, vol. 311, no. 12, pp. 3235–3238, 2009, doi: 10.1016/j.jcrysgro.2009.03.020.
- [186] O. Bilani-Zeneli *et al.*, “SrTiO<sub>3</sub> on piezoelectric PMN-PT(001) for application of variable strain,” *J. Appl. Phys.*, vol. 104, no. 5, p. 054108, 2008, doi: 10.1063/1.2975167.
- [187] A. Kumar Biswas, H. Ahmad, J. Atulasimha, and S. Bandyopadhyay, “Experimental Demonstration of Complete 180° Reversal of Magnetization in Isolated Co Nanomagnets on a PMN–PT Substrate with Voltage Generated Strain,” *Nano Lett.*, vol. 17, no. 6, pp. 3478–3484, 2017, doi: 10.1021/acs.nanolett.7b00439.
- [188] J. Cui *et al.*, “A method to control magnetism in individual strain-mediated magnetoelectric islands A method to control magnetism in individual strain-mediated magnetoelectric islands,” *Appl. Phys. Lett.*, vol. 103, p. 232905, 2015, doi: 10.1063/1.4838216.
- [189] C. Y. Liang *et al.*, “Electrical control of a single magnetoelastic domain structure on a clamped piezoelectric thin film - Analysis,” *J. Appl. Phys.*, vol. 116, no. 12, p. 123909, 2014, doi: 10.1063/1.4896549.
- [190] S. R. Sutton and M. L. Rivers, “Hard X-ray synchrotron microprobe techniques and applications,” in *In D. Schulze, P. Bertsch, and J. Stucki, Eds. Synchrotron X-ray Methods in Clay Science*, Clay Mineral Society of America, Aurora, CO, 1999, pp. 146–163.
- [191] A. R. Bishop, T. Lookman, A. Saxena, K. Rasmussen, and S. R. Shenoy, “Ferroelastic dynamics and strain compatibility,” *Phys. Rev. B - Condens. Matter Mater. Phys.*, vol. 67, no. 2, p. 024114, 2003, doi: 10.1103/PhysRevB.67.024114.

- [192] H. Wan, C. Luo, W. Y. Chang, Y. Yamashita, and X. Jiang, “Effect of poling temperature on piezoelectric and dielectric properties of 0.7Pb(Mg $_{1/3}$ Nb $_{2/3}$ )O $_3$ -0.3PbTiO $_3$  single crystals under alternating current poling,” *Appl. Phys. Lett.*, vol. 114, no. 17, pp. 0–5, 2019, doi: 10.1063/1.5094362.
- [193] J. Zhao, “Inhomogeneous Electric Field-Induced Domain Reorientation and Phase Transitions in Ferroelectrics,” North Carolina State University, 2020.
- [194] W. Y. Chang *et al.*, “Patterned nano-domains in PMN-PT single crystals,” *Acta Mater.*, vol. 143, pp. 166–173, 2018, doi: 10.1016/j.actamat.2017.10.016.
- [195] J. Wang *et al.*, “Ferroelectric domain configuration and piezoelectric responses in (001)-oriented PMN-PT films,” *Mater. Charact.*, vol. 48, no. 2–3, pp. 215–220, 2002, doi: 10.1016/S1044-5803(02)00242-5.
- [196] Jonas, “Violin Plots for plotting multiple distributions (distributionPlot.m),” *MATLAB Central File Exchange*, 2020. [Online]. Available: <https://www.mathworks.com/matlabcentral/fileexchange/23661-violin-plots-for-plotting-multiple-distributions-distributionplot-m>.
- [197] C. V. Stan and N. Tamura, “Synchrotron X-ray microdiffraction and fluorescence imaging of mineral and rock samples,” *J. Vis. Exp.*, vol. 136, no. 136, p. e57874, 2018, doi: 10.3791/57874.
- [198] G. Esteves, K. Ramos, C. M. Fancher, and J. L. Jones, “LIPRAS : Line-Profile Analysis Software Peak Fitting with LIPRAS,” no. March. p. LIPRAS, 2017, doi: 10.13140/RG.2.2.29970.25282/3.
- [199] T. H. Topper, J. J. F. Bonnen, M. Khalil, and A. Varvani-Farahani, “The influence of biaxial strain ratio and strain range on crack growth mode and crack shape,” *J. Mater. Sci.*, vol. 46, no. 1, pp. 215–227, 2011, doi: 10.1007/s10853-010-4928-z.